International Journal of Biomedical Imaging

Recent Advances in Mathematical Methods for the Analysis of Biomedical Images

Guest Editor: Guowei Wei

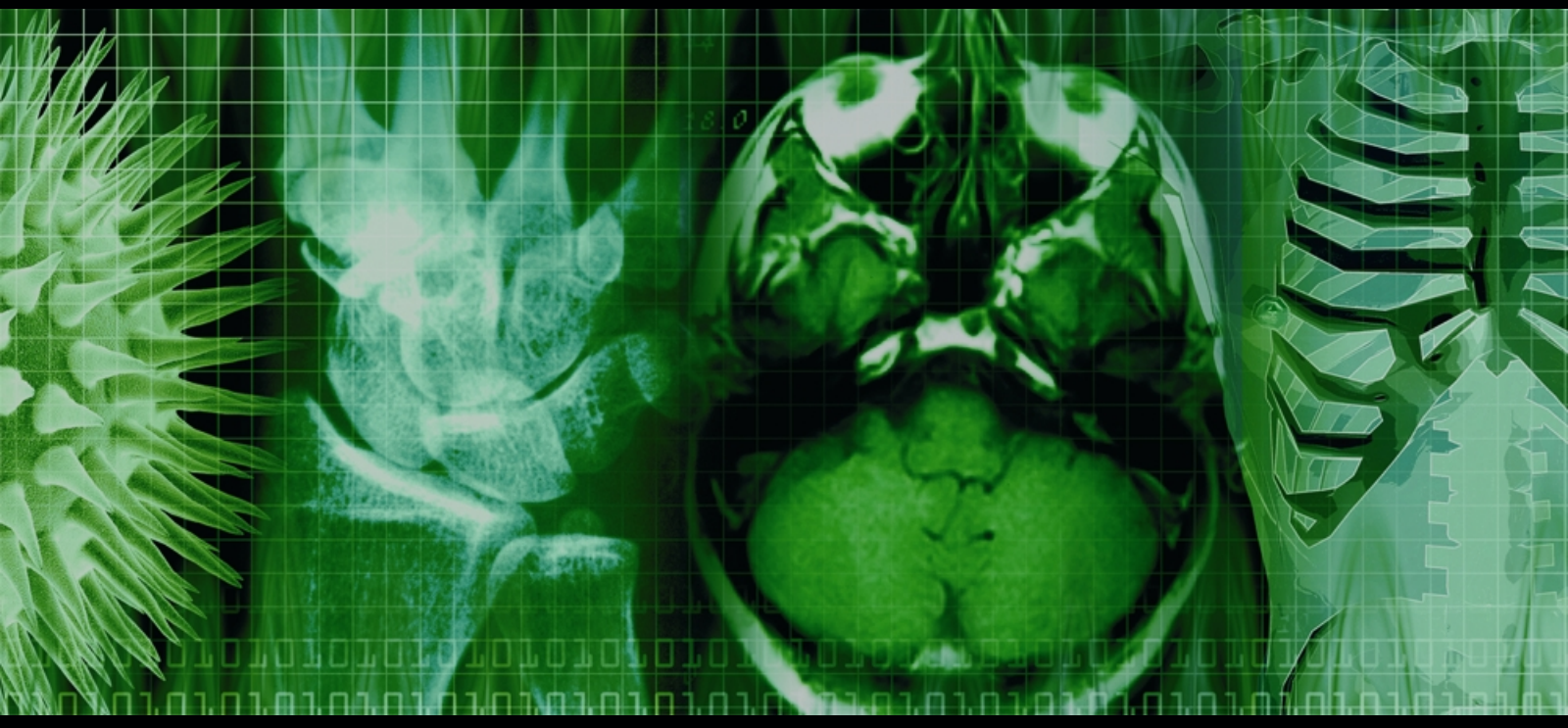

International Journal of Biomedical Imaging

Recent Advances in Mathematical Methods for the Analysis of Biomedical Images

International Journal of Biomedical Imaging

Recent Advances in Mathematical Methods for the Analysis of Biomedical Images

Guest Editor: Guowei Wei

Contents

Recent Advances in Mathematical Methods for the Analysis of Biomedical Image, Guowei Wei
Volume 2006 (2006), Article ID 70578, 1 pages

A Stochastic-Variational Model for Soft Mumford-Shah Segmentation, Jianhong (Jackie) Shen
Volume 2006 (2006), Article ID 92329, 14 pages

3D Brain Segmentation Using Dual-Front Active Contours with Optional User Interaction, Hua Li, Anthony Yezzi, and Laurent D. Cohen
Volume 2006 (2006), Article ID 53186, 17 pages

Total Variation Wavelet-Based Medical Image Denoising, Yang Wang and Haomin Zhou
Volume 2006 (2006), Article ID 89095, 6 pages

BOLD Noise Assumptions in fMRI, Alle Meije Wink and Jos B. T. M. Roerdink
Volume 2006 (2006), Article ID 12014, 11 pages

Unsupervised Detection of Suspicious Tissue Using Data Modeling and PCA, Ikhlas Abdel-Qader, Lixin Shen, Christina Jacobs, Fadi Abu Amara, and Sarah Pashaie-Rad
Volume 2006 (2006), Article ID 57850, 11 pages

Intervention Models in Functional Connectivity Identification Applied to fMRI, João Ricardo Sato, Daniel Yasumasa Takahashi, Ellison Fernando Cardoso, Maria da Graça Morais Martin, Edson Amaro Júnior, and Pedro Alberto Morettin
Volume 2006 (2006), Article ID 27483, 7 pages

Virtual Contrast for Coronary Vessels Based on Level Set Generated Subvoxel Accurate Centerlines, Ingmar Bitter, Robert Van Uitert, Ivo Wolf, Efstathia Tzatha, Ahmed M Gharib, Ronald Summers, Hans-Peter Meinzer, and Roderic Pettigrew
Volume 2006 (2006), Article ID 94025, 8 pages

Probabilistic Model-Based Cell Tracking, Nezamoddin N. Kachouie, Paul Fieguth, John Ramunas, and Eric Jervis
Volume 2006 (2006), Article ID 12186, 10 pages

Reciprocal Benefits of Mass-Univariate and Multivariate Modeling in Brain Mapping: Applications to Event-Related Functional MRI, H215O-, and FDG-PET, James R. Moeller and Christian G. Habeck
Volume 2006 (2006), Article ID 79862, 13 pages

A Review on MR Image Intensity Inhomogeneity Correction, Zujun Hou
Volume 2006 (2006), Article ID 49515, 11 pages

Hindawi Publishing Corporation
International Journal of Biomedical Imaging
Volume 2006, Article ID 70578, Pages 1–1
DOI 10.1155/IJBI/2006/70578

Editorial

Recent Advances in Mathematical Methods for the Analysis of Biomedical Image

Guowei Wei

Department of Mathematics and Department of Electrical and Computer Engineering, Michigan State University, East Lansing, MI 48824, USA

Received 10 September 2006; Accepted 10 September 2006

Image analysis, an interdisciplinary field where one witnesses the crossing contribution from engineers, scientists and mathematicians, is of paramount importance for a wide range of technologies, such as computer vision, pattern recognition, artificial intelligence, and biomedical imaging. During the last few years, there have been important advances in the development of the next generation of mathematical methods for image analysis. While progress in the fundamentals and applications has been rapid, many challenges remain. This special issue is a collection of high quality, peer-reviewed, original research papers illustrating recent progress and future directions in the area of mathematical analysis of biomedical images.

The editor of this special issue expresses his sincere thanks to the contributing authors and reviewers for making this publication possible and successful.

Guowei Wei

Guowei Wei received his Ph.D. degree from the University of British Columbia in 1996. With a postdoctoral fellowship Award from the NSERC of Canada, he did research work at the University of Houston, where he was appointed as a Research Assistant Professor in 1997. In 1998, he joined the Faculty of the National University of Singapore and was promoted to Associate Professor in 2001. In 2002, he relocated to Michigan State University, where he is currently an Associate Professor of Mathematics and Electrical and Computer Engineering. He has advised 10 doctoral students, 7 master students, and 8 postdoctoral fellows. He has authored or coauthored over 130 refereed journal papers. His current research interests include scientific and engineering computations, biomedical image analysis, controlling chaos and turbulence, mathematical modeling, and computation of protein structures and interactions.

Hindawi Publishing Corporation
International Journal of Biomedical Imaging
Volume 2006, Article ID 92329, Pages 1–14
DOI 10.1155/IJBI/2006/92329

A Stochastic-Variational Model for Soft Mumford-Shah Segmentation

Jianhong (Jackie) Shen[1, 2]

[1] *School of Mathematics, Institute of Technology, University of Minnesota, Minneapolis, MN 55455, USA*
[2] *Lotus Hill Institute for Computer Vision and Information Science, E'Zhou, Wuhan 436000, China*

Received 20 September 2005; Revised 13 February 2006; Accepted 17 February 2006

Recommended for Publication by Guowei Wei

In contemporary image and vision analysis, stochastic approaches demonstrate great flexibility in representing and modeling complex phenomena, while variational-PDE methods gain enormous computational advantages over Monte Carlo or other stochastic algorithms. In combination, the two can lead to much more powerful novel models and efficient algorithms. In the current work, we propose a stochastic-variational model for *soft* (or fuzzy) Mumford-Shah segmentation of mixture image patterns. Unlike the classical *hard* Mumford-Shah segmentation, the new model allows each pixel to belong to each image pattern with some probability. Soft segmentation could lead to hard segmentation, and hence is more general. The modeling procedure, mathematical analysis on the existence of optimal solutions, and computational implementation of the new model are explored in detail, and numerical examples of both synthetic and natural images are presented.

1. INTRODUCTION: SOFT VERSUS HARD SEGMENTATION

Segmentation is the key step towards high-level vision modeling and analysis, including object characterization, detection, and classification. There have been some recent developments indicating that certain high-level visual tasks such as global scene interpretation might be able to bypass segmentation [1, 2]. Nevertheless, segmentation still remains perhaps *the* most important and inspiring task to date in low- or middle-level vision analysis and image processing.

The segmentation problem can be formulated as follows. Given an image $I \in L^2(\Omega)$ on a 2-dimensional (2D) domain Ω (assumed to be bounded, smooth, and open), one seeks out a *closed* "edge set" Γ, and all the connected components $\Omega_1, \ldots, \Omega_K$ of $\Omega \setminus \Gamma$, such that by certain suitable visual measure (e.g., textural or photometric), the image I is discontinuous along Γ while smooth or homogeneous on each segment Ω_i. Each image patch $I_i = I|_{\Omega_i}$ is also called a *pattern*, and Ω_i is its *support*.

We will call this most common practice "hard" segmentation. A hard segmentation partitions the image domain Ω along a *definitive* edge set Γ, and outputs *nonoverlapping* pattern supports $\Omega_1, \ldots, \Omega_K$.

The present work introduces the notion of "soft" segmentation. Mathematically, a hard segmentation amounts to the partition of the unit using indicator functions:

$$1_\Omega(x) = \sum_{i=1}^{K} 1_{\Omega_i}(x), \quad \text{a.e. (in Lebesgue) } x = (x_1, x_2) \in \Omega. \tag{1}$$

A soft segmentation seeks out instead a softer partition of the unit:

$$1_\Omega(x) = \sum_{i=1}^{K} p_i(x), \tag{2}$$

where p_i's are continuous or smoother functions. Formally, each p_i could be considered as the mollified version of $1_{\Omega_i}(x)$.

In the stochastic literature of image analysis and modeling, the above notion of soft segmentation is closely connected to *mixture image models* (e.g., [3]). Suppose a given image I is composed of K unknown patterns:

$$\omega = 1, \omega = 2, \ldots, \omega = K, \tag{3}$$

where ω denotes the pattern label variable. At each pixel $x \in \Omega$, $\omega(x) \in \{1, \ldots, K\}$ becomes a random variable. Then the

Figure 1: Natural images often do not have clear-cut "hard" boundaries between different patterns. Along the arrow, for example, one only observes that the sand pattern *gradually* becomes a grass pattern. Such a "soft" view is the stochastic view on the segmentation problem.

p_i's in (2) carry the natural stochastic interpretation:

$$p_i(x) = \text{Prob}\,(\omega(x) = i), \quad i = 1 : K. \tag{4}$$

For this reason, each p_i will be called the *ownership* of pattern i, following Jepson and Black [3]. (Some authors also prefer to call it the *membership* [4].) Instead of the repulsive ownership in a hard segmentation, a soft one allows each pattern to "own" a pixel with some likelihood.

Soft segmentation is more general since it can lead to natural hard segmentation under the *maximum-likelihood* (ML) principle. Given a soft segmentation $\{p_i(x) : i = 1 : K\}$, one can define for each pixel $x \in \Omega$ its unique owner $\omega_*(x)$ by

$$\omega_*(x) = \arg\max_{\omega \in 1:K} p_\omega(x), \tag{5}$$

and if the maxima are nonunique, accept the largest index from the arg max pool. The segments are then defined by

$$\Omega_i = \omega_*^{-1}(i) = \{x \in \Omega \mid \omega_*(x) = i\}, \quad i = 1 : K, \tag{6}$$

which leads to a natural hard segmentation. Formula (5) and (6) are called the *hardening formulae*.

Soft segmentation has been motivated by practical analysis of natural images. Patterns in natural scenes often do not have clear-cut boundaries. In Figure 1, for example, there does not seem to exist a "hard" boundary between the grass and sand areas. If one draws an oriented line as shown in the figure, it makes more sense to state that along the arrow, the pattern transits from being "more" sand-like to being "more" grass-like. Such consideration favors the following stochastic view that along the arrow, the ownership

$$\begin{aligned} &\text{Prob}\,(\omega(x) = \text{grass}) \text{ increases,} \\ &\text{while Prob}\,(\omega(x) = \text{sand}) \text{ decreases.} \end{aligned} \tag{7}$$

In the present work, we propose a new stochastic-variational soft segmentation model for the following celebrated Mumford-Shah model [5, 6]:

$$\min_{\Gamma,u} E[u, \Gamma \mid I] = \min_{\Gamma,u} \mathcal{H}^1(\Gamma) + \alpha \int_{\Omega\setminus\Gamma} |\nabla u|^2 + \lambda \int_\Omega (u - I)^2, \tag{8}$$

where $\mathcal{H}^1$ stands for the 1D Hausdorff measure [7], which is simply the length when Γ is regular enough. *For notational conciseness, the default area-element symbol $dx = dx_1 dx_2$ will be omitted in most integral formulae.*

As stated in the abstract, the stochastic softness induces more flexibility and universality in modeling, while the variational-PDE approach facilitates rigorous mathematical analysis as well as more efficient computational implementations compared with purely stochastic approaches including, for example, the Monte Carlo method or Gibbs' sampling [8–11].

The paper has been organized as follows. Section 2 builds up the soft Mumford-Shah (SMS) model under the Bayesian rationale and the MAP estimator [12, 13], which are the formal stochastic foundations of the present model. In Section 3, the prior energy on the ownerships p_i's is developed based on the celebrated work of Modica and Mortola [14] on phase-field modeling and Γ-convergence approximation in material sciences and phase transitions. In Section 4, we analyze the main mathematical properties of the proposed SMS model, including the admissible space, hidden symmetry and symmetry breaking via weak supervision, and the existence theorems. In Section 5, we then derive the system of Euler-Lagrange equations of the SMS model for which the role of the probability simplex constraint is discussed in detail. Section 5 also introduces the alternating-minimization algorithm to compute the Euler-Lagrange equations. Finally, the numerical performance of the SMS model is demonstrated in Section 6 via both synthetic and natural test images that are sufficiently representative and generic.

Throughout the manuscript, the notation $F[X, Y \mid Z]$ in the deterministic setting always denotes a quantity (often a functional, or an energy) F that depends on X, Y, and Z but with Z given or fixed. Similarly, $F[X \mid Y, Z]$ still denotes $F[X, Y \mid Z]$ modulo some additive quantity $g[Y, Z]$ that is often unimportant as far as the optimization on X (given Y and Z) is concerned. These notations therefore have been inspired by *conditional probabilities* in the stochastic setting (formally under the Gibbs' correspondence: $F[X \mid Y] = -\log p(X \mid Y)$).

2. BAYESIAN RATIONALE TO THE NEW MODEL AND GAUSSIAN MIXTURE

2.1. Bayesian rationale

Segmentation can be done in some feature spaces such as gradient-like highpass features or Gabor features (e.g., [11, 15, 16]). The Mumford-Shah model easily extends to such general features (e.g., [15]), even though it was originally

formulated only for intensity fields. For maximal clarity in exposing the core ideas of the current work, we will also focus only on the latter, while leaving as canonical exercises to adapt the new model for any given feature distribution.

Let K be the total number of intended patterns. As in [10, 11], K could also be treated as an unknown to be optimally estimated, which however does not add much to the most significant contribution (i.e., the modeling and computation of the "softening" procedure) of the present work.

Given an image input $I = I(x)$ on a bounded, regular, and open domain Ω, the primary goal of soft segmentation is to compute the ownerships

$$p_1(x), p_2(x), \ldots, p_K(x). \tag{9}$$

Define $\mathbf{P}(x) = (p_1(x), p_2(x), \ldots, p_K(x))$, and

$$\Delta_{K-1} = \text{convex hull of } \vec{e}_1, \ldots, \vec{e}_K, \tag{10}$$

where the $(\vec{e}_i \mid i = 1 : K)$ denotes the canonical Cartesian basis of $\mathbb{R}^K$. Δ_{K-1} is often called the *canonical* $(K-1)$-simplex, or the *probability* simplex in $\mathbb{R}^K$. Then

$$\mathbf{P} : \Omega \longrightarrow \Delta_{K-1}, \qquad x \longrightarrow \mathbf{P}(x), \tag{11}$$

meaning that the total ownerships always add up to 100% at any pixel $x \in \Omega$.

Associated with each pattern label, $\omega = i$ is a smooth function $u_i(x) \in H^1(\Omega)$, similar to the original Mumford-Shah model. Here the Sobolev space $H^1(\Omega)$ is defined by [17]

$$H^1(\Omega) = \{u \in L^2(\Omega) \mid \nabla u \in L^2(\Omega, \mathbb{R}^2)\}. \tag{12}$$

Define $\mathbf{U}(x) = (u_1(x), u_2(x), \ldots, u_K(x))$. Then the goal of soft segmentation is to estimate the optimal vectorial pair of ownerships and patterns given an image I:

$$(\mathbf{P}_*, \mathbf{U}_*) = \arg\max_{(\mathbf{P},\mathbf{U})} \text{Prob}\,(\mathbf{P}, \mathbf{U} \mid I). \tag{13}$$

By the Bayesian formula [12, 13], the posterior given I is expressible via

$$\frac{\text{Prob}\,(\mathbf{P}, \mathbf{U} \mid I) = \text{Prob}\,(I \mid \mathbf{P}, \mathbf{U})\,\text{Prob}(\mathbf{P})\,\text{Prob}(\mathbf{U})}{\text{Prob}(I)}, \tag{14}$$

assuming that the mixture patterns $\mathbf{U}$ and the mixture rules $\mathbf{P}$ are *independent* (as two vectorial random fields). We will call the first term a "mixture generation" model, since it reveals how the image data should look like given the information of the patterns and their ownerships.

By taking logarithmic likelihood $E[\cdot] = -\log \text{Prob}(\cdot)$, or the formally Gibbs' energy in statistical mechanics [18, 19], one attains the soft segmentation model in its "energy" form:

$$\begin{aligned} &\arg\min_{(\mathbf{P},\mathbf{U})} E[\mathbf{P}, \mathbf{U} \mid I] \\ &\quad = \arg\min_{(\mathbf{P},\mathbf{U})} E[I \mid \mathbf{P}, \mathbf{U}] + E[\mathbf{P}] + E[\mathbf{U}]. \end{aligned} \tag{15}$$

Assuming that all the pattern channels are independent of each other, one has

$$E[\mathbf{U}] = E[u_1, \ldots, u_K] = \sum_{i=1}^{K} E[u_i \mid i]. \tag{16}$$

That is, we assume that $\mathbf{U}$ as a random vector field has independent scalar components. It has been motivated by the facts that 2D images are the optical projections of 3D scenes and that different objects in 3D are independently positioned in different ranges or depths.

For Sobolev-regular patterns, that is, functions whose gradients are square integrable, one may impose the homogeneous Sobolev energies:

$$E[u_i \mid i] = E[u_i] = \alpha \int_\Omega |\nabla u_i|^2, \quad i = 1 : K, \tag{17}$$

for some scalar weight α that models the visual sensitivity to intensity roughness. Unlike the original Mumford-Shah model, the energy for each channel has been defined on the entire image domain Ω instead of on each "hard-cut" patch Ω_i. Thus the energy form (17) must carry out *extrapolation* for practical applications. Long-range extrapolations are, however, often unimportant after being weighed down by their negligible ownerships p_i's.

2.2. Gaussian mixture with smooth mean fields

In this section we discuss the mixture generation model $\text{Prob}(I \mid \mathbf{P}, \mathbf{U})$ or $E[I \mid \mathbf{P}, \mathbf{U}]$.

Assume that the patterns are all Gaussian with mean fields $u_1, u_2, \ldots, u_K$. For simplicity, also assume that they share the same variance σ^2 (which readily generalizes to the more general case with variations). Then at any given pixel $x \in \Omega$,

$$(I \mid \omega(x) = i) \sim N(u_i(x), \sigma^2), \quad i = 1 : K. \tag{18}$$

Define the Gaussian probability density function (pdf)

$$g(I \mid m, \sigma) = \frac{1}{\sqrt{2\pi}\sigma} \exp\left(-\frac{(I-m)^2}{2\sigma^2}\right). \tag{19}$$

The pdf of the mixture image I at any pixel x is given by

$$\begin{aligned} &\text{Prob}\,(I(x) \mid \mathbf{P}(x), \mathbf{U}(x)) \\ &\quad = \sum_{i=1}^{K} \text{Prob}\,(I \mid \omega(x) = i)\,\text{Prob}(\omega(x) = i) \\ &\quad = \sum_{i=1}^{K} g(I \mid u_i(x), \sigma)\, p_i(x). \end{aligned} \tag{20}$$

Thus *ideally* the "energy" for the mixture generation model should be given by

$$\begin{aligned} E[I \mid \mathbf{P}, \mathbf{U}] &= E_\mu[I \mid \mathbf{P}, \mathbf{U}] \\ &= -\mu \int_\Omega \log\left(\sum_{i=1}^{K} g(I \mid u_i(x), \sigma)\, p_i(x)\right), \\ &\qquad \text{for some } \mu > 0, \end{aligned} \tag{21}$$

provided that given two fields $\mathbf{P}$ and $\mathbf{U}$ on Ω, for any two disjoint and finite sets of pixels X and Y,

$$(I(X) \mid \mathbf{P}, \mathbf{U}) \text{ is independent of } (I(Y) \mid \mathbf{P}, \mathbf{U}). \tag{22}$$

Here $I(X) = \{I(x) \mid x \in X\}$. (We also must emphasize that the above derivation should be considered as motivational rather than rigorous, due to the continuum setting.)

In the current work, we will adopt a reduced form of the complex formula (21), which is simpler and easier to manage both in theory and for computation. Assume that each soft ownership $p_i(x)$ is closer to a hard one $p_i(x) \simeq 1_{\Omega_i}(x)$ for $i = 1 : K$. Then

$$\begin{aligned} &-\log\left(\sum_{i=1}^{K} g(I \mid u_i(x), \sigma)\, p_i(x)\right) \\ &\simeq -\log\left(\sum_{i=1}^{K} g(I \mid u_i(x), \sigma) 1_{\Omega_i}(x)\right) \\ &= -\sum_{i=1}^{K} \log g(I \mid u_i(x), \sigma) 1_{\Omega_i}(x) \quad \text{(a.e.)} \\ &\simeq -\sum_{i=1}^{K} \log g(I \mid u_i(x), \sigma)\, p_i(x) \\ &= \frac{1}{2\sigma^2} \sum_{i=1}^{K} (I - u_i(x))^2 p_i(x) + \text{const}, \end{aligned} \tag{23}$$

where the additive constant only depends on σ and K. This suggests the following convenient energy form for the mixture generation model:

$$E[I \mid \mathbf{P}, \mathbf{U}] = \lambda \int_\Omega \left(\sum_{i=1}^{K} (I - u_i(x))^2 p_i(x)\right), \tag{24}$$

which amounts to a weighted least-square energy [20]. The weight λ reflects visual sensitivity to synthesis errors.

In combination of (15), (17), and (24), the new soft segmentation model takes the form of minimizing

$$\begin{aligned} E[\mathbf{P}, \mathbf{U} \mid I] = \lambda &\sum_{i=1}^{K} \int_\Omega (I - u_i(x))^2 p_i(x) \\ &+ \alpha \sum_{i=1}^{K} \int_\Omega |\nabla u_i|^2 + E[\mathbf{P}]. \end{aligned} \tag{25}$$

Notice that here the ownership distribution $\mathbf{P}$ "softens" the "hard" segmentation boundary Γ in the original Mumford-Shah model (8). To complete the modeling process, it suffices to properly define the prior or regularity energy $E[\mathbf{P}]$, which is the main task of the next section.

3. MODICA-MORTOLA'S PHASE-FIELD MODEL FOR OWNERSHIP ENERGY

To generalize but not to deviate too far from classical hard segmentation, it is natural to impose the following two constraints:

(a) each pattern ownership $p_i(x)$ has almost only two phases: on (corresponding to $p_i = 1$) and off (to $p_i = 0$), and the transition band in between is narrow;
(b) the soft boundaries, or equivalently the transition bands, are *regular*, instead of being zigzag.

In combination, one imposes the following Modica-Mortola type of energy with a double-well potential [14]: $p_i \in H^1(\Omega)$,

$$E_\varepsilon[p_i] = \int_\Omega \left(9\varepsilon |\nabla p_i|^2 + \frac{(p_i(1 - p_i))^2}{\varepsilon}\right), \quad i = 1 : K. \tag{26}$$

Here $\varepsilon \ll 1$ controls the transition bandwidth. Since $\varepsilon \ll 1$, the second term necessarily demands $p_i \simeq 0$ or 1 to lower the energy, which well resonates with the expectation in (a). The first term, weighted by the small parameter ε, amounts to a regularity condition on each p_i, which meets the requirement in (b).

Energies in the form of (26) are very common in material sciences, including the theories of liquid crystals and phase transitions [21, 22]. Mathematically, they have been well studied in the framework of Γ-convergence [23], which we now give a brief introduction in the present context. We also refer the reader to the works of Ambrosio and Tortorelli [24, 25] on the Γ-convergence approximation to the classical Mumford-Shah segmentation model.

Recall that for any $q(x) \in L^1(\Omega)$, its *total variation* as a Radon measure is defined by [7, 26, 27]

$$\text{TV}[q] = \int_\Omega |Dq| = \sup_{\mathbf{g} \in C_0^1(\Omega, B^2)} \langle q, \nabla \cdot \mathbf{g} \rangle, \tag{27}$$

where B^2 stands for the unit disk centered at the origin in $\mathbb{R}^2$. (The TV measure was first introduced into image processing by Rudin et al. [28].) Define that for any $q \in L^1(\Omega)$,

$$E_0[q] = \begin{cases} \text{TV}[q] & \text{if } q = 0 \text{ or } 1, \text{a.e. on } \Omega, \\ \infty & \text{otherwise.} \end{cases} \tag{28}$$

As a result, a finite energy $E_0[q]$ necessarily implies that q has two phases only, and $E_0[q] = \text{TV}[q] = \text{Per}(q^{-1}(1))$ is the perimeter of the support region $V = q^{-1}(1)$.

Further define

$$L^1_{[0,1]}(\Omega) = \{q \in L^1(\Omega) \mid q(x) \in [0, 1],\ \forall x \in \Omega\} \tag{29}$$

to be a subspace of $L^1(\Omega)$ (as a metric space). Then Modica and Mortola's well-known results in [14] readily lead to the following theorem.

Theorem 1 (Γ-convergence approximation of a two-phase TV). *For any $q \in L^1_{[0,1]}(\Omega) \setminus H^1(\Omega)$, extend the definition of $E_\varepsilon[\cdot]$ in (26) by defining $E_\varepsilon[q] = +\infty$. Then*

$$E_\varepsilon \longrightarrow E_0$$
in the sense of Γ-convergence in the metric space $L^1_{[0,1]}(\Omega)$. (30)

That is,

(i) *for any $q_\varepsilon \to q$ in $L^1_{[0,1]}(\Omega)$ as $\varepsilon \to 0$,*

$$\liminf_{\varepsilon \to 0} E_\varepsilon[q_\varepsilon] \geq E_0[q]; \tag{31}$$

(ii) *for any* $q \in L^1_{[0,1]}(\Omega)$, *there exists some sequence* $(q^*_\varepsilon \mid \varepsilon)$, *such that* $q^*_\varepsilon \to q$ *as* $\varepsilon \to 0$, *and*

$$\lim_{\varepsilon\to 0} E_\varepsilon[q^*_\varepsilon] = E_0[q]. \tag{32}$$

We refer the reader to Modica and Mortola [14] for a proof (with some necessary modification). Here we only point out that the "tight" sequence $(q^*_\varepsilon \mid \varepsilon)$ in (ii) can be constructed using a smooth sigmoid transition across the hard boundary of a given two-phase function q. Recall as in the theory of neural networks [29] that a *sigmoid* transition between 0 and 1 is achieved by

$$\sigma(t) = \frac{1}{1+e^{-t}}, \quad -\infty < t < \infty. \tag{33}$$

The scaling parameter ε participates in the transition by the form of $\sigma(t/(3\varepsilon))$. In particular, ε indeed corresponds to the width of the transition band when t is a distance function.

This theorem reveals the close connection of the particular choice of $E_\varepsilon[p_i]$ in (26) with the original Mumford-Shah model.

Proposition 1. *Suppose that* p_ε*'s "optimally" (i.e., by the above sigmoidal transition) converge to a given 2-phase pattern* $1_V(x)$ *with a regular hard boundary* $\Gamma = \partial V$. *Then,*

$$E_\varepsilon[p_\varepsilon] \longrightarrow \mathit{length}(\Gamma) = \int_\Omega |D1_V(x)|. \tag{34}$$

Similar results have appeared in the earlier influential works of Ambrosio and Tortorelli [24, 25] on the Γ-convergence approximation to the Mumford-Shah model. The technique has also been extensively applied in image computation and modeling [30–35] to overcome the difficulty in representing and computing the free boundary Γ.

To summarize this section, we propose the following energy model for the ownership distribution $\mathbf{P}(x) = (p_1(x), p_2(x), \ldots, p_K(x))$:

$$E_\varepsilon[\mathbf{P}] = \sum_{i=1}^K E_\varepsilon[p_i] = \sum_{i=1}^K \int_\Omega \left(9\varepsilon |\nabla p_i|^2 + \frac{(p_i(1-p_i))^2}{\varepsilon}\right). \tag{35}$$

One, however, must realize that different ownerships are *not* decoupled by this energy though it has appeared so. The energy $E_\varepsilon[\mathbf{P}]$ must be coupled with the constraint of the probability simplex:

$$\mathbf{P}: \Omega \longrightarrow \Delta_{K-1}, \quad \text{or} \quad \sum_{i=1}^K p_i(x) \equiv 1, \quad p_i \geq 0, \ \forall x \in \Omega. \tag{36}$$

In particular, for small ε, although (35) implies that each ownership p_i tends to polarize to 0 or 1 independently, they have to cooperate with each other under the above simplex constraint to optimally share the ownerships.

4. SOFT MUMFORD-SHAH SEGMENTATION

4.1. The model and admission space

Combining the preceding two sections, we have developed the complete formula for soft Mumford-Shah segmentation with K patterns, that is, to minimize

$$E[\mathbf{P}, \mathbf{U} \mid I] = \lambda \sum_{i=1}^K \int_\Omega (u_i - I)^2 p_i + \alpha \sum_{i=1}^K \int_\Omega |\nabla u_i|^2 + \sum_{i=1}^K \int_\Omega \left(9\varepsilon |\nabla p_i|^2 + \frac{(p_i(1-p_i))^2}{\varepsilon}\right), \tag{37}$$

with the constraint that

$$\mathbf{P}: \Omega \longrightarrow \Delta_{K-1}, \quad \text{the probability } (K-1)\text{-simplex}, \tag{38}$$

that is, $p_i \geq 0$, $i = 1 : K$, and $\sum_{i=1}^K p_i = 1$. As discussed previously, it is this simplex constraint that induces coupling among different channels into the seemingly decoupled model (37).

Besides the simplex constraint, the last term in the energy (37) requires $p_i \in H^1(\Omega)$ for $i = 1 : K$. Similarly, the second term requires each pattern $u_i \in H^1(\Omega)$. Then with the assumption that

$$\text{"the given image } I \in L^2(\Omega)\text{,"} \tag{39}$$

$E[\mathbf{P}, \mathbf{U} \mid I]$ is well defined and finite for any admissible patterns $\mathbf{U}$ and pattern ownership distribution $\mathbf{P}$:

$$\text{adm}_K = \{(\mathbf{P}, \mathbf{U}) \mid p_i,\ u_i \in H^1(\Omega),\ i = 1 : K;\ \mathbf{P}: \Omega \longrightarrow \Delta_{K-1}\}. \tag{40}$$

4.2. Breaking the hidden symmetry via weak supervision

Let S_K denote the permutation group of $\{1, \ldots, K\}$. Each permutation $\sigma \in S_K$ is a 1-to-1 map:

$$\sigma: \{1, \ldots, K\} \longrightarrow \{1, \ldots, K\}, \tag{41}$$

so that $(\sigma(1), \ldots, \sigma(K))$ is a rearrangement of $\{1, \ldots, K\}$. For any K-tuple $F = (f_1, \ldots, f_K)$, one defines

$$F_\sigma = (f_{\sigma(1)}, f_{\sigma(2)}, \ldots, f_{\sigma(K)}). \tag{42}$$

Theorem 2 (hidden symmetry of SMS). *For any* $\sigma \in S_K$,

$$E[\mathbf{P}_\sigma, \mathbf{U}_\sigma \mid I] = E[\mathbf{P}, \mathbf{U} \mid I]. \tag{43}$$

In particular, suppose that

$$(\mathbf{P}^*, \mathbf{U}^*) = \arg\min_{(\mathbf{P},\mathbf{U})\in \text{adm}_K} E[\mathbf{P}, \mathbf{U} \mid I] \tag{44}$$

is an optimal pair. Then for any $\sigma \in S_K$, $(\mathbf{P}^*_\sigma, \mathbf{U}^*_\sigma)$ *is a minimizer as well.*

The proof is straightforward and thus omitted. Such symmetry not only worsens the nonuniqueness of the minima to the nonconvex energy functional in (37), but also potentially jitters intermediate solutions in iterative computational schemes (i.e., hysterical transitions in the admissible space).

To break the permutation symmetry, we turn to a weak supervision scheme in which a user specifies K distinct domain patches:

$$Q_1, Q_2, \ldots, Q_K, \tag{45}$$

and imposes the symmetry-breaking conditions:

$$p_i|_{Q_j} = \delta_{ij}, \quad i, j = 1 : K, \tag{46}$$

where δ_{ij} denotes Kronecker's delta. That is, a user requires each given patch Q_i to be a "pure" pattern exclusively labelled by i. Computationally, this weak supervision process can be automated based on multiscale patch statistics as in the contemporary works on scene recognition [1, 2], or more generally, the learning theory [36, 37].

4.3. Existence theorems for nonsupervision and supervision

In this section, we briefly state the existence theorems for the soft Mumford-Shah segmentation model (37) without or with the supervision (46). The detailed proof has been moved to the appendix, under the suggestion of one of our referees. Skipping this section will cause no serious problem in comprehending or implementing the models.

Theorem 3 (existence theorem for unsupervised SMS). *Suppose that $I \in L^2(\Omega)$. Then for any positive modeling parameters $(\lambda, \alpha, \varepsilon)$, a minimizer to the unsupervised soft Mumford-Shah model* (37) *must exist.*

Mathematically, the existence issue has special appeal to model developers, especially for models that are highly nonconvex. Nonconvex variational models normally fail to guarantee the uniqueness of optimal solutions, and existence is hence often the best one can attempt to establish theoretically [38]. Notice that most interesting variational models in contemporary image and visual analysis are nonconvex, which include, for example, the original Mumford-Shah model [6], various image restoration models (e.g., deblurring and dejittering) [7, 39], as well as most optical-flow models [38].

The theoretical proof in the appendix, however, does reveal an important behavior of the model (37) which carries practical implications. If certain channel i becomes dumb in the limiting process of the proof (i.e., the limit $p_i^* \equiv 0$ for a minimizing sequence), it has often been introduced unnecessarily in the first place, and the associated optimal pattern u_i^* could be any featureless constant image.

The related issue of determining an *optimal* class number K (i.e., without containing dumb channels nor missing visually important channels) is also intrinsically driven by the complexity theory of natural images, in particular, the multiscale complexity [40]. Theoretically, K could be any integer, ranging from zero to the infinity, as one zooms into the details of a continuum image from the atomic scale to the ordinary observational scales of the naked eyes. Thus ideally, K itself could be introduced as a random variable taking $0, 1, 2, \ldots$, and becomes part of the model itself. This idea has already been explored in purely stochastic settings, for example, see Tu and Zhu [10].

For the supervised scenario motivated earlier, the following existence theorem still holds.

Theorem 4. *Suppose that $I \in L^2(\Omega)$. Then an optimal pattern-ownership pair must exist to the soft Mumford-Shah segmentation model* (37) *with supervision* (46)*, assuming that each patch Q_i has a positive Lebesgue measure $|Q_i| > 0$.*

The proof is almost identical to the unsupervised case in the appendix, and simplifies substantially by noticing that no channel could become dumb due to supervision. Furthermore, the functions ρ_i's in the previous proof can be directly set to be

$$\rho_i = \frac{1}{|Q_i|} 1_{Q_i}(x), \quad i = 1 : K, \tag{47}$$

without the necessity of turning to Lemma 2.

4.4. Mixture of homogeneous Gaussians

When each pattern i is a homogeneous Gaussian $N(m_i, \sigma)$ with a distinct mean value m_i, one has

$$u_i(x) \equiv m_i, \quad x \in \Omega,\ i = 1 : K. \tag{48}$$

Define $\mathbf{m} = (m_1, \ldots, m_K)$. As a result, the soft Mumford-Shah model (37) simplifies to

$$\min_{(\mathbf{P},\mathbf{m})} E[\mathbf{P}, \mathbf{m} \mid I] = \min_{(\mathbf{P},\mathbf{m})} \lambda \sum_{i=1}^{K} \int_\Omega (I - m_i)^2 p_i + \sum_{i=1}^{K} \int_\Omega \left(9\varepsilon |\nabla p_i|^2 + \frac{(p_i(1-p_i))^2}{\varepsilon} \right). \tag{49}$$

Theorem 5. *Suppose that $I \in L^2(\Omega)$. Then a minimizer pair $(\mathbf{P}^*, \mathbf{m}^*)$ to $E[\mathbf{P}, \mathbf{m} \mid I]$ exists for both the unsupervised and supervised cases.*

The proof can be derived readily from the previous general cases and is hence left out. When $K = 2$, a similar model was proposed earlier by Shen [33] under the symmetrization transform:

$$p_1(x) = \frac{1 - z(x)}{2}, \quad p_2(x) = \frac{1 + z(x)}{2}, \quad z \in [-1, 1]. \tag{50}$$

The model (49) could be considered as the soft version of Chan-Vese model [41] from the point of view of region-based active contours. Chan and Vese have demonstrated that such a piecewise constant Mumford-Shah model (or the

CV model as popularly referred to in the present literature) is already powerful enough for a number of applications including medical imaging.

5. EULER-LAGRANGE EQUATIONS AND COMPUTATION ON $(K-1)$-SIMPLEX

5.1. Euler-Lagrange equations on $(K-1)$-simplex

To minimize the energy for the soft Mumford-Shah segmentation

$$E[\mathbf{P},\mathbf{U}\mid I]=\lambda\sum_{i=1}^{K}\int_{\Omega}(u_i-I)^2p_i+\alpha\sum_{i=1}^{K}\int_{\Omega}|\nabla u_i|^2 + \sum_{i=1}^{K}\int_{\Omega}\left(9\varepsilon|\nabla p_i|^2+\frac{(p_i(1-p_i))^2}{\varepsilon}\right), \tag{51}$$

one resorts to its gradient-descent flow or Euler-Lagrange equations. In this section, we discuss these equations and their practical computational schemes.

The first-order partial variation on $\mathbf{U}$ given $\mathbf{P}$ leads to, for $i=1:K$,

$$\alpha\Delta u_i+\lambda(I-u_i)p_i=0,\quad \text{on }\Omega;\qquad \frac{\partial u_i}{\partial\mathbf{n}}=0,\quad \text{along }\partial\Omega, \tag{52}$$

where $\mathbf{n}$ stands for the outer normal vector field along $\partial\Omega$. Thus the Euler-Lagrange equations on the patterns are all in the form of linear Poisson equations with variable coefficient fields:

$$-\alpha\Delta u_i+(\lambda p_i)u_i=f_i,\quad i=1:K, \tag{53}$$

with Neumann adiabatic boundary conditions, where the source terms are $f_i(x)=\lambda p_i(x)I(x)$.

The first-order variation on the ownerships $\mathbf{P}$ is carried out on the probability $(K-1)$-simplex Δ_{K-1}, which is a compact manifold (with border) of codimension 1 embedded in $\mathbb{R}^K$. Chan and Shen [42] developed a general framework for modeling and computing image features that "live" on general manifolds, and especially those that are embedded in $\mathbb{R}^K$. We will follow the approach there.

Without the simplex constraint on the ownerships, for any given $\mathbf{U}$, the first-order variation of the soft energy E under $\mathbf{P}\to\mathbf{P}+\delta\mathbf{P}$ is given by

$$\delta E=\int_{\Omega}\sum_{i=1}^{K}V_i\delta p_i\,dx+\int_{\partial\Omega}\sum_{i=1}^{K}v_i\delta p_i\,d\mathcal{H}^1, \tag{54}$$

where $\mathcal{H}^1$ is the 1D Hausdorff measure along $\partial\Omega$, and

$$V_i=\lambda(u_i-I)^2-18\varepsilon\Delta p_i+2\varepsilon^{-1}p_i(1-p_i)(1-2p_i), \tag{55}$$

$$v_i=18\varepsilon\frac{\partial p_i}{\partial\mathbf{n}},\quad \text{along }\partial\Omega. \tag{56}$$

Define $\mathbf{V}=(V_1,\ldots,V_K)$ and $\mathbf{v}=(v_1,\ldots,v_K)$. Then

$$\delta E=\int_{\Omega}\mathbf{V}\cdot\delta\mathbf{P}\,dx+\int_{\partial\Omega}\mathbf{v}\cdot\delta\mathbf{P}\,d\mathcal{H}^1, \tag{57}$$

which holds for any *free* variation of $\mathbf{P}$ in $\mathbb{R}^K$, or one writes in the free-gradient form

$$\frac{\partial E}{\partial_f\mathbf{P}}=\mathbf{V}\big|_{\Omega}+\mathbf{v}\big|_{\partial\Omega}. \tag{58}$$

In reality, $\mathbf{P}\in\Delta_{K-1}$. Let $T_{\mathbf{P}}\Delta_{K-1}$ denote the tangent space of Δ_{K-1} at any single point $\mathbf{P}\in\Delta_K$, and

$$\pi: T_{\mathbf{P}}\mathbb{R}^K\longrightarrow T_{\mathbf{P}}\Delta_{K-1} \tag{59}$$

the orthogonal projection onto the tangent space in $\mathbb{R}^K$. Since the normal direction of the tangent plane is given by $\mathbf{1}_K/\sqrt{K}=(1,\ldots,1)/\sqrt{K}$, the projection operator is explicitly given by, for any $\mathbf{w}\in T_{\mathbf{P}}\mathbb{R}^K$,

$$\pi(\mathbf{w})=\mathbf{w}-\frac{\mathbf{1}_K\langle\mathbf{w},\mathbf{1}_K\rangle}{K}=\mathbf{w}-\langle\mathbf{w}\rangle\mathbf{1}_K,\quad \text{with }\langle\mathbf{w}\rangle=\frac{1}{K}\sum_{i=1}^{K}w_i. \tag{60}$$

The constrained gradient of E on Δ_{K-1} is therefore given by

$$\frac{\partial E}{\partial\mathbf{P}}=\pi\left(\frac{\partial E}{\partial_f\mathbf{P}}\right)=(\mathbf{V}-\langle\mathbf{V}\rangle\mathbf{1}_K)\big|_{\Omega}+(\mathbf{v}-\langle\mathbf{v}\rangle\mathbf{1}_K)\big|_{\partial\Omega}. \tag{61}$$

In particular, the system of Euler-Lagrange equations on $\mathbf{P}$ given $\mathbf{U}$ is given by

$$\begin{aligned}&V_i(x)-\langle\mathbf{V}\rangle(x)=0,\quad x\in\Omega,\\ &v_i(z)-\langle\mathbf{v}\rangle(z)=0,\quad z\in\partial\Omega,\end{aligned} \tag{62}$$

for $i=1:K$. The coupling among different channels is evident from these two formulae.

Lemma 1. *Suppose that* $\mathbf{P}:\Omega\to\Delta_{K-1}$. *Then for any* $z\in\partial\Omega$, $\langle\mathbf{v}\rangle(z)=0$, *where the boundary "flux"* $\mathbf{v}$ *is defined in* (56).

Proof. This is obtained by direct computation: at any $z\in\partial\Omega$,

$$\begin{aligned}\langle\mathbf{v}\rangle&=\frac{1}{K}\sum_{i=1}^{K}v_i=\frac{18\varepsilon}{K}\sum_{i=1}^{K}\frac{\partial p_i}{\partial\mathbf{n}}\\ &=\frac{18\varepsilon}{K}\frac{\partial}{\partial\mathbf{n}}\left(\sum_{i=1}^{K}p_i\right)=\frac{18\varepsilon}{K}\frac{\partial 1}{\partial\mathbf{n}}=0.\end{aligned} \tag{63}$$

□

As a result, the boundary conditions in (62) simplify to the ordinary Neumann conditions $\partial p_i/\partial\mathbf{n}=0, i=1:K$. Combining all the above derivations, we have established the following theorem.

Theorem 6 (Euler-Lagrange equations). *The system of Euler-Lagrange equations of* $E[\mathbf{P},\mathbf{U}\mid I]$ *is given by*

$$\begin{aligned}&-\alpha\Delta u_i+(\lambda p_i)u_i=(\lambda p_i)I,\\ &-18\varepsilon\Delta p_i+2\varepsilon^{-1}p_i(1-p_i)(1-2p_i)\\ &\quad=\langle\mathbf{V}\rangle-\lambda(u_i-I)^2,\quad i=1:K,\end{aligned} \tag{64}$$

on Ω*, all with Neumann boundary conditions along* $\partial\Omega$*. Here* $\mathbf{V} = \mathbf{V}(\mathbf{P}, \mathbf{U})$ *is defined as in* (55)*. Furthermore, under supervision* (46)*, the ownerships must satisfy the interpolation conditions:*

$$p_i|_{Q_j} = \delta_{i,j}, \quad i, j = 1 : K, \tag{65}$$

or equivalently, the equations on p_i*'s in* (64) *hold on* $\Omega \setminus (\bigcup_{i=1}^{K} Q_i)$ *with Neumann conditions along* $\partial\Omega$*, and Dirichlet conditions along* $\bigcup_{i=1}^{K} \partial Q_i : p_i|_{\partial Q_j} = \delta_{i,j}$.

Similarly, one has the following result for the piecewise constant SMS model (49), which carries much lower complexity compared with the full SMS model.

Proposition 2 (Euler-Lagrange equations for piecewise constant SMS). *The Euler-Lagrange equations for* $E[\mathbf{P}, \mathbf{m} \mid I]$ *in* (49) *are given by*

$$\begin{aligned} m_i = \langle I \rangle_{p_i} &:= \frac{\int_\Omega I p_i}{\int_\Omega p_i}, \\ -18\varepsilon\Delta p_i + 2\varepsilon^{-1} p_i(1-p_i)(1-2p_i) &= \langle \mathbf{V} \rangle - \lambda (m_i - I)^2, \quad i = 1 : K, \end{aligned} \tag{66}$$

with Neumann conditions for all the ownerships p_i*'s along* $\partial\Omega$.

5.2. Computation of the Euler-Lagrange equations

Computationally, as well practiced in multivariate optimization problems, (64) and (66) can be solved via the algorithm of *alternating minimization* (AM) [30, 39]. The AM algorithm is closely connected to the celebrated expectation-maximization (EM) algorithm in statistical estimation problems with hidden variables [3, 43]. In the current context, the ownership distributions p_i's could be treated as the hidden variables.

Like EM, the AM algorithm is progressive. Given the current ($t = n$) best estimation of the patterns $\mathbf{U}^n = (u_i^n \mid i = 1 : K)$, by solving

$$\mathbf{P}^n = \arg\min_{\mathbf{P}} E[\mathbf{P} \mid \mathbf{U}^n, I], \tag{67}$$

or equivalently,

$$\begin{aligned} -18\varepsilon\Delta p_i + 2\varepsilon^{-1} p_i(1-p_i)(1-2p_i) \\ = \langle \mathbf{V}^n \rangle - \lambda (u_i^n - I)^2, \quad i = 1 : K, \end{aligned} \tag{68}$$

with Neumann boundary conditions, one obtains the current best estimation of the ownerships $\mathbf{P}^n = (p_i^n \mid i = 1 : K)$. Subsequently, based on $\mathbf{P}^n$, by solving

$$\mathbf{U}^{n+1} = \arg\min_{\mathbf{U}} E[\mathbf{U} \mid \mathbf{P}^n, I], \tag{69}$$

or equivalently,

$$-\alpha\Delta u_i + (\lambda p_i^n) u_i = (\lambda p_i^n) I, \quad i = 1 : K, \tag{70}$$

with Neumann boundary conditions, one completes a single round of pattern updating $\mathbf{U}^n \to \mathbf{U}^{n+1}$. The same procedure applies to the piecewise constant SMS equations in (66).

(a) (b)

Figure 2: Examples of (a) a 3-phase supervision and (b) a 4-phase supervision to break the symmetry in the model. Such weak supervision can also be automated based on multiscale patch statistics [1, 2].

Since the system (70) is linear and decoupled, the main computational complexity resides in the integration of (68), which is coupled and nonlinear due to the simplex constraint and the double-well potential in the energy. Define $e_i(x) = (u_i(x) - I(x))^2$ and $\mathbf{e} = (e_i \mid i = 1 : K)$. In order to solve

$$-18\varepsilon\Delta p_i + 2\varepsilon^{-1} p_i(1-p_i)(1-2p_i) = \langle \mathbf{V} \rangle - \lambda e_i \tag{71}$$

given $\mathbf{e}$ and $\mathbf{V} = \mathbf{V}(\mathbf{P}, \mathbf{U}) = \mathbf{V}(\mathbf{P}, \mathbf{e})$ (see (55)), first notice that

$$\begin{aligned} \langle \mathbf{V}(\mathbf{P}, \mathbf{e}) \rangle &= \frac{1}{K} \sum_{i=1}^{K} \left(-18\varepsilon\Delta p_i + \lambda e_i + 2\varepsilon^{-1} p_i(1-p_i)(1-2p_i) \right) \\ &= \frac{\lambda}{K} \sum_{i=1}^{K} e_i + \frac{2\varepsilon^{-1}}{K} \sum_{i=1}^{K} (2p_i^3 - 3p_i^2) + \frac{2\varepsilon^{-1}}{K}, \end{aligned} \tag{72}$$

since $\sum_{i=1}^{K} p_i = 1$ and $\Delta(\sum_{i=1}^{K} p_i) = 0$. We also split the double-potential force in (71) by

$$p_i(1-p_i)(1-2p_i) = p_i(1-p_i)^2 - p_i^2(1-p_i). \tag{73}$$

In combination, the nonlinear equation (71) can then be solved iteratively:

$$\cdots \longrightarrow \mathbf{P}^{\langle j \rangle} \longrightarrow \mathbf{P}^{\langle j+1 \rangle} \longrightarrow \cdots \tag{74}$$

by the following linearization procedure:

$$\begin{aligned} -18\varepsilon\Delta p_i^{\langle j+1 \rangle} + 2\varepsilon^{-1} p_i^{\langle j+1 \rangle} \left(1 - p_i^{\langle j \rangle}\right)^2 &= f_i^{\langle j \rangle}, \\ f_i^{\langle j \rangle} = -\lambda e_i + \langle \mathbf{V}(\mathbf{P}^{\langle j \rangle}, \mathbf{e}) \rangle + 2\varepsilon^{-1} \left(p_i^{\langle j \rangle}\right)^2 \left(1 - p_i^{\langle j \rangle}\right), \end{aligned} \tag{75}$$

with Neumann adiabatic boundary conditions for all the channels $i = 1 : K$. This system of linear Poisson equations can be conveniently integrated using any elliptic solvers. The detailed *numerical analysis* on the convergence behavior of the entire algorithm above, however, is still an open problem and well deserves some systematic investigation.

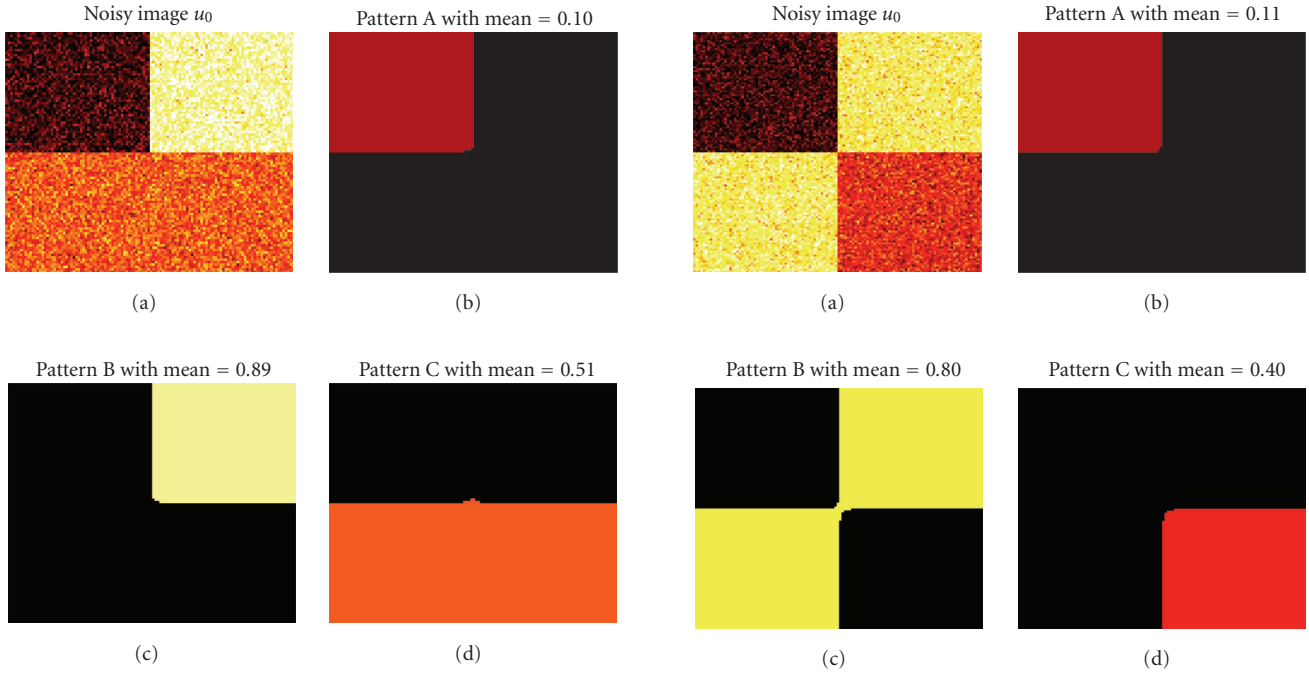

FIGURE 3: Synthetic image of a T-junction: hard segmentation from the SMS model via "hardening" formulae (5) and (6). The 120-degree regularization behavior at the junction point is also well known in the classical Mumford-Shah model [6].

FIGURE 4: Synthetic image of a narrow bottleneck: hard segmentation from the SMS model via "hardening" formulae (5) and (6). The thickening regularization at the bottleneck junction can be explained similarly by the classical Mumford-Shah model for which minimum-surface or "soap-foam" behavior arises due to the surface tension energy. Also, see the recent work by Kohn and Slastikov [45] for the singularity analysis of a similar problem arising from micromagnetism.

6. COMPUTATIONAL EXAMPLES

In this section, we present the computational results of the proposed soft Mumford-Shah model. Notice that the extension of the above SMS models to color images is straightforward by having the gray values u_i's replaced by RGB vectors. (We, however, must remind the reader that *perceptually* RGB may not be the most ideal representation of colors compared with other nonlinear approaches, e.g., brightness-chromaticity [42] and HSV [44].)

Figures 3 and 4 illustrate the performance of the SMS model on two synthetic images with multiple phases. Figure 3 shows a typical T-junction and Figure 4 shows a 3-phase image with a narrow bottleneck. Plotted in the figures are the hard segments obtained from the SMS model via the hardening formulae (5) and (6).

Plotted in Figures 5 and 6 are the hardened segments of two MRI brain images computed by the soft Mumford-Shah segmentation model via formulae (5) and (6). For this application, a user specifies three small patches (three rectangles in both examples) Q_1, Q_2, and Q_3, and the SMS model proceeds with the extra interpolation conditions in (46) for the ownerships. Notice in the second example that the detailed branching of the complex boundary is well resolved by the model.

In Figure 7, another example of a natural image is segmented via the SMS model and the "hardening" formulae (5) and (6). A user supervises with three patches Q_1, Q_2, and Q_3, and designates the two on the body to a pattern ownership p_{body} and the third (from the ocean) to p_{ocean}. If the three are treated as distinct patterns, the SMS model still works, but one needs an extra step of high-level vision processing (e.g., based on Grenander's graph models [46]) to group the skin-tone and the purple-shirt patterns in order to capture the entire body faithfully.

Finally, plotted in Figures 8 and 9 are the ownerships from the SMS model based on the 3-phase and 4-phase supervisions separately in Figure 2. The stochastic nature of the outcomes (i.e., the softly transiting ownerships p_i's instead of hard segmentation) is closer to the way a human subject may perceive such a natural scene. In particular, the SMS model seems to be consistent with the most recent theory that *hard* pattern segments may not be absolutely necessary for natural scene recognition [1, 2].

7. CONCLUSION

In this work, we have improved the celebrated Mumford-Shah segmentation to allow stochastic fuzziness of individual patterns. The proposed model outputs the ownership (or membership) probability distributions for all the patterns, from which the classical *hard* segmentation can be obtained based on stochastic decision rules such as the principle of maximum likelihood or the Bayesian classifier.

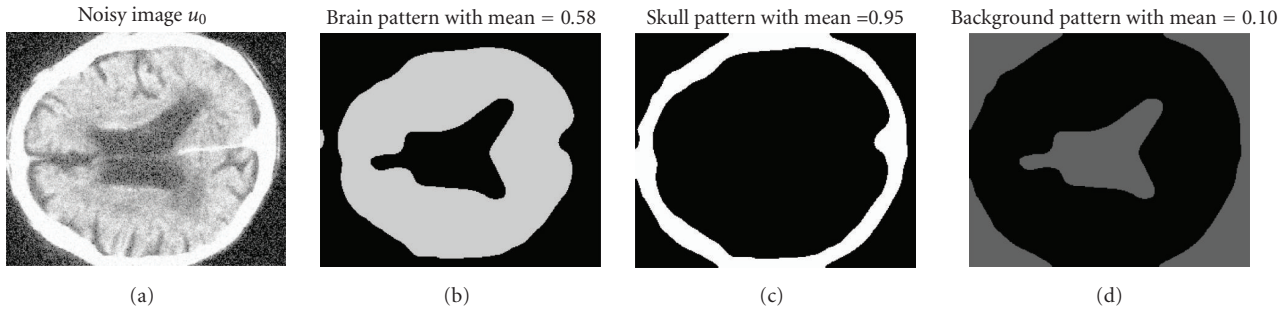

Figure 5: A real noisy brain image: hard segmentation from the SMS model via "hardening" formulae (5) and (6).

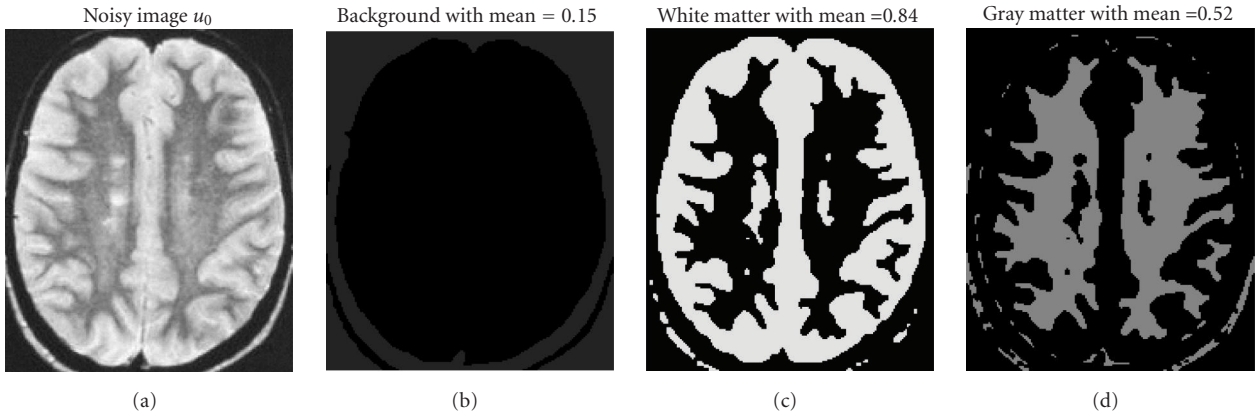

Figure 6: A brain image with low noise: hard segmentation from the SMS model via "hardening" formulae (5) and (6). Notice how the detailed branching of the gray matter has been successfully resolved by the model.

The key component of the new model is an ensemble of regularized double-well potentials inspired by the literature of material sciences and variational calculus. The model is nonconvex and the existence of optimal soft segmentation has been proven. A preliminary algorithm has been proposed and implemented, but without convergence analysis. Several generic numerical examples have demonstrated the flexibility and performance of the new model.

Our future work will mainly focus on (1) automating the weak supervision process based on statistical patch analysis, as inspired by the recent work of Li and Perona [1], and (2) developing a comprehensive framework for the effective computation of such a nonconvex and multivariate variational model (with Alan Yuille).

APPENDIX

PROOF OF THE EXISTENCE THEOREM 3

We will need the following lemma for the proof.

Lemma 2. *Let $(f_n \mid n)$ be a sequence of functions in $L^2(\Omega)$, and $(p^n \mid n)$ a sequence of nonnegative measurable functions on Ω and valued in $[0,1]$. Suppose that*

(i) $p^n \to p^*$, *a.e. on* Ω, *and* $\int_\Omega p^* > 0$;
(ii) $\int_\Omega f_n^2 p^n \le A$ *for some* $A > 0$ *and* $n = 1 : \infty$.

Then there exists some function $\rho \in L^2(\Omega)$, such that

(a) $\rho \ge 0$ *and* $\int_\Omega \rho = 1$;
(b) *for some fixed* $B > 0$, $|\int_\Omega f_n \rho| \le B$ *for* $n = 1 : \infty$.

Proof. Denote the Lebesgue measure of a measurable set W by $|W|$. Since $p^* \ge 0$ and $\int_\Omega p^* > 0$, there must exist some $c > 0$, such that

$$V = \{x \in \Omega \mid p^* > 2c\} \quad \text{has a finite but positive measure.} \tag{A.1}$$

On the other hand, by Egorov's theorem [47] on a.e. convergence, there must exist a subset $W \subset V$, such that

(a′) $|V - W| \le |V|/2$, and hence $|W| > 0$;
(b′) $p^n \to p^*$ uniformly on W.

In particular, there exists some N, such that for any $n > N$, $p^n > c$ on W. Define

$$\rho(x) = \frac{1_W(x)}{|W|} \in L^2(\Omega). \tag{A.2}$$

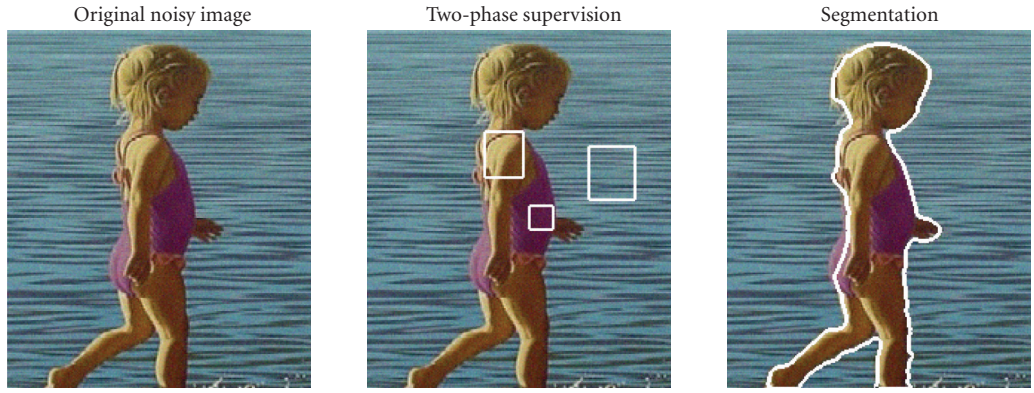

FIGURE 7: Hard segmentation from the SMS model via "hardening" formulae (5) and (6), based on a 2-phase supervision. Denote the two rectangles on the body by Q_1 and Q_2, and the third by Q_3. Supervision provides the ownership interpolation condition: $p_{\text{body}} = 1$ on $Q_1 \cup Q_2$ and 0 on Q_3, while $p_{\text{ocean}} = 1$ on Q_3 and 0 on $Q_1 \cup Q_2$. Patch selection can also be automated based on multiscale patch statistics (e.g., see Li and Perona [1]).

Then $\int_\Omega \rho = 1$, and for any $n > N$,

$$\int_\Omega f_n^2 \rho = \frac{1}{c|W|}\int_W f_n^2 c \le \frac{1}{c|W|}\int_\Omega f_n^2 p^n \le \frac{A}{c|W|}. \quad \text{(A.3)}$$

Thus by the Schwarz inequality (or $\mathrm{E}[X]^2 \le \mathrm{E}[X^2]$ in probability theory),

$$\left|\int_\Omega f_n \rho\right| \le \left(\int_\Omega f_n^2 \rho\right)^{1/2} \le \left(\frac{A}{c|W|}\right)^{1/2}, \quad n > N. \quad \text{(A.4)}$$

The lemma holds if one defines

$$B = \max\left(\left(\frac{A}{c|W|}\right)^{1/2}, \left|\int_\Omega f_1\rho\right|, \ldots, \left|\int_\Omega f_N \rho\right|\right). \quad \text{(A.5)}$$

□

We are ready to prove Theorem 3.

Proof. Take the special pattern distribution:

$$u_i \equiv 0, \quad i = 1:K; \qquad p_1 \equiv 1, \qquad p_j \equiv 0, \quad j = 2:K. \quad \text{(A.6)}$$

Then

$$E[\mathbf{P}, \mathbf{U} \mid I] = \lambda \int_\Omega I^2 < \infty. \quad \text{(A.7)}$$

Thus the infimum of the energy must be finite. Let $(\mathbf{P}^n, \mathbf{U}^n \mid n) \subseteq \mathrm{adm}_K$ (see (40)) be a minimizing sequence for the soft Mumford-Shah energy (37). That is, $E[\mathbf{P}^n, \mathbf{U}^n \mid I]$ converges to $\inf_{\mathbf{P},\mathbf{U}} E[\mathbf{P}, \mathbf{U} \mid I]$.

Due to the third term in the energy and the simplex constraint, for each channel i, $(p_i^n \mid n)$ must be bounded in $H^1(\Omega)$. By the L^2-weak compactness, there must exist some $\mathbf{P}^* \in L^2(\Omega, \mathbb{R}^K)$, and a subsequence of $(\mathbf{P}^n \mid n)$, which after relabelling will still be denoted by $(\mathbf{P}^n \mid n)$ for convenience, such that

$$\mathbf{P}^n \longrightarrow \mathbf{P}^* \quad \text{in } L^2(\Omega, \mathbb{R}^K), \ n \to \infty. \quad \text{(A.8)}$$

Then by the L^2 lower semicontinuity of Sobolev measures,

$$9\varepsilon \int_\Omega |\nabla p_i^*|^2 \le \liminf_{n\to\infty} 9\varepsilon \int_\Omega |\nabla p_i^n|^2, \quad i = 1:K. \quad \text{(A.9)}$$

Furthermore, with possibly another round of subsequence refinement, one can assume that

$$\mathbf{P}^n(x) \longrightarrow \mathbf{P}^*(x), \quad \text{a.e. } x \in \Omega, \ n \to \infty. \quad \text{(A.10)}$$

Since the probability simplex Δ_{k-1} is closed and $\mathbf{P}^n(x) \in \Delta_{K-1}$, one concludes that

$$\mathbf{P}^*(x) \in \Delta_{K-1}, \quad \text{a.e. } x \in \Omega. \quad \text{(A.11)}$$

And by Fatou's lemma [47, 48], one has

$$\int_\Omega \frac{(p_i^*(1-p_i^*))^2}{\varepsilon} \le \liminf_{n\to\infty} \int_\Omega \frac{(p_i^n(1-p_i^n))^2}{\varepsilon}, \quad i = 1:K. \quad \text{(A.12)}$$

(In fact, the equality holds by *Lebesgue's dominated convergence* [48].)

After the above subsequence selection on $\mathbf{P}^n$'s, one naturally has an associated subsequence of $(\mathbf{U}^n \mid n)$, which for convenience is still denoted by $(\mathbf{U}^n \mid n)$ after relabelling. For each *specific* channel i, we then consider two scenarios separately.

Suppose that $p_i^*(x) \equiv 0$, a.e. $x \in \Omega$. We then define for that channel

$$u_i^*(x) \equiv 0, \quad x \in \Omega. \quad \text{(A.13)}$$

Such a channel is called a "dumb" channel.

Otherwise, one must have $\int_\Omega p_i^* > 0$, and from the first term in (37),

$$\int_\Omega (u_i^n - I)^2 p_i^n \le \text{const}, \quad n = 1:\infty. \quad \text{(A.14)}$$

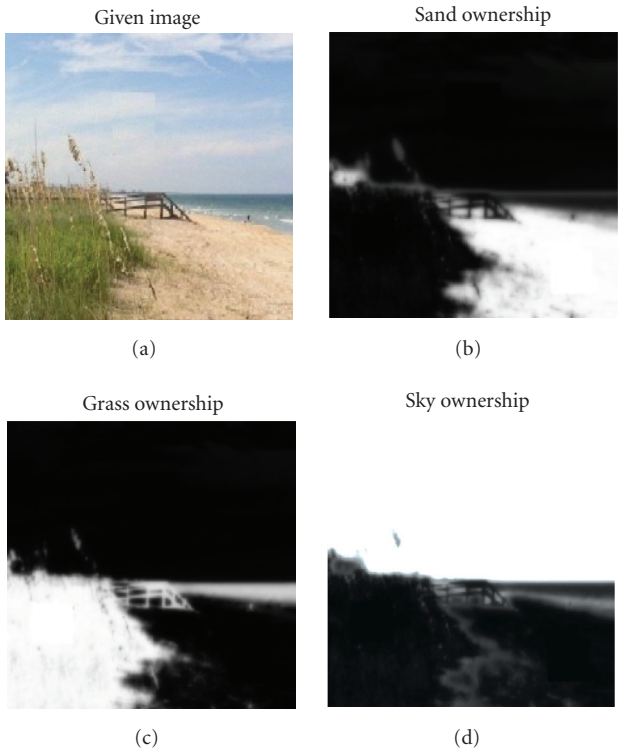

Figure 8: Soft Mumford-Shah segmentation with three phases corresponding to the supervision on Figure 2(a). Plotted here are the three ownership distributions $p_1(x), p_2(x)$, and $p_3(x)$. Due to "under"-supervision, namely the number K of specified patterns is less than that of the visually meaningful ones, the grass pattern has "absorbed" the ocean pattern due to the greenish color they happen to share.

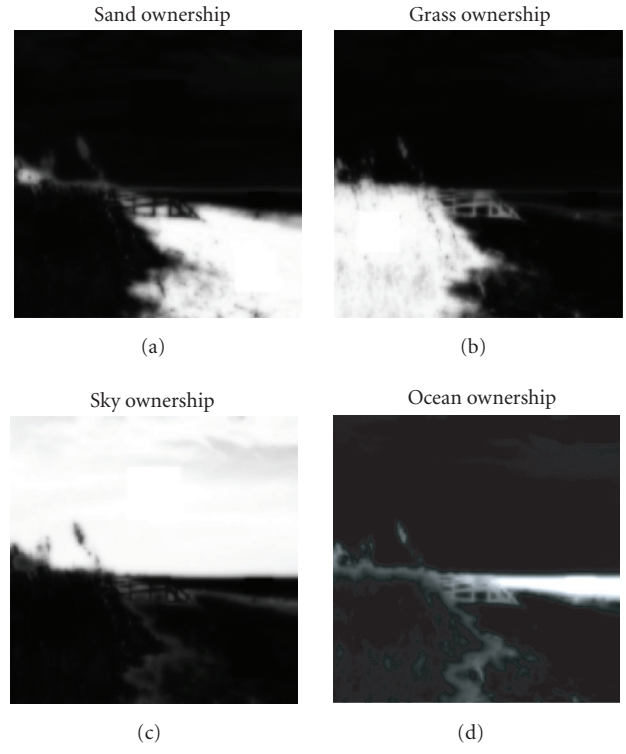

Figure 9: Soft Mumford-Shah segmentation with four phases corresponding to the supervision on Figure 2(b). Plotted here are the four ownership distributions $p_1(x), p_2(x), p_3(x)$, and $p_4(x)$. Unlike Figure 8, the narrow ocean pattern is now softly segmented due to the extra fourth patch Q_4.

Since $\int_\Omega I^2 p_i^n \le \int_\Omega I^2$, by the triangle inequality,

$$\int_\Omega (u_i^n)^2 p_i^n \le \text{const}, \quad n = 1:\infty, \tag{A.15}$$

where the constant only depends on I and the model parameters. Then by Lemma 2, there exists some $\rho_i(x) \ge 0$, with $\int_\Omega \rho_i = 1$, some constant $B_i > 0$ such that

$$\left| \int_\Omega u_i^n \rho_i \right| \le B_i, \quad n = 1:\infty. \tag{A.16}$$

On the other hand, by the second term in the energy (37),

$$\int_\Omega |\nabla u_i^n|^2 \le C_i = C_i(I, \lambda, \alpha, \varepsilon), \quad n = 1:\infty, \tag{A.17}$$

for some constant C_i independent of n. Then by the generalized Poincaré inequality [48, 49] on Ω,

$$\|w - \langle w, \rho_i \rangle\|_{L^2} \le A_i \|\nabla w\|_{L^2}, \tag{A.18}$$

where $A_i = A_i(\rho_i, \Omega)$ is independent of $w \in H^1(\Omega)$, one concludes that

$$\|u_i^n\|_{L^2} \le D_i = D_i(A_i, B_i, C_i), \quad n = 1:\infty, \tag{A.19}$$

for some constant D_i. As a result, $(u_i^n \mid n)$ must be bounded in $H^1(\Omega)$. By the L^2-weak compactness of bounded H^1-sequences, there is a subsequence of $(u_i^n \mid n)$, for convenience still denoted by $(u_i^n \mid n)$ after relabelling, such that

$$u_i^n \longrightarrow u_i^* \in L^2(\Omega), \quad n \longrightarrow \infty, \tag{A.20}$$

converging in the sense of both L^2 and almost everywhere. Then by the lower semicontinuity,

$$\int_\Omega |\nabla u_i^*|^2 \le \liminf_{n\to\infty} |\nabla u_i^n|^2. \tag{A.21}$$

Finally, since $u_i^n(x) \to u_i^*(x)$ and $p_i^n(x) \to p_i^*(x)$, a.e. $x \in \Omega$, Fatou's lemma gives

$$\int_\Omega (u_i^* - I)^2 p_i^* \le \liminf_{n\to\infty} \int_\Omega (u_i^n - I)^2 p_i^n. \tag{A.22}$$

Combining both cases just analyzed above, we have established that

$$\lambda \sum_{i=1}^K \int_\Omega (u_i^* - I)^2 p_i^* + \alpha \sum_{i=1}^K \int_\Omega |\nabla u_i^*|^2 \le \liminf_{n\to\infty} \lambda \sum_{i=1}^K \int_\Omega (u_i^n - I)^2 p_i^n + \alpha \sum_{i=1}^K \int_\Omega |\nabla u_i^n|^2. \tag{A.23}$$

Together with (A.9) and (A.12), this implies that

$$E[\mathbf{P}^*, \mathbf{U}^* \mid I] \leq \liminf_{n\to\infty} E[\mathbf{P}^n, \mathbf{U}^n \mid I] = \inf_{(\mathbf{P},\mathbf{U})} E[\mathbf{P}, \mathbf{U} \mid I], \tag{A.24}$$

and hence $(\mathbf{P}^*, \mathbf{U}^*)$ must be a minimizer. (We must caution our reader that since index relabelling has been performed for a couple of times to simplify notations, this last sequence $(\mathbf{P}^n, \mathbf{U}^n)$ is not the one we have started with originally.) This completes the proof. □

ACKNOWLEDGMENTS

The author is very grateful to Professor Alan Yuille for an enlightening discussion after the current work was first presented. For their generous teaching and continual inspiration, the author is always profoundly indebted to Professors Gil Strang, Tony Chan, Stan Osher, David Mumford, Jean-Michel Morel, and Stu Geman. The author must thank his wonderful former teacher, Professor Dan Kerstan at the Psychology Department of the University of Minnesota, for his first introduction on mixture image models and stochastic visual processing several years ago. The author also thanks the Institute of Mathematics and its Applications (IMA) and the Institute of Pure and Applied Mathematics (IPAM) for their persistent role in supporting this new emerging field. Finally, the author would like to dedicate this paper to his dear friends Yingnian Wu and Song-Chun Zhu for the unique friendship cultivated by the intellectually rich soil of vision and cognitive sciences. The generous help from our referees is also enormous. This work has been partially supported by the NSF (USA) under Grant no. DMS-0202565.

REFERENCES

[1] F.-F. Li and P. Perona, "A Bayesian hierarchical model for learning natural scene categories," in *IEEE Computer Society Conference on Computer Vision and Pattern Recognition (CVPR '05)*, vol. 2, pp. 524–531, San Diego, Calif, USA, June 2005.

[2] F.-F. Li, R. VanRullen, C. Koch, and P. Perona, "Rapid natural scene categorization in the near absence of attention," *Proceedings of the National Academy of Sciences of the United States of America*, vol. 99, no. 14, pp. 9596–9601, 2002.

[3] A. D. Jepson and M. J. Black, "Mixture models for image representation," PRECARN ARK Project Technical Report ARK96-PUB-54, University of Toronto, Toronto, Ontario, Canda, March 1996.

[4] D. L. Pham, C. Xu, and J. L. Prince, "Current methods in medical image segmentation," *Annual Review of Biomedical Engineering*, vol. 2, pp. 315–337, 2000.

[5] J.-M. Morel and S. Solimini, *Variational Methods in Image Segmentation*, vol. 14 of *Progress in Nonlinear Differential Equations and Their Applications*, Birkhäuser, Boston, Mass, USA, 1995.

[6] D. Mumford and J. Shah, "Optimal approximations by piecewise smooth functions and associated variational problems," *Communications on Pure and Applied Mathematics*, vol. 42, pp. 577–685, 1989.

[7] T. F. Chan and J. Shen, *Image Processing and Analysis: Variational, PDE, Wavelet, and Stochastic Methods*, SIAM, Philadelphia, Pa, USA, 2005.

[8] P. Brémaud, *Markov Chains: Gibbs Fields, Monte Carlo Simulation, and Queues*, Springer, New York, NY, USA, 1998.

[9] S. Geman and D. Geman, "Stochastic relaxation, Gibbs distributions, and the Bayesian restoration of images," *IEEE Transactions on Pattern Analysis and Machine Intelligence*, vol. 6, pp. 721–741, 1984.

[10] Z. Tu and S. C. Zhu, "Image segmentation by data-driven Markov chain Monte Carlo," *IEEE Transactions on Pattern Analysis and Machine Intelligence*, vol. 24, no. 5, pp. 657–673, 2002.

[11] S. C. Zhu and A. Yuille, "Region competition: unifying snakes, region growing, and Bayes/MDL for multi-band image segmentation," *IEEE Transactions on Pattern Analysis and Machine Intelligence*, vol. 18, no. 9, pp. 884–900, 1996.

[12] D. C. Knill and W. Richards, *Perception as Bayesian Inference*, Cambridge University Press, Cambridge, UK, 1996.

[13] D. Mumford, "The Bayesian rationale for energy functionals," in *Geometry Driven Diffusion in Computer Vision*, pp. 141–153, Kluwer Academic, Dordrecht, The Netherlands, 1994.

[14] L. Modica and S. Mortola, "Un esempio di Gamma-convergenza," *Bollettino della Unione Matematica Italiana B*, vol. 5–14, no. 1, pp. 285–299, 1977.

[15] B. Sandberg, T. F. Chan, and L. Vese, "A level-set and Gabor-based active contour algorithm for segmenting textured images," CAM report 02–39, UCLA Department of Mathematics, Los Angeles, Calif, USA, 2002.

[16] S. C. Zhu, Y. N. Wu, and D. Mumford, "Minimax entropy principle and its applications to texture modeling," *Neural Computation*, vol. 9, pp. 1627–1660, 1997.

[17] R. A. Adams and J. J. F. Fournier, *Sobolev Spaces*, Academic Press, New York, NY, USA, 2nd edition, 2003.

[18] D. Chandler, *Introduction to Modern Statistical Mechanics*, Oxford University Press, New York, NY, USA, 1987.

[19] W. Gibbs, *Elementary Principles of Statistical Mechanics*, Yale University Press, New Haven, Conn, USA, 1902.

[20] G. Strang, *Introduction to Applied Mathematics*, Wellesley-Cambridge Press, Wellesley, Mass, USA, 1993.

[21] J. L. Ericksen, "Equilibrium theory of liquid crystals," in *Advances in Liquid Crystals*, pp. 233–299, Academic Press, New York, NY, USA, 1976.

[22] V. L. Ginzburg and L. D. Landau, "On the theory of superconductivity," *Soviet Physics JETP*, vol. 20, pp. 1064–1082, 1950.

[23] G. Dal Maso, *An Introduction to Γ-Convergence*, Birkhäuser, Boston, Mass, USA, 1992.

[24] L. Ambrosio and V. M. Tortorelli, "Approximation of functionals depending on jumps by elliptic functionals via Γ-convergence," *Communications on Pure and Applied Mathematics*, vol. 43, pp. 999–1036, 1990.

[25] L. Ambrosio and V. M. Tortorelli, "On the approximation of free discontinuity problems," *Bollettino della Unione Matematica Italiana B*, vol. 6-B, pp. 105–123, 1992.

[26] L. C. Evans and R. F. Gariepy, *Measure Theory and Fine Properties of Functions*, CRC Press, Boca Raton, Fla, USA, 1992.

[27] E. Giusti, *Minimal Surfaces and Functions of Bounded Variation*, Birkhäuser, Boston, Mass, USA, 1984.

[28] L. Rudin, S. Osher, and E. Fatemi, "Nonlinear total variation based noise removal algorithms," *Physica D*, vol. 60, no. 1–4, pp. 259–268, 1992.

[29] C. M. Bishop, *Neural Networks for Pattern Recognition*, Oxford University Press, New York, NY, USA, 1995.

[30] S. Esedoglu and J. Shen, "Digital inpainting based on the Mumford-Shah-Euler image model," *European Journal of Applied Mathematics*, vol. 13, pp. 353–370, 2002.

[31] R. March, "Visual reconstruction with discontinuities using variational methods," *Image and Vision Computing*, vol. 10, no. 1, pp. 30–38, 1992.

[32] R. March and M. Dozio, "A variational method for the recovery of smooth boundaries," *Image and Vision Computing*, vol. 15, no. 9, pp. 705–712, 1997.

[33] J. Shen, "Γ-convergence approximation to piecewise constant Mumford-Shah segmentation," in *Proceedings of the 7th international Conference on Advanced Concepts for Intelligent Vision Systems*, vol. 3708 of *Lecture Notes in Computer Science*, pp. 499–506, Antwerp, Belgium, September 2005.

[34] J. Shen, "On the foundations of vision modeling II. Mining of mirror symmetry of 2-D shapes," *Journal of Visual Communication and Image Representation*, vol. 16, no. 3, pp. 250–270, 2005.

[35] J. Shen and Y.-M. Jung, "Weberized Mumford-Shah model with Bose-Einstein photon noise," to appear in *Applied Mathematics and Optimization*.

[36] F. Cucker and S. Smale, "On the mathematical foundations of learning," *Bulletin of the American Mathematical Society*, vol. 39, no. 1, pp. 1–49, 2001.

[37] S. Smale and D.-X. Zhou, "Shannon sampling and function reconstruction from point values," *Bulletin of the American Mathematical Society*, vol. 41, pp. 279–305, 2004.

[38] G. Aubert and P. Kornprobst, *Mathematical Problems in Image Processing*, Springer, New York, NY, USA, 2001.

[39] J. Shen, "Bayesian video dejittering by BV image model," *SIAM Journal on Applied Mathematics*, vol. 64, no. 5, pp. 1691–1708, 2004.

[40] D. Mumford and B. Gidas, "Stochastic models for generic images," *Quarterly of Applied Mathematics*, vol. 59, pp. 85–111, 2001.

[41] T. F. Chan and L. A. Vese, "Active contours without edges," *IEEE Transactions on Image Processing*, vol. 10, no. 2, pp. 266–277, 2001.

[42] T. F. Chan and J. Shen, "Variational restoration of non-flat image features: models and algorithms," *SIAM Journal on Applied Mathematics*, vol. 61, no. 4, pp. 1338–1361, 2000.

[43] R. J. A. Little and D. B. Rubin, *Statistical Analysis with Missing Data*, John Wiley & Sons, New York, NY, USA, 2002.

[44] T. F. Chan, S.-H. Kang, and J. Shen, "Total variation denoising and enhancement of color images based on the CB and HSV color models," *Journal of Visual Communication and Image Representation*, vol. 12, no. 4, pp. 422–435, 2001.

[45] R. V. Kohn and V. V. Slastikov, "Geometrically constrained walls," to appear in Calculus of Variations and PDE.

[46] U. Grenander, *Lectures in Pattern Theory I, II and III*, Springer, Berlin, Germany, 1976–1981.

[47] G. B. Folland, *Real Analysis - Modern Techniques and Their Applications*, John Wiley & Sons, New York, NY, USA, 2nd edition, 1999.

[48] E. H. Lieb and M. Loss, *Analysis*, American Mathematical Society, Providence, RI, USA, 2nd edition, 2001.

[49] L. C. Evans, *Partial Differential Equations*, American Mathematical Society, Providence, RI, USA, 1998.

Jianhong (Jackie) Shen received the Ph.D. degree in applied mathematics from the Massachusetts Institute of Technology in 1998, and the B.S. degree from the University of Science and Technology of China (USTC) in 1994. He was a Computational and Applied Mathematics (CAM) Assistant Professor at University of California, Los Angeles (UCLA), from 1998 to 2000. He is currently an Assistant Professor of applied mathematics at the University of Minnesota, Minn, USA. His current research interests include image, signal, and information processing, vision modeling and computation, as well as multiscale and stochastic modeling in medical and biological sciences. His new book *Image Processing and Analysis—variational, PDE, wavelets, and stochastic methods,* coauthored with Professor Tony F. Chan (Dean of Physical Sciences, UCLA), has been published by the SIAM (Society for Industrial and Applied Mathematics) Publisher in September 2005. Most of his research activities can be found at http://www.math.umn.edu/~jhshen

Hindawi Publishing Corporation
International Journal of Biomedical Imaging
Volume 2006, Article ID 53186, Pages 1–17
DOI 10.1155/IJBI/2006/53186

3D Brain Segmentation Using Dual-Front Active Contours with Optional User Interaction

Hua Li,[1] Anthony Yezzi,[1] and Laurent D. Cohen[2]

[1] *School of Electrical and Computer Engineering, Georgia Institute of Technology, Atlanta, GA 30332, USA*
[2] *CEREMADE, CNRS UMR 7534, Université Paris-Dauphine, 75775 Paris Cedex, France*

Received 1 December 2005; Revised 30 May 2006; Accepted 31 May 2006

Important attributes of 3D brain cortex segmentation algorithms include robustness, accuracy, computational efficiency, and facilitation of user interaction, yet few algorithms incorporate all of these traits. Manual segmentation is highly accurate but tedious and laborious. Most automatic techniques, while less demanding on the user, are much less accurate. It would be useful to employ a fast automatic segmentation procedure to do most of the work but still allow an expert user to interactively guide the segmentation to ensure an accurate final result. We propose a novel 3D brain cortex segmentation procedure utilizing dual-front active contours which minimize image-based energies in a manner that yields flexibly global minimizers based on active regions. Region-based information and boundary-based information may be combined flexibly in the evolution potentials for accurate segmentation results. The resulting scheme is not only more robust but much faster and allows the user to guide the final segmentation through simple mouse clicks which add extra seed points. Due to the flexibly global nature of the dual-front evolution model, single mouse clicks yield corrections to the segmentation that extend far beyond their initial locations, thus minimizing the user effort. Results on 15 simulated and 20 real 3D brain images demonstrate the robustness, accuracy, and speed of our scheme compared with other methods.

1. INTRODUCTION

Three-dimensional image segmentation is an important problem in medical image analysis. Determining the location of the cortical surface of the human brain from MRI imagery is often the first step in brain visualization and analysis. Generally, the normal human brain consists of three kinds of tissues: white matter (WM), gray matter (GM), and cerebrospinal fluid (CSF). Due to the geometric complexity of the human brain cortex, manual slice by slice segmentation is quite difficult and time consuming. Thus, many semiautomatic or automatic segmentation methods have been proposed in recent years.

The active contour model, which was first introduced in [1] as "snakes," is an energy minimization method and has been widely applied in medical imaging. Cohen first extended snakes to 3D models and also used them for 3D medical image segmentation [2–4]. Malladi et al. [5] also showed their application to 3D medical image segmentation. Afterwards, they proposed a hybrid strategy of level set/fast marching segmentation for 3D brain cortex segmentation [6]. In their method, a small front is initialized inside the desired region, and then the fast marching method [7] is used to greatly accelerate the initial propagation from the seed structure to the near boundary, which gives a fast and rough initialization to a costly segmentation. Then the narrow band level set method [8] is used to achieve the final result.

In addition to the above method, numerous contributions [4, 9–19] have been made on the segmentation of complex brain cortical surfaces based on active contour models. Davatzikos and Bryan [9] used the homogeneity of intensity levels within the gray matter region to introduce a force that would drive a deformable surface towards the center of the gray matter, and built the cortex representation by growing out from the white matter boundary. Based on this parameterization, the cortical structure is characterized through its depth map and curvature map. This model explicitly used the structural information of the cortex. However, close initialization and significant human interaction are needed to force the ribbon into sulcal folds.

Pham and Prince proposed an adaptive fuzzy segmentation method [15] for brain cortex extraction from images which have been corrupted by intensity inhomogeneities. In their method, the minimized objective function has two additional regularization terms added to the gain field, which is different from object functions in standard fuzzy C-means

algorithms [20]. Their method iteratively estimates the fuzzy membership functions for each tissue class, the mean intensities of each class, and the inhomogeneity of the processed image, and models the intensity inhomogeneities to a smoothing varying gain field. They reported that their method yields lower error rates than standard fuzzy C-means algorithms [20].

Lately, Xu et al. [13] described a systematic method for obtaining a surface representation of the geometric central layer of the brain cortex. It is a four-step method including brain extraction, fuzzy segmentation, isosurface generation, and a deformable surface model using gradient vector flow [21]. They defined the central cortical layer as the layer lying in the geometric center of the cortex, and applied a deformable surface model on the membership functions computed by the adaptive fuzzy segmentation [15] instead of image intensity volumes. Han et al. [18] also proposed a topology-preserving geometric deformable surface model for brain segmentation.

Teo et al. [11] proposed a four-step segmentation method based on deformable models. They first segmented white matter and cerebral spinal fluid regions by anisotropic smoothing of the posterior probabilities of different predefined regions, then selected the desired white matter components and verified and corrected the white matter structure based on cavities and handles. Finally a representation of the gray matter was created by constrained growth starting from the white matter boundary. Their work focused on creating a representation of cortical gray matter for functional MRI visualization. Dale et al. [12] concentrated on cortical surface-based analysis. They started by deforming a tessellated ellipsoidal template into the shape of the inner surface of the skull under the influence of MRI-based forces and curvature reducing forces. White matter was then labeled and the cortical surfaces were reconstructed with validation of topology and geometry.

MacDonald et al. [16] proposed to use an intersurface proximity constraint in a two-surface model of the inner and outer cortex boundaries in order to guarantee that surfaces do not intersect themselves or each other. Their method was an iterative algorithm for simultaneous deformation of multiple surfaces formulated as an energy minimization problem with constraints. This method was applied to 3D MR brain data to extract surface models for the skull and the cortical surfaces, and it took advantage of the information of the interrelation between the surfaces of interest. However, its main drawbacks include an extremely high computational expense and the difficulty of tuning the weighting factors of the cost function, due to the complexity of the problem.

Zeng et al. [14] used the fact that each cortical layer has a nearly constant thickness to design a coupled surfaces model, in which two embedded surfaces evolve simultaneously, each driven by its own image-based forces so long as the intersurface distance remained within a predefined range. They measured the likelihood of a voxel to be on the boundary between two issues and used this as a local feature to guide the surface evolution. Gomes and Faugeras [22] also implemented the above coupled surfaces model with a different scheme that preserves the level-set surface representation function as a distance map, so that reinitialization is not required every iteration. Goldenberg et al. [17] proposed a similar coupled surfaces principle and developed a model using a variational geometric framework. In their method, surface propagation equations are derived from minimization problems and implemented based on a fast geodesic active contours approach [23] for improving computational speed.

Kapur et al. [10] presented a method for the segmentation of brain tissues from MRI images which is a combination of EM segmentation, binary mathematical morphology, and active contours. EM segmentation is used for intensity-based correction and data classification. Binary morphology and connectivity is used for incorporation of topological information, and balloon-based deformable contours [3] are used for the addition of spatial information to the segmentation process. Cristerna et al. [19] proposed a hybrid methodology for brain multispectral MRI segmentation, which couples a Bayesian classifier based on a radial basis network with an active contour model based on cubic spline interpolation.

Many other automatic methods for brain cortex segmentation using T1-weighted or multispectral MR data were also proposed such as histogram threshold determinations [24, 25], fuzzy set methods [15, 26], Bayesian methods [27], Markov random field methods [28–31], expectation-maximization (EM) algorithms [10, 32], and so on.

These methods were aimed at segmenting the brain tissues automatically, and eliminating or nearly eliminating user interaction for choosing the parameters of the automatic process, setting initial surfaces for surface evolution, or restricting regions to be processed. However, there is something to be said for allowing trained users to guide the segmentation process with their expert knowledge of what constitutes a correct segmentation. Methods that allow simple and intuitive user interaction (while minimizing the need for such interaction as much as possible) are therefore potentially more useful than totally automatic methods given the importance of high accuracy and detail in cortical segmentation.

In this paper, we propose a novel 3D brain cortex segmentation scheme based on dual-front active contours which are faster and yield flexibly global image-based energy minimizers related to active regions compared to other active contours models. This scheme also adapts easily to user interaction, making it very convenient for experts to guide the segmentation process by adding useful seed points with simple mouse clicks. This scheme is very fast and the total computational time is less than 20 seconds. Experimental results on 15 simulated and 20 real 3D brain images demonstrate the robustness of the result, the high reconstruction accuracy, and the low computational cost compared with other methods.

This paper is organized into the following sections. In Section 2, we review the dual front active contour model and a number of its properties. In Section 3, we extend dual-front active contours to 3D brain cortex segmentation. Section 3.1 introduces the overall diagram of 3D brain cortex segmentation based on dual-front active contours. Section 3.2 describes how to choose active regions and potentials for the

dual-front active contours based on histogram analysis. In Section 4, we show experimental results on various simulated and real brain images as well as comparisons with other cortex segmentation methods. We also demonstrate some of the features and properties of our scheme such as simple and useful user interactions and high computational efficiency. Finally, conclusions and future research work are presented in Section 5.

2. DUAL-FRONT ACTIVE CONTOURS

The basic idea of dual-front active contours was proposed in [33, 34] for detecting object boundaries. It is an iterative process motivated by the minimal path technique [35] utilizing fast sweeping methods [36, 37]. In this section, we give a review of dual-front active contours.

2.1. Background-minimal path techniques

Since dual-front active contours are motivated by the minimal path technique proposed by Cohen and Kimmel [35, 38, 39], we give a brief summary of this technique in this subsection. Their technique is a boundary extraction approach which detects the global minimum of an active contour model's energy between two user-defined points located on the boundary, and avoids local minima arising from the sensitivity to initialization in geodesic active contours [4, 40]. Contrary to energy functionals defined in snakes [1], they proposed a simplified energy minimization model,

$$E(C) = \int_{\Omega} \{w + P(C(s))\}\, ds = \int_{\Omega} \widetilde{P}(C) ds, \tag{1}$$

where s represents the arc-length parameter of a curve $C(s) \in \mathbb{R}^n$. P is a pointwise potential associated to image features, while w is a real positive constant.

Given a potential $P > 0$ that takes lower values near the desired boundary, the objective of the minimal path technique is to look for a path (connecting two user-defined points) along which the integral of $\widetilde{P} = P + w$ is minimal. In [35], a minimal action map $U_{p_0}(p)$ was defined as the minimal energy integrated along a path between a starting point p_0 and any point p:

$$U_{p_0}(p) = \inf_{A_{p_0,p}} \left\{ \int_{\Omega} \widetilde{P}(C(s)) ds \right\} = \inf_{A_{p_0,p}} \{E(C)\}, \tag{2}$$

where $A_{p_0,p}$ is defined as the set of all paths between p_0 and p. The value of each point p in the minimal action map $U_{p_0}(p)$ corresponds to the minimal energy integrated along a path starting from point p_0 to point p.

So the minimal path between point p_0 and point p can be easily deduced by calculating the action map $U_{p_0}(p)$ and then sliding back from point p to point p_0 via gradient descent.

They also noted that given a minimal action map U_{p_0} to point p_0 and a minimal action map U_{p_1} to point p_1, the minimal path between points p_0 and p_1 is exactly the set of points p_g which satisfy

$$U_{p_0}(p_g) + U_{p_1}(p_g) = \inf_{p} \{U_{p_0}(p) + U_{p_1}(p)\}. \tag{3}$$

A saddle point p' is the first point where two action maps U_{p_0} and U_{p_1} meet each other, which means that p' satisfies $U_{p_0}(p') = U_{p_1}(p')$ and (3) simultaneously. The minimal path between points p_0 and p_1 may also be determined by calculating U_{p_0} and U_{p_1} and then, respectively, sliding back from the saddle point p' on the action map U_{p_0} to point p_0 and from the saddle point p' on the action map U_{p_1} to point p_1 according to the gradient descent. This idea was used in [39] for finding closed contours as a set of minimal paths from an unstructured set of points. It was also used in [41] in order to reduce the computational cost of a variety of fast marching applications. In order to compute $U_{p_0}(p)$, they formulated a PDE equation:

$$\frac{\partial L(v,t)}{\partial t} = \frac{1}{\widetilde{P}} \vec{n}(v,t), \tag{4}$$

to describe the level sets L of U_{p_0}, where "time" t represents heights of the level sets of U_{p_0}. $v \in \mathbb{S}^1$ is an arbitrary parameter, and $\vec{n}(v,t)$ is the normal to the closed curve $L(v,t)$. By definition we have $U_{p_0}(L(v,t)) = t$, and by differentiation of this equation by t and v it can be deduced that U_{p_0} satisfies the Eikonal equation

$$||\nabla U_{p_0}|| = \widetilde{P} \quad \text{with} \quad U_{p_0}(p_0) = 0. \tag{5}$$

This equation can be numerically solved using the fast marching method [7] because of its lower complexity compared to the direct front propagation approach implied by (3) while maintaining the same spirit of front propagation in the way that the grid points are visited during the marching procedure.

2.2. Dual-front active contours with flexibly global minimizers

In this section, we briefly review the dual-front active contour model [34]. We assume that an image I has two regions R_{in} and R_{out} with B as their common boundary. We choose one point p_0 from R_{in} and another point p_1 from R_{out}, then we define a velocity $1/\widetilde{P}$ taking lower values near the boundary B and define two minimal action maps $U_{p_0}(p)$ and $U_{p_1}(p)$ according to (2). Contrary to just considering the saddle point p' which satisfies $U_{p_0}(p') = U_{p_1}(p')$ and (3) simultaneously, we consider the set of points p_e which satisfies $U_{p_0}(p_e) = U_{p_1}(p_e)$. These points p_e form a partition curve B' which divides I into two regions. This partition is also a velocity- (or potential-) weighted Voronoi diagram. The region containing p_0 will be referred to as R'_{in}, while the other region containing p_1 will be referred to as R'_{out}. All points in R'_{in} are closer (in this weighted sense) to p_0 than to p_1 and contrariwise for points in R'_{out}. Because the action maps are potential weighted distance maps which can be endowed with Riemannian metrics, B' is called *the potential weighted minimal partition curve*.

The level sets of U_{p_0} and U_{p_1} represent the evolving fronts, and the front velocity $1/\widetilde{P}$ takes on lower values near B. When an evolving front arrives at the actual boundary B, it evolves slowly and therefore takes a long time to cross B. By

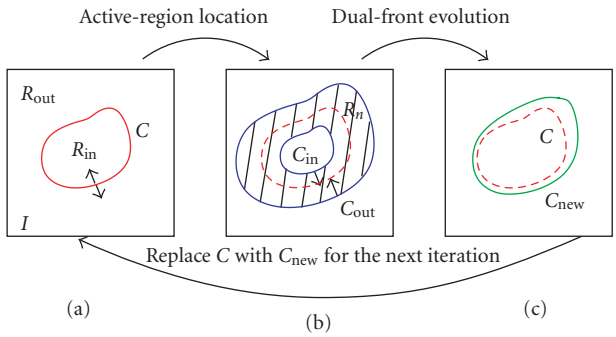

Figure 1: Iteration process of dual-front evolution and active-region location. (a) An initial contour C separates image I to two regions R_{in} and R_{out}; (b) the curve C is dilated to form a narrow active region R_n; (c) the inner and outer boundaries C_{in} and C_{out} of R_n are set as the initializations of two minimal action maps $U_{C_{\text{in}}}$ and $U_{C_{\text{out}}}$, and the set of meeting points of the level sets of $U_{C_{\text{in}}}$ and $U_{C_{\text{out}}}$ forms a new minimal partition curve C_{new} inside R_n. C_{new} divides image I into two regions. Curve C is replaced by curve C_{new} for the next iteration.

choosing appropriate potentials when defining U_{p_0} and U_{p_1}, we may cause the partition curve B' formed by the meeting points of the level sets of U_{p_0} and U_{p_1} to correspond with the actual boundary B. In other words, we can detect B by setting appropriate potentials and finding the minimal partition curve B'.

Now let us consider minimal action maps having a set of starting points. Similar to the definitions in [39], we let X be a set of points in image I (e.g., X is a 2D curve or a 3D surface), and define a minimal action map $U_X(p)$ as the minimal energy integrated along a path between a starting point $p_0 \in X$ and any point $p \notin X$:

$$U_X(p) = \min_{p_0 \in X} \left(\inf_{A_{p_0,p}} \left\{ \int_\Omega \widetilde{P}(C(s))\, ds \right\} \right). \tag{6}$$

We choose a set of points X_i from R_{in} and another set of points X_j from R_{out}, and define two minimal action maps $U_{X_i}(p)$ and $U_{X_j}(p)$ according to (6). All points satisfying $U_{X_i}(p) = U_{X_j}(p)$ form a partition boundary B'' and divide I into two regions. One region contains X_i and the other region contains X_j. Because $U_{X_i}(p)$ and $U_{X_j}(p)$ are the potential weighted distance maps, B'' is a potential weighted minimal partition of I. With appropriate potentials, it is also possible that B'' is exactly the actual boundary B of R_{in} and R_{out}.

Therefore, the dual front evolution principle proposed in [33] is to find a potential weighted minimum partition curve within an active region.

This principle is shown in Figure 1. A narrow active region R_n is formed by extending an initial curve C. For example, it may be generated from C using morphological dilation. R_n has an inner boundary C_{in} and an outer boundary C_{out}. Two minimal action maps $U_{C_{\text{in}}}$ and $U_{C_{\text{out}}}$ are defined by different potentials $\widetilde{P}_{\text{in}}$ and $\widetilde{P}_{\text{out}}$, respectively, based on (6). When the level sets of $U_{C_{\text{in}}}$ and $U_{C_{\text{out}}}$ meet each other, the meeting points form a potential weighted minimal partition curve C_{new} in active region R_n. The evolution of curves C_{in} and C_{out} and their meeting locations p_g can also be obtained using the "time of arrival" functions which satisfy Eikonal equations

$$\begin{aligned} \|\nabla U_{C_{\text{in}}}\| &= \widetilde{P}_{\text{in}} \quad \text{with } U_{C_{\text{in}}}(C_{\text{in}}) = 0, \\ \|\nabla U_{C_{\text{out}}}\| &= \widetilde{P}_{\text{out}} \quad \text{with } U_{C_{\text{out}}}(C_{\text{out}}) = 0, \\ U_{C_{\text{in}}}(p_e) &= U_{C_{\text{out}}}(p_e) \quad \text{on } C_{\text{new}}. \end{aligned} \tag{7}$$

Since the dual front evolution is to find the global minimal partition curve only within an active region, not in the whole image, the degree of this global minima changes flexibly by adjusting the size of active regions.

The dual-front active contour model is an iterative process including the dual front evolution followed by relocation of the active region. The minimum partition curve formed by the dual front evolution is extended to form a new active region. We extract the boundaries of the new active region, and define potentials for the evolution of the separated boundaries again. Then we repeat the dual front evolution and the active region location to find new global minimal partition curves until certain stopping conditions are satisfied. For example, we may compare the difference between two consecutive minimal partition curves, to determine when we have converged to a final result.

As shown in (7), two minimal action maps $U_{C_{\text{in}}}$ and $U_{C_{\text{out}}}$ may be obtained by solving Eikonal equations. In the minimal path technique proposed in [35], they used fast marching methods described in [7] to solve Eikonal equations. Tsitsiklis [42] first used heap-sort structures to solve Eikonal equations, Sethian [7] and Helmsen et al. [43] reported similar approaches lately. Fast marching methods are computationally efficient tools to solve Eikonal equations, in which upwind difference schemes and heap-sort algorithms are used for guaranteeing the solution is strictly increasing or decreasing on grid points. The computational complexity of fast marching methods is $\mathcal{O}(N \log N)$, where N is the number of grid points, and $\log N$ comes from the heap-sort algorithm.

Another algorithm for solving Eikonal equations is the fast sweeping method presented in [37, 44]. It is for computing the solution of Eikonal equations on a rectangular grid based on iteration strategies. In fast sweeping methods [37, 44], the characteristics are divided into a finite number of groups according to their directions and each sweep of Gauss-Seidel iterations with a specific order covers a group of characteristics simultaneously. 2^n Gauss-Seidel iterations (n is the spatial dimension) with alternating sweeping order are used to compute a first order accurate numerical solution for the distance function in n dimensions. Fast sweeping methods have an optimal complexity of $\mathcal{O}(N)$ for N grid points, which are extremely simple to implement in any dimension, and give similar results as fast marching methods. The details of fast sweeping methods may be seen in [37, 44].

Both fast marching methods and fast sweeping methods can be used in the dual front evolution for finding the minimal partition curve in an active region. In this paper, the dual front evolution scheme utilizes fast sweeping methods because of its low complexity $\mathcal{O}(N)$, where N is the number

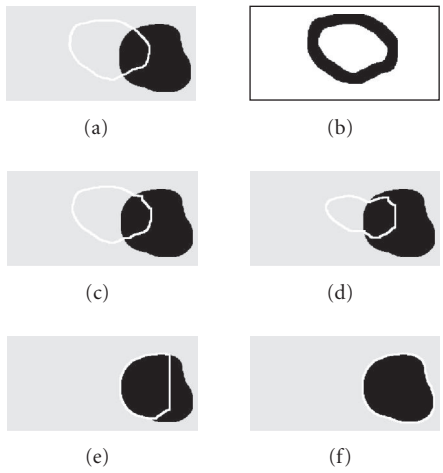

Figure 2: The segmentation result on a 2D synthetic image based on dual-front active contours. (a) The original image and the initial curve (the red line), (b) the black region is the defined active region which is extended from the initial curve using morphological dilation, (c) the new formed global partition curve within the active region after dual-front evolution, (d) to (f) the different new global minimal partition curves after 5, 10, 15 iterations.

of grid points in R_n. Because the low computational cost of fast sweeping methods is maintained, and the calculation of all minimal action maps can be finished simultaneously, the complexity of the dual front evolution is still $\mathcal{O}(N)$, where N is the number of grid points in an active region. The 3D dual front evolution scheme is shown in the appendix.

In dual front active contours, potentials may combine region and edge-based information. For example, we may consider the mean values μ_{in}, μ_{out}, the variance values σ^2_{in}, σ^2_{out} of region $(R_{\text{in}} - R_{\text{in}} \cap R_n)$ and region $(R_{\text{out}} - R_{\text{out}} \cap R_n)$ to decide the evolution potentials for the labeled points (x, y) as

$$\begin{aligned}\widetilde{P}_{\text{in}}(x,y) &= w^r_{\text{in}} f\left(\left|I(x,y) - \mu_{\text{in}}\right|, \sigma^2_{\text{in}}\right),\\ &\quad + w^b_{\text{in}} g\left(\nabla I(x,y)\right) + w_{\text{in}} \quad \text{if } l(x,y) = l_{\text{in}},\\ \widetilde{P}_{\text{out}}(x,y) &= w^r_{\text{out}} f\left(\left|I(x,y) - \mu_{\text{out}}\right|, \sigma^2_{\text{out}}\right),\\ &\quad + w^b_{\text{out}} g\left(\nabla I(x,y)\right) + w_{\text{out}} \quad \text{if } l(x,y) = l_{\text{out}},\end{aligned} \tag{8}$$

where ω^r_{in} and ω^r_{out} are positive weights for the region-based terms, ω^b_{in} and ω^b_{out} are positive weights for the edge-based items, and ω_{in} and ω_{out} are positive constants for controlling the smoothness of the partition curves. We choose $g(\nabla I(x, y))$ as a positive decreasing function of the image gradient, and f as a function related to the region-based information. As with any segmentation algorithm, the optimal set of parameters is very application-dependent.

In Figure 2, we give the segmentation process on a 2D synthetic image to show the basic principle of dual-front active contours. Here we use morphological dilation to define the active region for each iteration. The structuring element for morphological dilation was a 15×15 circle mask. For this example, the potential at a point (x, y) was $\widetilde{P}(x, y) = (|I(x, y) - \mu_l| + 0.1)$, where μ_l is the mean value of points having the same label l as the point (x, y).

2.3. Properties of dual-front active contours

The dual front active contour model has several nice properties. First, the final contour is not just a local minimizer. It possesses a controllable global minima related to certain active regions which vary according to the user-specified amount of dilation used to form the active regions at each step. The result of the dual front evolution is a potential weighted global minimum partition curve within an active region. So the size and shape of active regions affect the final segmentation result. This ability to gracefully move from capturing minima that are more local to minima that are more global makes it much easier to obtain "desirable" minimizers (which often are neither the most local nor the most global).

In Figure 3, we demonstrate that by choosing different active regions with different sizes, dual-front active contours may achieve different global minima within different active regions. Here, the potential at a point (x, y) was defined as $\widetilde{P}(x, y) = |I(x, y) - \mu_l| + (1 + |\nabla I|)^2/10 + 0.1$, where μ_l is the mean value of points having the same label l as the point (x, y).

Most edge-based active contour models [4, 40] were designed to find local minima of data-dependent energy functionals with the hope that reasonable initial placement of the active contour will drive it towards a "desirable" local minimum rather than an undesirable configuration that can occur due to noise or complex image structure. The minimal path technique proposed by Cohen and Kimmel [35, 38, 39] attempts to capture the global minimum of an active contour model's energy between two user-defined points. Furthermore, a large class of region-based models, such as [45–47], have utilized image information not only near the evolving contour but also image statistics inside and outside the contour in order to improve the performance. Most of these more global region-based energy functionals assume highly constrained models for pixel intensities within each region, and require a priori knowledge of the number of region types. Sometimes, though, minimizers that are too global (or region-based energies using information that is too global) are just as undesirable as minimizers that are too local.

An example of this is illustrated in Figure 4. In this figure, we compare geodesic active contours [40], the minimal path technique [35], Chan-Vese's method [45], and Mumford-Shah method [47] with dual-front active contours. The test image is part of a 2D human brain MRI image, and the objective is to find the interface of gray matter and white matter. The image size is 80×80 pixels. The structure element for morphological dilation in dual-front active contours is a 5×5 circle. As this figure indicates, dual-front active contours can control the degree of global or local minima which are related to active regions, find correct boundaries, and perform better than the other methods.

Second, the computational cost of dual-front active contours is reduced significantly. The iteration process in dual front active contours causes the initial and intermediate curves move in large "jumps" in order to arrive at the objective boundary, which substantially reduces the number of

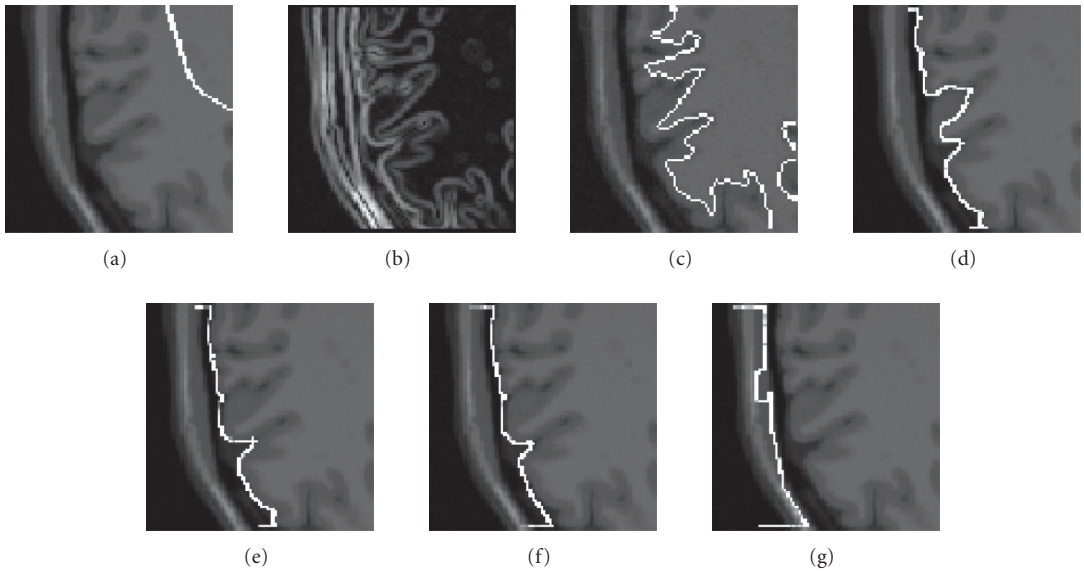

Figure 3: By choosing active regions with different sizes, the dual-front active contour model may achieve different global minima related to different active regions and iteration times. (a) The original image with the initialization. (b) The corresponding gradient information. (c) Segmentation result using a 5×5 structuring element with 15 iterations of morphological dilation. (d) Segmentation result using a 7×7 structuring element with 15 iterations of morphological dilation. (e) Segmentation result using an 11×11 structuring element with 15 iterations of morphological dilation. (f) Segmentation result using a 15×15 structuring element with 15 iterations of morphological dilation. (g) Segmentation result using a 23×23 structuring element with 15 iterations of morphological dilation.

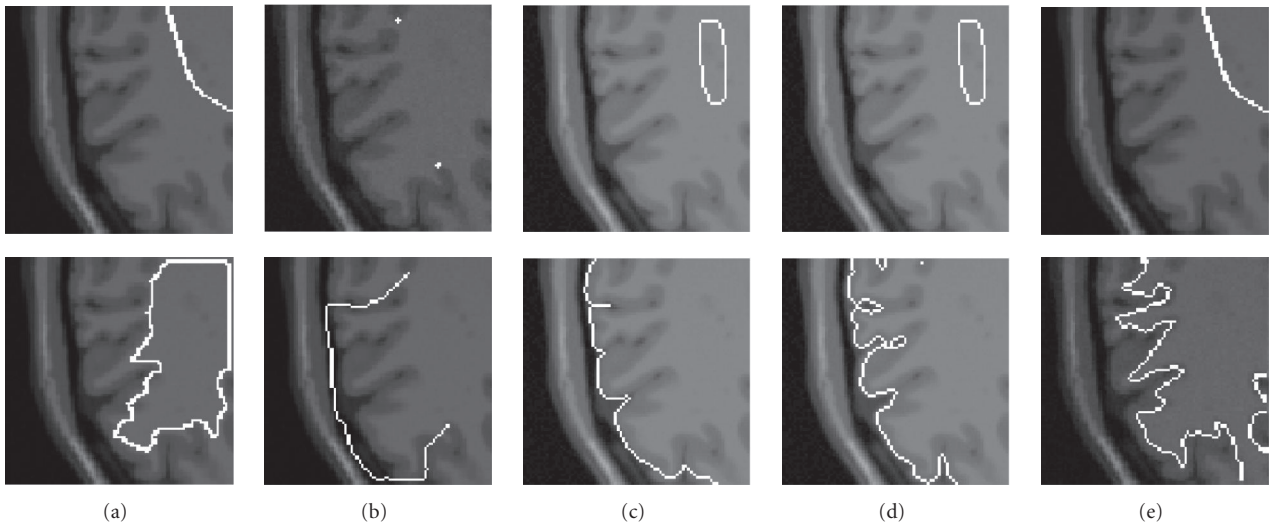

Figure 4: Comparison of different segmentation results for the white matter and gray matter boundaries using different active contour models. The gradient information used in panels (a), (b), and (e) is shown in Figure 3. The top row shows the original image and initializations. The bottom row shows the corresponding segmentation results. (a) Geodesic active contours suffer from undesirable local minima; (b) the minimal path technique relies on the location of initial points and strong gradient information; (c) and (d) Chan-Vese method and Mumford-Shah method find more global minima over the whole image. (e) Improved edge extraction using dual-front active contours with the same initialization used for geodesic active contours.

iterations needed to converge. We also use a fast sweeping numerical scheme [37] for the dual front evolution because of its lower complexity ($\mathcal{O}(N)$, where N is the number of grid points in the band). As a result, the dual-front active contour model enjoys a low complexity of $\mathcal{O}(N)$.

Third, dual-front active contours provide an automatic stopping criterion. In the dual front evolution, whenever two contours from the same group meet, they merge into a single contour. On the other hand, whenever two contours from different groups meet, both contours stop evolving and a

common boundary is formed by their meeting points automatically. The iterative process of dual-front active contours stops when the difference between two consecutive minimal partition curves is less than a predefined amount.

Fourth, in dual-front active contours, we provide a very flexible way to define active regions. Generally, we use morphological dilation to generate an active region around the current curve. In this way, the size and shape of the active region can be controlled easily by adjusting the associated structuring elements and dilation times. However, by regarding the active region as a restricted search space, we may use methods such as those presented for active contours with restricted search spaces in [48–51] to form the active regions.

A final observation to make about the dual-front active contour model is to note that while it is vaguely related to a variety of couple surface models [14, 16, 17, 22] discussed in Section 1, it is an altogether different approach. Coupled surfaces models were proposed to evolve a pair of curves together to find a pair of desired contours while exploiting some sensible constraints between the two curves as they evolved. The dual front active contour model, however, seeks to find a single potential weighted minimal partition curve within an active region, which is formed by the meeting points of dual evolving curves. By iteratively forming a new narrow active region based on the current partition curve and then using the dual front evolution to find a new partition curve, dual-front active contours can find the boundary of a *single* desired object. Furthermore, the "dual fronts" can be generalized to multiple fronts. The boundaries of an active region may be composed of multiple separating curves, each independent curve evolves with different potential and different label, whenever two (or more) evolving curves meet each other, both (or more) curve evolutions stop at the meeting points. All the meeting points form a partition curve automatically. The full details are outlined in the appendix.

3. CORTEX SEGMENTATION BY DUAL-FRONT ACTIVE CONTOURS

3.1. 3D brain cortex segmentation with flexible user interaction

Due to the complex and convoluted nature of the human brain cortex and partial volume effects of MRI imaging, the brain cortex segmentation must be considered in three dimensions. In this section, we give a 3D brain cortex segmentation scheme based on dual-front active contours.

Generally, in dual front active contours, morphological dilation is used to form an active region from an initial curve. However, it is not a good choice to form active regions for segmentation of the brain cortex. One example is illustrated in Table 1 and the corresponding 3D models are shown in Figure 9. The test image is generated from the normal brain database, BrainWeb [52], using T1 modality, 1 mm slice thickness, 3% noise level, and 20% intensity nonuniformity settings (INU). we assume the brain skull is stripped and that other nonbrain tissues are also removed. The remainder consists of only three kinds of tissues: WM, GM, and CSF. The initialization for this segmentation was a sphere mask centered at $(100, 100, 95)$ with size $75 \times 75 \times 150$. The potential at a point (x, y, z) was chosen as $\widetilde{P}(x, y, z) = (|I(x, y, z) - \mu_l| + 0.1)$, where μ_l is the mean value of the points having the same label l as the point (x, y, z). The structuring element used for morphological dilation was a $7 \times 7 \times 7$ sphere mask. We first used dual-front active contours to segment the CSF boundary, and then processed only the remaining interior region to capture the WM/GM boundary.

Table 1: Comparison of tissue segmentation results of our method. Dual-front active contour (1) using morphological dilation to generate the active regions and (2) using histogram analysis to generate active regions.

Rate	Dual-front active contours (1)			Dual-front active contours (2)		
	CSF	GM	WM	CSF	GM	WM
TP (%)	96.3	78.0	84.3	96.6	93.3	95.1
FN (%)	3.7	22.0	15.7	3.4	6.7	4.9
FP (%)	44.6	13.0	5.7	5.7	5.6	5.8
Overlap metric	0.666	0.689	0.797	0.914	0.883	0.898

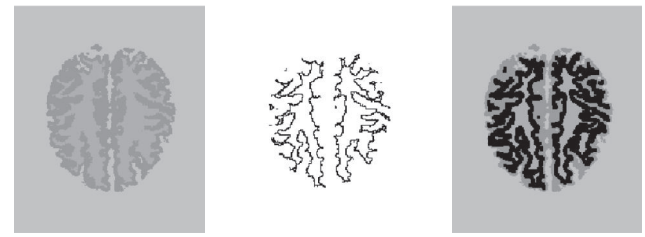

(a) (b) (c)

Figure 5: Morphological dilation affects the topology structure of evolving fronts and also affects the accuracy of segmentation results. (a) The formed partition diagram on one slice after a number of iterations and different regions with different gray values represent different tissues; (b) the extracted boundary between GM and WM tissues on the same slice as that shown in (a); (c) the formed active region (the most black region) by dilating the boundary shown in (b).

As shown in Table 1, the quantitative evaluation of the segmentation result using this morphological dilation is not very good, as the dilation process is blind to the complex and convoluted structure of the brain cortex. Because of the convoluted geometry of the cortex, each time we dilate the partition curve to form a new active region for next iteration, the dilation may change the topology of the partition curve. An example is illustrated in Figure 5. The 3D models shown in panels (a) and (b) of Figure 9 demonstrate the poor performance of this morphological approach.

Since morphological dilation is not the only way to obtain active regions, we may choose another method. Here we propose a scheme based on histogram analysis. This scheme is simple, fast, and accurate with flexible user interaction. In Figure 6, we show an overall diagram of this scheme.

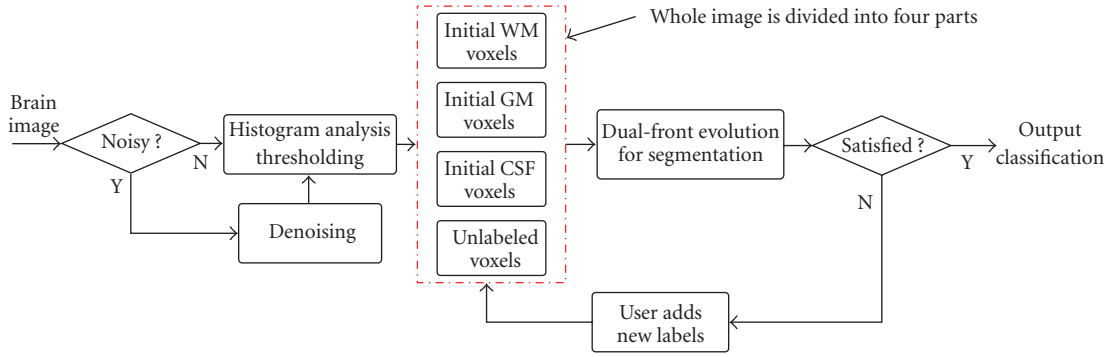

Figure 6: Overall diagram of 3D brain cortex segmentation process.

In this scheme, we first assume the brain skull is stripped and that other nonbrain tissues are also removed. The remainder consists of three kinds of tissues: white matter (WM), gray matter (GM), and cerebrospinal fluid (CSF). If an image is noisy, we first preprocess it to reduce the effects. Next, we divide the whole brain image into four regions: WM seed voxels, GM seed voxels, CSF seed voxels, and unlabeled voxels. All the voxels in the same region (WM, GM, or CSF) have the same label. The background is ignored for the computation. Here, the unlabeled voxels make the "active region" among the labeled WM, GM, CSF voxels, and the active region may be composed of isolated points, sets of points, and so forth. After running the dual front evolution, all the points in the active region are assigned a label which is one of the three labels for GM, WM, and CSF. The final grid is therefore separated into these three tissue classes.

If this initial segmentation does not give satisfactory results, users can modify the initial active region just by adding (or deleting) some labels (via mouse-clicks) as desired, afterwhich the dual-front evolution is automatically rerun to yield an updated segmentation.

3.2. Active region and potential decision based on histogram analysis

In this section, we describe a method for creating the active regions, required by the dual-front active contour, by analyzing histograms of normal MRI brain images. A histogram, which is simply a frequency count of the gray levels in the image, is important in many areas of image processing, such as segmentation and thresholding. Analysis of histograms gives useful information about image contrast. For 3D T1-weighted brain cortex images, the reasonable contrast is obtained between the three main tissue classes in brain, which are GM, WM, and CSF. Some brain cortex segmentation approaches [24, 25, 53] were based on automatic gray-level thresholding, and in common, a histogram is first determined, from which the threshold levels are determined by Gaussian fitting algorithms to produce a binary mask. Five Gaussian representing three pure tissue classes (GM, WM, CSF) and two partial volume compartments (GM/WM, CSF/GM) are fitted at a local level and are used to generate either discrete or continuous segmentations [24]. But the problems with these methods include their sensitivity to partial volume effects, which produces speckled regions in the final segmentation. In order to reduce the impact of the noise, some Markov-random-field-based methods [28–31] were proposed.

Figure 7 shows the histogram analysis of these three brain tissues. panel (a) is the histogram of a sample 3D MRI elderly brain image. There are three peaks and two troughs in this histogram. The locations of these peaks approximate the average mean values of the GM, WM, and CSF tissues. The regions around these two troughs correspond to the voxels located around the boundaries of different tissues. Because of the effect from noise and partial volume problems, it is hard to locate the actual boundaries just by simple thresholding.

In this paper, we use histogram analysis for a special purpose. After a histogram is first determined, we may use simple thresholding to choose regions which include the actual boundaries instead of the boundaries themselves. We treat all the voxels in these chosen regions as unlabeled voxels and use a dual-front active contour to assign a unique label to each voxel in this region. The 3D dual front evolution scheme is detailed in the appendix. This process is shown in panel (b) and panel (c) of Figure 7. By setting different thresholds, a 3D brain image may be divided into GM seeds, WM seeds, CSF seeds, and unlabeled voxels which comprise two active regions R_1 and R_2 around the two troughs in the histogram. As shown in panel (c) of Figure 7, a 3D brain image may be separated into different regions by the previous procedure. The voxels with different gray values represent different initial CSF, GM, and WM voxels. The most black voxels represent the unlabeled pixels which compose the active region. The 3D dual-front evolution scheme may be used to assign a unique label to each voxel in this active region. For images with high noise levels, we smooth the image first and then calculate the histogram. The main purpose of this smoothing process is to eliminate extraneous peaks/troughs in the histogram. Then we may use thresholding to separate an image into different regions. While smoothing makes some parts of the boundaries list distinct, quantitative analysis on several sample images indicate that a limited amount of smoothing actually improves the segmentation results. The details are given in Section 4.1.

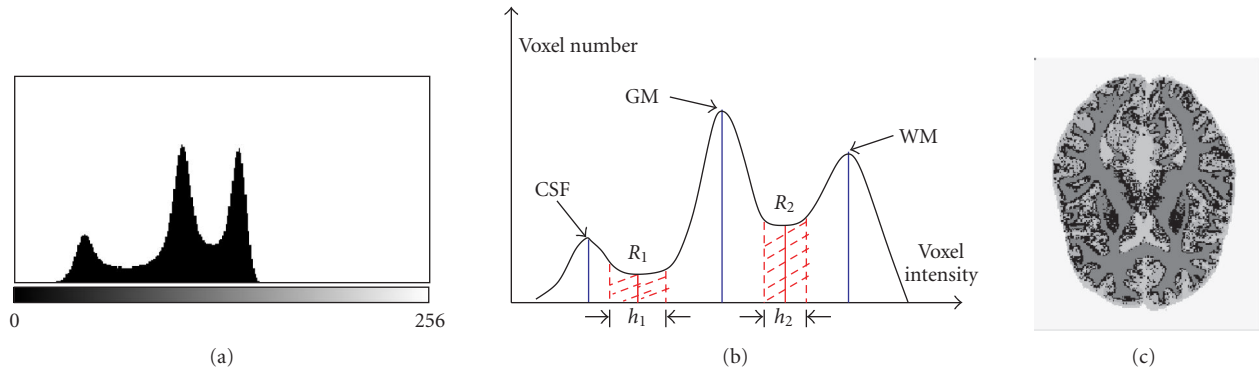

FIGURE 7: Active regions are determined by histogram analysis and thresholding of 3D MRI brain images. (a) The histogram of a sample 3D MRI brain image; (b) the center of R_1 is the trough between the CSF and GM peaks, the center of R_2 is the trough between the GM and WM peaks. h_1 and h_2 decide the size of R_1 and R_2. (c) The brain image is separated into different regions by thresholding. The most black voxels represent the unlabeled pixels, and voxels with different gray values represent different initial CSF, GM, and WM voxels.

We use region-based information during the front evolutions in our scheme because the tested MRI images rarely provide reliable edge information. We calculate the mean values μ_{CSF}, μ_{GM}, and μ_{WM}, and the variance values σ^2_{CSF}, σ^2_{GM}, σ^2_{WM}, of the three different seed voxel classes with labels l_{CSF}, l_{GM}, and l_{WM}. Then the potential for a labeled point (x, y, z) is set to

$$\widetilde{P}_l(x,y,z) = \omega_1 \cdot \exp\left(\frac{\left|\overline{I}(x,y,z) - \mu_l\right|^2}{2\sigma_l^2}\right) + \omega_2 \quad \text{if } L(x,y,z) = l \ (l = l_{\mathrm{CSF}}, l_{\mathrm{GM}}, l_{\mathrm{WM}}), \tag{9}$$

where $\overline{I}(x, y, z)$ is the average image intensity in a window of size $3 \times 3 \times 3$ around the given voxel. ω_1 is a real positive weight for the region-based image potential, while ω_2 is a real positive constant to control the smoothness of the partition curves obtained from the dual front evolution.

4. EXPERIMENTAL RESULTS

In this section, we validate our approach on various 3D simulated and real MRI brain image data sets. We use T1-weighted images on account of their better GM/WM contrast [14, 54]. All the experimental results shown in this section are obtained from 3D volume processing directly.

To evaluate the efficiency of our method for every tissue type T (GM, WM, and CSF), four probabilities are defined:

$$\mathrm{TP} = \frac{N_B \cap N_R}{N_R}, \qquad \mathrm{FN} = \frac{N_R - N_B \cap N_R}{N_R},$$
$$\mathrm{FP} = \frac{N_B - N_B \cap N_R}{N_R}, \qquad \mathrm{OM} = \frac{\mathrm{TP}}{1 + \mathrm{FP}}, \tag{10}$$

where N_R is the number of reference ground truth voxels of tissue T. N_B is the number of voxels detected by our algorithm for tissue T. $N_B \cap N_R$ is the number of correct voxels detected by our method for tissue T. TP means true positive, which is the probability of correct detection relative to the ground truth for tissue T. FN means false negative, which is the probability of misdetection relative to the ground truth for tissue T. FP means false positive, which is the probability of false detection relative to the ground truth for tissue T. OM means overlap metric, which is defined for a given voxel class assignment as the sum of the number of voxels that both have the class assignment in each segmentation divided by the sum of voxels where either segmentation has the class assignment [55]. This measurement is more critical than comparisons using the volume only, it is the same as the Tanimoto coefficient [56]. This metric approaches a value of 1.0 for results that are very similar and is near 0.0 when they share no similarly classified voxels. In the following experiments we use these parameters to quantitatively analyze our segmentation results.

4.1. Validation on simulated MR brain images

In Figure 8, we present the results of the segmented WM tissues for five different slices of one 3D simulated brain image provided by BrainWeb [52], which is generated from the normal brain database using the T1 modality, 1 mm slice thickness, 3% noise level, and 20% intensity nonuniformity settings (INU).

For this segmentation, we use the potentials defined by (9) with $\omega_1 = 1$ and $\omega_2 = 0.1$. The size of R_1, h_1 is equal to 20, and the size of R_2, h_2 is equal to 10 (shown in Figure 7). In fact, ω_1 and ω_2 are two parameters for adjusting potentials, while h_1 and h_2 are two parameters for adjusting the size of active regions. The best or most appropriate values for these parameters have to be chosen for different classes of images. In this paper, we manually choose these parameters by testing on a few sample images, and then using the same values for all of the rest. Adaptive tuning of these parameters is one of the subjects for future research.

In Table 1, we give the quantitative results of two brain cortex segmentations on the same 3D simulated image as that in Figure 8. This 3D simulated brain image is provided by BrainWeb [52], and is generated from the normal brain database using the T1 modality, 1 mm slice thickness, 3%

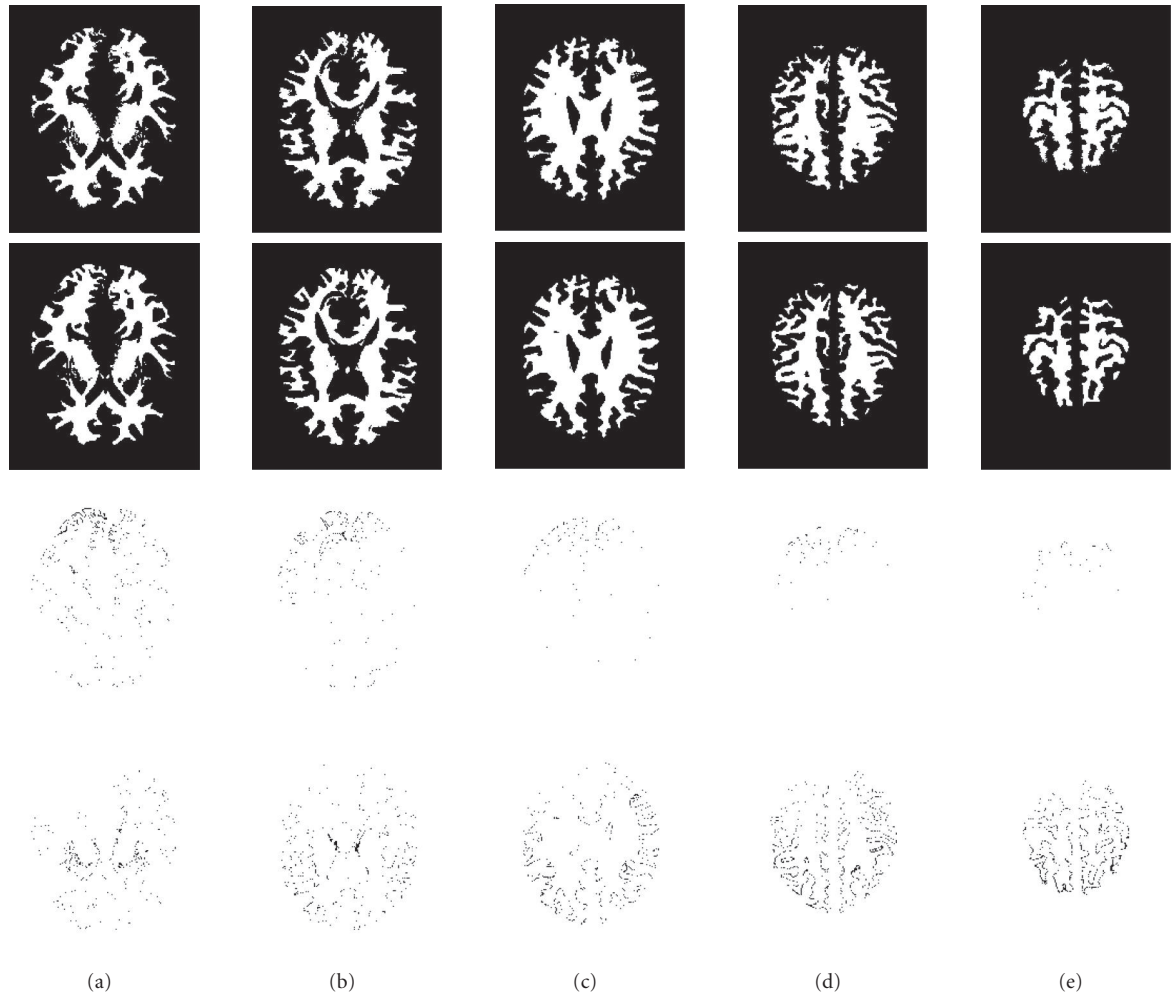

Figure 8: Comparison of the segmentation results from our method with the ground truth data of five slices of one 3D simulated brain image provided by BrainWeb [52], which is of T1 modality, 1 mm slice thickness, 3% noise level, 20% INU. The image size is $181 \times 217 \times 181$. The top row presents the segmentation results obtained from our method. The second row shows the ground truth data provided by BrainWeb database. The third row shows the false negative difference between the segmentation results from our method and the ground truth data. The fourth row shows the false positive difference between the segmentation results from our method and the ground truth data. These five columns correspond to five slices of the test 3D image.

noise level, and 20% intensity nonuniformity settings (INU). One result is obtained by using dual front active contours with active regions obtained by morphological dilation. The second result is obtained by using dual front active contours with active regions obtained by the same histogram analysis as in Figure 8. Figure 9 shows the corresponding 3D models of the segmented GM and WM surfaces from these two methods explained in Table 1 and from the ground truth data. From these segmentation results we can see that our scheme based on histogram analysis performs better than the dual-front active contours based on morphological dilation.

We also tested our method on 15 3D simulated brain images provided by BrainWeb [52, 57], which are of T1 modality, 1 mm slice thickness, different noise levels 1%, 3%, 5%, 7%, and 9%, and different INU settings 0%, 20%, and 40%. All images are $181 \times 217 \times 181$. For this segmentation, we continued to use the same potentials defined by (9) with $\omega_1 = 1$ and $\omega_2 = 0.1$. The size of R_1, h_1 is 20, and the size of R_2, h_2 is 10.

For images with high noise levels 5%, 7%, and 9%, we first use the isotropic nonlinear diffusion proposed by Perona and Malik [58] to smooth the images. Since the ground truth data is also provided by BrainWeb website, it is easy for us to compare the accuracy from the original images and the corresponding smoothed image. For the segmented results, the overlap metrics of three tissues for 5 images with different noise levels and same 0% INU setting are from 0.813 to 0.944, the overlap metrics of three tissues for 5 images with different noise levels and same 20% INU setting are from 0.814 to 0.914, the overlap metrics of three tissues for 5 images with different noise levels and same 40% INU setting are from 0.747 to 0.835. In Figure 10, we also show these segmentation results. In Figure 10, some CSF segmentation results of images having 0% INU are worse than the results of images

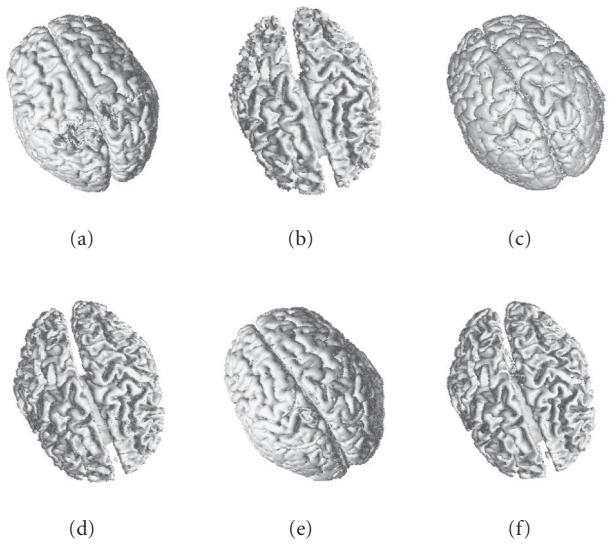

Figure 9: Comparison of the 3D models of GM and WM surfaces from our method and from the ground truth data. The test image is the same as in Figure 8. (a) and (b) are the 3D models of the GM and WM surfaces obtained from our method using morphological dilation; (c) and (d) are the 3D models of the GM and WM surfaces obtained from our method using histogram analysis; (e) and (f) are the 3D models of the GM and WM surfaces from the ground truth.

having 20% INU. We think there are three reasons. One is that the two parameters h_1 and h_2 are constants. The chosen parameters are not the best or most appropriate values for processing all the images and segmenting all the tissues. Furthermore, when we choose these parameters, we consider more on their performance on the GM and WM segmentation results than that of the CSF segmentation results. The best or most appropriate values for these parameters have to be chosen based on different applications. How to set adaptive tuning of these parameters is very application-dependent and still needs further research work. The second reason is that we use some smoothing operators to smooth the images with noise levels 5%, 7%, and 9% first and then segment them. These smoothing processes may also effect the final results. Furthermore, CSF tissues are much thinner than GM and WM tissues, which also may effect the segmentation results.

4.2. Validation on real MR brain images

To further evaluate our segmentation method under more realistic conditions, we test it on 20 real MRI brain images and compare the segmentation results with those of human experts as well as to those obtained by other segmentation algorithms. These 20 normal MR brain data sets are provided by the Center for Morphometric Analysis at Massachusetts General Hospital on the IBSR website http://www.cma.mgh.harvard.edu/ibsr/. The IBSR website also provides the segmentation results on GM, WM, and CSF tissues from the adaptive MAP method, the biased MAP method, the fuzzy C-means method, the maximum a posteriori probability method, the maximum-likelihood method, and the tree-structure k-means method on these 20 normal brain-only MR data sets along with the manual segmentation results on GM and WM tissues from two experts [59]. Since the segmentation results provided by the IBSR website are measured by two parameters "overlap metric" and "average overlap metric," we will also measure the results from our method by these same two parameters for the sake of meaningful comparison.

Figure 11 shows the overlap metric of CSF, GM, and WM segmentation results (compared to expert manual results) on 20 normal brains for various automatic segmentation results provided by IBSR, for the hidden Markov method [28] provided by the FMRIB website (http://www.fmrib.ox.ac.uk/fsl/), and for our proposed scheme. For the segmentation of these real brain images, we still use the potentials defined by (9) with $\omega_1 = 1$ and $\omega_2 = 0.1$. The size of R_1, h_1 is 20, the size of R_2, h_2 is 10.

Figure 12 shows the average overlap metric of GM and WM segmentation results on these 20 normal brains provided by the IBSR website for various methods. The figures show that the overlap metric and the average overlap metric of the segmentation results from our method are either higher than or at least close to the other methods. However, the computational time for our method is around 20 seconds, which is much faster than other methods.

In these comparisons shown in Figures 11 and 12, in addition to the comparison with the methods provided by IBSR [55, 60], we also compare our method with other three recently proposed methods, the Bayesian method proposed in [27] (MPM-MAP); the coupled surfaces method [14] (ZENG), and the hidden Markov method [28] (FAST). This study is just the initial step of our research work on brain image analysis. We will still work on it, and try to improve the model's robustness and the segmentation's accuracy further.

4.3. Simple and useful user interaction

In the previous two subsections, various segmentation results of our scheme on simulated and real 3D brain datasets are shown, and simple thresholding operators are used for defining active regions in the dual-front evolution. Generally, most automatic techniques, while less demanding on the user, are much less accurate. It would be useful to employ a fast automatic segmentation procedure to do most of the work but still allow an expert user to interactively guide the segmentation to ensure an accurate final result. An attractive feature of our scheme is that it is extremely simple for users to add seed points just by mouse clicks to yield corrections to the segmentation that extend far beyond their initial locations (due to the flexibly global nature of dual front active surfaces), thus minimizing the user effort. Figure 13 shows an example of this interaction.

In Figure 13, we use the same image as the one used for the test shown in Figure 8. One slice of the test 3D image (panel (a)), the ground truth data for the WM tissue in this slice (panel (b)), and the 3D model of the ground truth WM tissue (panel (c)) are shown in the first row. The second row

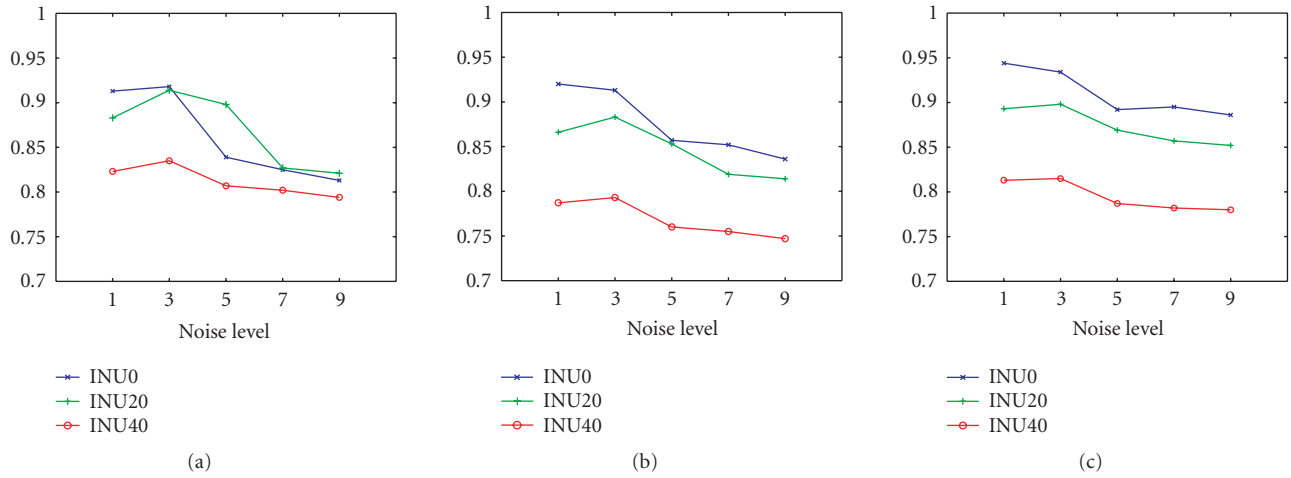

FIGURE 10: Overlap metric for CSF, GM, and WM segmentations on simulated brain images provided by BrainWeb website. The different noise levels are 1%, 3%, 5%, 7%, and 9%. The three curves labeled INU0, INU20, and INU40 represent the overlap metric of the segmentation results of the images with 0%, 20%, and 40% INU settings based on our proposed method. (a) The overlap metric of CSF segmentation results for images with different noise levels (1%, 3%, 5%, 7%, and 9%) and different INU settings (0%, 20%, and 40%). (b) The overlap metric of GM segmentation results for images with different noise levels (1%, 3%, 5%, 7%, and 9%) and different INU settings (0%, 20%, and 40%). (c) The overlap metric of WM segmentation results for images with different noise levels (1%, 3%, 5%, 7%, and 9%) and different INU settings (0%, 20%, and 40%).

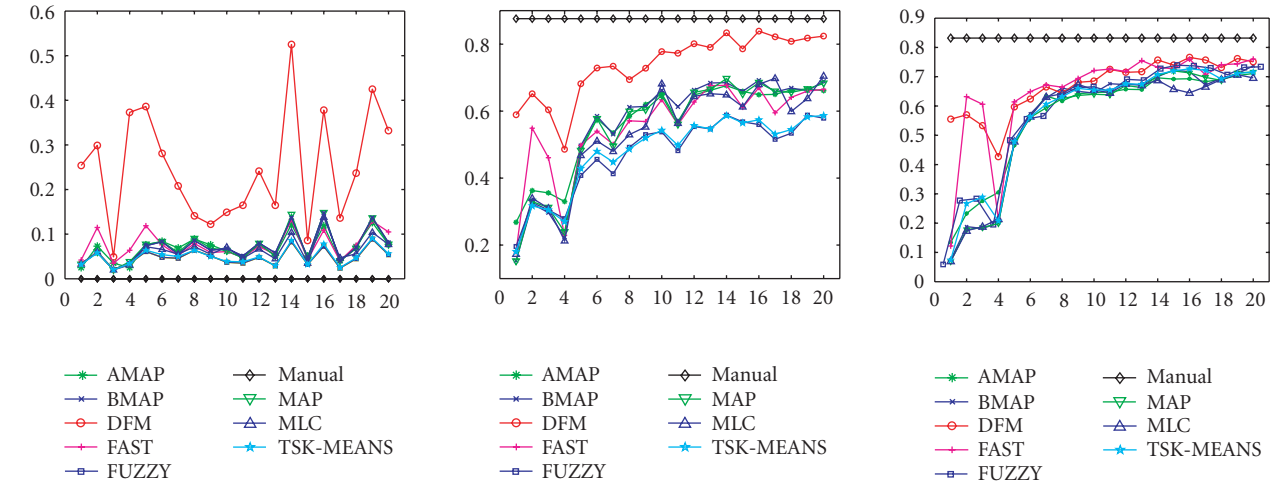

(a) Overlap metric comparison for CSF segmentation

(b) Overlap metric comparison for GM segmentation

(c) Overlap metric comparison for WM segmentation

FIGURE 11: The overlap metric of CSF, GM, and WM segmentations results on 20 normal real brain images for various segmentation methods. The results of some automatic segmentation methods provided by IBSR. AMAP: adaptive MAP; BMAP: biased MAP; FUZZY: fuzzy C-means; MAP: maximum a posteriori probability; MLC: maximum likelihood; TSKMEANS: tree-structure k-means; FAST: hidden Markov method [28]; DFM: our scheme.

shows the segmentation result using dual-front active contours, in which active regions are chosen based on automatic thresholding. In this test, we set a different active region between the WM and GM tissues by changing the size and location of R_2 according to Figure 7. The most black region in panel (d) presents unlabeled voxels in the active region, and different regions with different gray values represent different tissues' initial seed points. panel (e) shows the segmentation result. The 3D model of the segmented WM is shown in panel (g). These figures illustrate that if automatic thresholding cannot provide enough WM seed points, the segmented WM tissue may be incorrect. So in addition to employing a fast automatic segmentation procedure to do most of the work, it would be useful to still allow an expert user to interactively guide the segmentation to ensure an accurate final result. We show segmentation result after user interaction in the third row of Figure 13. As shown in panel (h), the user interaction simply consists of a few mouse clicks to add

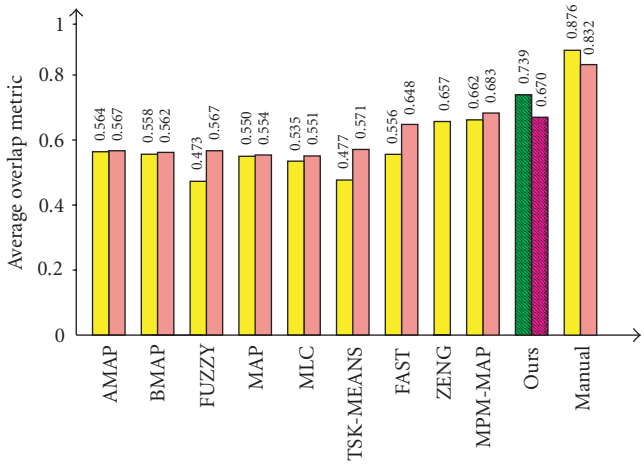

Figure 12: Average overlap metric for GM and WM segmentations on 20 normal real brains for various segmentation methods. The results of some automatic segmentation methods were provided by IBSR or related papers. For each method, the left column represents the average overlap metric of GM segmentation, the right column represents the average overlap metric of WM segmentation. For our method, the left column represents the average overlap metric of GM segmentation, the right column represents the average overlap metric of WM segmentation. AMAP: adaptive MAP; BMAP: biased MAP; FUZZY: fuzzy C-means; MAP: maximum a posteriori probability; MLC: maximum likelihood; TSK-MEANS: tree-structure k-means; FAST: hidden Markov method [28]; ZENG: coupled-surface method [14]; MPM-MAP: Bayesian method [27]; DFM: our scheme.

some new seed points. We then run the dual-front evolution again to segment the GM and WM. The segmented boundary of GM/WM is shown in panel (i), the extracted WM tissue and the corresponding 3D model are shown in panel (j) and panel (k). The figures show that the accuracy of the result after user interaction is much better than that just based on automatic thresholding.

We provide a flexible way to combine histogram analysis and dual-front active contours. We may first set certain predefined parameters such as the different weights in potentials, and the width of h_1 and h_2, then do histogram analysis and the dual front evolution to obtain the segmentation result directly. We may also do histogram analysis separately and let experts choose appropriate parameters for the dual-front evolution based on histogram analysis and their experience. In most fully automatic methods, users need to repeat the whole process to obtain different results, and it is hard to tune the associated parameters flexibly. But our method provides a fast automatic segmentation procedure to do most of the work but still allow an expert user to interactively guide the segmentation to ensure an accurate final result.

4.4. Computational time

Another nice property of our method is its high computational efficiency. We test our method on 15 simulated 3D MR brain images provided by BrainWeb [57], and 20 real normal 3D MR brain images provided by IBSR website. The average computational time is around 20 seconds on a 2.5 GHz Pentium4 PC processor, out of which the average computational time for the histogram analysis is about 5 seconds and the average computational time for the dual front evolution is less than 15 seconds.

Since most methods introduced in Section 1 were tested on different images and run on the different processors, it is hard for us to give exact quantitative comparisons on the computational time between our method and these other methods. Here we just give a brief discussion on the computational time reported for various cortex segmentation methods.

We downloaded the software for the hidden Markovian method from the website of the FMRIB Software Library (http://www.fmrib.ox.ac.uk/fsl/) to compare its computational speed with our method. On the same computer, the average computational time for the hidden Markovian method for same test images was around 550 seconds. Xu's method [13] combined the adaptive fuzzy C-means algorithm [15]; they reported that the computational time for the final deformable surface algorithm was about 3 hours using an SGI workstation with a 174 MHz R10000 processor.

For the coupled surface method proposed by Zeng et al. [14], it was reported that for a 3D image of the whole brain with a voxel size of $1.2 \times 1.2 \times 1.2\,\text{mm}^3$, their algorithm runs in about 1 hour on a SGI Inigo2 machine with a 195 MHz R10000 processor for the implementation of skull stripping, cortex segmentation, and measurement simultaneously. Goldenberg et al. [17] also adopted the coupled surfaces principle and used the fast geodesic active contour approach to improve the computational time for cortex segmentation. They reported that the computational time of their method was about 2.5 minutes for a $192 \times 250 \times 170$ MR image of the whole brain on a Pentium3 PC. But they did not give the quantitative analysis of the segmentation results.

Teo et al. [11] reported that their entire procedure takes about 0.5 hours. Prior to the procedure, gray matter needs to be identified manually in a single occipital lobe of one hemisphere using rudimentary segmentation tools, which requires about 18 hours for an expert. Much of the time is spent on visually inspecting connectivity and ensuring topological correctness. In MacDonald's method [16], the processing time for each object was reported to be 30 hours on an SGI Origin 200 R10000 processor running at 180 MHz. Dale et al. [12] reported that their entire procedure runs automatically in about 1.5 hours. Kapur et al. [10] reported that their method required about 20 minutes to process a single 3D image.

In Marroquin's method [27], it was reported that the average total processing time (including registration for peeling the skull and nonbrain material and segmentation) on 20 normal brain data sets from IBSR is 29 minutes on a single processor of an SGI ONYX machine. In the adaptive fuzzy C-means algorithm (AFCM) [15], they reported that execution times for 3D T1-weighted MR data sets with 1 mm cubic voxels are typically between 45 minutes and 3 hours when using full multigrid AFCM, and that execution

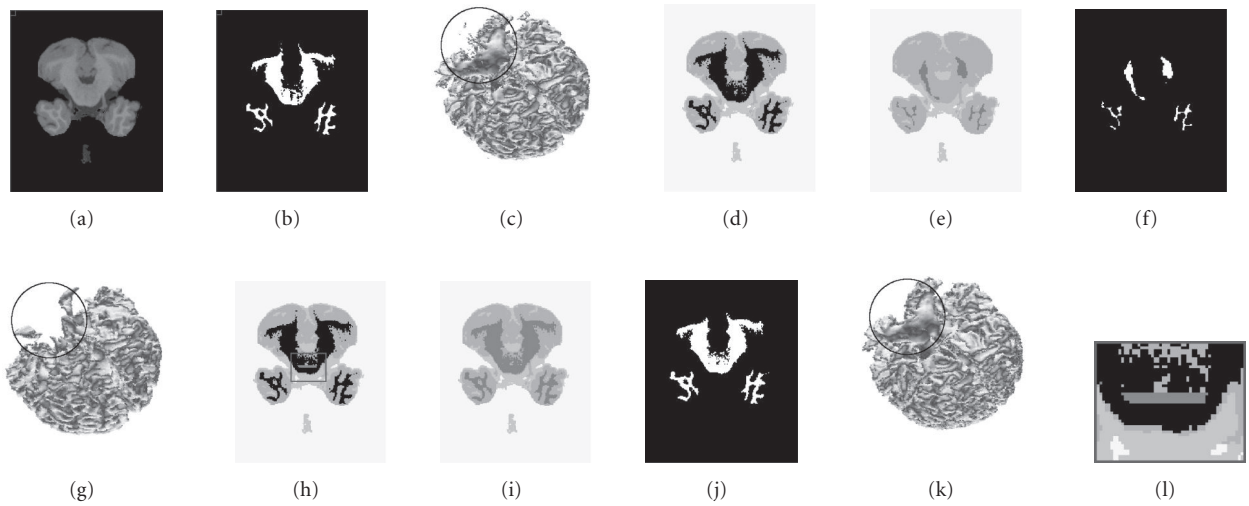

Figure 13: Simple user interaction can improve the segmentation accuracy dramatically (see text). (a) One slice of the original 3D brain image, (b) the ground truth data of WM tissue in the slice shown in panel (a), (c) the corresponding 3D model of ground truth data of WM tissue, (d) based on histogram analysis, the whole brain is divided into GM tissue, WM tissue, CSF tissue with different gray values, and unlabeled tissues in active regions with the most black values, (e) the segmentation result by using dual-front active contours, (f) the segmented WM tissue (the white part), (g) the 3D model of segmented WM tissue, (h) manually added seed points for WM tissue, (i) the new segmentation result with added seed points, (j) the segmented WM tissue, (k) the corresponding 3D model of the segmented WM tissue, (l) the horizontal line is the zoom-in of the user-added seed points in panel (h).

times are between 10 minutes and 1 hours when using truncated multigrid AFCM. In the graph-based topology correction algorithm (GTCA) [18] proposed by Han et al., they reported that the processing time depends on the total number of foreground/background filters required. For the brain volumes with typical size $140 \times 200 \times 160$ used in their experiments, each filter took less than 3 minutes on an SGI Onyx2 workstation with a 250 MHz R10000 processor, and the total processing time for each brain volume took less than 10 minutes. Normally, manual segmentation of one type tissue segmentation for an experienced person is about 18 hours.

5. CONCLUSIONS AND FUTURE WORK

In this paper, we proposed a novel scheme for 3D brain cortex segmentation based on dual-front active contours and local histogram analysis. The experimental section illustrated several advantages of our scheme. The first is that our scheme exhibited better results than most other methods when tested on 20 real normal brain images as demonstrated in Figures 11 and 12. The second is that the average computational time of our method is less than 20 seconds, which is much faster than most other methods, as discussed in Section 4.4. The third is that our method facilitates optional user interaction which is crucial when highly accurate results are needed, as it allows a trusted and trained user to guide the segmentation processes. This is discussed and illustrated in Section 4.3.

Our future research work will continue on the following aspects because of the complexity and variety of medical brain images. Since the dual-front active contour model is fast and easy to implement, it is easily combined with other preprocessing and postprocessing methods to improve the segmentation accuracy further. From the segmentation results shown in Section 4, we can see, for images with high INU settings and high noise levels, the segmentation results are not as good. We will work on combing our current model with INU bias compensation methods and smoothing methods to improve its performance in these conditions. In recent years, several methods have been proposed to correct INU settings [15, 26], and some other methods were also proposed to remove image noise. We will investigate on how other methods might be used in conjunction with our model.

Second, we have just used potentials based on region-based information because the interfaces between different tissues in the tested images were not very clear (due to partial volume effects). However, edge-based information is important and widely exploited for image segmentation and feature extraction. We are working on developing more robust local edge operators, and combining them with region-based information in our potentials to further improve the accuracy of our results.

Third, our model can be generalized to multispectral data sets commonly used in MR imaging. When processing such data sets, vectors may be used to represent intensities of image voxels instead of scalars, and how to design appropriate potentials and active regions for this case is a very interesting topic needing further investigation.

Fourth, we use histogram analysis to determine the active regions. The test images in this paper are normal elderly brain images, but young normal histograms have small CSF compartments compared to those seen in the elderly histograms. Additionally, in diseased brains, the contrast between gray and white matter is considerably reduced, and the two histogram peaks sometimes merge. In fact, when

we tested our method on two of the 20 real MR brain images, we had to choose the cutoff values for the active regions manually. Now, we are working on finding better methods to choose active regions for improving the method's generality.

APPENDIX

3D DUAL-FRONT EVOLUTION SCHEME

Initialization

Label map L: Initial contours $B_1, \ldots, B_n$ with labels $l_i, \ldots, l_n$; otherwise, $l(p) = -1$.

Action map U: for any point p of the initial contours, set $U(p) = 0$; for other points, set $U(p) = \infty$.

Potentials $\widetilde{P}_{l_i}(p)$: which is calculated based on the label l_i of the point p.

Input: active region R_n in image A ($I \times J \times K$), initial label map L, initial action map U.

Sweeping forward loop

(1) For each point $x(i, j, k)$ in R_n, calculate its new label and new action value by the ordering $i = 1 \to I$, $j = 1 \to J$, $k = 1 \to K$, as the following steps:

(i) the new label of x is the label of the point, which has the smallest U value among the point x and its 6-connected neighbors,

$$\begin{aligned} x_{\min} = \{x \mid u(x) = & \\ & \min\left(u_{i,j,k}, u_{i-1,j,k}, u_{i+1,j,k}, u_{i,j-1,k},\right. \\ & \left. u_{i,j+1,k}, u_{i,j,k-1}, u_{i,j,k+1}\right)\}; \\ l^{\text{new}}_{i,j,k} = l(x_{\min}); & \end{aligned} \tag{A.1}$$

(ii) calculate the new potential $h^{\text{new}}_{i,j,k}$ of point x, and find three minimum U in the 6-connected neighbors of point x:

$$\begin{gathered} h^{\text{new}}_{i,j,k} = \widetilde{P}_{l^{\text{new}}_{i,j,k}}(i, j, k); \\ a = \min\left(u_{i-1,j,k}, u_{i+1,j,k}\right); \qquad b = \min\left(u_{i,j-1,k}, u_{i,j+1,k}\right); \\ c = \min\left(u_{i,j,k-1}, u_{i,j,k+1}\right); \end{gathered} \tag{A.2}$$

(iii) arrange a, b, and c as $U_A \le U_B \le U_C$, and calculating new U from the current value of its 6-connected neighbors:

(a) if $|U_A - U_B| \ge h^{\text{new}}_{i,j,k}$, $\overline{u_{i,j,k}} = U_A + h^{\text{new}}_{i,j,k}$,

(b) if $|U_A - U_B| < h^{\text{new}}_{i,j,k}$, $\Delta_1 = 2(h^{\text{new}}_{i,j,k})^2 - (U_B - U_A)^2$,

(c) if $\sqrt{\Delta_1} \le 2U_C - (U_A + U_B)$, $\overline{u_{i,j,k}} = (U_A + U_B) + \sqrt{\Delta_1}/2$,

(d) if $\sqrt{\Delta_1} > 2U_C - (U_A + U_B)$, $\Delta_2 = (U_A + U_B + U_C)^2 - 3(U_A^2 + U_B^2 + U_C^2 - (h^{\text{new}}_{i,j,k})^2)$,

$$\overline{u}_{i,j,k} = (U_A + U_B + U_C) + \frac{\sqrt{\Delta_2}}{3}, \tag{A.3}$$

– updating $u_{i,j,k}$: $u^{\text{new}}_{i,j,k} = \min(u_{i,j,k}, \overline{u})$.

(2) Repeat the above computation 2^3 times with alternating sweeping orders.

Output is the label map L which divides the active region R_n to n regions.

ACKNOWLEDGMENTS

The authors would like to thank the anonymous reviewers for valuable comments and suggestions, and to thank Dr. Sebastien Fourey and Dr. Regis Clouard of GREYC-ENSICAEN, France, for providing MVox 3D model visualization and PANDORE image processing platform. This work is supported by NSF Grant CCR-0133736 and NIH Grant R01NS037747.

REFERENCES

[1] M. Kass, A. Witkin, and D. Terzopoulos, "Snakes: active contour models," *International Journal of Computer Vision*, vol. 1, no. 4, pp. 321–332, 1988.

[2] L. D. Cohen, "On active contour models and balloons," *Computer Vision Graphics Image Processing: Image Understanding*, vol. 53, no. 2, pp. 211–218, 1991.

[3] L. D. Cohen and I. Cohen, "Finite-element methods for active contour models and balloons for 2D and 3D images," *IEEE Tranactions on Pattern Analysis and Machine Intelligence*, vol. 15, no. 11, pp. 1131–1147, 1993.

[4] A. Yezzi, S. Kichenassamy, A. Kumar, P. Olver, and A. Tannenbaum, "Geometric snake model for segmentation of medical imagery," *IEEE Transactions on Medical Imaging*, vol. 16, no. 2, pp. 199–209, 1997.

[5] R. Malladi, R. Kimmel, D. Adalsteinsson, G. Sapiro, V. Caselles, and J. A. Sethian, "Geometric approach to segmentation and analysis of 3D medical images," in *Proceedings of the Workshop on Mathematical Methods in Biomedical Image Analysis (MMBIA '96)*, pp. 244–252, San Francisco, Calif, USA, June 1996.

[6] R. Malladi and J. A. Sethian, "A real-time algorithm for medical shape recovery," in *Proceedings of the IEEE International Conference on Computer Vision*, pp. 304–310, Bombay, India, January 1998.

[7] J. A. Sethian, "A fast marching level set method for monotonically advancing fronts," *Proceedings of the National Academy of Sciences of the United States of America*, vol. 93, no. 4, pp. 1591–1595, 1996.

[8] D. Adalsteinsson and J. A. Sethian, "A fast level set method for propagating interfaces," *Journal of Computational Physics*, vol. 118, no. 2, pp. 269–277, 1995.

[9] C. Davatzikos and R. N. Bryan, "Using a deformable surface model to obtain a shape representation of the cortex," *IEEE Transactions on Medical Imaging*, vol. 15, no. 6, pp. 785–795, 1996.

[10] T. Kapur, W. E. L. Grimson, W. M. Wells III, and R. Kikinis, "Segmentation of brain tissue from magnetic resonance images," *Medical Image Analysis*, vol. 1, no. 2, pp. 109–127, 1996.

[11] P. C. Teo, G. Sapiro, and B. A. Wandell, "Creating connected representations of cortical gray matter for functional MRI visualization," *IEEE Transactions on Medical Imaging*, vol. 16, no. 6, pp. 852–863, 1997.

[12] A. M. Dale, B. Fischl, and M. I. Sereno, "Cortical surface-based analysis," *NeuroImage*, vol. 9, no. 2, pp. 179–194, 1999.

[13] C. Xu, D. L. Pham, M. E. Rettmann, D. N. Yu, and J. L. Prince, "Reconstruction of the human cerebral cortex from

magnetic resonance images," *IEEE Transactions on Medical Imaging*, vol. 18, no. 6, pp. 467–480, 1999.

[14] X. Zeng, L. H. Staib, R. T. Schultz, and J. S. Duncan, "Segmentation and measurement of the cortex from 3D MR images using coupled-surfaces propagation," *IEEE Transactions on Medical Imaging*, vol. 18, no. 10, pp. 927–937, 1999.

[15] D. L. Pham and J. L. Prince, "Adaptive fuzzy segmentation of magnetic resonance images," *IEEE Transactions on Medical Imaging*, vol. 18, no. 9, pp. 737–752, 1999.

[16] D. MacDonald, N. Kabani, D. Avis, and A. Evans, "Automated 3D extraction of inner and outer surfaces of cerebral cortex from MRI," *NeuroImage*, vol. 12, no. 3, pp. 340–356, 2000.

[17] R. Goldenberg, R. Kimmel, E. Rivlin, and M. Rudzsky, "Cortex segmentation: a fast variational geometric approach," *IEEE Transactions on Medical Imaging*, vol. 21, no. 12, pp. 1544–1551, 2002.

[18] X. Han, C. Xu, U. Braga-Neto, and J. L. Prince, "Topology correction in brain cortex segmentation using a multiscale, graph-based algorithm," *IEEE Transactions on Medical Imaging*, vol. 21, no. 2, pp. 109–121, 2002.

[19] R. Valdés-Cristerna, V. Medina-Bañuelos, and O. Yáñez-Suárez, "Coupling of radial-basis network and active contour model for multispectral brain MRI segmentation," *IEEE Transactions on Biomedical Engineering*, vol. 51, no. 3, pp. 459–470, 2004.

[20] J. C. Bezdek, *Pattern Recognition with Fuzzy Objective Function Algorithms*, Plenum, New York, NY, USA, 1981.

[21] C. Xu and J. L. Prince, "Snakes, shapes, and gradient vector flow," *IEEE Transactions on Image Processing*, vol. 7, no. 3, pp. 359–369, 1998.

[22] J. Gomes and O. Faugeras, "Reconciling distance functions and level sets," *Journal of Visual Communication and Image Representation*, vol. 11, no. 2, pp. 209–223, 2000.

[23] R. Goldenberg, R. Kimmel, E. Rivlin, and M. Rudzsky, "Fast geodesic active contours," *IEEE Transactions on Image Processing*, vol. 10, no. 10, pp. 1467–1475, 2001.

[24] N. Kovacevic, N. J. Lobaugh, M. J. Bronskill, B. Levine, A. Feinstein, and S. E. Black, "A robust method for extraction and automatic segmentation of brain images," *NeuroImage*, vol. 17, no. 3, pp. 1087–1100, 2002.

[25] Z. Y. Shan, G. H. Yue, and J. Z. Liu, "Automated histogram-based brain segmentation in T1-weighted three-dimensional magnetic resonance head images," *NeuroImage*, vol. 17, no. 3, pp. 1587–1598, 2002.

[26] A. W.-C. Liew and H. Yan, "An adaptive spatial fuzzy clustering algorithm for 3D MR image segmentation," *IEEE Transactions on Medical Imaging*, vol. 22, no. 9, pp. 1063–1075, 2003.

[27] J. L. Marroquin, B. C. Vemuri, S. Botello, F. Calderon, and A. Fernandez-Bouzas, "An accurate and efficient Bayesian method for automatic segmentation of brain MRI," *IEEE Transactions on Medical Imaging*, vol. 21, no. 8, pp. 934–945, 2002.

[28] Y. Zhang, M. Brady, and S. Smith, "Segmentation of brain MR images through a hidden Markov random field model and the expectation-maximization algorithm," *IEEE Transactions on Medical Imaging*, vol. 20, no. 1, pp. 45–57, 2001.

[29] S. Ruan, C. Jaggi, J. Xue, J. Fadili, and D. Bloyet, "Brain tissue classification of magnetic resonance images using partial volume modeling," *IEEE Transactions on Medical Imaging*, vol. 19, no. 12, pp. 1179–1187, 2000.

[30] S. Ruan, B. Moretti, J. Fadili, and D. Bloyet, "Fuzzy Markovian segmentation in application of magnetic resonance images," *Computer Vision and Image Understanding*, vol. 85, no. 1, pp. 54–69, 2002.

[31] K. Van Leemput, F. Maes, D. Vandermeulen, and P. Suetens, "Automated model-based tissue classification of MR images of the brain," *IEEE Transactions on Medical Imaging*, vol. 18, no. 10, pp. 897–908, 1999.

[32] K. M. Pohl, W. M. Wells III, A. Guimond, et al., "Incorporating non-rigid registration into expectation maximization algorithm to segment MR images," in *Proceedings of the 5th International Conference on Medical Image Computing and Computer Assisted Intervention (MICCAI '02)*, pp. 564–572, Tokyo, Japan, September 2002.

[33] H. Li, A. Elmoataz, J. Fadili, and S. Ruan, "Dual front evolution model and its application in medical imaging," in *Proceedings of the 7th International Conference on Medical Image Computing and Computer-Assisted Intervention (MICCAI '04)*, vol. 3216 of *Lecture Notes in Computer Science*, pp. 103–110, Saint-Malo, France, September 2004.

[34] H. Li and A. Yezzi, "Local or global minima: flexible dual front active contours," in *Proceedings of Workshop-Computer Vision for Biomedical Image Applications (CVBIA '05)*, pp. 356–366, Beijing, China, October 2005.

[35] L. D. Cohen and R. Kimmel, "Global minimum for active contour models: a minimal path approach," in *Proceedings of the IEEE Computer Society Conference on Computer Vision and Pattern Recognition (CVPR '96)*, pp. 666–673, San Francisco, Calif, USA, June 1996.

[36] E. Rouy and A. Tourin, "A viscosity solutions approach to shape-from-shading," *SIAM Journal on Numerical Analysis*, vol. 29, no. 3, pp. 867–884, 1992.

[37] H. Zhao, "A fast sweeping method for Eikonal equations," *Mathematics of Computation*, vol. 74, no. 250, pp. 603–627, 2005.

[38] L. D. Cohen and R. Kimmel, "Global minimum for active contour models: a minimal path approach," *International Journal of Computer Vision*, vol. 24, no. 1, pp. 57–78, 1997.

[39] L. D. Cohen, "Multiple contour finding and perceptual grouping using minimal paths," *Journal of Mathematical Imaging and Vision*, vol. 14, no. 3, pp. 225–236, 2001.

[40] V. Caselles, R. Kimmel, and G. Sapiro, "Geodesic active contours," *International Journal of Computer Vision*, vol. 22, no. 1, pp. 61–79, 1997.

[41] T. Deschamps and L. D. Cohen, "Fast extraction of minimal paths in 3D images and applications to virtual endoscopy," *Medical Image Analysis*, vol. 5, no. 4, pp. 281–299, 2001.

[42] J. N. Tsitsiklis, "Efficient algorithms for globally optimal trajectories," *IEEE Transactions on Automatic Control*, vol. 40, no. 9, pp. 1528–1538, 1995.

[43] J. Helmsen, E. G. Puckett, P. Colella, and M. Dorr, "Two new methods for simulating photolithography development in 3D," in *Optical Microlithography IX*, vol. 2726 of *Proceedings of SPIE*, pp. 253–261, 1996.

[44] M. Boué and P. Dupuis, "Markov chain approximations for deterministic control problems with affine dynamics and quadratic cost in the control," *SIAM Journal on Numerical Analysis*, vol. 36, no. 3, pp. 667–695, 1999.

[45] T. F. Chan and L. A. Vese, "Active contours without edges," *IEEE Transactions on Image Processing*, vol. 10, no. 2, pp. 266–277, 2001.

[46] A. Yezzi, A. Tsai, and A. Willsky, "A fully global approach to image segmentation via coupled curve evolution equations," *Journal of Visual Communication and Image Representation*, vol. 13, no. 1-2, pp. 195–216, 2002.

[47] D. Mumford and J. Shah, "Optimal approximation by piecewise smooth functions and associated variational problems,"

Communications on Pure and Applied Mathematics, vol. 42, pp. 577–685, 1989.

[48] M. Dawood, X. Jiang, and K. P. Schäfers, "Reliable dual-band based contour detection: a double dynamic programming approach," in *Proceedings of International Conference on Image Analysis and Recognition (ICIAR '04)*, vol. 3212 of *Lecture Notes in Computer Science*, pp. 544–551, Porto, Portugal, September-October 2004.

[49] G. B. Aboutanos, J. Nikanne, N. Watkins, and B. M. Dawant, "Model creation and deformation for the automatic segmentation of the brain in MR images," *IEEE Transactions on Biomedical Engineering*, vol. 46, no. 11, pp. 1346–1356, 1999.

[50] C. E. Erdem, A. M. Tekalp, and B. Sankur, "Video object tracking with feedback of performance measures," *IEEE Transactions on Circuits and Systems for Video Technology*, vol. 13, no. 4, pp. 310–324, 2003.

[51] N. Xu, R. Bansal, and N. Ahuja, "Object segmentation using graph cuts based active contours," in *Proceedings of the IEEE Computer Society Conference on Computer Vision and Pattern Recognition (CVPR '03)*, vol. 2, pp. 46–53, Madison, Wis, USA, June 2003.

[52] BrainWeb, "Mcconnell Brain Imaging Center, Montreal Neurological Institute," http://www.bic.mni.mcgill.ca/brainweb/.

[53] T. J. Grabowski, R. J. Frank, N. R. Szumski, C. K. Brown, and H. Damasio, "Validation of partial tissue segmentation of single-channel magnetic resonance images of the brain," *NeuroImage*, vol. 12, no. 6, pp. 640–656, 2000.

[54] R. T. Schultz and A. Chakraborty, "Magnetic resonance image analysis," in *Handbook of Human Brain Function: Neuroimaging*, E. Bigler, Ed., pp. 9–51, Plenum, New York, NY, USA, 1996.

[55] D. N. Kennedy, P. A. Filipek, and V. S. Caviness Jr., "Anatomic segmentation and volumetric calculations in nuclear magnetic resonance imaging," *IEEE Transactions on Medical Imaging*, vol. 8, no. 1, pp. 1–7, 1989.

[56] R. Duda and P. Hart, *Pattern Classification and Scene Analysis*, John Wiley and Sons, New York, NY, USA, 1973.

[57] C. A. Cocosco, V. Kollokian, R. K.-S. Kwan, and A. C. Evans, "Brain web: online interface to a 3D MRI simulated brain database," *NeuroImage*, vol. 5, no. 4, part 2/4, p. S425, 1997.

[58] P. Perona and J. Malik, "Scale-space and edge detection using anisotropic diffusion," *IEEE Transactions on Pattern Analysis and Machine Intelligence*, vol. 12, no. 7, pp. 629–639, 1990.

[59] J. C. Rajapakse and F. Kruggel, "Segmentation of MR images with intensity inhomogeneities," *Image and Vision Computing*, vol. 16, no. 3, pp. 165–180, 1998.

[60] P. A. Filipek, C. Richelme, D. N. Kennedy, and V. S. Caviness Jr., "The young adult human brain: an MRI-based morphometric analysis," *Cerebral Cortex*, vol. 4, no. 4, pp. 344–360, 1994.

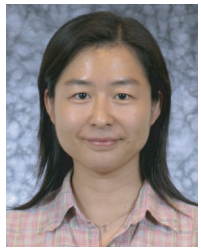

Hua Li received her Ph.D. degree in 2001 from the Department of Electronics and Information Engineering at Huazhong University of Science and Technology, China. Currently, she is a Postdoctoral Research Fellow at the School of Electrical and Computer Engineering, Georgia Institute of Technology. Her research interests are in the fields of image processing and computer vision; in particular PDEs, active contour models, curve and surface evolution theory, and mathematical morphology for 3D image segmentation and analysis with applications to medical imaging.

Anthony Yezzi obtained his Ph.D. degree in 1997 from the Department of Electrical Engineering at the University of Minnesota. After completing a postdoctoral research position in the Laboratory for Information and Decision Systems (LIDS) at Massachusetts Institute of Technology, he joined the faculty of the School of Electrical and Computer Engineering at Georgia Institute of Technology in 1999, where he currently holds the position of Associate Professor. He has also consulted a number of medical imaging companies including GE, Picker, and VTI, and has been an IEEE Member since 1999. His research lies primarily within the fields of image processing and computer vision. He has worked on a variety of problems including image denoising, edge detection, segmentation and grouping, shape analysis, multiframe stereo reconstruction, tracking, and registration. Some central themes of his research include curve and surface evolution theory, differential geometry, and partial differential equations.

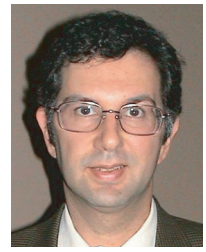

Laurent D. Cohen was at École Normale Supérieure, Ulm, in Paris from 1981 to 1985. He received M.S. and Ph.D. degrees in applied mathematics from the University of Paris 6 in 1983 and 1986. From 1985 to 1987, he was a Member at the Computer Graphics and Image Processing Group at Schlumberger Palo Alto Research, California, and Schlumberger Montrouge Research, and remained Consultant there for a few years afterwards. He began working with INRIA, France, in 1988, mainly with the Medical Image Understanding Group Epidaure. Since 1990, he has been a Research Scholar (Charge then Directeur de Recherche) with CNRS in the Applied Mathematics and Image Processing Group at CEREMADE, University Paris-Dauphine. His research interests and teaching at the university are applications of variational methods and partial differential equations to image processing and computer vision, like deformable models, minimal paths, surface reconstruction, image registration, image segmentation and restoration. He obtained CS 2002 Prize for Image and Signal Processing. He has been a member in program committees for boards for about 20 international conferences.

Hindawi Publishing Corporation
International Journal of Biomedical Imaging
Volume 2006, Article ID 89095, Pages 1–6
DOI 10.1155/IJBI/2006/89095

Total Variation Wavelet-Based Medical Image Denoising

Yang Wang and Haomin Zhou

School of Mathematics, Georgia Institute of Technology, Atlanta, GA 30332-0430, USA

Received 30 January 2006; Revised 12 May 2006; Accepted 12 May 2006

We propose a denoising algorithm for medical images based on a combination of the total variation minimization scheme and the wavelet scheme. We show that our scheme offers effective noise removal in real noisy medical images while maintaining sharpness of objects. More importantly, this scheme allows us to implement an effective automatic stopping time criterion.

1. INTRODUCTION

The advent of digital imaging technologies such as MRI has revolutionized modern medicine. Today, many patients no longer need to go through invasive and often dangerous procedures to diagnose a wide variety of illnesses. With the widespread use of digital imaging in medicine today, the quality of digital medical images becomes an important issue. To achieve the best possible diagnoses it is important that medical images be sharp, clear, and free of noise and artifacts. While the technologies for acquiring digital medical images continue to improve, resulting in images of higher and higher resolution and quality, noise remains an issue for many medical images. Removing noise in these digital images remains one of the major challenges in the study of medical imaging.

While noise in medical images present a problem because they could mask and blur important but subtle features in the images, many proposed denoising techniques have their own problems. One of the widely discussed techniques is the wavelet thresholding scheme, which recognizes that by performing a wavelet transform of a noisy image, random noise will be represented principally as small coefficients in the high frequencies. Thus in theory a thresholding, by setting these small coefficients to zero, will eliminate much of the noise in the image. The *wavelet hard thresholding scheme*, which sets wavelet coefficients below certain threshold in magnitude to 0, is easy to implement and fast to perform, and depending on the threshold, it removes noise adequately. However, at the same time it also introduces artifacts as a result of the Gibbs oscillation near discontinuities. Since artifacts in medical images may lead to wrong diagnoses, the wavelet hard thresholding scheme is not practical for use in medical imaging without being combined with other techniques. An improvement over the wavelet hard thresholding is the *wavelet soft thresholding scheme* [1, 2], which significantly reduces the Gibbs oscillation but does not eliminate it. The effectiveness of wavelet thresholding schemes in general are limited with combining them with other techniques. These other more complex techniques often try to take account of geometric informations by using wavelet-like bases that better characterize discontinuities, such as curvelets [3, 4]. Nevertheless, they do not completely eliminate the Gibbs phenomenon. Other methods with varying success have also been studied by different authors, for example, [5–7].

Another approach employs variational principles and PDE-based techniques. In this approach, a noisy image is modeled as $z(x) = u_0(x) + n(x)$ where u_0 denotes the uncontaminated underlying image and n denotes the noise. To reconstruct u_0 one considers the problem of minimizing

$$E(u) = \frac{\lambda}{2}\|u - z\|^2_{L^2(\omega)} + R(u), \tag{1}$$

where $\lambda > 0$, Ω is the domain on which z is defined, and the term $R(u)$ is a regularization functional. Earlier efforts focused on least square-based functionals $R(u)$'s such as $\|\Delta\|^2_{L^2(\omega)}$, $\|\nabla u\|^2_{L^2(\omega)}$, and others. While noise can be effectively removed, these regularization functionals penalize discontinuity, resulting in soft and smooth reconstructed images, with subtle details lost. Again, for medical imaging this is not practical, as subtle details could very well yield crucial information about the patients.

A better choice for $R(u)$ was proposed in [8], in which $R(u)$ is the *total variation (TV)* of u given by

$$R(u) = TV(u) := \int_\Omega |\nabla u| dx. \tag{2}$$

Intensive studies have shown that the total variation better preserves edges in u, thus it allows for sharper reconstructions, for example, [9–12]. Among all the PDE-based techniques, the TV minimization scheme is a candidate that offers the best combination of noise removal and feature preservation.

Solving the minimizers for the TV minimization (2), or (1) in general, amounts to solving certain PDEs, which is very similar to the anisotropic diffusion scheme proposed first in [13]. For the TV minimization it is easy to show that the PDE is given by

$$\nabla \cdot \left(\frac{\nabla u}{|\nabla u|} \right) - \lambda(u - z) = 0. \tag{3}$$

But in practice, one introduces the time variable t and solves for $u(x, t)$ by time-marching the equation

$$u_t = \nabla \cdot \left(\frac{\nabla u}{|\nabla u|} \right) - \lambda(u - z), \quad u(x, 0) = z(x). \tag{4}$$

The end result $u(x, T)$, if T is large enough, will have all noise removed. An important attribute of the TV minimization scheme is that it takes the geometric information of the original images into account, in that it preserves significant edges. In fact significant edges are sharpened. This is similar to the anisotropic diffusion methods see [13, 14] and references therein.

The time-marching of (4) is in essence solving for the minimizer of $E(u)$ by gradient flow. Two approaches are used for achieving the best combination of noise removal and feature preservation. The straighforward approach is to tune the parameter λ. Obviously if λ is too large we may not remove enough noise. On the other hand, if λ is too small it is well known that the scheme will remove too many features and end up with a cartoon-like piecewise constant image [15, 16]. But tuning the parameter λ is time consuming. Since in practice there is no original image to compare to, and the assumption of i.i.d. Gaussian noise is not always realistic, tuning λ often relies on experience and visual inspection. There is no automatic way for it as far as we know. A more widely used approach is to choose λ in a reasonable range without being precise about the choice. Instead, we try to stop the time-marching before it reaches the ground state at a point that offers a good combination of noise removal and feature preservation. But again here we face the problem of deciding when to stop. There have been efforts in this direction, see, for example, [17, 18]. These proposed criteria are typically cumbersome and are based on some a priori knowledge about the noise such as the variance and type, which may not be realistic. With the explosion in volumes of medical images, this is a very significant issue.

In this paper we propose a *wavelet TV* denoising scheme. In our scheme, the wavelet coefficients are selected and modified subjecting to minimizing the TV norm of the reconstructed images. We demonstrate that while being as effective as the TV scheme in removing noise, the wavelet TV scheme allows us to modify the wavelet coefficients primarily in the high frequency domain, something that the regular TV scheme cannot do. Experiments show that the wavelet TV scheme preserves details like the regular TV scheme but offers a slightly higher PSNR in the reconstruction. It is also significantly faster in that far fewer iterations are needed for noise removal. The details of these improvements will be presented in a separate paper [19]. And unlike the traditional wavelet thresholding scheme, it does not introduce Gibbs' oscillations near discontinuities. These properties are consistent with other investigations that combine variational approaches with wavelet framework [20–24]. But more importantly, this scheme allows for an effective automatic stopping time criterion based on a certain statistical property of wavelet coefficients. An added advantage for our approach is that it leads to superior JPEG2000 compression for denoised images [21]. Given the increased use of JPEG2000 standard in medical imaging, this is a significant bonus.

2. THE WAVELET TOTAL VARIATION DENOISING METHOD

In this section, we describe our image denoising algorithm based on wavelet and TV minimization.

We start with a standard noisy monochromatic image model

$$z(x) = u_0(x) + n(x), \tag{5}$$

where $z(x)$, $u_0(x)$, and $n(x)$ are real valued functions defined on $\mathbb{R}^2$, and they are compactly supported since they represent images in our study. The function $u_0(x)$ denotes the underlying noise-free image, $z(x)$ the observed image, and $n(x)$ the noise. In our general model, we assume that $z(x)$, $u_0(x)$, and $n(x)$ are in some space of functions $\mathcal{F}$, such as $L^2(\Omega)$ for some domain Ω. Let $\{\psi_j : j \in I\}$ be a basis for $\mathcal{F}$. This basis can be an orthonormal basis, such as wavelets [25, 26] if $\mathcal{F}$ is a Hilbert space, or any other type of bases in general. So for any $f(x) \in \mathcal{F}$ we have

$$f(x) = \sum_{j \in I} c_j \psi_j(x), \tag{6}$$

for some real (c_j).

In [21] a wavelet TV minimization model is proposed, in which $\{\psi_j\}$ is taken to be a wavelet basis for $\mathcal{F} = L^2(\Omega)$. In that model, the wavelet coefficients are selected and modified to achieve the goals of image processing such as denoising and compression. In this paper, we refine the above model. Key to our innovation is an automatic stopping criterion, a feature we believe to be very important for medical applications. Another improvement is the multiscale fitting parameters targeting denoising in the high frequency domain, which yields a significant reduction in number of iterations needed to achieve the desired denoising as well as a small performance improvement in terms of PSNR on simulated noisy images.

We first describe the denoising part in the general setting. Let

$$z(x) = \sum_{j\in I} \alpha_j \psi_j(x) \tag{7}$$

and denote

$$u(x,\boldsymbol{\beta}) := \sum_{j\in I} \beta_j \psi_j(x), \tag{8}$$

where $\boldsymbol{\beta} = (\beta_j)$. Define the *total variation* functional by

$$F(u) := \int_{\mathbb{R}^2} |\nabla_x u(x,\boldsymbol{\beta})|\, dx + \frac{1}{2}\sum_{j\in I} \lambda_j (\beta_j - \alpha_j)^2, \tag{9}$$

where $u = u(x,\boldsymbol{\beta})$, $\lambda_j > 0$. In practice we often replace $|\nabla_x u(x,\boldsymbol{\beta})|$ by

$$|\nabla_x u|_\epsilon = \sqrt{|\nabla_x u|^2 + \epsilon}, \quad \text{with } 0 < \epsilon \ll 1. \tag{10}$$

The small parameter ϵ is used to prevent denominators from vanishing in numerical implementations. The goal of denoising is to minimize $F(u)$ and find the minimizer $u^* := u(x,\boldsymbol{\beta}^*)$ such that

$$F(u^*) = \min_{\boldsymbol{\beta}} F(u). \tag{11}$$

The objective functional in (9) differs somewhat from the one used in [21], where all λ_j's are uniformly set to a single parameter λ. With uniform parameter λ and an orthonormal basis $\{\psi_j\}$ the objective functional $F(u)$ is the same as the objective functional $E(u)$ in (1). Hence the minimizer of $F(u)$ would be the same as that of $E(u)$ for the regular TV scheme. By taking a basis that is not an orthonormal basis, such as a biorthogonal wavelet basis as we do in our implementation, $F(u)$ is typically not the same as $E(u)$, even with uniform parameter λ_j. With nonuniform λ_j's the objective functional $F(u)$ can be significantly different from $E(u)$ in the original TV scheme. Like the regular TV denoising scheme, the wavelet TV scheme proposed here retain sharp edges without creating Gibbs' phenomenon.

One can use simple calculus of variation to obtain the derivative of the objective functional (9). For $u = u(x,\boldsymbol{\beta})$ where $\boldsymbol{\beta} = (\beta_j)$,

$$\begin{aligned}\frac{\partial F(u)}{\partial \beta_j} &= \int_{\mathbb{R}^2} \frac{\nabla_x u}{|\nabla_x u|}\cdot \nabla_x \psi_j dx + \lambda_j(\beta_j - \alpha_j)\\ &= -\int_{\mathbb{R}^2} \nabla_x \cdot \left[\frac{\nabla_x u}{|\nabla_x u|}\right]\psi_j dx + \lambda_j(\beta_j - \alpha_j).\end{aligned} \tag{12}$$

Then the Euler-Lagrange equation for the model is

$$-\int_{\mathbb{R}^2} \nabla_x \cdot \left(\frac{\nabla_x u}{|\nabla_x u|}\right)\psi_j(x)dx + \lambda_j(\beta_j - \alpha_j) = 0. \tag{13}$$

In practice, rather than solving the Euler-Lagrange equation (13) directly to denoise an image, we introduce an artificial time parameter t and time-march the image using gradient flow. More precisely, we set $\boldsymbol{\beta} = \boldsymbol{\beta}(t) = (\beta_j(t))$ and solve the following time evolution equation:

$$\frac{\partial \beta_j}{\partial t} = \int_{\mathbb{R}^2} \nabla_x \cdot \left(\frac{\nabla_x u}{|\nabla_x u|}\right)\psi_j(x)dx - \lambda_j(\beta_j - \alpha_j), \quad \beta_j(0) = \alpha_j. \tag{14}$$

The minimizer of the TV wavelet model is the steady state of the above equation.

However, it is well known that TV minimization often leads to images with cartoonish features. More precisely, the denoising algorithm will remove noise as well as fine structures, such as textures and subtle details, from an image. The consequence is that unless the parameter λ in (1) is carefully calibrated, if one evolves (14) for an extended time, the denoised image is often over-smoothed to the point that it is almost piecewise constant. The wavelet TV denoising scheme has the same issue. This is often unacceptable for most medical applications. In the original TV minimization scheme introduced in [8] or similar schemes such as anisotropic diffusion, there was no mechanism for stopping the time evolution. In fact, since the objective functionals do not measure information pertaining to noise in the processes, a mechanism to stop the time evolution automatically is virtually impossible. But in our wavelet TV denoising scheme this can be naturally done. The reason is that high frequency wavelet coefficients are well known to encode information about noise in images. This property of high frequency wavelet coefficients has served as the basis for virtually all wavelet denoising methods, such as the widely used hard or soft thresholdings, or wavelet shrinkage. Now, by choosing $\{\psi_j\}$ to be a wavelet basis, the same principle allows us to design a natural automatic stopping criterion for the wavelet TV minimization method, making it an extremely viable scheme for medical applications.

We now describe our automatic stopping criterion with the basis $\{\psi_j : j \in I\}$ being a wavelet basis—in our case we usually take the biorthogonal wavelet basis generated by the well-known 7–9 biorthogonal wavelets. (We remark that the conventional notation for wavelet bases use two or more indices, such as $\{\psi_{jk}\}$. In this paper we only use one index for conciseness, and there should not be any confusion). Like in the wavelet hard thresholding scheme, we first choose a threshold $\rho > 0$. Let $J_\rho = \{j \in I_D : |\beta_j(0)| = |\alpha_j| \le \rho\}$, where $I_D \subset I$ is the index set corresponding to the diagonial portion of the highest frequency wavelet coefficients. Intuitively speaking, as in the wavelet hard thresholding scheme, the coefficients $\{\beta_j(0) : j \in J_\rho\}$ will indicate how noisy the image is. In a noise-free image these wavelet coefficients will mostly be very close to 0. But in a noisy image they will be more substantial. Define $\mu(t) = (1/|J_\rho|)\sum_{j\in J_\rho} |\beta_j(t)|$. So $\mu(t)$ measures the noise in the image at time t. The key idea is that an automatic stopping criterion of the time evolution can be designed by measuring the reduction in the value $\mu(t)$ from the original value $\mu(0)$.

We can use two different approaches in setting the automatic stopping criterion. The first approach is the *relative criterion*. In the relative criterion, we consider $\mu(t)/\mu(0)$. We will stop the time evolution whenever this value goes below a threshold b. For example, we may set $b = 0.1$. This threshold

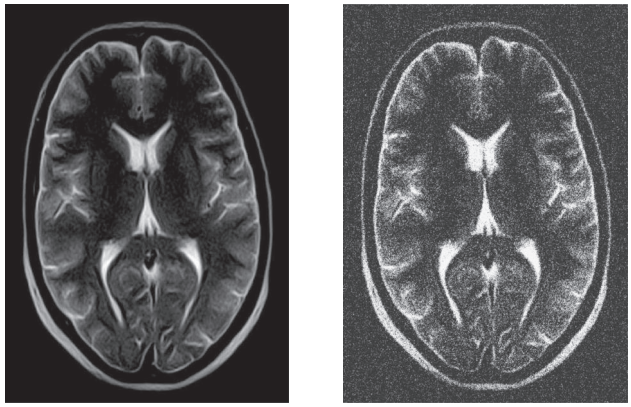

(a) (b)

Figure 1: (a) Original image. (b) Image with artificial additive Gaussian white noise, with PSNR = 2.55 (dB).

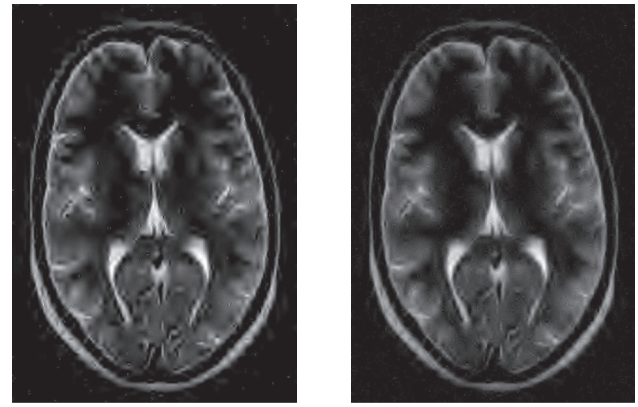

(a) (b)

Figure 2: (a) Denoised image by wavelet hard thresholding PSNR = 8.65 (dB), with the selected threshold that returns the best PSNR performance. (b) Denoised image by wavelet soft thresholding PSNR = 8.36 (dB); the threshold is selected to reach the best PSNR improvement. We note that the hard thresholding gives better PSNR performance because it is optimal in the L^2 norm sense, but the soft thresholding gives better visual quality because its Gibbs' oscillations are less severe.

intuitively says that we stop the time evolution when we have reduced noise by 90%. The second approach is the *absolute criterion*. In the absolute criterion, we stop the time evolution if $\mu(t)$ drops below a threshold c. Since in a noise-free image we expect $\mu(t)$ to be very close to zero, it is reasonable to set an absolute threshold for $\mu(t)$ to achieve a desired denoising effect.

In the actual implementation the value ρ does not seem to affect the automatic stopping time sensitively. We usually take $\rho = (2/|I_D|)\sum_{j\in I_D}|\alpha_j|$. Both the relative criterion and the absolute criterion work well, although we typically use the relative criterion. For an image with moderate noise we set the threshold b to be between 0.05 and 0.1. In the more noisy cases such as the images shown in this paper, we use smaller threshold b around 0.03. We tested the automatic stopping time criterion on a number of MRI images for one lab. The thresholds for optimal performance stayed remarkably consistent. This is an important property for batch processing of medical images.

3. EXAMPLES

In this section we provide some examples to illustrate the performance of our algorithm. The first example is for testing. Artificial noise is added to an otherwise rather clean brain scan shown in Figure 1(a). The standard peak signal-to-noise ratio (PSNR) is employed to quantify the performance of denoising, where

$$\mathrm{PSNR} = 10\log_{10}\left(\frac{255^2}{||u-u_0||_2^2}\right)\ (\mathrm{dB}), \tag{15}$$

where 255 is the maximum intensity value of the gray-scale images, u_0 the noise-free original image, u the noise added image, and $\|\cdot\|_2$ the standard L^2 norm. A conventional criterion is that larger PSNR signifies better performance. In addition, we use visual inspection to compare the performance in preservation of edges and other geometric features, which is not reflected through the PSNR measurement. In all examples shown here, we use Daubechies 7–9 biorthogonal wavelets with symmetric extensions at the boundaries.

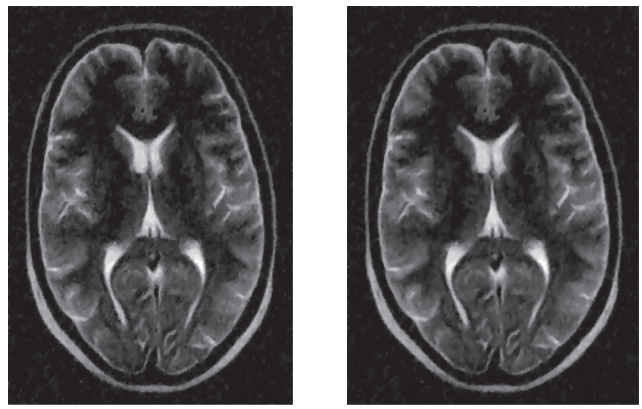

(a) (b)

Figure 3: (a) Denoised image by TV wavelet with fixed fitting parameter λ_j, the PSNR = 10.05 (dB). This image and the PSNR measurement are very similar to those of the regular TV scheme with the same parameter. (b) Denoised image by TV wavelet with variable fitting parameter λ_j on different wavelet scales, the PSNR = 10.28 (dB).

We performed denoising on the noise-added brain scan image using the standard wavelet thresholding schemes (Figure 2) and our wavelet TV schemes (Figure 3). The thresholds in the wavelet hard and soft thresholding were chosen after some trials to ensure the best performance (in terms of PSNR) for fairness. This actually exemplifies the problem we try to solve: the only way to get optimal result is through trial and error experiments with the threshold.

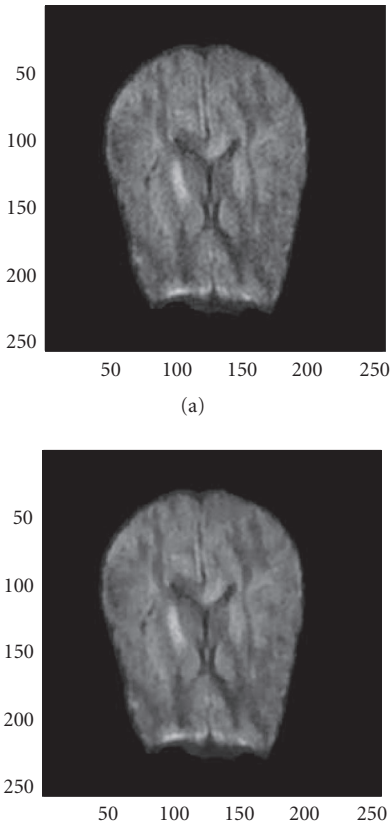

FIGURE 4: (a) Original image. (b) Denoised image using the TV wavelet algorithm.

For our wavelet TV scheme we use the relative approach and have set the autostopping threshold $b = 0.03$. We show results for two different choices of the parameters λ_j. In the first one we choose uniform $\lambda_j = 5$. In the second, the fitting parameters λ_j for the coarsest level wavelet coefficients (including low frequencies) are all set to $\lambda_j = 400$. Afterwards with each finer level we decrease λ_j's by a factor of 4. Similar idea of choosing the parameters has appeared in [27] for a different purpose. As one can see, the wavelet TV scheme in both examples outperforms the wavelet thresholding significantly. But more importantly, the wavelet TV image maintained sharpness and many fine details, while the wavelet thresholding image looks soft with details lost. The uniform fitting parameter example performed similarly to the regular TV scheme with the same parameter. The multiscale fitting parameters wavelet TV scheme has a small advantage in PSNR, and in our opinion is visually better. However, the number of iterations is significantly smaller than either the uniform λ_j wavelet TV scheme or the regular TV scheme.

In the next example (Figure 4), we apply the algorithms with uniform $\lambda_j = 5$ to a real image without artificial noise. The original image appears quite noisy. We cannot judge the performance by examining the PSNR as we do not have a noise-free image with which we can compare. However, by visual inspection it is evident that the denoised image, while removing a substantial amount of noise, suffers virtually no degradation in sharpness and details.

ACKNOWLEDGMENTS

We would like to thank Dr. Xiaoping Hu and his lab for providing us with the original image in Figure 2 and very helpful discussions. We would like to thank Dr. Guowei Wei for providing us with the image in Figure 1. Finally, we thank the anonymous referees for their valuable comments. The first author was supported in part by the National Science Foundation Grant no. DMS-0456538. The second author was supported in part by the National Science Foundation Grant no. DMS-0410062.

REFERENCES

[1] D. L. Donoho, "De-noising by soft-thresholding," *IEEE Transactions on Information Theory*, vol. 41, no. 3, pp. 613–627, 1995.

[2] D. L. Donoho and J. M. Johnstone, "Ideal spatial adaptation by wavelet shrinkage," *Biometrika*, vol. 81, no. 3, pp. 425–455, 1994.

[3] E. J. Candès and D. Donoho, "Curvelets—a surprisingly effective nonadaptive representation for objects with edges," in *Curves and Surfaces*, A. Cohen, C. Rabut, and L. L. Schumaker, Eds., pp. 105–120, Vanderbilt University Press, Nashville, Tenn, USA, 1999.

[4] E. J. Candès and F. Guo, "Edge-preserving image reconstruction from noisy radon data," (Invited *special issue of the Journal of Signal Processing on Image and Video Coding Beyond Standards.*), 2001.

[5] A. Buades, B. Coll, and J.-M. Morel, "A non-local algorithm for image denoising," in *Proceedings of the IEEE Computer Society Conference on Computer Vision and Pattern Recognition (CVPR '05)*, vol. 2, pp. 60–65, San Diego, Calif, USA, June 2005.

[6] R. H. Chan, S. D. Riemenschneider, L. Shen, and Z. Shen, "Tight frame: an efficient way for high-resolution image reconstruction," *Applied and Computational Harmonic Analysis*, vol. 17, no. 1, pp. 91–115, 2004.

[7] J. Portilla, V. Strela, M. J. Wainwright, and E. P. Simoncelli, "Image denoising using scale mixtures of Gaussians in the wavelet domain," *IEEE Transactions on Image Processing*, vol. 12, no. 11, pp. 1338–1351, 2003.

[8] L. I. Rudin, S. Osher, and E. Fatemi, "Nonlinear total variation based noise removal algorithms," *Physica D*, vol. 60, no. 1–4, pp. 259–268, 1992.

[9] R. Acar and C. R. Vogel, "Analysis of total variation penalty methods for ill-posed problems," *Inverse Problems*, vol. 10, no. 6, pp. 1217–1229, 1994.

[10] A. Chambolle and P.-L. Lions, "Image recovery via total variation minimization and related problems," *Numerische Mathematik*, vol. 76, no. 2, pp. 167–188, 1997.

[11] T. F. Chan, S. Osher, and J. Shen, "The digital TV filter and nonlinear denoising," *IEEE Transactions on Image Processing*, vol. 10, no. 2, pp. 231–241, 2001.

[12] D. C. Dobson and C. R. Vogel, "Convergence of an iterative method for total variation denoising," *SIAM Journal on Numerical Analysis*, vol. 34, no. 5, pp. 1779–1791, 1997.

[13] P. Perona and J. Malik, "Scale-space and edge detection using anisotropic diffusion," *IEEE Transactions on Pattern Analysis and Machine Intelligence*, vol. 12, no. 7, pp. 629–639, 1990.

[14] Y. Sun, P. Wu, G. W. Wei, and G. Wang, "Evolution-operator-based single-step method for image processing," *International Journal of Biomedical Imaging*, vol. 2006, Article ID 83847, pp. 27 pages, 2006.

[15] Y. Meyer, *Oscillating Patterns in Image Processing and Nonlinear Evolution Equations*, vol. 22 of *University Lecture Series*, American Mathematical Society, Providence, RI, USA, 2001.
[16] S. Osher, A. Solé, and L. Vese, "Image decomposition and restoration using total variation minimization and H^1," *Multiscale Modeling and Simulation*, vol. 1, no. 3, pp. 349–370, 2003.
[17] P. Mrázek and M. Navara, "Selection of optimal stopping time for nonlinear diffusion filtering," *International Journal of Computer Vision*, vol. 52, no. 2-3, pp. 189–203, 2003.
[18] J. Weickert, "Coherence-enhancing diffusion of colour images," *Image and Vision Computing*, vol. 17, no. 3-4, pp. 201–212, 1999.
[19] Y. Wang and H.-M. Zhou, "Denoising natural color images," preprint.
[20] A. Chambolle, R. A. DeVore, N.-Y. Lee, and B. J. Lucier, "Nonlinear wavelet image processing: variational problems, compression, and noise removal through wavelet shrinkage," *IEEE Transactions on Image Processing*, vol. 7, no. 3, pp. 319–335, 1998.
[21] T. F. Chan and H. Zhou, "Optimal constructions of wavelet coefficients using total variation regularization in image compression," UCLA CAM Report 00-27, Department of Mathematics, UCLA, Los Angeles, Calif, USA, July 2000.
[22] T. F. Chan and H. Zhou, "Total variation wavelet thresholding," submitted to *Journal of Computational Physics*.
[23] S. Durand and J. Froment, "Artifact free signal denoising with wavelets," in *Proceedings of IEEE International Conference on Acoustics, Speech and Signal Processing (ICASSP '01)*, vol. 6, pp. 3685–3688, Salt Lake City, Utah, USA, May 2001.
[24] F. Malgouyres, "Mathematical analysis of a model which combines total variation and wavelet for image restoration," *Journal of Information Processes*, vol. 2, no. 1, pp. 1–10, 2002.
[25] I. Daubechies, *Ten Lectures on Wavelets*, SIAM, Philadelphia, Pa, USA, 1992.
[26] G. Strang and T. Nguyen, *Wavelets and Filter Banks*, Wellesley-Cambridge Press, Wellesley, Mass, USA, 1996.
[27] Y. Lu, L. Shen, and Y. Xu, "Shadow block iteration for solving linear systems obtained from wavelet transforms," *Applied and Computational Harmonic Analysis*, vol. 19, no. 3, pp. 359–385, 2005.

Yang Wang graduated from the University of Science and Technology of China in 1983 with B.S. degree in mathematics, and received his doctorate degree in mathematics from Harvard University in 1990 under the guidance of David Mumford. He has been a Faculty Member at Georgia Tech since, and is currently the Asscoiate Chair and the Undergraduate Coordinator of Mathematics. His research interests include wavelets and applications, tiling, fractal geometry and applications, image processing, among others.

Haomin Zhou graduated from the Peking University in 1991 with B.S. degree in mathematics. He received his M. Phil. degree in applied mathematics from the Chinese University of Hong Kong in 1996 and his Ph.D. degree in mathematics from University of California, Los Angeles, in 2000. He spent 3 years in California Institute of Technology as a Postdoctoral Researcher before he became a Faculty Member of Georgia Institute of Technology, in 2003. His research interests include wavelets and applications, numerical PDEs, image processing, as well as stochastic differential equations and applications.

Hindawi Publishing Corporation
International Journal of Biomedical Imaging
Volume 2006, Article ID 12014, Pages 1–11
DOI 10.1155/IJBI/2006/12014

BOLD Noise Assumptions in fMRI

Alle Meije Wink[1] and Jos B. T. M. Roerdink[2, 3]

[1] *Brain Mapping Unit, Department of Psychiatry, University of Cambridge, Addenbrooke's Hospital, Hills Road, Cambridge CB2 2QQ, UK*
[2] *Institute for Mathematics and Computing Science, University of Groningen, P.O. Box 800, 9700 AV Groningen, The Netherlands*
[3] *Institute for Behavioral and Cognitive Neurosciences and BCN Neuroimaging Center, University of Groningen, The Netherlands*

Received 30 January 2006; Revised 13 June 2006; Accepted 17 June 2006

This paper discusses the assumption of Gaussian noise in the blood-oxygenation-dependent (BOLD) contrast for functional MRI (fMRI). In principle, magnitudes in MRI images follow a Rice distribution. We start by reviewing differences between Rician and Gaussian noise. An analytic expression is derived for the null (resting-state) distribution of the difference between two Rician distributed images. This distribution is shown to be symmetric, and an exact expression for its standard deviation is derived. This distribution can be well approximated by a Gaussian, with very high precision for high SNR, and high precision for lower SNR. Tests on simulated and real MR images show that subtracting the time-series mean in fMRI yields asymmetrically distributed temporal noise. Subtracting a resting-state time series from the first results in symmetric and nearly Gaussian noise. This has important consequences for fMRI analyses using standard statistical tests.

1. INTRODUCTION

Functional magnetic resonance imaging (fMRI) measures activity in different areas of the brain under different experimental conditions (e.g., active, rest). In the medical imaging literature, magnitudes in MR images are assumed to follow a Rice distribution [1–7], first studied by Rice [8, pages 100–103]. Most statistical analyses of fMRI images test the difference between experimental conditions against a *null distribution*, which applies when no task is performed. Parametric statistical fMRI analysis often assumes Gaussian noise [9–14], but findings contradicting this assumption have already been reported by Hanson and Bly [15], and tests for the distribution of the residual (noise) signal in fMRI data sets have been developed [16].

In this paper, we examine the properties of Rician noise, and the distribution of resting state images that are made by pairwise subtraction of MR images. Most standard tests, such as the t-test, F-test, and the z-test, rely on Gaussian distributed noise. Petersson et al. [17] argue that with Gaussian spatial smoothing, many degrees of freedom, and the multivariate central limit theorem, these tests are valid in functional neuroimaging, but they warn that low-count PET data show departures from normality. Similar effects can be seen in functional MR images. The Rician probability density function is very asymmetric if the signal is weak compared to the noise, so for low signal intensities and with a low signal-to-noise ratio (SNR), Rician noise and Gaussian noise behave very differently and the Rician distribution has to be taken into account in order to prevent biased statistical results.

This problem is important for fMRI, because the scans may have relatively low SNRs, and the values of the BOLD contrast are very small compared to the noise. This is especially true for data with high temporal and/or spatial resolution: this will inevitably lead to lower SNR values.

The remainder of this paper is organised as follows. Section 2 introduces the Rician noise model for MR images. Section 3 derives analytical expressions for the probability distribution of the difference between two MR images, which are verified in a series of tests on synthetic noise images. Section 4 investigates the noise distributions in MR template images contaminated with noise and in a real fMRI time series, and discusses implications for the design of fMRI experiments. Section 5 contains some general conclusions.

2. NOISE IN MR IMAGES

During image acquisition in an MR scanner, magnetic fields are transmitted in pulses varying in frequency and phase. Voxel locations are selected by frequency and phase, and the resulting data consist of complex values. The frequency space

in which these data are represented is known as the k-space. The values in the real and imaginary parts of the image are Gaussian distributed. The k-space data are transformed to a Cartesian space via an inverse Fourier transform (IFT). The noise distribution in the resulting image is still Gaussian, because the IFT is a linear transform.

Most applications of MR imaging only use the magnitudes of the signal, because those magnitudes represent a physical property of the scanned object [18]. Let $A(\mathbf{x})$ represent the magnitude of the MR image at voxel location $\mathbf{x}$ in the absence of noise. The magnitude $r(\mathbf{x})$ of the signal at voxel location $\mathbf{x}$ in the magnitude image is

$$r(\mathbf{x}) = \sqrt{\left(A(\mathbf{x}) + n_1(\mathbf{x})\right)^2 + n_2(\mathbf{x})^2}, \quad n_1(\mathbf{x}), n_2(\mathbf{x}) \sim N(0, \sigma^2), \tag{1}$$

where $n_1(\mathbf{x})$ and $n_2(\mathbf{x})$ are the real and imaginary parts of the noise and $N(0, \sigma^2)$ is the Gaussian distribution with mean zero and standard deviation σ.

The magnitude signal in each voxel $\mathbf{x}$ is Rician distributed [1–3], that is, $\text{Prob}[r \le r(\mathbf{x}) \le r + \mathrm{d}r] = p_{A(\mathbf{x}),\sigma}(r)$, where $p_{A,\sigma}(r)$ is the Rician probability density with parameters A and σ defined by

$$p_{A,\sigma}(r) = \begin{cases} 0, & r < 0 \\ \dfrac{r}{\sigma^2} e^{-(A^2+r^2)/2\sigma^2} I_0\left(\dfrac{Ar}{\sigma^2}\right), & r \ge 0, \end{cases} \tag{2}$$

where

$$I_k(z) = \frac{1}{\pi} \int_0^{\pi} e^{z\cos(\theta)} \cos(k\theta)\mathrm{d}\theta \tag{3}$$

is the modified Bessel function of the first kind of order k, $k \in \mathbb{N}$. Figure 1 shows the Rician probability density function (pdf) for varying values of A and σ. The shape of the PDF changes with both parameters. The distribution for $A = 0$ is called the *Rayleigh distribution*. For high SNRs, the Rician distribution approaches a Gaussian distribution [3].

The mean $\mu_r = \int_0^{\infty} r p_{A,\sigma}(r)\mathrm{d}r$ of the Rice distribution is given by [8, pages 100–103, Appendix 4B]

$$\mu_r = \sigma\sqrt{\frac{\pi}{2}} e^{(-z^2/4)4} \left\{ \left[1 + \frac{z^2}{2}\right] I_0\left(\frac{z^2}{4}\right) + \frac{z^2}{2} I_1\left(\frac{z^2}{4}\right) \right\}, \tag{4}$$

where $z = A/\sigma$ is the SNR, and I_k, $k = 0, 1$, is defined in (3). The standard deviation $\sigma_r = \sqrt{\int_0^{\infty} r^2 p_{A,\sigma}(r)\mathrm{d}r - \mu_r^2}$ of the Rice distribution satisfies the relation [3]

$$\sigma_r = \sqrt{A^2 + 2\sigma^2 - \mu_r^2}. \tag{5}$$

As A/σ goes to infinity, these formulas yield $\mu_r \to A$, $\sigma_r \to \sigma$, that is, the mean approaches the noise-free intensity and the standard deviation approaches the corresponding value of the underlying noise distribution $N(0, \sigma^2)$.

MR noise was modelled by computing the intensity distribution as in (1). To make a Rice-distributed noisy image from a real-valued noise-free image $f(\mathbf{x})$, we use the

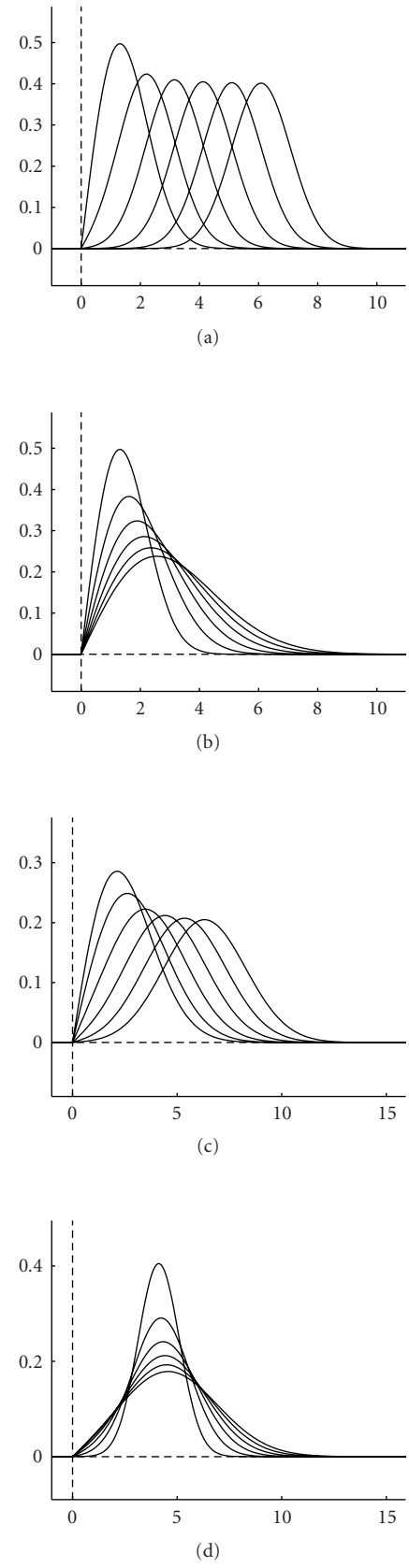

Figure 1: (a) Rician PDFs for $\sigma^2 = 1$ and $A \in \{1, \ldots, 6\}$, (b) Rician PDFs for $A = 1$ and $\sigma_r^2 \in \{1, \ldots, 6\}$, (c) Rician PDFs for $\sigma^2 = 4$ and $A \in \{1, \ldots, 6\}$, (d) Rician PDFs for $A = 4$ and $\sigma_r^2 \in \{1, \ldots, 6\}$.

following procedure for each voxel location $\mathbf{x}$:

(1) $n_1(\mathbf{x}), n_2(\mathbf{x}) \sim N(0, \sigma^2)$,
(2) $r(\mathbf{x}) = \sqrt{[f(\mathbf{x}) + n_1(\mathbf{x})]^2 + n_2(\mathbf{x})^2}$.

Again, the noisy image is denoted by $r(\mathbf{x})$. The local SNR is controlled through the ratio $f(\mathbf{x})/\sigma$, where $f(\mathbf{x})$ and σ determine μ_r and σ_r as described in (4) and (5), respectively.

3. MATHEMATICAL ANALYSIS OF fMRI NOISE

3.1. Statistical testing in fMRI

In fMRI analysis, one searches for activation in certain brain areas via statistical hypothesis testing. The null hypothesis H_0 states that there is no activation, other hypotheses correspond to several kinds of activation. Most fMRI analysis methods, such as statistical parametric mapping [13], use the general linear model (GLM). The GLM treats fMRI responses as the outputs of a linear time-invariant (LTI) system using a number of temporal basis functions, $f_1(\cdot), \ldots, f_M(\cdot)$, called *explanatory variables*. The GLM has the form

$$Y_{k,s} = \beta_{k,1} f_1(t_s) + \cdots + \beta_{k,M} f_M(t_s) + e_{k,s}, \tag{6}$$

where $Y_{k,s}$ is the observed data at voxel k, $k = 1, \ldots, N$, and time index s, $s = 1, \ldots, T$; $f_m(t_s)$ is value of the mth basis function at time t_s, $m = 1, \ldots, M$; the $\beta_{k,m}$ are weight factors of each temporal component at each voxel (to be determined from the measurements); and $e_{k,s}$ is the error (noise) at voxel k and time index s. In matrix form, the GLM may be succinctly written as

$$\mathbf{Y} = \mathbf{X}\boldsymbol{\beta} + \mathbf{e}, \tag{7}$$

where $\mathbf{Y}$ is a $T \times N$ matrix, $\mathbf{X}$ is the $T \times M$ design matrix containing the $f_m(t_s)$ values, $\boldsymbol{\beta}$ is $T \times N$ weight matrix, and $\mathbf{e}$ is the $T \times N$ residual matrix containing the part of the signal not modelled by any component in $\mathbf{X}$. Statistical parametric tests often assume that the error values in $\mathbf{e}$ are independent and identically normally distributed, that is, $e_{k,s} \sim N(0, \sigma_k^2)$, where the standard deviation may depend on the voxel location.

In brain activation studies, one considers an equation of the form (6) for both the activated and the rest (null) condition. Let $Y_{k,s}^q$ denote the observed signals under condition q (0 = "rest," 1 = "active"). Then a test statistic is formed at each voxel, for example, a t-statistic T_k defined by

$$T_k = \frac{\overline{Y}_k^1 - \overline{Y}_k^0}{S_k^2 \cdot (2/M)}, \tag{8}$$

where $\overline{Y}_k^q$ is the temporal average per voxel and S_k^2 is the pooled variance estimate, that is,

$$\begin{aligned} \overline{Y}_k^q &= \frac{1}{T} \sum_{s=1}^{T} Y_{k,s}^q, \\ S_k^2 &= \frac{1}{2M-2} \sum_{q=0}^{1} \sum_{s=1}^{T} \left(Y_{k,s}^q - \overline{Y}_k^q\right)^2. \end{aligned} \tag{9}$$

Under the assumption of Gaussian noise, that is, $e_{k,s}^q \sim N(0, \sigma_k^2)$, $Y_{k,s}^q$ is normally distributed with mean μ_q and standard deviation σ_k, and also the differences $Y_{k,s}^q - \overline{Y}_k^q$ are normally distributed. This implies that $T_k \sim t_{2M-2}$, that is, T_k has a t-distribution with $2M - 2$ degrees of freedom *under the null hypothesis* $H_0 : \mu_0 = \mu_1$, that is, no mean effect of activation occurs. For this reason the distribution of T_k under this hypothesis is called the *null distribution*. Voxels where this hypothesis can be rejected are therefore designated as activated voxels. The significance of a certain observed voxel value is expressed by a so-called *p-value*, which is the probability of that voxel's intensity being attributable to mere chance. A p-value is calculated as the area under the graph of the t-distribution to the right of a given intensity value on the horizontal axis. A low p-value (say lower than 0.05) indicates that the measured value is probably not due to mere chance, that is, that it is a real activation.

The Rician distribution which applies to MRI data has a heavier right tail than a Gaussian, so p-values based on a Gaussian noise assumption with the standard deviation of the Rice distribution will be too low, introducing false positives. Hanson and Bly [15] found similar deviations, using gamma distributions instead of Rician PDFs.

As we have seen, it is the *null distribution* which is needed to compute p-values. From the discussion above, it is apparent that a sufficient condition for the usual statistical analysis to hold is that the *difference signal* at each voxel corresponding to the case of no activation has a Gaussian distribution. Therefore, our object of study in the remainder of this paper is the distribution of the noise in difference images of Rician-distributed MRI images without activation. As we will see, this distribution is indeed very close to a Gaussian, albeit with a standard deviation different from that of the initial Rice distribution.

3.2. Null distribution of the difference fMRI signal

The difference of two noisy versions $r_1(\mathbf{x})$ and $r_2(\mathbf{x})$, containing Rician noise, of the same underlying image $f(\mathbf{x})$, is *not* Rician distributed. Let the null image $s(\mathbf{x})$ be defined as $s(\mathbf{x}) = r_2(\mathbf{x}) - r_1(\mathbf{x})$. Its probability density function (PDF) is denoted by $C_{A,\sigma}(s)$, where we write A instead of $f(\mathbf{x})$ and σ is the standard deviation of the underlying noise distribution (cf. (1)). Then $C_{A,\sigma}(s)$ is the probability that the value of the difference $s(\mathbf{x})$ falls in an infinitesimal interval around $s : C_{A,\sigma}(s) = \mathrm{Prob}[s \le s(\mathbf{x}) \le s + \mathrm{d}s]$. We will refer to $C_{A,\sigma}(s)$ as the null distribution.

Since it is easy to see that $C_{A,\sigma}(s)$ is symmetric, that is, $C_{A,\sigma}(s) = C_{A,\sigma}(-s)$, we have the following expression valid for arbitrary values of $s \in \mathbb{R}$:

$$\begin{aligned} C_{A,\sigma}(s) &= \iint_0^\infty p_{A,\sigma}(r_1)\, p_{A,\sigma}(r_2)\, \delta(r_2 - r_1 - |s|)\, \mathrm{d}r_1 \mathrm{d}r_2 \\ &= \int_0^\infty p_{A,\sigma}(r_1)\, p_{A,\sigma}(r_1 + |s|)\, \mathrm{d}r_1, \end{aligned} \tag{10}$$

where $\delta(r)$ denotes the Dirac delta function. That is, $C_{A,\sigma}(s)$ is the cross-correlation of two identical Rice distributions.

The mean μ_s and standard deviation σ_s of the null distribution $C_{A,\sigma}(s)$ are given by

$$\mu_s = 0, \qquad \sigma_s = \sqrt{2}\sigma_r, \tag{11}$$

where σ_r is the standard deviation of the Rice distribution, see (5). For the derivation, see Appendix A.1. In the case $A = 0$, the PDF of r_1, as well as that of r_2, is

$$p_{0,\sigma}(r) = \frac{r}{\sigma^2} e^{-r^2/2\sigma^2}. \tag{12}$$

For the Rayleigh case ($A = 0$), the integral in (10) can be explicitly evaluated. The resulting expression for $C_{0,\sigma}(s)$ is

$$\frac{1}{2\sigma} e^{-s^2/4\sigma^2} \left[\frac{|s|}{2\sigma} e^{-s^2/4\sigma^2} + \frac{\sqrt{\pi}}{2} \left(1 - \frac{s^2}{2\sigma^2}\right) \operatorname{erfc}\left(\frac{|s|}{2\sigma}\right) \right], \tag{13}$$

where $\operatorname{erfc}(z) = (2/\sqrt{\pi}) \int_z^\infty e^{-t^2} dt$ is the complementary error function [19]. For the derivation of this formula, we refer to Appendix A.2.

The following experiments investigate how well the PDF $C_{A,\sigma}(s)$ can be approximated by a Gaussian distribution.

3.3. Numerical approximation by a normal distribution

The distribution $C_{A,\sigma}(s)$, see (10), was numerically approximated by a Gaussian via the Levenberg-Marquardt curve-fitting algorithm. The fit was carried out on an interval centered around zero with negligible function values outside this interval. Figure 2 shows the PDF $C_{A,\sigma}(s)$, as well as the Gaussian fitted to this distribution, for a number of values of A and σ. The plots show an excellent fit.

Table 1 presents some quantitative results. It shows, for various values of A and σ, (i) the exact standard deviation $\sigma_s = \sqrt{2}\sigma_r$ of the null distribution (11), where σ_r was computed according to (4)-(5); (ii) the width σ^{Gauss} of the Gaussian fitted to $C_{A,\sigma}(s)$; and (iii) the mean square error of the difference between $C_{A,\sigma}(s)$ itself and the fitted Gaussian. The difference between the width σ^{Gauss} of the fitted Gaussian and the exact value σ_s is very small, especially for high SNR (i.e., A/σ). Since σ_r approaches σ for high SNR (see Section 2), σ_s approaches $\sqrt{2}\sigma$ in this limit. The mean square error should decrease when the SNR increases; this is confirmed by the experimental results. The null distribution does not have a heavy tail (it is slightly lighter than a Gaussian of width σ, see below). Function values outside the interval used in the fitting procedure represent a negligible portion of the distribution. Therefore, p-values from statistical tests based on Gaussian noise with an estimated standard deviation σ^{Gauss} will be very accurate, and (because of the light tail) where there is a difference, the estimates will be conservative.

3.4. Tail of the null distribution

An important property of the PDF $C_{A,\sigma}(s)$ for statistical fMRI analysis is the tail behaviour (as $|s|$ approaches infinity) of the distribution under the null hypothesis, because this determines the p-value corresponding to a certain threshold (cf. Section 3.1).

Table 1: Accuracy of Gaussian fits to the PDF $C_{A,\sigma}$ for various values of A and σ. Shown are the exact standard deviation σ_s computed from (11), the width σ^{Gauss} of the fitted Gaussian, and the mean square error of the difference between the exact distribution and the fitted Gaussian.

A	σ	σ_s	σ^{Gauss}	Error
0	1	0.9265	0.9103	0.0080
0	3	2.7795	2.7315	0.0045
0	5	4.6325	4.5526	0.0035
2	1	1.2933	1.3071	0.0030
2	3	3.0463	3.0085	0.0035
2	5	4.8079	4.7291	0.0033
8	1	1.4086	1.4086	0.0000
8	3	4.0552	4.0780	0.0008
8	5	6.1567	6.2188	0.0013

For the limiting cases of low and high SNR, that is, $A = 0$ and A/σ large, we mathematically analysed the behaviour of the PDF $C_{A,\sigma}(s)$ when $|s|$ becomes very large. The details are presented in Appendix A.3. We find that both in the Rayleigh case ($A = 0$) and for large values of A/σ, the tails of the distribution (10) are lighter than the tail of a Gaussian distribution:

$$C_{A,\sigma}(s) \sim \text{constant} \cdot \frac{1}{|s|} e^{-(|s|-A)^2/2\sigma^2}, \quad s \longrightarrow \infty, \tag{14}$$

where the constant depends on A and σ. This is a Gaussian tail of width σ multiplied by a factor $1/|s|$, which means that the distribution approaches zero even faster than a Gaussian distribution of width σ. This implies that if p-values based on a Gaussian are used, the test is slightly conservative, and will not give extra false positives.

3.5. Statistical tests of normality

An image of a uniform underlying intensity with Rician noise has a spatially stationary noise distribution. The distribution of the difference between two such images is symmetric.

To test whether this distribution is close to Gaussian, the Kolmogorov-Smirnov (KS) test was employed as follows. We created two images of a uniform intensity A with Rician distributed noise, and computed the difference between the noisy images. The KS test was applied to the difference image. The null hypothesis of the KS test is that the data are normally distributed, and this is rejected if the p-value of the KS test statistic is below 0.05. For a number of intensities A, images of different sizes were tested, and for each size and intensity, the test was repeated 32 times. Table 2 shows the mean p-values of the KS test statistics for each size, with intensity $A = 1$ and $A = 5$. As a reference, 32 images of the same size containing $N(0, 1)$ noise were also tested, and their mean p-values are in the right column. This table shows that deviations from normality can only be detected in very large images with low intensities: for high intensities, they are too small to measure.

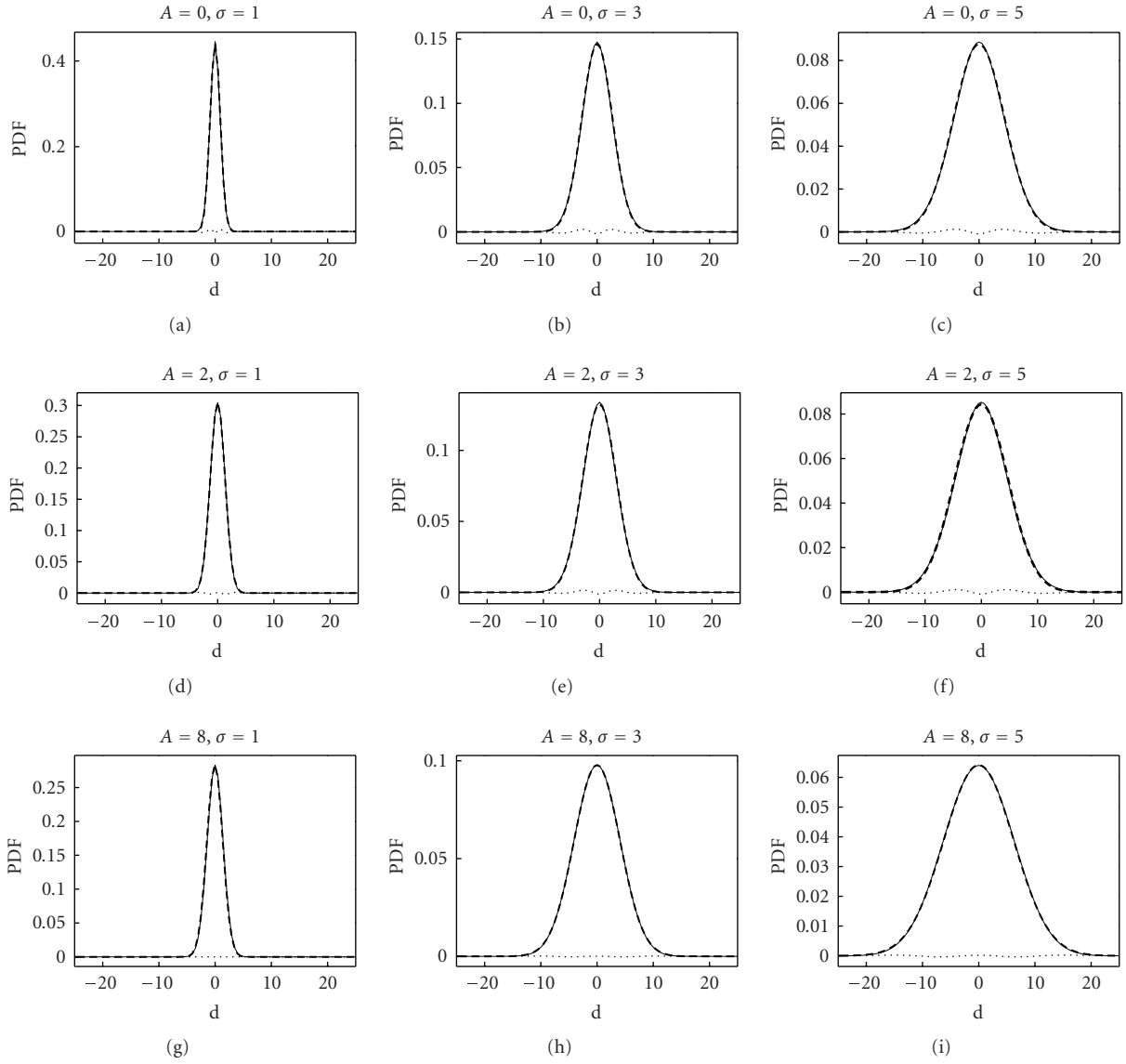

FIGURE 2: The exact null distribution $C_{A,\sigma}(s)$ (solid), the fitted Gaussian (dashed), and the difference between $C_{A,\sigma}(s)$ and the Gaussian (dotted). Note that the fitted Gaussian is hardly distinguishable from the exact distribution.

3.6. Parameter estimation in fMRI with the general linear model

For fMRI analysis, the possibility of accurately estimating the parameters of the noise is at least as important as using the right noise model. We tested the applicability of the GLM (see Section 3.1) by estimating the noise parameters in difference images created in the same way as $s(\mathbf{x})$ in Section 3.2, and comparing them with the real underlying parameters.

A matrix $\mathbf{e}$ of error signals was created by making a time series of 128 difference images. The standard deviation of the temporal noise was computed in each voxel. Table 3 shows, for the same input A and σ as before, the measured temporal standard deviation σ^{temp}, the mean standard deviation σ_s in the difference images (which equals $\sqrt{2}\sigma_r$, see Section 3.2), and the ratio $\sigma_s/\sigma^{\text{temp}}$. It shows that the standard deviation σ_s is very accurately predicted by formula (11).

3.7. Evaluation of the test results

The statistical tests, the analytical results, and the numerical computations, all show that the difference between two MR images whose intensities are Rician distributed, can be very well approximated by a Gaussian distribution. The approximation is closest for high SNR, but is still very good for lower SNR. Given the parameters A and σ of the Rician spatial noise in a series of MR images and defining null images as pairwise difference images, the parameters of the Gaussian distribution that describes the temporal noise can be accurately estimated.

Table 2: p-values produced by the KS test for the difference between images with Rician distributed noise with signal amplitudes $A = 1$ and $A = 5$, and for images of the same size with $N(0, 1)$-noise.

Size	p-value ($A = 1$)	p-value ($A = 5$)	p-value $N(0, 1)$
2×2	0.6573	0.5607	0.4569
4×4	0.5761	0.5565	0.4249
8×8	0.5511	0.5493	0.4894
16×16	0.5801	0.5564	0.5854
32×32	0.5833	0.5378	0.5946
64×64	0.5629	0.4869	0.4816
128×128	0.5270	0.5426	0.5147
256×256	0.4390	0.5554	0.5225
512×512	0.3210	0.5219	0.4006
1024×1024	0.0587	0.5236	0.5037

Table 3: Measured temporal standard deviation σ^{temp}, the mean standard deviation σ_s in the difference images, and the ratio $\sigma_s/\sigma^{\text{temp}}$.

A	σ	σ_s	σ^{temp}	$\sigma_s/\sigma^{\text{temp}}$
0	1	1.4280	1.4338	0.9959
0	3	4.2854	4.3017	0.9962
0	5	7.1352	7.1667	0.9956
2	1	1.8001	1.8071	0.9961
2	3	4.4708	4.4890	0.9959
2	5	7.2472	7.2815	0.9953
8	1	2.1579	2.1667	0.9959
8	3	5.7924	5.8157	0.9960
8	5	8.5195	8.5542	0.9959

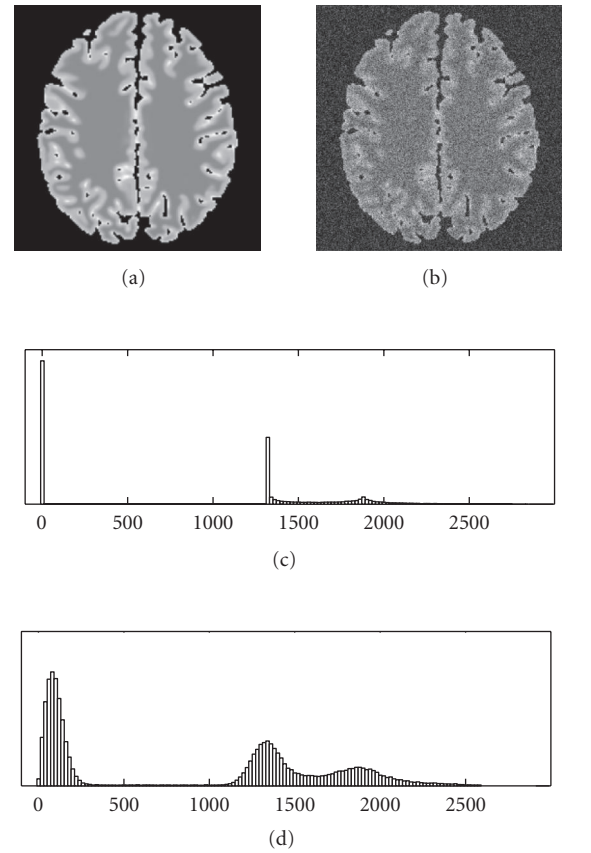

Figure 3: (a) A noise-free T2-weighted MR image. (b) Image (a) with Rician noise of $\sigma = 81.67$ (SNR 10 dB). The histogram of a noise-free T2*-weighted MR image (c) and of the same image with Rician noise of $\sigma = 81.67$, SNR = 10 dB (d).

4. THE NOISE DISTRIBUTION IN fMRI

Images in an fMRI time series have a range of intensities, so the noise distribution is a sum of Rician PDFs (sums of Gamma PDFs have also been used, see [15] for an example). For each intensity A in the image, the noise is distributed differently (see Figure 3(c)), and this will have an influence on the parameter estimates of the GLM. Areas with a "true" grey value of 0, like the space around the body, have Rayleigh-distributed noise, and the areas with higher grey values have more symmetric distributions, which are quite similar to a Gaussian, and they are centered around the grey value at that location. The total noise distribution is a mixture of all those distributions. The question is whether the conclusions about the noise in the difference image obtained in Section 2 also hold for noisy images with mixed distributions.

4.1. Shape of the noise distribution in MR images

A simulated MR image was acquired from the BrainWeb Magnetic Resonance Imaging simulator [20] with the following parameters: modality T2, slice thickness 1 mm, noise 0%, intensity nonuniformity 0%. Nonbrain voxels were excluded with the Brain Extraction Tool [21]. This noise-free T2*-weighted image (Figure 3(a)) was contaminated by Rician noise with a known σ (see Figure 3(b)). A residual image was obtained by subtracting the original MR image from the noisy MR image, and a null image was made using the procedure proposed in Section 3, that is, as the difference between two MR images containing Rician noise.

The dissimilarity between a Rician distribution and a Gaussian is largest for low signal intensities A. The previous section showed that the difference between two images of a uniform intensity A and Rician noise has zero mean and is near-Gaussian distributed, also for low signal intensities. This section examines the difference images when the noise-free images contain more than one intensity. Figure 4 shows the histograms of a noisy MR image, the difference between a noisy MR image and the noise-free image, and the difference between two noisy MR images, respectively. The histograms were computed for a range of values for σ and are presented together as surface plots. As σ decreases, the histogram of the noisy MR image changes from one Rayleigh-like PDF to a number of near-Gaussian PDFs (see Figure 4(a)). The histogram of the noisy image after subtraction of the original is asymmetric for high σ, and becomes more symmetric as σ decreases (see Figure 4(b)). The histogram of the difference images is symmetric for all σ (see Figure 4(c)).

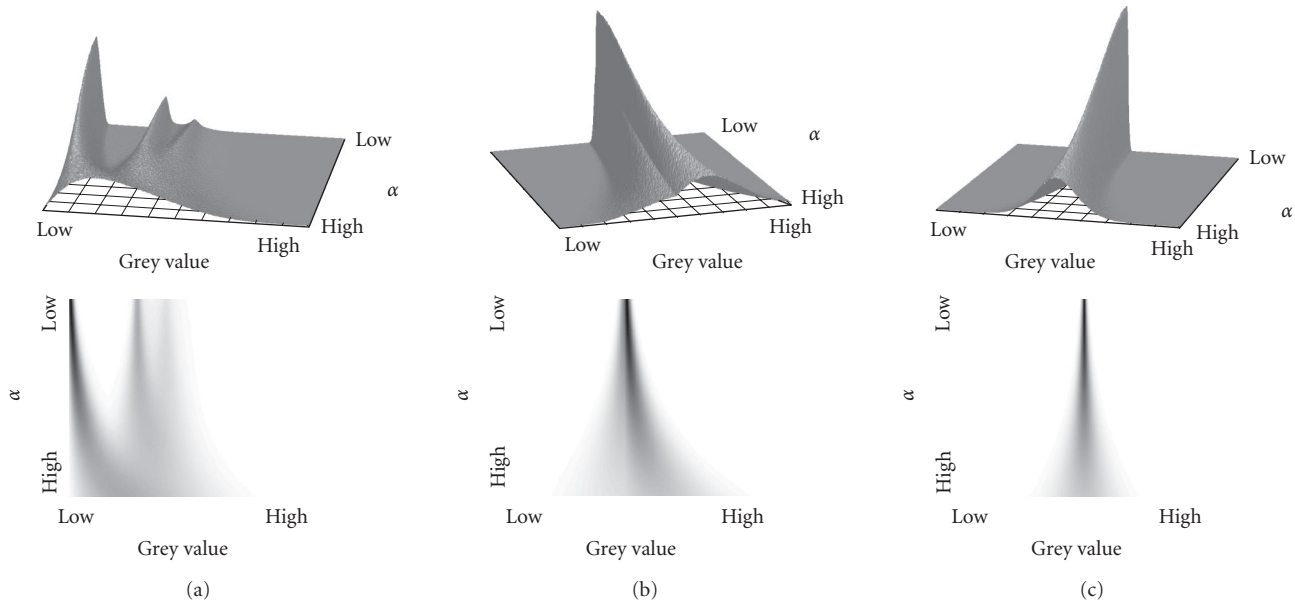

Figure 4: (a) Histogram of a noisy MR image, (b) histogram of the difference between a noisy MR image and the noise-free MR image, and (c) histogram of the difference of two noisy MR images, for various σ. Top: surface plots, bottom: grey-value maps.

4.2. Time series of MR images

A time series of 164 EPI scans was made on a 3 Tesla Intera scanner (Philips Medical Systems, The Netherlands), with repetition time TR = 3 seconds, volume size = $64 \times 64 \times 46$ voxels of $3.5 \times 3.5 \times 3.5$ mm^3. No stimuli were presented, and the null hypothesis of no activation was assumed to be true throughout the experiment. Alignment of the images was done with SPM′99 program [13].

The time series was split in two disjoint sets: TS_1 (images $1, \ldots, 82$) and TS_2 (images $83, \ldots, 164$). The noise of TS_1 was centered around 0 by subtracting the time series mean image of TS_1 from each image. Note that although this is a common procedure in fMRI analysis, this means treating Rician noise as additive noise. To obtain an image with a symmetric noise distribution, difference images were made by subtracting the corresponding image of TS_2 from each image of TS_1.

The histogram of the time series mean image (see Figure 5) was used to divide the images into three intensity ranges: low intensity (grey value $0, \ldots, 300$), medium intensity (grey value $301, \ldots, 600$), and high intensity (grey value > 600).

Figure 6 shows the histograms of the grey values in the resulting time series within the three ranges. Gaussians were fitted to the histograms with the Levenberg-Marquardt curve-fitting algorithm. For medium and high intensities, the time series histograms show no significant asymmetries. For low intensities however, the time series TS_1 after subtracting the mean has an asymmetric histogram, while the time series TS_1 after subtracting TS_2 has a symmetric histogram. The fits are never perfect, except in the case of low intensities and after subtracting TS_2. In that case, the intensity distribution has one predominant intensity ($A = 0$, see Figure 5), and the difference distribution is close to those in the $A = 0$ cases of the previous section. In the other cases, the noise originates from voxels with various intensities, and the noise distribution resembles a mixture of Gaussians with mean $\mu = 0$ and various σ.

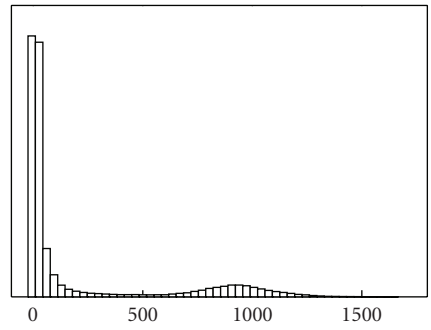

Figure 5: Histogram of the time series mean image of TS_1.

Because the amount of asymmetry in the medium and high grey-value ranges is very small, the combination of thresholding and subtracting the time series mean may solve most of the problems concerning the Rician distribution of the noise. However, the new method presented in this paper of subtracting a second-time series is preferable: it has proved to yield symmetric noise distributions in all measurements considered.

4.3. Implications for fMRI designs

The assumption of Gaussian noise in the analysis of fMRI data should be used with care. Relying on the robustness of

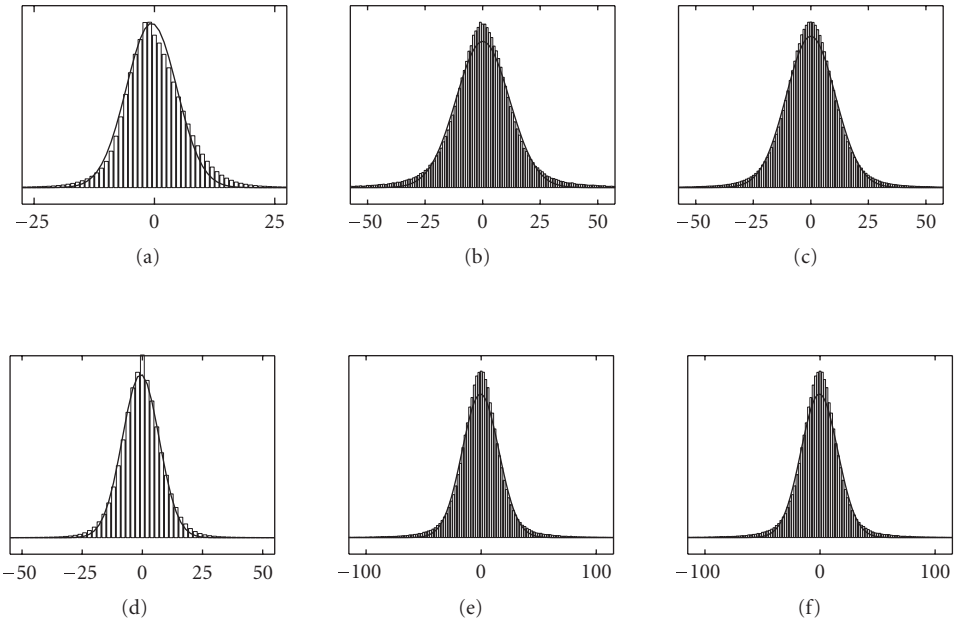

FIGURE 6: Histograms of three intensity ranges of the images in the time series. Top: time series TS_1 after subtracting the time series mean: (a) low intensity, (b) medium intensity, (c) high intensity. Bottom: time series TS_1 after subtracting the corresponding images of time series TS_2: (d) low intensity, (e) medium intensity, (f) high intensity.

the standard tests most often works, but it does not solve the problem of the asymmetric noise distribution. A recent maximum-likelihood test based on the Rician distribution shows to be as powerful as the GLM-based test with a high SNR, but performs much better with a low SNR [22]. For using the assumption of Gaussian noise, difference distributions like the one presented here will be required. The example presented here of using an extra data set for every experiment is difficult for large studies, but this can be solved in a more practical way: a relatively small set of "null data" can be reused after randomisation in the time dimension. The only change in the formula for the GLM (7) is using $\mathbf{Y} - \mathbf{Y}_0$ instead of $\mathbf{Y}$, with $\mathbf{Y}_0$ the resting-state data set. It is trivial to see that this does not change the way the estimates are computed, even if different (more complex) design matrices $\mathbf{X}$ are used.

5. CONCLUSIONS

We have presented a noise model in BOLD fMRI that takes into account the Rician distribution of MR noise known from the literature. BOLD noise was defined as the difference between two MR images with Rician noise. We investigated the properties of the difference image under the null hypothesis (no brain activation), which is needed to determine p-values in a statistical analysis. The problem was studied in several complementary ways: analytical calculation, numerical simulation, statistical estimation, and experimental validation on real EPI data. An analytic expression was derived for the statistical null distribution $C_{A,\sigma}(s)$ as an integral in terms of two underlying Rician probability densities with parameters A and σ. From this basic formula, analytical expressions were derived for the mean and standard deviation of the null distribution, as well as for its tail, that is, its asymptotic behaviour as s goes to infinity.

The null distribution $C_{A,\sigma}(s)$ was numerically approximated by a Gaussian function with the Levenberg-Marquardt nonlinear curve-fitting algorithm. The approximation by a Gaussian distribution was very good, with the accuracy increasing with SNR (i.e., A/σ). The standard deviation of the fitted Gaussian was found to be in excellent agreement with the exact standard deviation σ_s derived from the analytical expressions.

The statistical properties of the noise were examined in two ways. The Kolmogorov-Smirnov test was applied to difference images of noise-only images with Rician distributed noise. A second test using the general linear model (GLM) compared the estimated noise parameters to the value predicted by the model, and showed that the agreement is excellent.

From the analytical results, the numerical computations, and the statistical tests, we concluded that the assumption of Gaussian distributed noise used in the fMRI literature could be justified. That is, the difference between two images whose intensities follow a Rice distribution can be very well approximated by a Gaussian distribution. The approximation is closest for high SNR, but is still quite good for lower SNR. Given the parameters A and σ of the Rician spatial noise in a series of MR images, the standard deviation of the Gaussian that describes the temporal noise can be accurately predicted.

The noise model was tested on simulated and real MR images. In a test that contaminated noise-free MR templates with Rician noise, MR noise was shown to have an asymmetric distribution when it is—incorrectly—treated as additive noise. As in the test with noise-only images, difference

images of noisy MR pictures were found to have a symmetric distribution. The consequence for fMRI time series analysis is that subtracting the time series mean does not get rid of the asymmetry in temporal noise.

We tested thresholding the MR images as a fast and simple alternative to the difference image approach: it can remove asymmetry in the noise distribution to a large extent, depending on the robustness of the test that is used. Subtracting a second time series from the time series being analysed yields symmetric and close to Gaussian distributed noise.

APPENDIX

A. MATHEMATICAL ANALYSIS OF THE NULL DISTRIBUTION

This appendix presents the derivations of the exact analytical results in Section 3 on the distribution of the difference signal under the null hypothesis. Extensive use is made of the concept of asymptotic expansions. We first provide a few formal definitions. Let $\phi(x)$ and $\psi(x)$ be two functions defined for $x \geq x_0$. One writes $\phi(x) = O(\psi(x))$, $x \to \infty$, when constants K and x_1 exist such that $|\phi(x)| \leq K|\psi(x)|$ for $x \geq x_1$. We call $\sum_{n=0}^{\infty} a_n\phi_n(x)$ the asymptotic expansion of a function f when, for every N, $|f(x) - \sum_{n=0}^{N} a_n\phi_n(x)| = O(\phi_{N+1}(x))$, and write

$$f(x) \sim \sum_{n=0}^{\infty} a_n\phi_n(x), \quad x \longrightarrow \infty. \tag{A.1}$$

Below, we only use the first term in the asymptotic expansion of some special functions (error function, Bessel function), and use the shorthand notation

$$f(x) \sim a_0\phi_0(x), \quad x \longrightarrow \infty. \tag{A.2}$$

To make this precise, one has to refer to the full asymptotic expansions, as can be found in Abramowitz and Stegun [19]; for easy reference, we refer to the relevant sections of this handbook at the appropriate places.

A.1. Mean and variance of the null distribution

First, the mean μ_s is zero because of the symmetry of $C_{A,\sigma}(s)$. Second, since the mean is zero, the variance of the null distribution satisfies (see (10))

$$\begin{aligned}
\sigma_s^2 &= \int_{-\infty}^{\infty} \mathrm{d}s\, s^2 C(s) \\
&= \int_{-\infty}^{\infty} \mathrm{d}s\, s^2 \int_0^{\infty} \mathrm{d}r_1 \int_0^{\infty} \mathrm{d}r_2\, p_{A,\sigma}(r_1)\, p_{A,\sigma}(r_2)\, \delta(r_2 - r_1 - |s|) \\
&= \int_0^{\infty} \mathrm{d}r_1 \int_0^{\infty} \mathrm{d}r_2\, p_{A,\sigma}(r_1)\, p_{A,\sigma}(r_2) \int_{-\infty}^{\infty} \mathrm{d}s s^2 \delta(r_2 - r_1 - |s|),
\end{aligned} \tag{A.3}$$

where $\delta(\cdot)$ denotes the Dirac delta function. Since $\delta(r_2 - r_1 - |s|)$ is zero except when $r_2 - r_1 - |s| = 0$, we find

$$\begin{aligned}
\sigma_s^2 &= \int_0^{\infty} \mathrm{d}r_1 \int_0^{\infty} \mathrm{d}r_2\, p_{A,\sigma}(r_1)\, p_{A,\sigma}(r_2)\, (r_1 - r_2)^2 \\
&= \int_0^{\infty} \mathrm{d}r_1 \int_0^{\infty} \mathrm{d}r_2\, p_{A,\sigma}(r_1)\, p_{A,\sigma}(r_2)\, (r_1^2 + r_2^2 - 2r_1 r_2) \\
&= \int_0^{\infty} \mathrm{d}r_1 r_1^2\, p_{A,\sigma}(r_1) + \int_0^{\infty} \mathrm{d}r_2 r_2^2\, p_{A,\sigma}(r_2) \\
&\quad - 2\left(\int_0^{\infty} \mathrm{d}r_1 r_1\, p_{A,\sigma}(r_1) \right) \left(\int_0^{\infty} \mathrm{d}r_2 r_2\, p_{A,\sigma}(r_2) \right) \\
&= 2\mathbb{E}(r^2) - 2\mathbb{E}(r)^2 = 2\sigma_r^2.
\end{aligned} \tag{A.4}$$

Here $\mathbb{E}(\cdots)$ denotes the average of the quantity within the brackets. So we have found that $\sigma_s^2 = 2\sigma_r^2$, which directly yields (11).

A.2. Exact form of the null distribution in the Rayleigh case

Substituting the form (12) of the Rayleigh distribution in expression (10), we find

$$C_{0,\sigma}(s) = \int_0^{\infty} \mathrm{d}r \frac{r}{\sigma^2} e^{-r^2/2\sigma^2} \frac{r + |s|}{\sigma^2} e^{-(r+s)^2/2\sigma^2}. \tag{A.5}$$

Putting $r/\sigma = x$, $|s|/\sigma = q$, $A/\sigma = a$, we find after some algebra

$$C_{0,\sigma}(s) = \frac{1}{\sigma} \int_0^{\infty} \mathrm{d}x \left\{ \left(x + \frac{q}{2} \right)^2 - \frac{q^2}{4} \right\} e^{-(x+q/2)^2 - q^2/4}. \tag{A.6}$$

Again, putting $y = x + q/2$,

$$C_{0,\sigma}(s) = \frac{1}{\sigma} e^{-q^2/4} \int_{q/2}^{\infty} \mathrm{d}y \left(y^2 - \frac{q^2}{4} \right) e^{-y^2}. \tag{A.7}$$

Writing $\tau = q/2$, we can write this integral as the sum of two terms, each of which can be expressed in terms of the complementary error function

$$C_{0,\sigma}(s) = \frac{1}{\sigma} e^{-\tau^2} S_2 - \frac{1}{\sigma} e^{-\tau^2} \tau^2 S_0, \tag{A.8}$$

where

$$\begin{aligned}
S_0 &= \int_{\tau}^{\infty} \mathrm{d}y e^{-y^2} = \frac{\sqrt{\pi}}{2} \mathrm{erfc}(\tau), \\
S_2 &= \int_{\tau}^{\infty} \mathrm{d}y\, y^2 e^{-y^2} = \frac{1}{2} \tau e^{-\tau^2} + \frac{\sqrt{\pi}}{4} \mathrm{erfc}(\tau).
\end{aligned} \tag{A.9}$$

Substitution of these expressions in (A.8) yields

$$C_{0,\sigma}(s) = \frac{1}{2\sigma} e^{-\tau^2} \left\{ \tau e^{-\tau^2} + \frac{\sqrt{\pi}}{2} (1 - 2\tau^2) \mathrm{erfc}(\tau) \right\}. \tag{A.10}$$

Reexpressing τ in terms of the original variable s (i.e., $\tau = q/2 = |s|/(2\sigma)$), we obtain formula (13).

A.3. Tails of the null distribution

We consider the limiting case of low versus high SNR, that is, $A = 0$ and A/σ large.

$A = 0$. This is the Rayleigh case, for which we have derived an exact expression for the null distribution, see formula (13). When s is large, we can use the asymptotic behaviour of the error function [19, section 7.1.23]

$$\operatorname{erfc}(z) \sim \frac{1}{\sqrt{\pi}z} e^{-z^2}, \quad z \longrightarrow \infty. \tag{A.11}$$

Substituting this in (13), we find (after rearrangement of terms)

$$C_{0,\sigma}(s) \sim \frac{1}{2|s|} e^{-s^2/2\sigma^2}, \quad s \longrightarrow \infty, \tag{A.12}$$

which behaves as a Gaussian tail of width σ multiplied by a factor $1/|s|$.

A/σ large. Since A/σ is large, we apply the Gaussian approximation of the Rice distribution:

$$p_{A,\sigma}(r) \sim \frac{1}{\sqrt{2\pi\sigma^2}} e^{-(r-A)^2/2\sigma^2}. \tag{A.13}$$

As shown in [3], this approximation is already accurate for $A \geq 2\sigma$. This formula is easy to derive by using the asymptotic expansion of the Bessel function I_0 as given in [19, Section 9.7.1]. Substituting this in (10), we get

$$C_{A,\sigma}(s) \sim \int_0^\infty \mathrm{d}r \frac{1}{2\pi\sigma^2} e^{-(r-A)^2/2\sigma^2} e^{-(r+|s|-A)^2/2\sigma^2}. \tag{A.14}$$

Putting $r/\sigma = x$, $|s|/\sigma = q$, $A/\sigma = a$, we find after some algebra

$$\begin{aligned} C_{A,\sigma}(s) &\sim \frac{1}{2\pi\sigma} \int_0^\infty \mathrm{d}x e^{-(x-a)^2/2} e^{-(x+q-a)^2/2} \\ &= \frac{1}{2\pi\sigma} e^{-q^2/4} \int_0^\infty \mathrm{d}x e^{-(x+q/2-a)^2}. \end{aligned} \tag{A.15}$$

Again, putting $y = x + q/2 - a$,

$$\begin{aligned} C_{A,\sigma}(s) &\sim \frac{1}{2\pi\sigma} e^{-q^2/4} \int_{q/2-a}^\infty \mathrm{d}y e^{-y^2} \\ &= \frac{1}{2\pi\sigma} e^{-q^2/4} \frac{\sqrt{\pi}}{2} \operatorname{erfc}\left(\frac{q}{2} - a\right). \end{aligned} \tag{A.16}$$

In terms of the original variable s,

$$C_{A,\sigma}(s) \sim \frac{1}{4\sqrt{\pi}\sigma} e^{-s^2/4\sigma^2} \operatorname{erfc}\left(\frac{|s|/2 - A}{\sigma}\right). \tag{A.17}$$

Applying the asymptotic expansion (A.11) of the erfc function for large argument, we find

$$C_{A,\sigma}(s) \sim \frac{1}{2\pi(|s| - 2A)} e^{-((|s|-A)^2+A^2)/2\sigma^2}. \tag{A.18}$$

Finally, since $|s|$ is large, we can replace $|s| - 2A$ by $|s|$:

$$C_{A,\sigma}(s) \sim \text{constant} \cdot \frac{1}{|s|} e^{-(|s|-A)^2/2\sigma^2}, \quad s \longrightarrow \infty, \tag{A.19}$$

which again behaves as a Gaussian tail of width σ multiplied by a factor $1/|s|$.

ACKNOWLEDGMENTS

This research was part of the project "wavelets and their applications," funded by the Dutch National Science Foundation (NWO), Project no. 613.006.570. We thank Dr. N. M. Temme of the Centre for Mathematics and Computer Science in Amsterdam for helpful comments on the asymptotic expansions used in this paper.

REFERENCES

[1] W. A. Edelstein, P. A. Bottomley, and L. M. Pfeifer, "A signal-to-noise calibration procedure for NMR imaging systems," *Medical Physics*, vol. 11, no. 2, pp. 180–185, 1984.

[2] R. M. Henkelman, "Measurement of signal intensities in the presence of noise in MR images," *Medical Physics*, vol. 12, no. 2, pp. 232–233, 1985.

[3] H. Gudbjartsson and S. Patz, "The Rician distribution of noisy MRI data," *Magnetic Resonance in Medicine*, vol. 34, no. 6, pp. 910–914, 1995.

[4] J. Sijbers, A. J. den Dekker, P. Scheunders, and D. Van Dyck, "Maximum-likelihood estimation of Rician distribution parameters," *IEEE Transactions on Medical Imaging*, vol. 17, no. 3, pp. 357–361, 1998.

[5] R. D. Nowak, "Wavelet-based Rician noise removal for magnetic resonance imaging," *IEEE Transactions on Image Processing*, vol. 8, no. 10, pp. 1408–1419, 1999.

[6] J. C. Wood and K. M. Johnson, "Wavelet packet denoising of magnetic resonance images: importance of Rician noise at low SNR," *Magnetic Resonance in Medicine*, vol. 41, no. 3, pp. 631–635, 1999.

[7] A. Pižurica, W. Philips, I. Lemahieu, and M. Acheroy, "A versatile wavelet domain noise filtration technique for medical imaging," *IEEE Transactions on Medical Imaging*, vol. 22, no. 3, pp. 323–331, 2003.

[8] S. O. Rice, "Mathematical analysis of random noise," *The Bell System Technical Journal*, vol. 24, no. 1, pp. 46–156, 1945.

[9] G. K. Aguirre, E. Zarahn, and M. D'Esposito, "Empirical analyses of BOLD fMRI statistics. II. Spatially smoothed data collected under null-hypothesis and experimental conditions," *NeuroImage*, vol. 5, no. 3, pp. 199–212, 1997.

[10] K. J. Friston, O. Josephs, E. Zarahn, A. P. Holmes, S. Rouquette, and J.-B. Poline, "To smooth or not to smooth? Bias and efficiency in fMRI time-series analysis," *NeuroImage*, vol. 12, no. 2, pp. 196–208, 2000.

[11] M. J. Fadili and E. T. Bullmore, "Wavelet-generalized least squares: a new BLU estimator of linear regression models with 1/f errors," *NeuroImage*, vol. 15, no. 1, pp. 217–232, 2002.

[12] K. J. Friston, C. D. Frith, R. Turner, and R. S. J. Frackowiak, "Characterizing evoked hemodynamics with fMRI," *NeuroImage*, vol. 2, no. 2 Pt 1, pp. 157–165, 1995.

[13] K. J. Friston, A. P. Holmes, K. J. Worsley, J.-P. Poline, C. D. Frith, and R. S. J. Frackowiak, "Statistical parametric maps in functional imaging: a general linear approach," *Human Brain Mapping*, vol. 2, no. 4, pp. 189–210, 1994, http://www.fil.ion.ucl.ac.uk/spm/.

[14] K. J. Worsley and K. J. Friston, "Analysis of fMRI time-series revisited - again," *NeuroImage*, vol. 2, no. 3, pp. 173–181, 1995.

[15] S. J. Hanson and B. M. Bly, "The distribution of BOLD susceptibility effects in the brain is non-Gaussian," *NeuroReport*, vol. 12, no. 9, pp. 1971–1977, 2001.

[16] W.-L. Luo and T. E. Nichols, "Diagnosis and exploration of massively univariate neuroimaging models," *NeuroImage*, vol. 19, no. 3, pp. 1014–1032, 2003.

[17] K. M. Petersson, T. E. Nichols, J.-B. Poline, and A. P. Holmes, "Statistical limitations in functional neuroimaging II. Signal detection and statistical inference," *Philosophical Transactions of the Royal Society*, vol. 354, no. 1387, pp. 1261–1281, 1999.

[18] J. Sijbers, A. J. den Dekker, J. Van Audekerke, M. Verhoye, and D. Van Dyck, "Estimation of the noise in magnitude MR images," *Magnetic Resonance Imaging*, vol. 16, no. 1, pp. 87–90, 1998.

[19] M. Abramowitz and I. A. Stegun, Eds., *Handbook of Mathematical Functions*, vol. 55 of *Applied Mathematics Series*, National Bureau of Standards USA, Washington, DC, USA, 10th edition, 1972.

[20] R. K.-S. Kwan, A. C. Evans, and G. B. Pike, "An extensible MRI simulator for post-processing evaluation," in *Proceedings of 4th International Conference Visualization in Biomedical Computing (VBC '96)*, vol. 1131 of *Lecture Notes in Computer Science*, pp. 135–140, Hamburg, Germany, September 1996, http://www.bic.mni.mcgill.ca/brainweb.

[21] S. M. Smith, "Fast robust automated brain extraction," *Human Brain Mapping*, vol. 17, no. 3, pp. 143–155, 2002.

[22] A. J. den Dekker and J. Sijbers, "Implications of the Rician distribution for fMRI generalized likelihood ratio tests," *Magnetic Resonance Imaging*, vol. 23, no. 9, pp. 953–959, 2005.

Alle Meije Wink received the M.S. degree (1999) in computing science from the University of Twente, The Netherlands. He has worked in image analysis (1999) at the University Hospital Groningen, The Netherlands, and received a Ph.D. degree (2004) in computing science, with a focus on fMRI analysis, from the University of Groningen. He is currently a Research Associate in the Brain Mapping Unit, University of Cambridge, United Kingdom.

Jos B. T. M. Roerdink received his M.S. degree (1979) in theoretical physics from the University of Nijmegen, the Netherlands. Following his Ph.D. degree (1983) from the University of Utrecht and a two-year position (1983–1985) as a Postdoctoral Fellow at the University of California, San Diego, both in the area of stochastic processes, he joined the Centre for Mathematics and Computer Science in Amsterdam. There he worked from 1986 to 1992 on image processing and tomographic reconstruction. He was appointed as an Associate Professor (1992) and Full Professor (2003), respectively, at the Institute for Mathematics and Computing Science of the University of Groningen, where he currently holds a Chair in scientific visualization and computer graphics. His research interests include mathematical morphology, biomedical visualization, neuroimaging, and bioinformatics.

Hindawi Publishing Corporation
International Journal of Biomedical Imaging
Volume 2006, Article ID 57850, Pages 1–11
DOI 10.1155/IJBI/2006/57850

Unsupervised Detection of Suspicious Tissue Using Data Modeling and PCA

Ikhlas Abdel-Qader,[1] Lixin Shen,[2] Christina Jacobs,[3] Fadi Abu Amara,[1] and Sarah Pashaie-Rad[4]

[1] *Department of Electrical and Computer Engineering, Western Michigan University, MI 49008, USA*
[2] *Department of Mathematics, Western Michigan University, Kalamazoo, MI 49008, USA*
[3] *Radiology Department, Bronson Methodist Hospital, Kalamazoo, MI 49007, USA*
[4] *Automated Test Engineering Department, Saint Jude Medical, Valencia, CA 91381, USA*

Received 22 January 2006; Revised 20 May 2006; Accepted 6 June 2006

Breast cancer is a major cause of death and morbidity among women all over the world, and it is a fact that early detection is a key in improving outcomes. Therefore development of algorithms that aids radiologists in identifying changes in breast tissue early on is essential. In this work an algorithm that investigates the use of principal components analysis (PCA) is developed to identify suspicious regions on mammograms. The algorithm employs linear structure and curvelinear modeling prior to PCA implementations. Evaluation of the algorithm is based on the percentage of correct classification, false positive (FP) and false negative (FN) in all experimental work using real data. Over 90% accuracy in block classification is achieved using mammograms from MIAS database.

1. INTRODUCTION

Breast cancer is the second leading cause of cancer death in women in the United States. Early detection is crucial for treatment success as tumor size is a major prognostic indicator. Studies have shown that early detection and treatment improve the chances of survival for breast cancer patients [1, 2]. The American Cancer Society recommends all women 40 years and older undergo yearly screening mammograms. The goal of screening mammography is the detection of cancer before it becomes palpable. Unfortunately, mammograms are not 100% accurate. False positive rates of 15–30% and false negative rates of 10–30% have been reported [3]. False-positives (labeling a finding as suspicious which later is found to be benign) lead to unnecessary biopsies and anxiety, while false-negatives (failure to detect presence of cancer) result in later detection and often poorer prognosis. Nonetheless, mammography has an overall accuracy rate of 90% [2].

Although radiologists are capable of detecting a number of findings suggesting cancerous tissues in radiographic images, a significant percentage of abnormalities are missed [3]. Screening programs typically require radiologists to read large numbers of mammograms with great attention to fine details. As less than 10% of exams will have abnormalities that need further attention and only around 1% will actually have cancer, this is a rather tedious process. Fatigue, satisfaction of search (failing to detect additional abnormalities once one finding is detected), and failure to perceive subtle changes are common causes of false negative exams. Development of computer algorithms to assist radiologists in detection of abnormalities would be extremely beneficial. Masses can be hidden by normal dense glandular tissue and fine microcalcifications can blend in with background tissue. Computer-aided image analysis enables detection of mass-like structures only a few millimeters in size and even smaller microcalcifications. Cancerous tissues usually arise in duct channels and lobules. It is critical to define the degree of abnormality compared to normal cells and growth rate of abnormal cells, which is named tumor grade.

Computerized feature extraction techniques are used to extract features in mammographic images that may not be readily perceived by radiologists. Many methods have been proposed in the literature for mammography detection and classification utilizing a wide variety of algorithms to achieve their goals. Chan et al. [4] used artificial neural networks to extract features from mammograms to predict whether the presence of microcalcifications is associated with malignant or benign pathology. A back-propagation artificial neural network classifier was trained and tested with a

leave-one-case-out method to recognize the malignant or benign microcalcification clusters. 11 out of the 28 benign cases were correctly identified (39%) without missing any malignant cases. Lemaur et al. [5] used wavelets having a high Sobolev regularity to detect clustered microcalcification in digitized mammograms. Morrow et al. [6] used each pixel in the mammographic images as a seed to grow a region. Then, the contrast of each region is calculated and enhanced by applying an empirical transformation based on each region's seed pixel value, its contrast, and its background. The validity of microcalcification clusters and anatomic details is considerably improved in the processed images. Shen et al. [7] developed a set of shape factors to measure the roughness of contours of calcifications in mammograms and for use in microcalcification classification as malignant or benign. Wang and Karayiannis [8] used wavelet transform to decompose the mammograms into different frequency subbands. They suppressed the low-frequency subbands, making microcalcifications correspond to high-frequency components, and reconstructed the mammogram from the subbands containing only high frequencies. Zwiggelaar [3] used fractals and statistical modeling to separate the structure and texture background that are present in mammographic images.

Utilizing PCA and feature modeling in this work is to target identifying abnormal mammograms in a local processing setting. It identifies the region of suspicious tissues in an area size of 120×120. This paper is organized as follows. Section 2 presents a procedure of PCA. Section 3 presents the linear and curvelinear modeling of the data. Simulation results are presented in Section 4 followed by the conclusions in Section 5.

2. BACKGROUND ON PCA

Principal component analysis has proven to be one of the best methods to find similar patterns or features in a data set. It is an essential statistical tool in pattern recognition applications which includes medicine (such as sample identification), industry (quality control and document image analysis), and government (fingerprint identification and face recognition) [9–11]. Ye and Auner [11] used PCA to reduce the dimensionality of signatures for different types of samples to create a real-time approach of sample analysis using a Raman spectrometer directly mounted at the end-effector of medical robot to enhance the remote robot surgery. Chen et al. [9] developed algorithms based on PCA to generate a set of new identifying keys for a given set of patterns to reduce the number of comparisons during the near-matching process. Pinkowski [10] used PCA for feature reduction on a speaker-dependent data set to achieve high recognition rate analyzing spectrograms, which contain human speech utterances. 97.5% correct recognition rate is achieved using PCA. Also, Swiniarski and Swiniarsk [12] used PCA with rough set methods for feature selection in mammograms and reported good results.

In general, PCA algorithm can be useful whenever an automated feature extraction or identification from a digital image is required. It is based on finding a match for the specific feature in the test image from image database using some similarity measures. These measures are defined based on statistical characteristics of the data: variance, covariance, eigenvectors, and eigenvalues. A brief description of PCA is given in the following subsection and followed by an introduction of two distance measures used in this work.

2.1. A brief description of PCA

Suppose that we have m training data vectors $\mathbf{x}_1, \mathbf{x}_2, \ldots, \mathbf{x}_m$ of n dimensions each, that is, $\mathbf{x}_j = [x_{1j}, \ldots, x_{nj}]^T$. There are two phases in the algorithm of PCA. The first phase is to find p orthogonal and uncorrelated vectors and the second phase is to project the given data set into a subspace spanned by these p orthogonal vectors.

The first phase of PCA is as follows.

(i) Construct an $n \times 1$ vector $\mathbf{m}$ whose ith element m_i is the mean of the ith dimension of all data $\mathbf{x}$, that is,

$$m_i = \frac{1}{m} \sum_{k=1}^{m} x_{ik}. \tag{1}$$

(ii) Form an $n \times m$ matrix $\mathbf{X} = [\mathbf{x}_1 - \mathbf{m}, \mathbf{x}_2 - \mathbf{m}, \ldots, \mathbf{x}_m - \mathbf{m}]$, that is, $[\mathbf{X}]_{ij} = x_{ij} - m_i$.

(iii) The $n \times n$ covariance matrix $\mathbf{C}$ of $\mathbf{X}$ is

$$\mathbf{C} = \mathbf{X}\mathbf{X}^T. \tag{2}$$

(iv) Let λ_i and $\mathbf{v}_i$, $i = 1, 2, \ldots, n$, be eigenvalues and normalized eigenvectors of the matrix $\mathbf{C}$ with $\mathbf{C}\mathbf{v}_i = \lambda_i \mathbf{v}_i$ and $\lambda_1 \geq \lambda_2 \geq \cdots \geq \lambda_n \geq 0$. Eigenvectors are called the principal components.

Note that the covariance matrix $\mathbf{C}$ is symmetric and semidefinite. We have $\mathbf{v}_i^T \cdot \mathbf{v}_j = 0$ for all $\lambda_i \neq \lambda_j$. If λ_i is the repeated eigenvalue of $\mathbf{C}$, the associated principle component $\mathbf{v}_i$ is not unique.

The second phase of PCA is to project a given $n \times 1$ testing data $\mathbf{x}$ into a space spanned by $\mathbf{v}_1, \mathbf{v}_2, \ldots, \mathbf{v}_p$, the eigenvectors associated with the first p largest eigenvalues of the covariance matrix $\mathbf{C}$. This space is called eigenspace. The projection of the testing data $\mathbf{x}$ on the eigenspace is

$$\mathbf{y} = \mathbf{P}^T(\mathbf{x} - \mathbf{m}), \tag{3}$$

where $\mathbf{P} = [\mathbf{v}_1 \ \ \mathbf{v}_2 \ \ \cdots \ \ \mathbf{v}_p]$.

Discarding small eigenvalues, and consequently corresponding eigenvectors, results in dimension reduction and increases the speed of computations. The highest eigenvalues are associated with the eigenvectors that contain the major modes of variation in the data. Once test mammogram and training set all projected in the eigenspace, a distance measure is used to find the nearest match of the test mammogram to the mammogram in the training set. Approximately 90% of the total variance is contained in the first 5 to 10 of the dimensions. In most implementations of PCA for feature

extraction applications, the important decision is how much of the original data variation is needed to be captured in the eigen features. Most researches choose to work with 88% to 98% of original data variations (see [11]). Including all of the principal components would be equivalent to working with the original data since each one of these vectors is a linear combination of the original vectors. It is worth mentioning that keeping the first few components and discarding the others will result in a loss of the original data, however, in this utilization of the PCA, this loss is insignificant due to the fact that the principal components are used as feature vectors to match them with the feature vectors from mammograms in the training set. The original mammogram is preserved and the output for the radiologist is the original mammogram with identified blocks as suspicious block.

Thresholding is implemented by throwing away all eigenvalues that are below a threshold T, which is basically a measure of how much variation in the original data is accounted for in the eigenvalues and their corresponding eigenvectors that are preserved. The threshold T is calculated as follows:

$$T = \frac{\sum_{k=1}^{L} \lambda_k}{\sum_{k=1}^{n} \lambda_k}, \tag{4}$$

where L is usually kept much smaller than the original total number of the eigenvalues n. In our simulation, we choose $L = 36$.

2.2. Distance measurements

A common way of finding similarities between two patterns is to find the difference. Since minimum distance means maximum similarity, different types of distance measurements are being used. In this study, two types are employed: Euclidean and Chebyshev with the intention to compare them and find the optimum one for mammographic data.

(i) *Euclidean distance*

This type of distance is the standard metric, which is the shortest distance between two vectors ($\mathbf{x}$ and $\mathbf{y}$) and is defined as follows:

$$d_e(\mathbf{x}, \mathbf{y}) := \sqrt{\sum_i (x_i - y_i)^2}. \tag{5}$$

(ii) *Chebyshev distance*

This type of distance is also known as maximum value distance. It examines the absolute magnitude of the differences between coordinates of a pair of objects. When computation time is extremely imperative, Chebyshev distance is used. It is defined as follows:

$$d_{\mathrm{ch}}(\mathbf{x}, \mathbf{y}) := \max_i |x_i - y_i|. \tag{6}$$

3. MODELING OF IMAGE FEATURES

Initially the intention was to identify the image features using a linear structure model in an effort to improve the results obtained by utilizing PCA alone [13]. Indeed, a proper choice of a modeling technique that suites the features in the data can be combined with PCA to improve results as reported in [10, 11, 13]. In this work, the search is for suspicious tissue which can be identified by regions surrounded by an edge. Edges in images can be detected using several algorithms such as directional morphology, curve-linear structure detection, directional second-order Gaussian derivative, and convolution-based edge detection algorithms [14–21]. Also, edges may have several shapes such as straight lines, circles, ellipses, and parabola. Thus it is important that a suitable data modeling is utilized to better fit the nature of the features captured in the data.

3.1. Linear modeling

Convolution-based edge detector is used in this work. Four masks with the size of 5×5 pixels are used for vertical, horizontal, and oblique ($\pm 45^\circ$) structure detection such as

$$R(n_1, n_2) = \sum_{k_1=-2}^{2} \sum_{k_2=-2}^{2} a(k_1, k_2) b(n_1 - k_1, n_2 - k_2), \tag{7}$$

where R is the resultant image, a is the mask, and b is the input image. When a vertical mask is convolved with an image, the longitudinal linear structures are extracted in the resultant image. Using other masks results in similar outputs. Once all edges in all directions are identified, an edge mammogram is generated. It is more common to use mask size of 3×3 and they are seldom to be greater than 7×7, we decide to use 5×5. Masks used in this implementation for detecting vertical, horizontal, oblique with 45° and -45° edges are

$$\begin{bmatrix} -1 & -1 & 4 & -1 & -1 \\ -1 & -1 & 4 & -1 & -1 \\ -1 & -1 & 4 & -1 & -1 \\ -1 & -1 & 4 & -1 & -1 \\ -1 & -1 & 4 & -1 & -1 \end{bmatrix}, \quad \begin{bmatrix} -1 & -1 & -1 & -1 & -1 \\ -1 & -1 & -1 & -1 & -1 \\ 4 & 4 & 4 & 4 & 4 \\ -1 & -1 & -1 & -1 & -1 \\ -1 & -1 & -1 & -1 & -1 \end{bmatrix},$$

$$\begin{bmatrix} -1 & -1 & -1 & -1 & 4 \\ -1 & -1 & -1 & 4 & -1 \\ -1 & -1 & 4 & -1 & -1 \\ -1 & 4 & -1 & -1 & -1 \\ 4 & -1 & -1 & -1 & -1 \end{bmatrix}, \quad \begin{bmatrix} 4 & -1 & -1 & -1 & -1 \\ -1 & 4 & -1 & -1 & -1 \\ -1 & -1 & 4 & -1 & -1 \\ -1 & -1 & -1 & 4 & -1 \\ -1 & -1 & -1 & -1 & 4 \end{bmatrix}, \tag{8}$$

respectively.

3.2. Curvilinear modeling

Hough Transform (HT) was introduced by Hough in 1962 for detecting and recognizing complex patterns in data [22].

HT does not require connected or even nearby edge points. Literature is rich in articles on HT and its abilities in tracking edges, lines, curves, and parabolic features in images. Fundamentally it is a mapping process of edge pixels into a parameter space [22, 23]. Edges that represent straight lines, for example, are identified with their slope-intercept (m, b) parameters and the line for edge pixel (x, y) is

$$y = mx + b. \tag{9}$$

However, due to the difficulty dealing with vertical lines in the image space, a different description for straight line is commonly used [23]. Lines are parameterized by the orientation of the line θ and the distance of the line from the origin ρ as follows:

$$\rho = (x_i - x_0)\cos\theta + (y_i - y_0)\sin\theta, \tag{10}$$

where all points (x_i, y_i) of an edge in the image space are represented by (θ, ρ) point in the transform space, and (x_0, y_0) is the origin of the image space. While this algorithm has proved its efficiency in applications where features are straight lines, however, suspicious regions tend to have circular shapes. Thus HT for curves is a mapping of a pixel point (x_i, y_i) in an image space to a sinusoidal curvilinear in the Hough space (ρ, θ). A complete review of detecting Hough transforms curves can be found in [24, 25]. In general, curves of various sizes can be identified in the image scene by introducing a new parameter such as a radius of a circle r. The transform makes use of the circle formula

$$(x - x_0)^2 + (y - y_0)^2 = r^2 \tag{11}$$

to find the pixels that fall on this circle and simultaneously increases the particular accumulator positions.

HT can be high in computational cost and complexity and has some disadvantages such as the fact that some lines are replicated during detection due to spatial sampling. Nevertheless, HT is a powerful tool for detecting features with various sizes and orientations with high accuracy and research is ongoing in developing computationally efficient algorithms [26]. Recently, Olson in [27] has presented superior algorithm to provide accurate and fast Hough curves with a worst-case complexity of $O(n)$.

4. EXPERIMENTAL RESULTS

The algorithm outlined above was simulated on mammograms from the Mammographic Image Analysis Society (MIAS) database using Matlab . The simulations can be categorized as follows: the first is utilizing PCA with linear modeling in local processing, and the second is utilizing PCA with HT as a method for curvilinear modeling. In a global approach one would consider each mammogram is an image as where in local processing each mammogram is segmented into blocks prior to any processing and each block is processed as it was an image. Instead of a training set of mammograms, we are training a set of blocks from several mammograms. Earlier work showed that PCA using a local processing is performing better [13]. This is an attempt to examine PCA performance in a small neighborhoods that may contain some mamographic features of interest.

Table 1: Decision table for training set segments.

Training set		Segments												Image is
		1	2	3	4	5	6	7	8	9	10	11	12	
1	mdb001	n	n	n	n	s	n	s	s	s	n	n	n	**S**
2	mdb002	n	n	n	n	n	n	s	s	s	n	s	s	**S**
3	mdb003	n	n	n	n	n	n	n	n	n	n	n	n	**N**
4	mdb004	n	n	n	n	n	n	n	n	n	n	n	n	**N**
5	mdb058	n	n	n	n	n	n	s	n	n	n	n	n	**S**
6	mdb072	n	n	n	n	n	n	n	s	n	n	s	n	**S**
7	mdb008	n	n	n	n	n	n	n	n	n	n	n	n	**N**
8	mdb009	n	n	n	n	n	n	n	n	n	n	n	n	**N**
9	mdb012	n	n	n	n	s	n	n	n	n	n	n	n	**S**
10	mdb013	n	n	n	n	n	n	n	s	s	n	n	n	**S**
11	mdb075	n	n	n	n	s	n	n	n	n	n	n	n	**S**
12	mdb090	n	n	n	s	s	n	s	s	n	n	n	n	**S**

Twelve images are segmented into 12 blocks each resulting in 144 elements trained. These mammograms are combinations of normal, benign, and malignant mammograms. All these images/blocks from MIAS database are labeled and their information are tabulated in Table 1. Table 1 is the decision table, where the status of each block is visually inspected and labeled by a radiologist. As for the blocks, each block is defined to be either normal (n) or suspicious (s). Figure 1 shows one of the images of each group. Figure 1(a) is a benign mammogram in training set database, the area around nipple is defined to be suspicious. Tissues of interest are referred to as suspicious in this paper, whether they are malignant or benign. Making final decision is left to a specialist. Figure 1(b) is a normal mammogram in the training set database. Figure 1(c) is a malignant mammogram, and areas around milk ducts are suspicious. The local processing can be computationally expensive depending on the training set size and number of blocks in each image. Moreover, adding more mammograms to the training set increases memory requirements.

Fifteen mammograms were used as testing set, which mounts to 180 block testing and matchings results. Figure 2 shows three samples of test images. Each of them belongs to one of the three classified groups: benign, normal, and malignant, respectively.

4.1. Results from linear structure modeling

This algorithm is based on extracting the linear models in each image or block using a convolution process. The detectors are composed of four 5×5 masks responding to vertical, horizontal, and oblique $(\pm 45^\circ)$ lines. This method

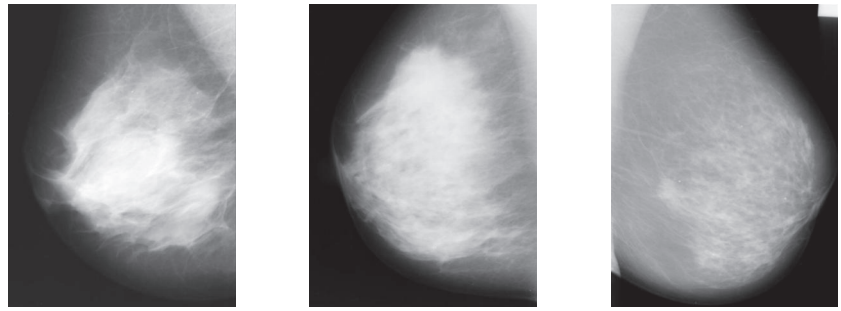

(a) (b) (c)

Figure 1: (a) Benign mammogram in training set mdb001; (b) normal mammogram in training set mdb003; and (c) malignant mammogram in training set mdb058.

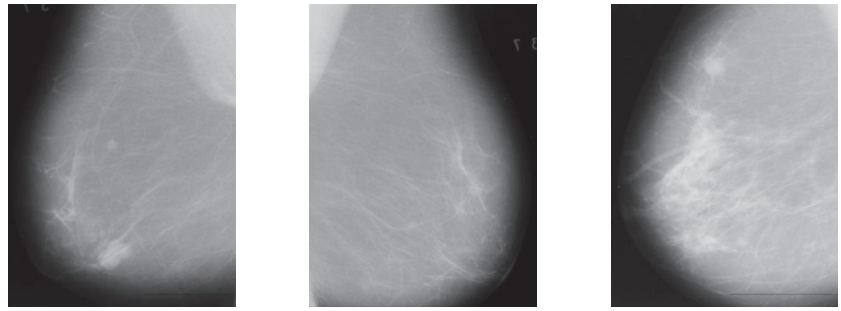

(a) (b) (c)

Figure 2: (a) Benign mammogram in testing set mdb005; (b) normal mammogram in testing set mdb006; and (c) malignant mammogram in testing set mdb023.

was applied to 15 randomly selected images such as the ones displayed in Figure 2 using both Euclidean distance and Chebyshev distance. Total number of testing blocks are 180 and total number of trained blocks are 144.

Results with Euclidean and Chebyshev distance measures are tabulated in Tables 2 and 3, respectively. These results indicate that Euclidian distance is capable of achieving similar results to Chebyshev distance in terms of a mammogram classification as suspicious or not, both at 60% correct, 26.6% FP, and 13.3% FN. Out of the fifteen tests performed, 9 were correct, 4 were FP, and 2 FN using both distance measures. However, the Euclidian distance has shown much higher accuracy with PCA using block statistics. That is, in the Euclidean distance simulations, 159 (88.33%) blocks were correctly classified, while 9 (5%) FP, and 12 (6.66%) FN classifications. As for the Chebyshev results they are at 157 (87.22%) blocks correctly classified, 11 (6.11%) FP, and 12 (6.66%) FN classifications. The Euclidean distance has a comparable accuracy to Chebyshev's with the first has two less FP block classification which requires less viewing time by the radiologist.

4.2. Results from curvilinear modeling

The results of using HT transform as an algorithm to identify the curvilinear features in the mammogram as opposed to straight edges are displayed in Tables 4 and 5.

From these tables, it is observed that the correct mammogram classifications is improved to 73.3% with 20% FP and 6.67% FN classifications for the Eculidean disteance while the results of the Chebyshev distance are improved to 66.67% correct classifications, and 26.67% FP, and 6.67% FN. However, since the objective here is to alert a radiologist to suspicious regions in the test mammogram, it is more proper again to look at the block classification results. These are at 91.11% correct classifications, 3.33% FP, and 5.55% FN for the Euclidean distance measure while the Chebyshev results are at 90% correct block classifications, 4.44% FP, and 5.55% FN. It is worth noting that mdb016 was consistently classified as suspicious mammogram when it is a normal mammogram. This is due to the fact that this image is a mammogram of fatty and glandular tissue. Tissue composition ion mammography is important as the detection of cancer is easier in fatty tissue and mammography becomes less sensitive the more dense tissue (the greater the proportion of fibroglandular tissue). While this mammogram is not suspicious, it is not uncommon for a CAD system to mark an area of normal overlapping tissue as suspicious since its tissue is highly glandular tissue.

5. CONCLUSION

Our goal is to detect abnormalities in screening mammograms as an additional support system to assist radiologists.

Table 2: Results using block processing with Euclidean distance. Note: first number indicates the block number and second one signifies the image number in training set.

Testing set		Segments												Image is
		1	2	3	4	5	6	7	8	9	10	11	12	
mdb005	**S**	11,10 n	5,10 n	9,10 s	11,11 n	5,11 s	9,8 n	2,3 n	8,7 n	9,8 n	11,11 n	11,8 n	12,3 n	**S**
mdb006	**N**	1,7 n	8,5 n	9,7 n	4,4 n	8,9 n	9,5 n	7,7 n	8,7 n	9,7 n	10,4 n	2,2 n	11,6 s	**S**
mdb007	**N**	1,10 n	2,3 n	6,8 n	12,12 n	5,8 n	9,8 n	7,11 n	8,8 n	9,8 n	10,3 n	11,3 n	12,3 n	**N**
mdb010	**S**	1,12 n	2,12 n	6,4 n	7,6 n	5,5 n	6,4 n	7,6 n	8,5 n	9,5 n	10,6 n	12,10 n	12,12 n	**N**
mdb023	**S**	10,3 n	2,1 n	3,8 n	10,3 n	5,10 n	6,10 n	7,1 s	2,11 n	6,10 n	10,3 n	8,1 s	9,8 n	**S**
mdb028	**S**	1,7 n	2,12 n	6,7 n	4,2 n	5,9 s	9,5 n	4,2 n	8,9 n	12,7 n	10,5 n	11,9 n	9,5 n	**S**
mdb011	**N**	0,3 n	2,1 n	3,8 n	7,1 s	5,10 n	6,10 n	10,10 n	8,11 n	12,8 n	10,3 n	7,1 s	3,7 n	**S**
mdb014	**N**	1,7 n	5,6 n	3,7 n	1,5 n	8,12 s	6,7 n	7,4 n	8,5 n	9,5 n	10,7 n	11,12 n	12,12 n	**S**
mdb016	**N**	4,12 s	5,5 n	12,1 n	7,12 s	8,9 n	9,5 n	4,12 s	8,5 n	12,7 n	7,1 s	11,6 s	12,12 n	**S**
mdb015	**S**	10,11 n	5,10 n	6,11 n	7,1 s	5,11 s	3,1 n	7,1 s	8,11 n	6,1 n	4,11 n	6,4 n	3,12 n	**S**
mdb017	**S**	12,12 n	5,3 n	2,6 n	4,3 n	5,3 n	9,1 s	12,12 n	8,1 s	9,7 n	4,1 n	11,10 n	12,7 n	**S**
mdb019	**S**	1,10 n	2,1 n	3,8 n	11,11 n	5,11 s	3,10 n	2,10 n	8,7 n	6,10 n	2,3 n	8,7 n	12,8 n	**S**
mdb095	**S**	7,1 s	2,1 n	9,10 s	12,12 n	5,1 s	6,8 n	7,1 s	5,11 s	9,8 n	7,11 n	11,8 n	12,10 n	**S**
mdb102	**S**	1,12 n	2,12 n	12,11 n	7,6 n	5,6 n	6,4 n	1,12 n	2,12 n	3,12 n	10,6 n	12,10 n	3,12 n	**N**
mdb092	**S**	4,12 s	5,9 s	6,7 n	4,12 s	5,12 s	6,4 n	7,12 s	8,6 s	6,4 n	10,6 n	12,10 n	6,4 n	**S**

Table 3: Results using block processing with Chebyshev distance. Note: first number indicates the block number and second one signifies the image number in training set.

Testing set		Segments												Image is
		1	2	3	4	5	6	7	8	9	10	11	12	
mdb005	**S**	11,10 n	5,10 n	9,10 s	11,11 n	5,11 s	9,8 n	1,8 n	8,7 n	9,8 n	11,11 n	2,4 n	12,3 n	**S**
mdb006	**N**	1,7 n	8,5 n	9,7 n	4,4 n	5,7 n	9,5 n	10, 4 n	8,7 n	9,7 n	10,4 n	2,2 n	11,6 s	**S**
mdb007	**N**	1,3 n	2,3 n	6,8 n	6,12 n	5,8 n	9,8 n	7,11 n	8,8 n	9,8 n	10,1 n	11,3 n	12,3 n	**N**
mdb010	**S**	1,12 n	2,12 n	6,2 n	7,6 n	5,5 n	6,4 n	7,6 n	8,5 n	9,5 n	10,6 n	12,10 n	12,12 n	**N**
mdb023	**S**	10,3 n	2,1 n	3,8 n	7,1 s	5,10 n	6,10 n	7,1 s	2,11 n	6,3 n	7,1 s	8,1 s	9,8 n	**S**
mdb028	**S**	1,7 n	2,12 n	6,7 n	7,7 n	5,9 s	9,5 n	10,4 n	5,7 n	12,7 n	10,5 n	11,5 n	9,5 n	**S**
mdb011	**N**	10,11 n	2,1 n	3,8 n	7,1 s	5,10 n	6,10 n	10,10 n	8,11 n	12,8 n	10,3 n	7,1 s	3,7 n	**S**
mdb014	**N**	1,7 n	5,6 n	3,7 n	7,4 n	8,12 s	6,7 n	7,4 n	8,5 n	9,5 n	10,7 n	11,2 n	9,12 n	**S**
mdb016	**N**	4,12 s	5,12 s	12,1 n	4,12 s	8,9 n	12,1 n	4,12 s	8,5 n	12,7 n	7,1 s	11,6 s	12,2 s	**S**
mdb015	**S**	10,11 n	5,10 n	6,11 n	7,1 s	5,11 s	3,1 n	7,1 s	8,11 n	6,1 n	4,11 n	6,4 n	3,12 n	**S**
mdb017	**S**	6,12 n	5,3 n	2,6 n	7,10 n	5,3 n	9,1 s	6,12 n	8,1 s	9,1 s	4,1 n	11,10 n	11,6 s	**S**
mdb019	**S**	1,10 n	2,1 n	6,3 n	11,11 n	5,11 s	3,10 n	2,10 n	8,7 n	6,10 n	2,3 n	8,7 n	12,8 n	**S**
mdb095	**S**	7,1 s	2,1 n	9,10 s	4,3 n	5,1 s	6,8 n	7,1 s	5,11 s	9,8 n	7,11 n	11,8 n	12,10 n	**S**
mdb102	**S**	1,12 n	2,12 n	12,1 n	7,6 n	5,6 n	12,4 n	1,12 n	2,12 n	12,4 n	1,8 n	9,7 n	12,4 n	**N**
mdb092	**S**	7,6 n	5,9 s	6,7 n	4,12 s	5,6 n	6,2 n	4,12 s	8,6 s	6,2 n	10,6 n	9,7 n	6,2 n	**S**

Table 4: Results of using curvilinear modeling and PCA with Euclidean distance. Note: first number indicates the block number and second one signifies the image number in training set.

Testing set		Segments												Image is
		1	2	3	4	5	6	7	8	9	10	11	12	
mdb005	**S**	8,7 n	2,9 n	8,11 n	8,4 n	8,9 n	5,10 n	8,4 n	8,5 n	5,10 n	8,7 n	11,11 n	5,11 s	**S**
mdb006	**N**	1,2 n	2,2 n	3,6 n	7,2 s	8,9 n	6,6 n	4,12 s	8,7 n	6,6 n	10,9 n	11,7 n	12,6 n	**S**
mdb007	**N**	1,3 n	2,10 n	3,10 n	4,1 n	5,10 n	6,3 n	4,3 n	8,8 n	9,8 n	10,11 n	11,3 n	12,8 n	**N**
mdb010	**S**	1,6 n	2,12 n	3,12 n	4,12 s	5,12 s	9,4 n	4,12 s	8,5 n	9,4 n	10,6 n	11,6 s	12,2 s	**S**
mdb023	**S**	1,1 n	2,10 n	3,3 n	4,8 n	5,10 n	6,8 n	4,8 n	8,8 n	6,8 n	10,3 n	11,8 n	12,8 n	**N**
mdb028	**S**	1,4 n	2,12 n	3,4 n	4,4 n	5,2 n	9,7 n	7,2 s	8,7 n	9,7 n	10,2 n	11,7 n	12,7 n	**S**
mdb011	**N**	1,2 n	2,1 n	3,3 n	7,11 n	5,10 n	6,10 n	7,3 n	8,11 n	9,3 n	10,3 n	11,1 n	12,10 n	**N**
mdb014	**N**	1,9 n	2,7 n	3,7 n	4,7 n	5,5 n	9,4 n	7,9 n	8,5 n	9,5 n	10,9 n	11,2 s	12,6 n	**S**
mdb016	**N**	1,12 n	2,2 n	3,11 n	7,12 s	8,9 n	6,4 n	7,12 s	8,5 n	9,5 n	10,10 n	11,6 s	12,6 n	**S**
mdb015	**S**	1,1 n	2,11 n	3,11 n	4,1 n	8,8 n	9,11 n	4,3 n	8,11 n	9,1 s	10,1 n	11,1 n	12,4 n	**S**
mdb017	**S**	1,1 n	2,1 n	3,6 n	4,1 n	5,8 n	6,6 n	4,1 n	8,1 s	6,6 n	10,10 n	11,10 n	12,4 n	**S**
mdb019	**S**	1,10 n	2,1 n	3,3 n	7,3 n	5,1 s	6,8 n	4,6 n	8,7 n	6,3 n	10,5 n	11,7 n	12,8 n	**S**
mdb095	**S**	1,6 n	2,10 n	3,3 n	4,3 n	5,8 n	9,10 s	4,1 n	8,8 n	9,3 n	10,10 n	11,8 n	12,3 n	**S**
mdb102	**S**	1,6 n	2,12 n	3,5 n	4,12 s	5,6 n	6,4 n	4,6 n	8,6 s	9,4 n	10,6 n	11,6 s	12,4 n	**S**
mdb092	**S**	1,12 n	2,2 n	3,12 n	7,12 s	5,12 s	6,4 n	7,12 s	8,6 s	6,4 n	10,6 n	11,2 s	12,7 n	**S**

Table 5: Results of using curvilinear modeling and PCA with Chebyshev distance. Note: first number indicates the block number and second one signifies the image number in training set.

Testing set		Segments												Image is
		1	2	3	4	5	6	7	8	9	10	11	12	
mdb005	**S**	8,7 n	2,9 n	8,11 n	8,4 n	8,9 n	5,10 n	8,4 n	8,5 n	5,10 n	8,7 n	11,11 n	5,1 s	**S**
mdb006	**N**	1,2 n	2,2 n	3,9 n	4,12 s	8,9 n	6,6 n	4,12 s	8,7 n	6,6 n	10,8 n	11,7 n	12,6 n	**S**
mdb007	**N**	1,3 n	2,10 n	3,10 n	4,1 n	5,10 n	6,3 n	7,1 s	8,8 n	9,8 n	10,11 n	11,3 n	12,8 n	**S**
mdb010	**S**	1,6 n	2,12 n	3,12 n	4,12 s	5,12 s	9,4 n	7,6 n	8,5 n	9,4 n	10,6 n	11,6 s	12,2 s	**S**
mdb023	**S**	1,1 n	2,10 n	3,3 n	4,8 n	5,10 n	6,8 n	4,8 n	8,8 n	6,8 n	10,3 n	11,8 n	12,8 n	**N**
mdb028	**S**	1,4 n	2,2 n	3,4 n	4,4 n	5,2 n	9,7 n	7,2 s	8,7 n	9,7 n	10,2 n	11,7 n	12,5 n	**S**
mdb011	**N**	1,2 n	2,1 n	3,3 n	7,11 n	5,10 n	6,10 n	7,3 n	8,11 n	6,9 n	10,3 n	11,1 n	12,10 n	**N**
mdb014	**N**	1,9 n	2,7 n	3,7 n	4,7 n	5,12 s	9,4 n	4,7 n	8,5 n	9,5 n	10,7 n	11,2 s	12,6 n	**S**
mdb016	**N**	1,11 n	2,2 n	3,11 n	7,12 s	8,9 n	6,4 n	7,12 s	8,7 n	9,5 n	10,1 n	11,6 s	12,6 n	**S**
mdb015	**S**	1,1 n	2,11 n	3,11 n	4,1 n	8,8 n	9,11 n	4,3 n	2,11 n	9,1 s	10,1 n	11,6 s	12,4 n	**S**
mdb017	**S**	1,1 n	2,1 n	3,6 n	4,1 n	5,8 n	6,6 n	4,1 n	8,10 s	6,6 n	10,1 n	11,10 n	12,4 n	**S**
mdb019	**S**	1,3 n	2,1 n	3,3 n	7,3 n	5,1 s	6,8 n	4,12 s	8,7 n	6,3 n	10,5 n	11,7 n	12,8 n	**S**
mdb095	**S**	1,6 n	2,3 n	3,3 n	4,3 n	5,8 n	9,10 s	4,1 n	8,8 n	9,3 n	10,1 n	11,8 n	12,3 n	**S**
mdb102	**S**	1,6 n	2,12 n	3,5 n	4,12 s	5,6 n	6,4 n	4,6 n	8,6 s	6,7 n	10,6 n	11,2 s	12,4 n	**S**
mdb092	**S**	1,12 n	2,2 n	3,12 n	7,12 s	5,12 s	6,4 n	7,12 s	8,6 s	6,4 n	10,6 n	11,2 s	12,7 n	**S**

In this work, two different approaches are employed for the detection of suspicious tissues in mammograms utilizing local PCA with data modeling. Linear modeling, local PCA, and Euclidean distance algorithm showed better results compared to Chebyshev distance. Euclidean measure produces in general less false detections. However, since the nature of cancerous tissues is more circular, Hough transform was employed to search for curved shapes rather than straight edges. The Hough modeling of the data combined with local PCA, and Euclidean distance produces improved results. In all, all algorithms produced over 90% correct classifications of blocks. However, the algorithm has several parameters that can be investigated for improvements. Thus future work is planned for an investigation of the performance dependency on the Hough parameters, threshold for the principal components, and T which is a function of λ. The algorithm would improve if thresholding is optimized by using adaptive measures. Also, the distance measure is an important component of this framework, an optimum distance or even other similarity measures should be investigated. Moreover, block size is crucial for the performance and if smaller block size is used into the algorithm, the algorithm performance should improve, and hopefully, identify abnormalities in smaller size of neighborhoods down to pixel abnormality detection.

ACKNOWLEDGMENTS

Partial support of this work was provided by the National Science Foundation grant MRI-0215356 and by Western Michigan University FRACASF award. The authors would like also to acknowledge Western Michigan University for its support and contributions to the Information Technology and Image Analysis (ITIA) Center.

REFERENCES

[1] C. C. Boring, T. Squires, T. Tong, and S. Montgomery, "Cancer statistics," *Ca-A Cancer Journal for Clinicians*, vol. 44, no. 1, pp. 7–26, 1994.

[2] C. R. Smart, R. E. Hendrick, J. H. Rutledge III, and R. A. Smith, "Benefit of mammography screening in women ages 40 to 49 years: current evidence from randomized controlled trials," *Cancer*, vol. 75, no. 7, pp. 1619–1626, 1995.

[3] R. Zwiggelaar, "Separating background texture and image structure in mammograms," in *Proceedings of the British Machine Vision Conference (BMVC '99)*, pp. 362–371, British Machine Vision Association, Nottingham, UK, September 1999.

[4] H.-P. Chan, B. Sahiner, N. Patrick, et al., "Computerized classification of malignant and benign microcalcifications on mammograms: texture analysis using an artificial neural network," *Physics in Medicine and Biology*, vol. 42, no. 3, pp. 549–567, 1997.

[5] G. Lemaur, K. Drouiche, and J. DeConinck, "Highly regular wavelets for the detection of clustered microcalcifications in mammograms," *IEEE Transactions on Medical Imaging*, vol. 22, no. 3, pp. 393–401, 2003.

[6] W. M. Morrow, R. B. Paranjape, R. M. Rangayyan, and J. E. L. Desautels, "Region-based contrast enhancement of mammograms," *IEEE Transactions on Medical Imaging*, vol. 11, no. 3, pp. 392–406, 1992.

[7] L. Shen, R. M. Rangayyan, and J. E. L. Desautels, "Application of shape analysis to mammographic calcifications," *IEEE Transactions on Medical Imaging*, vol. 13, no. 2, pp. 263–274, 1994.

[8] T. C. Wang and N. B. Karayiannis, "Detection of microcalcifications in digital mammograms using wavelets," *IEEE Transactions on Medical Imaging*, vol. 17, no. 4, pp. 498–509, 1998.

[9] C. Y. Chen, C. C. Chang, and R. C. T. Lee, "A near pattern-matching scheme based upon principal component analysis," *Pattern Recognition Letters*, vol. 16, no. 4, pp. 339–345, 1995.

[10] B. Pinkowski, "Principal component analysis of speech spectrogram images," *Pattern Recognition*, vol. 30, no. 5, pp. 777–787, 1997.

[11] Z. Ye and G. Auner, "Principal component analysis approach for biomedical sample identification," in *Proceedings of IEEE International Conference on Systems, Man, and Cybernetics (SMC '04)*, pp. 1348–1353, The Hague, The Netherlands, October 2004.

[12] R. Swiniarski and A. Swiniarsk, "Comparison of feature extraction and selection methods in mammogram recognition," *Annals of the New York Academy of Sciences*, vol. 980, no. 12, pp. 116–124, 2002.

[13] I. Abdel-Qader, A. Kawshif, O. Abudayyeh, and D. Miller, "Feature extraction using pca and cluster analysis," in *Proceedings of the 4th IEEE Electro/Information Technology Conference*, Indianapolis, Ind, USA, June 2003.

[14] M. Brejl and M. Sonka, "Directional 3D edge detection in anisotropic data: detector design and performance assessment," *Computer Vision and Image Understanding*, vol. 77, no. 2, pp. 84–110, 2000.

[15] S. Duan and Q.-Q. Qin, "Edge detection based on dynamic morphology," in *MIPPR 2005: Image Analysis Techniques*, D. Li and H. Ma, Eds., vol. 6044 of *Proceedings of SPIE*, Wuhan, China, October-November 2005.

[16] A. Goshtasby and H.-L. Shyu, "Edge detection by curve fitting," *Image and Vision Computing*, vol. 13, no. 3, pp. 169–177, 1995.

[17] O. A. Zuniga and R. M. Haralick, "Integrated directional derivative gradient operator," *IEEE Transactions on Systems, Man and Cybernetics*, vol. 17, no. 3, pp. 508–517, 1987.

[18] W. E. Higgins and C. Hsu, "Edge detection using two-dimensional local structure information," *Pattern Recognition*, vol. 27, no. 2, pp. 277–294, 1994.

[19] S. Zhan and R. Mehrotra, "Zero-crossing-based optimal three-dimensional edge detector," *Computer Vision, Graphics, and Image Processing: Image Understanding*, vol. 59, no. 2, pp. 242–253, 1994.

[20] R. Mehrotra and S. Zhan, "A computational approach to zero-crossing-based two-dimensional edge detection," *Graphical Models and Image Processing*, vol. 58, no. 1, pp. 1–17, 1996.

[21] M. Song, X.-L. Hu, and Y. Gao, "Image edge detection based on omnidirectional multiscale morphology," *Journal of Yangzhou University(Natural Science Edition)*, vol. 8, no. 1, pp. 39–42, 2005.

[22] P. Hough, "Methods and means for recognizing complex patterns," US patent no. 069654, 1962.

[23] R. Duda and P. Hart, "Use of the hough transformation to detect lines and curves in pictures," *Communications of the ACM*, vol. 15, no. 1, pp. 11–15, 1972.

[24] J. Illingworth and J. Kittler, "A survey of the hough transform," *Computer Vision, Graphics, & Image Processing*, vol. 44, no. 1, pp. 87–116, 1988.

[25] V. F. Leavers, "Which hough transform?" *Computer Vision, Graphics, and Image Processing: Image Understanding*, vol. 58, no. 2, pp. 250–264, 1993.

[26] T. Rabbani and F. van den Heuvel, "Efficient hough transform for automatic detection of cylinders in point clouds," in *Proceedings of the 11th Annual Conference of the Advanced School for Computing and Imaging (ASCI '05)*, Het Heijderbos, Heijen, The Netherlands, June 2005.

[27] C. F. Olson, "Constrained hough transforms for curve detection," *Computer Vision and Image Understanding*, vol. 73, no. 3, pp. 329–345, 1999.

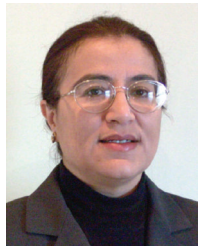

Ikhlas Abdel-Qader is currently an Associate Professor of Electrical and Computer Engineering, and is the Founder and Director of the Information Technology and Image Analysis (ITIA) Center in the College of Engineering and Applied Sciences at Western Michigan University. She earned her Ph.D. degree in electrical and computer engineering from North Carolina State University, Raleigh, in 1992. Her research expertise and interests include feature extraction, motion estimation, and image compression with applications in medical imaging, nondestructive testing, and intelligent transportation systems. She is also actively involved in promoting engineering careers and research to undergraduate students as well as to middle and high school students. She is a Member of the Institute of Electrical and Electronic Engineers (IEEE); the IEEE Acoustics, Speech, and Signal Processing Society; and the IEEE Engineering in Medicine and Biology Society. She is also a Member of the Society of Women Engineers, a Member of the Honor Society of Phi Kappa Phi, and an Associate Member of the Sigma Xi Scientific Research Society. She is a registered Professional Engineer in the State of Minnesota since 1996.

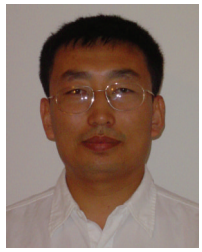

Lixin Shen received his B.S. and M.S. degrees from Peking University, China, in 1987 and 1990, respectively, and his Ph.D. degree from Zhongshan University, China, in 1996, all in mathematics. From September 1996 to July 2001, he was a Research Fellow at Center for Wavelets, Approximation, and Information Processing, National University of Singapore. From August 2001 to July 2002, he was a Post-Doctoral Fellow at Virtual Environments Research Institute, University of Houston. From August 2002 to July 2004, he was with the Department of Mathematics, West Virginia University. He is currently an Assistant Professor at the Department of Mathematics, Western Michigan University. His current research interests are wavelets and their application in image processing.

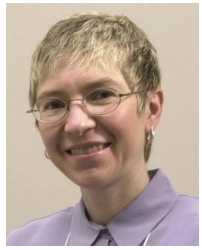

Christina Jacobs received her B.S. degree in neuroscience from University of Rochester in Rochestor, New York, in 1986 and her M.D. degree in medicine from New York University in New York City, in 1991. She is board certified in radiology from the American Board of Radiology since 1996. She is currently a Member of Advanced Radiology Services and serves as the Medical Director of Bronson Center for Women in Kalamazoo, Michigan. Her research interests include mammography and ovarian cancer detection using CT imaging. She is a Member of the Society of Breast Imaging, the Radiological Society of North America, the American College of Radiology, the American Association for Women Radiologists, and Michigan State Medical Society.

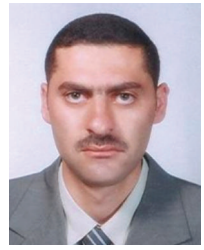

Fadi Abu Amara received his Computer Engineering bachelor degree from Faculty of Engineering Technology, Al-Balqa' Applied University, in Jordan, in 2001. Currently he is a Graduate Student in the Department of Electrical and Computer Engineering and a Research Assistant in the Information Technology and Image Analysis Center at Western Michigan University. His area of interests includes medical image analysis, fuzzy logic, and neural network.

Sarah Pashaie-Rad received the B.S. degree from Sharif University of Technology and the M.S. degree, with highest honor, from Western Michigan University, both in electrical engineering. Her graduate research interests involved digital image processing focused on medical applications. She joined St. Jude Medical, Inc. in September 2005. Her current responsibilities include test failure analysis for implantable cardioverter defibrillators (ICD).

Hindawi Publishing Corporation
International Journal of Biomedical Imaging
Volume 2006, Article ID 27483, Pages 1–7
DOI 10.1155/IJBI/2006/27483

Intervention Models in Functional Connectivity Identification Applied to fMRI

João Ricardo Sato,[1,2] Daniel Yasumasa Takahashi,[3] Ellison Fernando Cardoso,[2,3] Maria da Graça Morais Martin,[2,3] Edson Amaro Júnior,[2,3] and Pedro Alberto Morettin[1]

[1] *Departamento de Estatística, Instituto de Matemática e Estatística, Universidade de São Paulo, São Paulo, Sp 05508-090, Brazil*
[2] *Laboratório de Neuroimagem Funcional (NIF), Lim 44, Faculdade de Medicina, Universidade de São Paulo, São Paulo, Sp 05403-001, Brazil*
[3] *Departamento de Radiología, Hospital das Clínicas, Faculdade de Medicina, Universidade de São Paulo, São Paulo, Sp 05403-001, Brazil*

Received 31 January 2006; Revised 26 June 2006; Accepted 26 June 2006

Recent advances in neuroimaging techniques have provided precise spatial localization of brain activation applied in several neuroscience subareas. The development of functional magnetic resonance imaging (fMRI), based on the BOLD signal, is one of the most popular techniques related to the detection of neuronal activation. However, understanding the interactions between several neuronal modules is also an important task, providing a better comprehension about brain dynamics. Nevertheless, most connectivity studies in fMRI are based on a simple correlation analysis, which is only an association measure and does not provide the direction of information flow between brain areas. Other proposed methods like structural equation modeling (SEM) seem to be attractive alternatives. However, this approach assumes prior information about the causality direction and stationarity conditions, which may not be satisfied in fMRI experiments. Generally, the fMRI experiments are related to an activation task; hence, the stimulus conditions should also be included in the model. In this paper, we suggest an intervention analysis, which includes stimulus condition, allowing a nonstationary modeling. Furthermore, an illustrative application to real fMRI dataset from a simple motor task is presented.

1. INTRODUCTION

Functional magnetic resonance imaging (fMRI) based on blood oxygenation level-dependent (BOLD) signal has become one of the most prominent and powerful tools in cognitive neuroscience [1]. Most fMRI studies found in the literature focus on the detection of neuronal activation and brain mapping via statistical analysis. However, understanding cortical dynamics is a crucial step toward inferring cortical functioning.

Several evidences [2–4] suggest that modeling the interactions between different brain structures is paramount to understand the mechanisms guiding specific cognitive behaviour. However, the determination of parameters involved in cortical dynamics is still an open question. A number of techniques are being used to detect patterns of interaction between cortical areas, most using an *ad hoc* concept. So far, most connectivity studies have investigated temporal correlation as a measure of connectivity [3], even though it is not enough to identify the direction of information flow. In fact, Pearson correlation coefficient in time series analysis is just a measure of linear association. The connectivity mapping via correlation analysis is obtained firstly by selecting a seed voxel, and then Pearson correlation is calculated against all the other brain voxels. In most cases, the selection of the seed voxel is derived from the activation maps. Hence, as the activation detection is based on the similarity between the observed BOLD signal in a voxel and an expected haemodynamic curve, the correlation connectivity analysis is close to an activation mapping considering the seed voxel BOLD signal as the expected curve. Finally, we conclude that the correlation connectivity mapping is not sufficient to provide additional information in relation to the activation analysis based on general linear model (GLM).

Other statistical methods, such as the structural equation modeling (SEM), are more attractive to overcome this

shortcoming. Büchel and Friston [2] modeled the occipitoparietofrontal network involved in attention tasks using structural equation modeling. Zhuang et al. [5] applied SEM to a bimanual motor coordination experiment. Rowe et al. [6] modeled the prefrontal cortex in a color selection task. An improvement of SEM applied to fMRI analysis is the dynamic causal model (DCM), proposed by Friston et al. [7]. However, these two modeling approaches require a complete prespecification of the connectivity structure. Additionally, as DCM is estimated via Bayesian algorithms, it also requires the prior densities of the parameters of interest. In fact, these models measure the instantaneous connectivity, but require the direction of information flow. Therefore, these approaches are not enough to provide a complete identification of the connectivity pattern. Furthermore, the autocorrelation of BOLD signal is another obstacle for the application of these models and, in most cases, is simply ignored.

Granger causality [8] is a very prominent concept to describe information flow and connectivity. Baccalá et al. [9] and Baccalá and Sameshima [10] introduced a frequency-domain connectivity identification method for EEG using partial directed coherence and this causality concept. Goebel et al. [11] and Roebroeck et al. [12] introduced the concept of Granger causality in fMRI via vector autoregressive modeling (VAR). They have also shown the applicability of this approach to BOLD signals using simulations and illustrating it with real data derived from visuomotor studies. Compared to other approaches described previously, the main advantage of Granger causality identification via VAR models is the fact that prior specifications about connectivity structure are not necessary. Also, if one has prior partial knowledge about this structure, it can be naturally included in the model as a restriction in the parameters to be estimated.

The stationarity condition is one of the main obstacles to VAR modeling application in fMRI analysis. This assumption requires the connectivity structure to be the same during all acquisition times. Although acceptable in resting state or one-condition experiments, it may not be valid in paradigms with more than one condition. In that matter, as the connectivity structure may change according to the stimulus, comparisons between these structures are also an interesting point.

In this paper, we propose the use of a generalization of VAR models via intervention analysis (structural break models), which allows a natural modeling of connectivity and also statistical comparisons of the connectivity structures in experiments with different stimulus conditions.

2. GRANGER CAUSALITY AND CONNECTIVITY

In fMRI analysis, the definition of connectivity can be divided into two concepts: functional and effective connectivity. The first is defined as "*correlations between spatially remote neurophysiological events*" [4]. In contrast, effective connectivity is related to the "*influence of one neural system over another*" [4]. Note that effective connectivity implies in functional one, but the reciprocal may not be valid. The activity correlations or synchronisms may be observed due to external factors, not only due to synaptic interactions between the areas involved. An illustrative example involving differences between these two concepts of connectivity could be a paradigm with simultaneous stimulation of visual and auditory cortex. The neuronal activity in these areas will be correlated (functional), but not related to neural interactions (effective). However, the simplicity of functional connectivity concept makes it very useful, mainly in cases where the neural activity is measured indirectly, as in fMRI time series.

Granger causality is a very useful concept for the description of brain areas connectivity and direction of information flow identification [10, 13]. In the context of time series, Granger [8] defined causality in terms of predictability. This concept was originated in econometrics, focusing the understanding of relationships between financial time series such as prices, indexes, interest rates, and so forth. The basis of this concept is that effect cannot precede cause, suggesting that causality can be detected toward past and future relationships. A signal x_t is said to Granger-cause a signal y_t if the past values of x_t help the prediction of present values of y_t. In other words, if the variance of the prediction error of y_t, considering all the information until the time t, is less than the one obtained excluding the information of past values of x_t, then x_t is said to Granger-cause y_t.

Goebel et al. [11] introduced Granger causality identification between BOLD time series using VAR models, showing the applicability of this approach in simulated and real fMRI data. Note that Granger causality aims to identify interactions and relationships between signals via precedence and prediction. However, it is more related to functional connectivity than effective one, because it cannot distinguish real influences from prediction power.

Let a k-dimensional multivariate time series

$$\mathbf{Y}_t = \begin{bmatrix} y_{1t} & y_{2t} & \cdots & y_{kt} \end{bmatrix}', \quad t = 1, 2, \ldots, T, \tag{1}$$

composed by k signals measured on time t. In order to measure the prediction improvement of $\mathbf{Y}_t$ using a collection of p past values of the series $(\mathbf{Y}_{t-1}, \mathbf{Y}_{t-2}, \ldots, \mathbf{Y}_{t-p})$, assume a k-dimensional vector autoregressive model (VAR) of order p,

$$\mathbf{Y}_t = \mathbf{v} + \mathbf{A}_1\mathbf{Y}_{t-1} + \mathbf{A}_2\mathbf{Y}_{t-2} + \cdots + \mathbf{A}_p\mathbf{Y}_{t-p} + \mathbf{u}_t, \tag{2}$$

where $\mathbf{v}$ is the intercept vector (related to the process average), $\mathbf{u}_t$ is an error vector of random variables with zero mean and covariance matrix $\mathbf{\Sigma}$ given by

$$\mathbf{\Sigma} = \begin{bmatrix} \sigma_{11}^2 & \sigma_{12} & \cdots & \sigma_{k1} \\ \sigma_{21} & \sigma_{22}^2 & \cdots & \sigma_{k2} \\ \sigma_{31} & \sigma_{32} & \cdots & \sigma_{k3} \\ \vdots & \vdots & \ddots & \vdots \\ \sigma_{k1} & \sigma_{k2} & \cdots & \sigma_{kk}^2 \end{bmatrix}, \tag{3}$$

$\mathbf{v}$ and $\mathbf{A}_i$ are coefficient matrices given by

$$\mathbf{v} = \begin{bmatrix} v_1 \\ v_2 \\ \vdots \\ v_k \end{bmatrix}, \qquad \mathbf{A}_i = \begin{bmatrix} a_{11i} & a_{12i} & \cdots & a_{1ki} \\ a_{21i} & a_{22i} & \cdots & a_{2ki} \\ a_{31i} & a_{32i} & \cdots & a_{3ki} \\ \vdots & \vdots & \ddots & \vdots \\ a_{k1i} & a_{k2i} & \cdots & a_{kki} \end{bmatrix}, \quad i = 1, 2, \ldots, p. \tag{4}$$

As the error term $\mathbf{u}_t$ has zero mean, the predicted values of $\mathbf{Y}_t$ conditional to the past values are given by

$$\hat{\mathbf{Y}}_t = \mathbf{v} + \mathbf{A}_1\mathbf{Y}_{t-1} + \mathbf{A}_2\mathbf{Y}_{t-2} + \cdots + \mathbf{A}_p\mathbf{Y}_{t-p}. \tag{5}$$

The VAR model allows an easy way to identify Granger causality. If the coefficient a_{jli} for some i is nonzero, we say that signal y_{lt} Granger-causes the signal y_{jt}. In other words, the past values of the signal y_{lt} help the prediction of the present and future values of the signal y_{jt}. It is important to mention that this kind of relationship is not reciprocal, for example, y_{lt} may Granger-cause the signal y_{jt}, but not necessarily y_{jt} causes y_{lt}, indicating the direction of information flow.

Consider a functional magnetic resonance dataset. Select k voxels in the volume, obtaining a BOLD k-dimensional signal. Using the concept of Granger causality and the VAR modeling, it is possible to verify if the BOLD signal of certain brain areas Granger-causes another areas' BOLD signal, by testing the significance of the estimates of matrix $\mathbf{A}_t$. Therefore, we are able to test the functional connectivity and direction of the information flow.

However, VAR modeling is only suitable in cases of stationary time series with coefficients and error covariance matrix invariant on time. Hence, considering fMRI studies, a weakness of this approach is the assumption that both activation and connectivity functions are constant in the whole scanning interval. Let an epoch functional magnetic resonance image experiment with two conditions A and B. It is reasonable to expect functional connectivity under A, but it may not be the same under B. Therefore, we propose the use of intervention VAR (structural breaks model) focusing on the identification of changes in functional connectivity. The intervention VAR model is defined by

$$\mathbf{Y}_t = \mathbf{v}^{(C)} + \mathbf{A}_1^{(C)}\mathbf{Y}_{t-1} + \mathbf{A}_2^{(C)}\mathbf{Y}_{t-2} + \cdots + \mathbf{A}_k^{(C)}\mathbf{Y}_{t-k} + \mathbf{u}_t, \tag{6}$$

where the coefficient matrices are given by

$$\mathbf{v}^{(C)} = \begin{bmatrix} v_1 + \delta_1^{(C)} \\ v_2 + \delta_2^{(C)} \\ \vdots \\ v_k + \delta_k^{(C)} \end{bmatrix} = \mathbf{v} + \boldsymbol{\delta}^{(C)},$$

$$\mathbf{A}_i^{(C)} = \begin{bmatrix} a_{11i} + \partial_{11i}^{(C)} & a_{12i} + \partial_{12i}^{(C)} & \cdots & a_{1ki} + \partial_{1ki}^{(C)} \\ a_{21i} + \partial_{21i}^{(C)} & a_{22i} + \partial_{22i}^{(C)} & \cdots & a_{2ki} + \partial_{2ki}^{(C)} \\ a_{31i} + \partial_{31i}^{(C)} & a_{32i} + \partial_{32i}^{(C)} & \cdots & a_{3ki} + \partial_{3ki}^{(C)} \\ \vdots & \vdots & \ddots & \vdots \\ a_{k1i} + \partial_{k1i}^{(C)} & a_{k2i} + \partial_{k2i}^{(C)} & \cdots & a_{kki} + \partial_{kki}^{(C)} \end{bmatrix} = \mathbf{A}_i + \partial_i^{(C)}, \tag{7}$$

$\mathbf{u}_t$ is an error vector of random variables with zero mean and covariance matrix $\boldsymbol{\Sigma}^{(C)}$ defined by

$$\begin{aligned} \boldsymbol{\Sigma}^{(C)} &= \begin{bmatrix} \sigma_{11}^2 + \psi_{11}^{(C)} & \sigma_{12} + \psi_{12}^{(C)} & \cdots & \sigma_{1k} + \psi_{1k}^{(C)} \\ \sigma_{21} + \psi_{21}^{(C)} & \sigma_{22}^2 + \psi_{22}^{(C)} & \cdots & \sigma_{2k} + \psi_{2k}^{(C)} \\ \sigma_{31} + \psi_{31}^{(C)} & \sigma_{32} + \psi_{32}^{(C)} & \cdots & \sigma_{3k} + \psi_{3k}^{(C)} \\ \vdots & \vdots & \ddots & \vdots \\ \sigma_{k1} + \psi_{k1}^{(C)} & \sigma_{k2} + \psi_{k2}^{(C)} & \cdots & \sigma_{kk}^2 + \psi_{kk}^{(C)} \end{bmatrix} \\ &= \boldsymbol{\Sigma} + \Psi^{(C)}, \end{aligned} \tag{8}$$

and C indicates the block condition (A or B). For simplicity, assume that

$$\delta_j^{(A)} = 0, \qquad \partial_{jli}^{(A)} = 0, \qquad \psi_{jl}^{(A)} = 0 \tag{9}$$

for $j = 1, 2, \ldots, k$, $l = 1, 2, \ldots, k$, $i = 1, 2, \ldots$, and $\delta_j^{(B)}$, $\partial_{jli}^{(B)}$, and $\psi_{jl}^{(B)}$ are the increments on the coefficients during B condition. If at least one of the coefficients $\delta_j^{(B)}$, $\partial_{jli}^{(B)}$, and $\psi_{jl}^{(B)}$ is nonzero, it implies the existence of structural changes. In other words, we have different coefficient matrices for each condition. Thus, we have a VAR structure for each block, but all the parameters are globally estimated, allowing a statistical test to the connectivity changes. The intervention VAR model can be estimated using an interactive generalized least-square estimator. Consider the following vector and matrices:

$$\begin{aligned} \mathbf{y} &= \operatorname{vec}(\mathbf{Y}_t), \\ \mathbf{X} &= \begin{bmatrix} \mathbf{1} & \mathbf{Y}_{t-1} & \mathbf{Y}_{t-2} & \cdots & \mathbf{Y}_{t-p} \end{bmatrix}, \\ \mathbf{Z} &= \mathbf{I}_k \otimes ([\mathbf{1} \quad \Delta] \otimes^R \mathbf{X}), \end{aligned} \tag{10}$$

where vec is an operator that concatenates all the columns of a matrix in a column vector, Δ is a vector of zeros and ones indicating the stimulus condition at time t (the tth element of Δ is zero/one if the acquisition at time t occurs during A/B condition), $\mathbf{1}$ is a column vector of ones, and $\otimes^R$ is the row-Kronecker product, which is defined as the Kronecker product applied separately for each row, that is,

$$\begin{bmatrix} a_1 \\ a_2 \\ \vdots \\ a_k \end{bmatrix} \otimes^R \begin{bmatrix} b_1 \\ b_2 \\ \vdots \\ b_k \end{bmatrix} = \begin{bmatrix} a_1 \otimes b_1 \\ a_2 \otimes b_2 \\ \vdots \\ a_k \otimes b_k \end{bmatrix}. \tag{11}$$

The error covariance matrix is given by $\boldsymbol{\Gamma}$. The generalized least-square estimator of the coefficients of the intervention VAR model is given by [14, 15]

$$\hat{\boldsymbol{\beta}} = \left(\mathbf{Z}'\boldsymbol{\Gamma}^{-1}\mathbf{Z}\right)^{-1}\mathbf{Z}'\boldsymbol{\Gamma}^{-1}\mathbf{y}. \tag{12}$$

However, as the covariance matrix $\boldsymbol{\Gamma}$ is unknown, we propose the use of an interactive two-stage least-square estimator. The residuals are estimated on the first step and the covariance matrix $\boldsymbol{\Gamma}$ on the second one, as an extension of the Cochrane-Orcutt procedure. The variances/covariances in $\boldsymbol{\Gamma}$

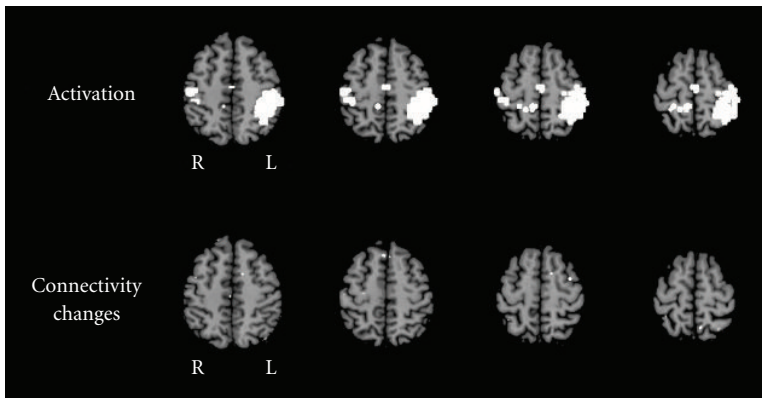

Figure 1: Group activation and connectivity changes maps for six subjects in a rest-fingertap block design paradigm. The connectivity changes map shows the voxels with significant changes in the information flow intensity from SMA, between rest and fingertap condition. The maps are presented on radiological convention.

may be consistently estimated considering the fits of an ordinary regression of squares/cross residuals as response and $[\mathbf{1} \quad \Delta]$ as model matrix. The Wald test statistic of linear combinations of parameter in $\boldsymbol{\beta}$ is given by

$$W = \frac{(\mathbf{C}\hat{\boldsymbol{\beta}} - \mathbf{m})' [\mathbf{C}(\mathbf{Z}'\boldsymbol{\Gamma}^{-1}\mathbf{Z})\mathbf{C}']^{-1} (\mathbf{C}\hat{\boldsymbol{\beta}} - \mathbf{m})}{\hat{\sigma}^2}, \tag{13}$$

where $\hat{\sigma}^2$ is the estimated residual variance, $\mathbf{m}$ is a vector, and $\mathbf{C}$ is a contrast matrix corresponding to the following test:

$$\begin{aligned} H_0 &: \mathbf{C}\boldsymbol{\beta} = \mathbf{m}, \\ H_A &: \mathbf{C}\boldsymbol{\beta} \neq \mathbf{m}. \end{aligned} \tag{14}$$

Under the null hypothesis, W has an asymptotic chi-square distribution with *rank* $(\mathbf{C})$ degrees of freedom [14]. Basically, this procedure performs simultaneous tests of the equality between $\mathbf{m}$ and linear combinations $(\mathbf{C})$ of parameters in $\boldsymbol{\beta}$. Note that the connectivity parameters can be easily tested considering the W statistic. Further, in case of non-Gaussian errors distribution, the martingales central limit theorem [16] implies that the classic asymptotic properties of the generalized least-square estimator are valid.

To finish this section, it is important to highlight some points about the application of the intervention VAR models to connectivity analysis in fMRI. Firstly, although Granger causality identification via VAR models is closely related to interactions, it cannot make a distinction between real influences or predictive power. Secondly, it is important to mention that this approach depends on sampling frequency. As Granger causality identification is based on information contained in past values, low sampling rates result in aliasing and data aggregation. In fact, sampling frequency represents a challenge for connectivity modeling in fMRI, as short acquisition time implies in low signal-to-noise ratio. On the other hand, neural interactions occur in a frequency much higher than fMRI acquisitions (TR). Thus, the connectivity structure identified via VAR models is only related to very low frequencies information, and fast interactions are not detected. Additionally, we would like to emphasize the point that although intervention model does not require the assumption of global stationarity, it depends on this assumption to be valid during each paradigm condition. The validity of this assumption is reasonable in block design paradigms, but it may not be true in event-related ones. The application of the proposed approach to fMRI data with event-related designs could result in an imprecise estimation, such as an average of the information flow intensity across the activation time-points.

3. APPLICATION TO REAL DATA

In order to illustrate the usefulness of the proposed approach, the intervention VAR modeling was applied to real fMRI data derived from a motor task study.

Six normal right-handed subjects performed a simple right hand fingertapping task, in an AB periodic block design experiment. The functional magnetic resonance images were acquired in a GE 1.5 T Signa LX MR system equipped with a 23 mT/m gradient, (TE: 40 milliseconds, TR: 2000 milliseconds, FA: 90°, FOV: 240 mm, 64×64 matrix; 15 slices, thickness: 7.0 mm, gap: 0.7 mm) oriented in the AC-PC plane in a single run. There were one hundred volumes collected during five cycles of rest-task performance. Each cycle had the duration of 40 seconds corresponding to 20 volumes, 10 volumes acquired during rest, and 10 volumes during the activation task. The subjects were in the dark room with noise-reducing headphones customized for functional MR. Instructions to begin and finish movements were given via auditory stimuli.

The images were preprocessed considering motion correction and spatial smoothing. The activation brain mapping was obtained using the XBAM software [17]. Spatial normalization transformation to the stereotatic space of Talairach and Tournoux [18] was performed using SPM2 [4]. Since the main interest was the study of motor function, the analyses were limited to the superior slices, reducing the number of multiple comparisons and consequently increasing the sensitivity of the statistical tests.

The group activation maps (cluster P value $< .01$) are presented in Figure 1 (top). Note that there are significant

activations found on the left primary and contralateral motor cortex (BA 4), supplementary and premotor areas (BA 6), and primary sensitive areas (BA 3, 2, 1), which are classically involved in motor control.

Taking into account a significant activation in the supplementary motor area (SMA), the intervention VAR analysis was performed in a bivariate fashion considering a seed in the activation local maxima of SMA against all other voxels in the whole brain. As changes in BOLD signal are not instantaneous, we considered a delay of 2 seconds in the condition specification. Statistical tests for differences in the information flow intensity from SMA to the voxel of interest, between rest and task, were performed in each individual separately. The individual W statistics were mapped to Gaussian quantiles, and the group analysis was performed in SPM2 (on-tailed t test, which is similar to a random effects analysis [4]). The connectivity changes map (voxel P value $< .005$) is presented in Figure 1 (bottom). The areas with significant changes in the information flow intensity from SMA were the premotor cortex, presupplementary motor area, and primary sensitive cortex.

The intervention VAR model was also applied in a trivariate analysis, considering the selected seed in SMA, and voxels (connectivity changes minimum P value) in the pre-motor cortex (PM) and pre-supplementary motor area (PSMA). In Figure 2 (top), diagrams (arrow P value $< .05$) describing the connectivity structure during rest and fingertap and also differences in information flow intensity are presented. The BOLD signals derived from selected ROI of one subject are presented in Figure 2 (bottom).

When contrasting fingertapping with rest we found significant changes in PM cortex, primary sensitive areas, and PSMA. All these areas are classically involved in movement control [19]. The current understanding of motor control in the literature suggests that PSMA provides the main input to SMA, which is possibly responsible for providing internal representation of movement sequences, and is involved in learning process of new movements. SMA is believed to send information to the PM and primary motor cortices, and is also associated with complex calculation to achieve maximum performance, based on feedback information from sensitive areas.

During the rest, we observed increased connectivity between the SMA and PM with pre-SMA. Some studies demonstrated that PSMA plays an important role in cognitive motor control, which involves sensory discrimination and movement decision making (go/nongo) or motor selection for the action after stimuli [20, 21]. In order to start the sequence of fingertapping, a motor decision must be made, based on the instruction previously given to the participant. All areas (pre-SMA, PM, and SMA) are involved in the initiation of movement and modification in their connectivity pattern might be explained by the attention to stimulus presentation and monitoring during the task.

4. CONCLUSION

Most connectivity studies results rely on analyzing second-order correlations that do not give additional information about neural interactions. Other advanced methods like structural equation modeling (SEM) or dynamic causal models (DCM) could be an attractive alternative. However, they heavily depend on a prior knowledge about involved neural circuitry.

Granger causality concept, in its most general form, is a flexible definition of relationship and temporal order. It could be tested by a simple VAR modeling without any connectivity prespecification. In this paper, we introduced a new approach for connectivity modeling based on Granger causality and intervention VAR models, which enabled us to compare differences in connectivity structures as a statistical hypothesis test. An initial application of intervention VAR models to fMRI data produced biologically plausible results, but further experiments are necessary to reveal its potential as a new tool to investigate neural systems.

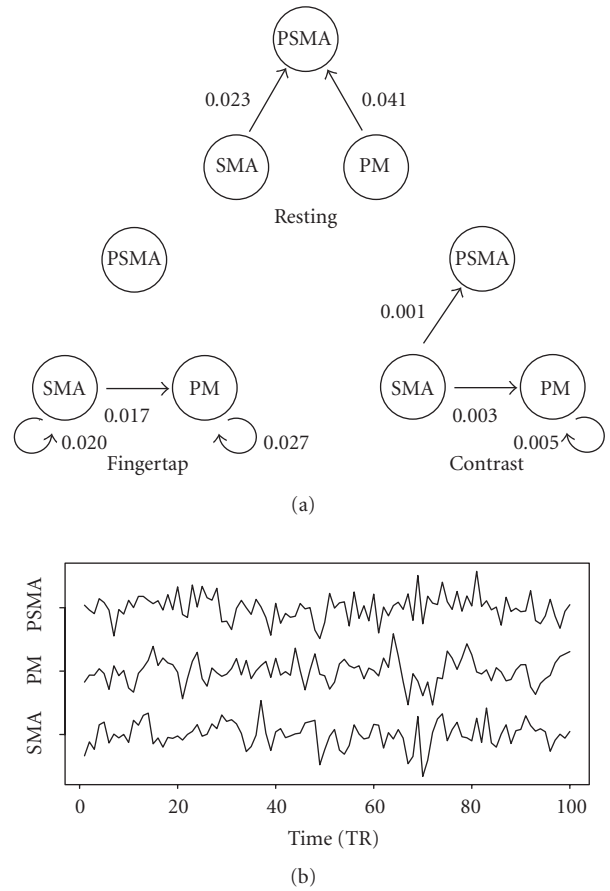

Figure 2: Group connectivity structure during resting, fingertapping, and information flow changes between these two conditions (top). The numbers in the arrows describe the information flow correspondent P value. An illustrative chart of ROI's BOLD signals of one subject is also presented.

ACKNOWLEDGMENT

This research was supported by FAPESP (03/10105-2) and CNPq (142616/2005-2), Brazil.

REFERENCES

[1] S. Ogawa, T.-M. Lee, A. S. Nayak, and P. Glynn, "Oxygenation-sensitive contrast in magnetic resonance image of rodent brain at high magnetic fields," *Magnetic Resonance in Medicine*, vol. 14, no. 1, pp. 68–78, 1990.

[2] C. Büchel and K. J. Friston, "Modulation of connectivity in visual pathways by attention: cortical interactions evaluated with structural equation modelling and fMRI," *Cerebral Cortex*, vol. 7, no. 8, pp. 768–778, 1997.

[3] B. Biswal, F. Z. Yetkin, V. M. Haughton, and J. S. Hyde, "Functional connectivity in the motor cortex of resting human brain using echo-planar MRI," *Magnetic Resonance in Medicine*, vol. 34, no. 4, pp. 537–541, 1995.

[4] R. S. J. Frackowiak, K. J. Friston, C. Frith, et al., *Human Brain Function*, Academic Press, San Diego, Calif, USA, 2nd edition, 2003.

[5] J. Zhuang, S. LaConte, S. Peltier, K. Zhang, and X. Hu, "Connectivity exploration with structural equation modeling: an fMRI study of bimanual motor coordination," *NeuroImage*, vol. 25, no. 2, pp. 462–470, 2005.

[6] J. B. Rowe, K. E. Stephan, K. Friston, R. S. J. Frackowiak, and R. E. Passingham, "The prefrontal cortex shows context-specific changes in effective connectivity to motor or visual cortex during the selection of action or colour," *Cerebral Cortex*, vol. 15, no. 1, pp. 85–95, 2005.

[7] K. J. Friston, J. Ashburner, C. D. Frith, J.-B. Poline, J. D. Heather, and R. S. J. Frackowiak, "Spatial registration and normalization of images," *Human Brain Mapping*, vol. 3, no. 3, pp. 165–189, 1995.

[8] C. W. J. Granger, "Investigating causal relations by econometric models and cross-spectral methods," *Econometrica*, vol. 37, no. 3, pp. 424–438, 1969.

[9] L. A. Baccalá, K. Sameshima, G. Ballester, A. C. Do Valle, and C. Timo-laria, "Studying the interaction between brain structures via directed coherence and Granger causality," *EURASIP Journal on Applied Signal Processing*, vol. 5, no. 1, pp. 40–48, 1998.

[10] L. A. Baccalá and K. Sameshima, "Partial directed coherence: a new concept in neural structure determination," *Biological Cybernetics*, vol. 84, no. 6, pp. 463–474, 2001.

[11] R. Goebel, A. Roebroeck, D.-S. Kim, and E. Formisano, "Investigating directed cortical interactions in time-resolved fMRI data using vector autoregressive modeling and Granger causality mapping," *Magnetic Resonance Imaging*, vol. 21, no. 10, pp. 1251–1261, 2003.

[12] A. Roebroeck, E. Formisano, and R. Goebel, "Mapping directed influence over the brain using Granger causality and fMRI," *NeuroImage*, vol. 25, no. 1, pp. 230–242, 2005.

[13] M. J. Kamiński, M. Ding, W. A. Truccolo, and S. L. Bressler, "Evaluating causal relations in neural systems: Granger causality, directed transfer function and statistical assessment of significance," *Biological Cybernetics*, vol. 85, no. 2, pp. 145–157, 2001.

[14] F. A. Graybill, *Theory and Application of the Linear Model*, Buxbury Press, Boston, Mass, USA, 1976.

[15] H. Lütkepohl, *Introduction to Multiple Time Series Analysis*, Springer, New York, NY, USA, 1993.

[16] P. K. Sen and J. M. Singer, *Large Sample Methods in Statistics - An Introduction with Applications*, Chapman and Hall, New York, NY, USA, 1980.

[17] M. J. Brammer, E. T. Bullmore, A. Simmons, et al., "Generic brain activation mapping in functional magnetic resonance imaging: a nonparametric approach," *Magnetic Resonance Imaging*, vol. 15, no. 7, pp. 763–770, 1997.

[18] J. Talairach and P. Tournoux, *A Co-Planar Stereotaxic Atlas of the Human Brain*, Thieme, Stuttgart, Germany, 1988.

[19] E. R. Kandel, J. H. Schwartz, and T. M. Jessell, *Principles of Neural Science*, McGraw-Hill Medical, New York, NY, USA, 4th edition, 2000.

[20] A. Ikeda, S. Yazawa, T. Kunieda, et al., "Cognitive motor control in human pre-supplementary motor area studied by subdural recording of discrimination/selection-related potentials," *Brain*, vol. 122, no. 5, pp. 915–931, 1999.

[21] M. Humberstone, G. Sawle, S. Clare, et al., "Functional MRI of single motor events," *Annals of Neurology*, vol. 42, no. 4, pp. 632–637, 1997.

João Ricardo Sato is a statistician and Ph.D. student. The main areas of his research are time series analysis and neuroimaging. Nowadays, he has been working at the Neuroimaging Laboratory of the University of São Paulo, Brazil.

Daniel Yasumasa Takahashi is pursuing graduate studies in bioinformatics, Bioinformatics Graduate Program, University of São Paulo, Brazil. His major interest is the application of mathematical techniques to the investigation of interaction between neural populations, which underlies important cognitive tasks.

Ellison Fernando Cardoso is a medical doctor (radiologist) and Ph.D. student. His work is focused on fMRI studies in patients with Parkinson's disease and major depressive disorder.

Maria da Graça Morais Martin is a medical doctor in Brazil. She graduated from the University of São Paulo Medical School (1992–1997), where she also completed her Radiology Residency (1998–2000). She held a Research Fellowship in fMRI at the University of California San Diego (2004-2005). Her research is focused on fMRI studies, and she is now a Ph.D. student on an fMRI normative database.

Edson Amaro Júnior is an Associate Professor of radiology, and lecturer at the postgraduate program in the Department of Radiology - HCFMUSP and Experimental Neuropsychology - USP. His areas of interest include clinical fMRI, local normative database, DBS in Parkinson's, Parkinson's and depression, ALS and early Alzheimer's disease. Related to these projects he is also supervising a number of doctoral students. Experiment design strategies and methods to deal with the scanner acoustic noise are the main areas of interest. Administrative job includes coordination of the Laboratory for Functional Neuroimaging (NIF), LIM 44, clinical reports in MR and CT scans, and teaching basic MRI to medical students.

Pedro Alberto Morettin received a Ph.D. degree in statistics from the University of California, Berkeley. He is a Professor of statistics at the Department of Statistics, University of São Paulo, Brazil. His interests are in the area of time series analysis and applications to medicine, physical sciences, economics, and finance.

Hindawi Publishing Corporation
International Journal of Biomedical Imaging
Volume 2006, Article ID 94025, Pages 1–8
DOI 10.1155/IJBI/2006/94025

Virtual Contrast for Coronary Vessels Based on Level Set Generated Subvoxel Accurate Centerlines

Ingmar Bitter,[1] Robert Van Uitert,[1] Ivo Wolf,[2] Efstathia Tzatha,[3] Ahmed M. Gharib,[3] Ronald Summers,[1] Hans-Peter Meinzer,[2] and Roderic Pettigrew[3]

[1] *Diagnostic Radiology Department, Clinical Center, National Institutes of Health, Bethesda, MD 20892-1182, USA*
[2] *Division of Medical and Biological Informatics, German Cancer Research Center, Heidelberg 69120, Germany*
[3] *National Heart Lung and Blood Institute, National Institutes of Health, Bethesda, MD 20892-2281, USA*

Received 31 January 2006; Revised 30 May 2006; Accepted 6 June 2006

We present a tool for tracking coronary vessels in MRI scans of the human heart to aid in the screening of heart diseases. The vessels are identified through a single click inside each vessel present in a standard orthogonal view. The vessel identification results from a series of computational steps including eigenvalue analysis of the Hessian of the MRI image followed by a level set-based extraction of the vessel centerline. All identified vessels are highlighted using a virtual contrast agent and displayed simultaneously in a spherical curved reformation view. In cases of over segmentation, the vessel traces can be shortened by a click on each vessel end point. Intermediate analysis results of the vessel computation steps can be displayed as well. We successfully validated the tool on 40 MRI scans demonstrating accuracy and significant time savings over manual vessel tracing.

1. INTRODUCTION

Coronary artery disease (CAD) is one of the leading causes of mortality and morbidity in the USA and other industrialized nations [1]. Although conventional cardiac angiography remains the "gold standard" for the evaluation of CAD, it is an invasive procedure that is associated with morbidity (1.5%) and mortality (0.15%) risks [2]. Coronary CT angiography (CTA) is emerging as a promising noninvasive alternative [3]. However, this technology requires patient exposure to substantial amounts of radiation [4] and potentially nephrotoxic contrast agents as in conventional angiography. As a result, coronary magnetic resonance angiography (CMRA) provides a more patient friendly option for CAD assessment [5] without the use of contrast agents and radiation. Unfortunately, currently the MRI image signal-to-noise ratios and the maximally achievable resolution are not as high as for CTA. This complicates the process of identifying the vessels and MRA targeted vessel segmentation and analysis tools usually fail. Thus, the common solution is still time consuming, manual vessel tracing. Our research presents an MRI coronary identification software tool that is able to track and intuitively display the MRI data along all three main coronary vessels. A typical screenshot of the software is presented in Figure 1.

A core component of the system is the computation of a centerline for each vessel. As the vessels are only a few voxels thick, it is important to compute the vessel centerlines at subvoxel accuracy. They must also be inherently smooth to yield a smooth display of the vessel in the spherical curved reformation view.

The next section describes the technical background of our methods followed by related work and a description of the novel methods used in our system. We conclude with showing and discussing results acquired with our software.

2. BACKGROUND

Many automatic and semiautomatic skeletonization techniques compute the centerline of an object on the voxel grid with optional subsequent smoothing [6–16]. These discrete centerline solutions are inappropriate for vessels that are only a few voxels thick. Subsequent smoothing may displace the centerline from the vessel center and is thus inappropriate as well. Another method [17] computes the centerline as a minimum cost B-spline. This delivers an inherently smooth centerline, but is computationally expensive due to the explicit global optimization. The same holds for [18], which iteratively computes a globally optimized NURBS curve that locally minimizes the vessel cross sections perpendicular to

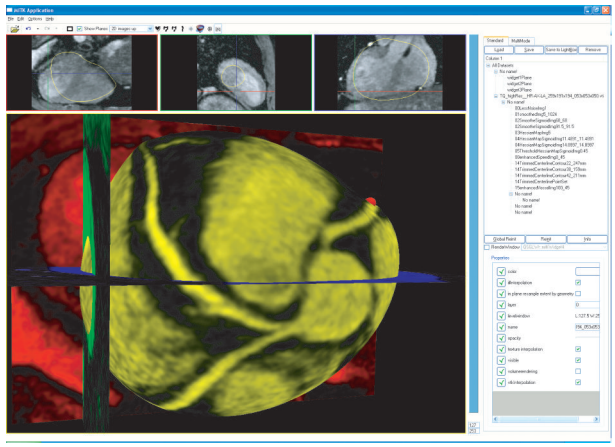

Figure 1: A screenshot of the MRI coronary vessel tracking tool with axial (red), sagittal (green), coronal (blue), and spherically fitted "thin plate spline" (yellow) 3D views showing all three main coronaries virtually enhanced.

the curve. In contrast, our prior centerline algorithm efficiently and automatically extracts a smooth, continuous centerline directly at subvoxel precision [19]. Our algorithm is based on level sets. Level set methods evolve an isosurface in the direction of the surface normal [20]. In its general form the evolution speed can depend on position, normal direction, curvature, and shape; and the isosurface can cross over the same point multiple times. In our centerline method the evolution speed is always positive and depends only on position. Hence, its boundary front moves only outwards. With these restrictions the isosurface can be represented by an Eikonal equation:

$$|\nabla T|F = 1, \quad T = 0 \text{ on } \Gamma, \tag{1}$$

where T is the arrival time function, F is the speed of evolution function, and Γ is the initial isosurface at time zero.

An efficient method to numerically evaluate the solution to the Eikonal equation is the fast marching method [20]. It processes the voxels in a sorted order based on increasing values of T. The fast marching method calculates a time crossing map, which indicates for each pixel how much time it would take for the level set front to arrive at the pixel location. The evolution only needs to be computed on a rectilinear grid. However, values at nongrid locations can be interpolated from these grid positions properly to simulate the true propagation value.

Several other centerline methods based on level sets have been previously presented [10–12]. One approach [10] computes centerlines by first detecting medial axis points at the locations where the level set fronts collide and form sharp discontinuities. However, the level sets are only computed on two dimensional cross-sections of the three dimensional data, which are not identical to the 3D discontinuities. Next, the algorithm performs topological thinning and filling in of gaps with voxels along straight lines which may not result in positions on the skeleton. Other methods [11, 12] make use of the full 3D data in its level set propagation and guarantee a minimum cost, discrete solution, but as pointed out before, do not extract the centerline with subvoxel accuracy. In addition, algorithms [6–10] require a segmentation of the vessel as input. In our images it is very difficult to segment the vessels accurately and completely. Hence, we were looking for an algorithm that does not require a segmented vessel as input. An algorithm that is subvoxel accurate and does not require vessel segmentation is presented in [21]. It directly traverses the centerline along ridges in a Hessian medialness measure, but it performs a sequence of local greedy decisions that do not guarantee a globally optimal solution. The methods in [11–17, 21] use Hessian matrix analysis to track a vessel with having to segment its boundaries first. Computing the Hessian at different scales proved to be beneficial for vessels varying greatly in thickness, but was not necessary for our data. Table 1 lists the prior methods and classifies them according to the main algorithm ideas. In [22], 94 vessel extraction algorithms are compared: only 50% of them do compute an explicit centerline, only one uses level set methods, but not for centerline tracking and only one uses Hessian eigenvalues, but not in combination with level sets. Our proposed algorithm combines the benefits of the previous methods without their shortcomings. It can find minimum cost, subvoxel accurate centerlines of thin vessels without the need of first segmenting them.

2.1. Subvoxel accurate centerline algorithm

The most closely related prior algorithm is our input segmentation dependent, subvoxel accurate centerline algorithm [19]. It uses a level set segmentation of the vessel to obtain a subvoxel accurate surface and a Euclidean distance transform of the object. This distance transform is then used as a speed image in a fast marching level set method with propagation starting at the global maximum point of the distance transform. The fast marching method propagation is augmented to calculate the geodesic distance in addition to the time crossing map. The furthest geodesic point from the global maximum point is used as the start point of the vessel centerline and the remaining points of the centerline are determined by performing a gradient descent on the time crossing map with a subvoxel step size.

The algorithm presented in this paper is an extension of this previous method, which handles the absence of vessel segmentation and improves upon the computation speed of the level set propagation.

2.2. Vessel enhancement

In order to track thin vessels without an explicit representation, we found it necessary to process the MRI images using vessel enhancing image filters. Given the eigenvalues $\lambda_3 \leq \lambda_2 \leq \lambda_1$ of the 3×3 Hessian matrix for each 3D image pixel, it is possible to compute a likelihood of the pixel being part of a linear structure [23, 24]. This measure, which we

Table 1: Comparison of ideas used in various vessel centerline computation methods. "+" stands for the best idea within a group, "0" for average, and "−" for the least desirable idea in a group.

Vessel centerline computation reference	[6–10]	[11]	[17]	[18]	[12]	[13]	[14, 15]	[16]	[19]	This paper
2D						−	−			
2D and 3D	+	+	+	+	+			+	+	+
Prior vessel segmentation required	−								−	
Vesselness from intensity only		−								
Vesselness from Hessian eigenvalues			+	+	+	+	+	+		+
Path cost from segmentation distance map	−								−	
Path cost from vesselness		0			0		0			0
Path cost from multiscale vesselness			+			+	+	+		
Discrete cost propagation	−					−	−	−		
Level set wave cost propagation		+			+				+	+
Centerline extraction as minimum cost B-spline			0							
Centerline as minimum vessel cross-section NURBS				0						
Discrete centerline, optional post smoothing	−	−			−	−	−	−		
Smooth centerline (wave gradient decent)									+	+
Computation only for the most obvious path										+

call *vesselness* (v), is defined as

$$v = \begin{cases} |\lambda_3| \cdot \psi(\lambda_2;\lambda_3) \cdot \omega(\lambda_1;\lambda_2) & \forall \lambda_3 \le \lambda_2 < \lambda_1, \\ 0 & \text{otherwise} \end{cases} \quad (2)$$

with

$$\psi(\lambda_2;\lambda_3) = \begin{cases} \left(\frac{\lambda_2}{\lambda_3}\right)^{\gamma} & \forall \lambda_3 \le \lambda_2 < 0, \\ 0 & \text{otherwise,} \end{cases} \quad (3)$$

$$\omega(\lambda_1;\lambda_2) = \begin{cases} \left(1 + \frac{\lambda_1}{|\lambda_2|}\right)^{\gamma} & \forall \lambda_2 \le \lambda_1 < 0, \\ \left(1 + \frac{\alpha\lambda_1}{|\lambda_2|}\right)^{\gamma} & \forall \frac{|\lambda_2|}{\alpha} > \lambda_1 > 0, \\ 0 & \text{otherwise} \end{cases} \quad (4)$$

and $\alpha = 1/4$ and $\gamma = 1/2$.

This *vesselness* v has been used before to improve visualizations of linear structures [23, 24], but we are using it to assist in vessel tracking. However, other similar equations have been used for vessel identification before [25].

2.3. Curved reformation vessel view

A good vessel centerline can be used to create a curved reformation vessel view. One such method is to stretch the vessel and display its surroundings with as little distortion as possible [26]; however this is not appropriate for a view that is supposed to include multiple vessels. The "soap bubble" method [27] allows projection of multiple vessels to a plane, preserving the relationship of the vessels to each other, but for roughly spherically arranged vessels, the projected vessels may overlap or surrounding tissue may be severely distorted. We use the spherical curved reformation method [28], which eliminates the problems of the "soap bubble" method for the specific case of coronary vessels. It achieves this through projecting a spherical approximation of the heart onto the vessels with little distortion, followed by a standard globe unrolling onto a rectangular view as done for any world map. The minimal distortion is the consequence of minimizing the energy of a "thin plate spline" being fit to the vessel points [28].

3. METHODS

While the system is designed to look at all vessels at once, processing is done one vessel at a time. The user identifies each vessel initially by clicking on one landmark point for each vessel.

3.1. Vessel centerline computation

The vessel centerline computation results from a series of computational steps (Figure 2). Initially, noise removal is performed on the MRI data by using edge preserving anisotropic diffusion filtering. Next, the intensities are normalized through a sigmoid window whose parameters are

(1) Remove noise
(2) Place landmark A inside vessel
(3) Normalize intensities
(4) Compute vesselness
(5) Sigmoid vesselness to speed image
(6) Propagate wave to spearhead start
(7) Propagate spearhead wave
(8) Autocreate landmark B at end
(9) Back trace partial centerline to A
(10) Intensify speed image on centerline
(11) Propagate wave to spearhead start
(12) Propagate spearhead wave
(13) Autocreate landmark C at end
(14) Back trace full centerline to B
(15) Create spherical reformation
(16) Crop vessel end points to D and E
(17) Repeat for other vessels

Figure 2: Steps of the algorithm needed to track and display vessels.

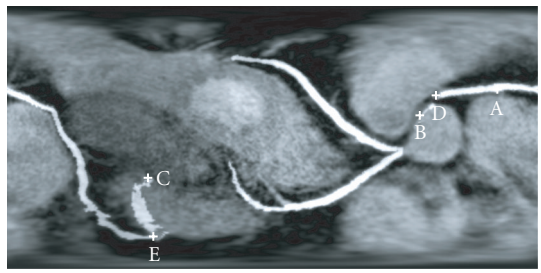

Figure 3: Landmark A is initially manually placed inside the vessel. Landmarks B and C are automatically placed by the algorithm. Vessel end points D and E are manual corrections of points B and C which are placed on the curved view without the need to scroll through multiple images.

determined from the MRI intensity I at the first landmark point (A in Figure 3) which must be inside the vessel and is assumed to be the maximum intensity in the local neighborhood. The width of the sigmoid window is equal to I and the center is at I/2. Subsequently the vesselness, v, is computed for each pixel in the image by (2) from the Hessian matrix of the image. The partial derivatives that form the Hessian matrix are a result of convolving the smoothed MRI image with the derivatives of a Gaussian with 3σ covering 2 mm, which is the median of the expected vessel diameter. This vesselness map is then normalized using a sigmoid window. Again the window parameters are relative to the landmark point (width = $\tilde{o}$, center = $\tilde{o}/2$), which maximizes the contrast in the transition region. Values in the normalized vesselness map are clamped to zero if they are less than 33% of the maximum value. The clamp threshold and σ were determined empirically for a single dataset and applied for all others.

This resulting *vesselness* map (middle image in Figure 4) is used as a speed function for a fast marching level set method that starts at the initial vessel landmark point A. However, instead of computing the fast marching through the complete image or at least until the entire vessel is covered (as in [11]), the computations are stopped when a point 1 cm from the landmark point is reached. Due to the nature of the *vesselness* computation, the highest speed values are found in the center of the vessel, and thus the point first reached at 1 cm distance (larger than the vessel radius) must be central to the vessel. This point is then defined as the "spearhead point." The fast marching method is now continued, but only newly discovered points that are within 1 cm of the "spearhead point" are allowed to be added to the evolving surface of the fast marching method. Each time a new furthest geodesic distance point is found, the "spearhead point" is updated. Consequently, only a small band of voxels along the vessel is involved in the computation. When the modified fast marching method has processed all of the points in the connected object, the final "spearhead point" is the most distant trackable vessel point. This becomes the second, automatic landmark point (B in Figure 3). The steepest gradient decent from the second to the first landmark point yields a partial vessel centerline. This centerline is not based on local greedy decisions, but is the minimum cost path with respect to the given *vesselness* speed image. Next, the speed image is intensified along this partial vessel. With the updated speed image, the above described fast marching method is started from the second automatic landmark. Again, only a small band of voxels along the vessel are involved in the computation. When the second fast marching method algorithm completes, the resulting "spearhead point" becomes the third, automatic landmark point (C in Figure 3). Intensifying the speed image along the first partial centerline is necessary to guarantee that the initial path of the second fast marching does not detour into a vessel branch. Finally, the steepest gradient decent from the third (C) to the second (B) landmark point yields the complete vessel centerline (Figure 5).

Once the centerline is computed, a virtual contrast dataset can be created. The virtual contrast dataset has the original data as its basis, but each pixel is intensified that is within 2 mm (expected vessel radius) of the computed centerline and also has at least 33% of the maximal vesselness intensity in the initial speed image.

The above process can be repeated for each of the desired vessels. After the centerline for each vessel has been computed, a new spherical curved reformation can be generated from all current vessel centerlines. The length of each of the vessels is displayed on the graphical user interface. In order to be able to bridge areas of stenosis or low signal, short (< 1 cm) sections of low *vesselness* (below 33% of the maximum intensity value) are allowed, as long as the tracking can be continued with more obvious *vesselness* pixels after the gap. Unfortunately, this sometimes also causes the tracking to go beyond the vessel ends into other nearby vessels or to jump onto the edge of the heart, which may not be totally suppressed in the speed image. In this case, the curved reformation view can be used

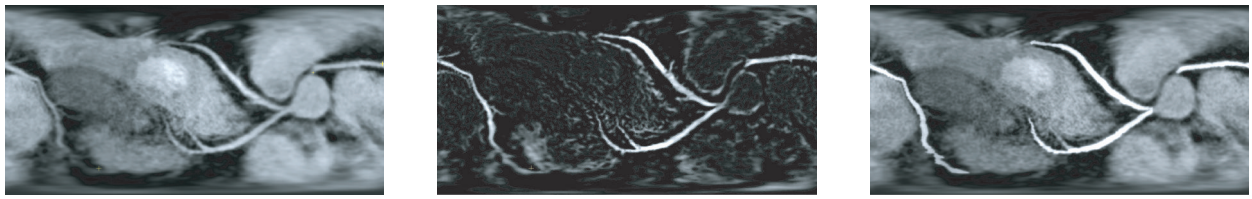

(a) (b) (c)

Figure 4: Three key steps along the processing pipeline: smoothed image, vesselness map speed image, and virtual contrast image.

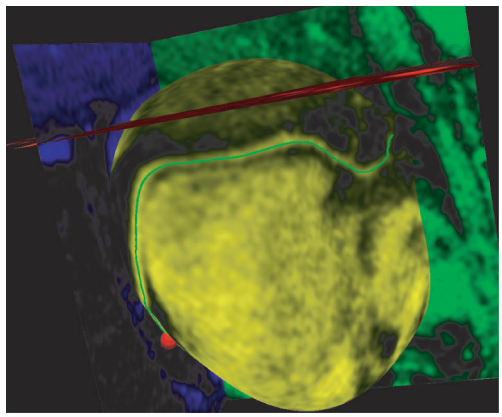

Figure 5: Spherical reformation with superimposed vessel centerline.

to allow the user to manually relocate the second and/or third landmark point to the desired vessel endpoint(s) (D and E in Figure 2). The system then adjusts the centerline to only cover the vessel between these updated vessel end points. System validation was based on visual assessment of completeness of the tracked vessels, partial success was defined as a section of the vessel being visible in the scan, but not tracked. The scanning protocols used for the validation were (A) standard imaging parameter, (B) shortened acquisition window, (C) isotropic acquisition voxel resolution, (D) short-axis plane aligned with the right coronary artery.

4. RESULTS

The algorithm presented was validated on 40 MRI cardiac scans with volume sizes of $512 \times 512 \times 100$ to $512 \times 512 \times 300$ containing 0.5×0.5 mm images with 0.5 to 1 mm spacing in the z-direction. The data came from 10 volunteers scanned each with four scanning protocols. The right coronary artery (RCA) was found completely for 90% of the volunteers on two protocols (A, B), for the other protocols 80% (B) and 70% (D) of the MRI scans had completely tracked vessels. For the incomplete scans it was possible to complete them by treating the missed vessel section as a new vessel. Figure 3 shows some intermediate and final results.

Completing the interactive part of the vessel tracking was accomplished within one minute. On a professional medical image analysis workstation a trained radiologist took 2.5 minutes to hand segment a vessel via coarse contours on every third slice that were then interpolated by the system.

5. DISCUSSION

The results in Figures 1, 3, and 5 show spherical curved reformations of the three main coronary arteries. In this example for two arteries joined near the aorta a single landmark was sufficient, but for the third both endpoints needed to be corrected. In either case, the user interaction time required is minimal when compared to manual vessel tracking.

All numerical parameters listed in this algorithm degrade gracefully. A 10% change of the parameter value has only a small impact on the final result, but doubling or halving it usually significantly shortens the identification of vessel segment.

The novelty of this research is two fold. First, it lies in the creation of a time saving tool that combines the idea of semi-automatic tracking with spherical curved reformation. Second, it improves over prior work on the method of finding the vessel centerline. Due to the low signal-to-noise ratio on the MRI input images, the *vesselness* map is a network of mutually connected vessels and pseudovessels. Following all branches as done in [10] frequently results in automatically found vessel end landmarks that are very far from the intended vessel end. The restriction of expanding the fast marching only near the "spearhead point" allows for a much more intuitive behavior of the algorithm. The manual clipping of the traced path to only the portion within the vessels is easily performed on the spherical curved reformation view and no scrolling through slices is needed.

6. CONCLUSIONS

This paper has presented a semi-automatic algorithm for determining centerlines of the main coronary vessels and its application to creating virtual contrast enhanced MRI scans that are displayed in an intuitive spherical curved reformation view. The method can track vessels even in the presence of low signal-to-noise ratios, is subvoxel accurate, and is more computationally efficient than previous methods.

REFERENCES

[1] AHA, "Heart Disease and Stroke Statistics-2005 Update," 2005, http://www.americanheart.org/.

[2] L. W. Johnson, R. Krone, M. J. Cowley, et al., "Cardiac catheterization 1991: a report of the Registry of the Society for Cardiac Angiography and Interventions (SCA and I)," *Catheterization and Cardiovascular Diagnosis*, vol. 28, no. 3, pp. 219–220, 1993.

[3] S. Schroeder, A. Kuettner, T. Beck, et al., "Usefulness of noninvasive MSCT coronary angiography as first-line imaging technique in patients with chest pain: initial clinical experience," *International Journal of Cardiology*, vol. 102, no. 3, pp. 469–475, 2005.

[4] C. H. McCollough, "Patient dose in cardiac computed tomography," *Herz*, vol. 28, no. 1, pp. 1–6, 2003.

[5] W. Y. Kim, P. G. Danias, M. Stuber, et al., "Coronary magnetic resonance angiography for the detection of coronary stenoses," *New England Journal of Medicine*, vol. 345, no. 26, pp. 1863–1869, 2001.

[6] I. Bitter, M. Sato, M. Bender, K. T. McDonnell, A. Kaufman, and M. Wan, "CEASAR: a smooth, accurate and robust centerline extraction algorithm," in *Proceedings of the IEEE Visualization Conference*, pp. 45–52, Salt Lake City, Utah, USA, October 2000.

[7] I. Bitter, A. E. Kaufman, and M. Sato, "Penalized-distance volumetric skeleton algorithm," *IEEE Transactions on Visualization and Computer Graphics*, vol. 7, no. 3, pp. 195–206, 2001.

[8] Y. Zhou and A. W. Toga, "Efficient skeletonization of volumetric objects," *IEEE Transactions on Visualization and Computer Graphics*, vol. 5, no. 3, pp. 196–209, 1999.

[9] D. Chen, B. Li, Z. Liang, M. Wan, A. Kaufman, and M. Wax, "Tree-branch searching, multiresolution approach to skeletonization for virtual endoscopy," in *Medical Imaging 2000: Image Processing*, vol. 3979 of *Proceedings of SPIE*, pp. 726–734, San Diego, Calif, USA, February 2000.

[10] A. Telea and A. Vilanova, "A robust level-set algorithm for centerline extraction," in *Symposium on Visualization (VisSym '03)*, pp. 185–194, Grenoble, France, May 2003.

[11] T. Deschamps and L. D. Cohen, "Fast extraction of minimal paths in 3D images and applications to virtual endoscopy," *Medical Image Analysis*, vol. 5, no. 4, pp. 281–299, 2001.

[12] O. Wink, A. F. Frangi, B. Verdonck, M. A. Viergever, and W. J. Niessen, "3D MRA coronary axis determination using a minimum cost path approach," *Magnetic Resonance in Medicine*, vol. 47, no. 6, pp. 1169–1175, 2002.

[13] O. Wink, W. J. Niessen, and M. A. Viergever, "Multiscale vessel tracking," *IEEE Transactions on Medical Imaging*, vol. 23, no. 1, pp. 130–133, 2004.

[14] E. Meijering, M. Jacob, J. C. F. Sarria, and M. Unser, "A novel approach to neurite tracing in florecence microscopy images," in *Proceedings of the 5th LASTED International Conference on Signal and Image Processing*, pp. 491–495, Honolulu, Hawaii, USA, August 2003.

[15] E. Meijering, M. Jacob, J. C. F. Sarria, P. Steiner, H. Hirling, and M. Unser, "Neurite tracing in fluorescence microscopy images using ridge filtering and graph searching: principles and validation," in *IEEE International Symposium on Biomedical Imaging: Macro to Nano*, vol. 2, pp. 1219–1222, Arlington, Va, USA, April 2004.

[16] C. M. Van Bemmel, M. A. Viergever, and W. J. Niessen, "Semiautomatic segmentation and stenosis quantification of 3D contrast-enhanced MR angiograms of the internal carotid artery," *Magnetic Resonance in Medicine*, vol. 51, no. 4, pp. 753–760, 2004.

[17] A. F. Frangi, W. J. Niessen, P. J. Nederkoorn, J. Bakker, W. P. T. M. Mali, and M. A. Viergever, "Quantitative analysis of vascular morphology from 3D MR angiograms: in vitro and in vivo results," *Magnetic Resonance in Medicine*, vol. 45, no. 2, pp. 311–322, 2001.

[18] W. Cai, F. Dachille, and M. Meissner, "Centerline optimization using vessel quantification model," in *Medical Imaging 2005—Physiology, Function, and Structure from Medical Images*, vol. 5746 of *Proceedings of SPIE*, no. II, pp. 796–803, San Diego, Calif, USA, February 2005.

[19] R. Van Uitert and I. Bitter, "Subvoxel Accurate Skeletons of Volumetric Data Based on Level Sets," submitted.

[20] J. A. Sethian, *Level Set Methods and Fast Marching Methods: Evolving Interfaces in Computational Geometry, Fluid Mechanics, Computer Vision, and Materials Science*, Cambridge University Press, Cambridge, UK, 1999.

[21] S. R. Aylward and E. Bullitt, "Initialization, noise, singularities, and scale in height ridge traversal for tubular object centerline extraction," *IEEE Transactions on Medical Imaging*, vol. 21, no. 2, pp. 61–75, 2002.

[22] C. Kirbas and F. Quek, "A review of vessel extraction techniques and algorithms," Tech. Rep., Vision Interfaces and Systems Laboratory (VISLab), Department of Computer Science and Engineering, Wright State University, Dayton, Ohio, USA, 2002.

[23] A. Huang, G. M. Nielson, A. Razdan, G. E. Farin, D. P. Baluch, and D. G. Capco, "Thin structure segmentation and visualization in three-dimensional biomedical images: a shape-based approach," *IEEE Transactions on Visualization and Computer Graphics*, vol. 12, no. 1, pp. 93–102, 2006.

[24] Y. Sato, C.-F. Westin, A. Bhalerao, et al., "Tissue classification based on 3D local intensity structures for volume rendering," *IEEE Transactions on Visualization and Computer Graphics*, vol. 6, no. 2, pp. 160–180, 2000.

[25] W. Cai, F. Dachille, H. Yoshida, and G. Harris, "Fast, interactive segmentation of vessel in computed-tomographic angiography (CTA) images using selective vesselness-priority region-growing method," in *Radiological Society of North America (RSNA '05)*, McCormick, Chicago, November-December 2005, LPL09-06.

[26] A. Kanitsar, D. Fleischmann, R. Wegenkittl, and E. Grooller, "Diagnostic relevant visualization of vascular structures," in *IEEE Visualization*, Boston, Mass, USA, October-November 2002.

[27] A. Etienne, R. M. Botnar, A. M. C. Van Muiswinkel, P. Boesiger, W. J. Manning, and M. Stuber, ""Soap-Bubble" visualization and quantitative analysis of 3D coronary magnetic resonance angiograms," *Magnetic Resonance in Medicine*, vol. 48, no. 4, pp. 658–666, 2002.

[28] I. Wolf, M. Hastenteufel, I. Wegner, et al., "Curved reformations using the Medical Imaging Interaction Toolkit (MITK)," in *Medical Imaging 2005—Visualization*, vol. 5744 of *Proceedings of SPIE*, no. II, pp. 831–838, San Diego, Calif, USA, February 2005.

Ingmar Bitter received the Ph.D. degree in computer science from the State University of New York at Stony Brook, in 2002. He then led the virtual colonoscopy and 3D medical visualization development as Director of Research and Development at Viatronix Inc, NY. Subsequently, he researched computer-aided detection of colon polyps as well as automated segmentation of blood vessels in CT and MRI as a Staff Scientist at the Diagnostic Radiology Department at the Warren G. Magnuson Clinical Center at the NIH, Bethesda, MD. Currently, he is Lead Engineer, Algorithmics at Claron Technology Inc., where he leads the R&D on efficient and effective CT analysis and interpretation software. He has coauthored over 40 scientific articles and is coinventor on 3 issued and 6 pending patents.

Robert Van Uitert received the B.S. degree in computer science from Stanford University, Stanford, CA, in 1998 and the Ph.D. degree in computer science from the University of Utah, Salt Lake City, UT, in 2004. He is currently a Staff Scientist in the Diagnostic Radiology Department of the Clinical Center at the National Institutes of Health. His research interests are in the field of medical image processing and analysis. His particular interests include the use of image processing for computer-aided detection and diagnosis of disease.

Ivo Wolf received the M.S. degree in physics in 1999 and the Ph.D. degree in medical informatics in 2003 from the University of Heidelberg. He is working as a Senior Scientist at the Division of Medical and Biological Informatics at the German Cancer Research Center. His research interests include image segmentation, quantitative image analysis for diagnosis support, software engineering methods to facilitate the transfer of medical image processing techniques into clinically useful software, and navigation systems.

Efstathia Tzatha received her B.S. degree in medical imaging from the Technological Institution of Athens, Greece, in 1999 and her M.D. degree from the University of Athens, in 2004. She was a Research Fellow at the National Institutes of Health (2004–2006) and she is currently pursuing further training in medical residency at Georgetown University Hospital. Her interests include assessment of coronary atherosclerosis with MR and molecular imaging.

Ahmed M. Gharib received his M.B., Ch.B. (Bachelor of Medicine and Surgery) degree from the Faculty of Medicine, the University of Alexandria, Egypt, in November 1993. Following this he served an internship in Internal Medicine at the University of Washington; a residency in Nuclear Medicine and Nuclear Cardiology at the University of Washington; and a residency in Diagnostic Radiology at the University of Louisville before joining the Johns Hopkins Hospital for Cross-Sectional Imaging fellowship for training in Cardiac and body MRI, CT in addition to ultrasound. He then joined the National Institutes of Health as a staff Radiologist, where he focused his research effort on molecular and anatomic imaging of atherosclerosis. He is certified by the American Board of Radiology.

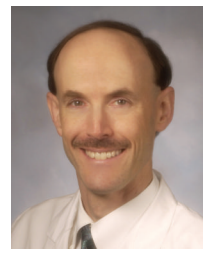

Ronald Summers received the B.A. degree in physics and the M.D. and Ph.D. degrees in medicine/anatomy & cell biology from the University of Pennsylvania. He completed a medical internship at the Presbyterian, University of Pennsylvania Hospital, Philadelphia, PA, a radiology residency at the University of Michigan, Ann Arbor, MI, and an MRI fellowship at Duke University, Durham, NC. In 1994, he joined the Diagnostic Radiology Department at the Warren G. Magnuson Clinical Center at the NIH, Bethesda, MD, where he is now a Senior Investigator and Staff Radiologist. He is currently Chief of the Clinical Image Processing Service and directs the Virtual Endoscopy and Computer-Aided Diagnosis (CAD) Laboratory. In 2000, he received the Presidential Early Career Award for Scientists and Engineers, presented by Dr. Neal Lane, President Clinton's science advisor. His research interests include virtual colonoscopy, CAD, and development of large radiologic image databases. His clinical areas of specialty are thoracic and gastrointestinal radiology, and body cross-sectional imaging. He Cochairs the special session on virtual endoscopy at the annual SPIE Medical Imaging Conference. He has coauthored over 100 journal articles, reviews, and conference proceedings articles.

Hans-Peter Meinzer is a Scientist at the German Cancer Research Center since 1974, is directing a 3D visualization of 3D tomographies research team since 1983. In this context he works on modeling and simulating tissues and tissue kinetics, neural nets, AI, human perception, cognitive texture analysis, morphology, segmentation, visualization, and medical imaging in general. He obtained at Karlsruhe University an M.S. (physics) and a B.S. (economics) degrees in 1973. At Heidelberg University Meinzer received a doctorate in medical computer science (formal languages) (1983) and habilitation (cell growth simulation) (1987) and is a Professor for medical computer science since 1999. Since 2000 Meinzer is the director of the Department of Medical and Biological Informatics at the German Cancer Research Center in Heidelberg. He is annually co-organizing the German Workshop on Medical Imaging "Bildverarbeitung fuer die Medizin". He won several scientific awards from the German Society of Heart Surgery (1992), the German Society of Pattern Recognition (1993), and the European Commission (1997 and 2003), twice the "European Information Technology Prize." Meinzer founded and directs the Steinbeis-Transferzentrum Medizinische Informatik (STZ-MI) in 1994, a software company specializing in telemedicine and teleradiology. In 2003 he cofounded Chili GmbH, a spin-off company for PACS, teleradiology, web-based image distribution.

Roderic Pettigrew graduated cum laude from Morehouse College with a B.S. degree in physics; earned an M.S. degree in nuclear medicine and engineering from Rennselear Polytechnic Institute; and as Whitaker Harvard-MIT Health Science Scholar a Ph.D. degree in applied radiation physics from the Massachusetts Institute of Technology, and earned an M.D. from the University of Miami, School of Medicine. He did his internship and residency in internal medicine at Emory University and completed a residency in nuclear medicine at the University of California, San Diego. Dr. Pettigrew spent a year as a Clinical Research Scientist with Picker International. In 1985, he joined Emory as a Robert Wood Johnson Foundation Fellow. Dr. Pettigrew, a Member of Phi Beta Kappa, is the Recipient of the Bennie Award (Benjamin E. Mays) for Achievement in 1989, and was named the Most Distinguished Alumnus of the University of Miami, in 1990. He has served as Chairman of the Diagnostic Radiology Study Section, Center for Scientific Review, NIH, and is an elected Fellow of the American Heart Association, the American College of Cardiology, The International Society of Magnetic Resonance in Medicine, The American Institute of Medical and Biological Engineering, and the Biomedical Engineering Society.

Hindawi Publishing Corporation
International Journal of Biomedical Imaging
Volume 2006, Article ID 12186, Pages 1–10
DOI 10.1155/IJBI/2006/12186

Probabilistic Model-Based Cell Tracking

Nezamoddin N. Kachouie,[1] Paul Fieguth,[1] John Ramunas,[2] and Eric Jervis[2]

[1] *Department of Systems Design Engineering, University of Waterloo, Waterloo, Ontario, Canada N2L 3G1*
[2] *Department of Chemical Engineering, University of Waterloo, Waterloo, Ontario, Canada N2L 3G1*

Received 3 February 2006; Revised 28 April 2006; Accepted 12 May 2006

The study of cell behavior is of crucial importance in drug and disease research. The fields of bioinformatics and biotechnology rely on the collection, processing, and analysis of huge numbers of biocellular images, including cell features such as cell size, shape, and motility. However manual methods of inferring these values are so onerous that automated methods of cell tracking and segmentation are in high demand. In this paper, a novel model-based cell tracker is designed to locate and track individual cells. The proposed cell tracker has been successfully applied to track hematopoietic stem cells (HSCs) based on identified cell locations and probabilistic data association.

1. INTRODUCTION

Recent advances in cell culture and cell imaging have made possible the automated acquisition of millions of cell images. The corresponding automation of the analysis of such huge sets of images would allow fundamentally new questions to be addressed in proteomics, genomics, and stem-cell research [1–8]. This paper proposes a coupling of advanced methods in pattern recognition and image processing [9–16] to an existing cell-imaging platform [17] in which the analysis, currently being undertaken by hand, is impossibly slow and tedious for the volumes of data being generated.

The object of this particular project is the analysis of stem-cell behavior and differentiation, the process by which stem cells specialize to different cell types, a process which is crucial to understand if stem cells are to be used in cell and tissue regeneration. Specifically, given a culture of cells, observed over time, we need some way of determining whether a given cell is likely to die, to cause cancer, to specialize into an incorrect tissue type, or, desirably, to specialize into the correct cell type.

The first major step in this process, and the end goal of the research described in this paper, is the automated construction of cell lineage trees, essentially the descendent family tree of a single ancestor cell, as illustrated in Figure 1. Building such a tree for each of multiple cells in a culture requires maintaining cell identity over time, clearly requiring the tracking and associating of cells over a long sequence of images, typically 7000 images taken over a period of several days.

2. PROBLEM FORMULATION

Although cell tracking is among the most important and common tasks for biomedical researchers it continues to be undertaken manually. Researchers visually perform cell motion analyses and observe cell movement or changes in cell shape for hours to discover when, where, and how fast a given cell moves, divides, or dies. This task is tedious due to the often corrupted or blurred images, the presence of clutter, the fixing of eyes for long periods of time, and repeating the same task for different cell types. Furthermore, with imaging data ever more simply and rapidly acquired, manual tracking becomes progressively impractical. As a result, automated cell tracking systems are mandatory to further advance the study of biological cells [2, 3, 6, 8, 18–20].

To produce the data for this study, HSC samples are first extracted from mouse bone marrow, then cultured in custom arrays having up to forty wells. A small fraction of a typical HSC microscopic image is depicted in Figure 2 with the superimposed dynamics of a mature blood stem cell before and after splitting. The cells were imaged using manual focusing through a 5X phase contrast objective using a digital camera (Sony XCD-900) and acquired by an IEEE 1394 standard (FireWire) connector. Images were sampled every three minutes over the course of several days.

To keep cells alive and healthy, light exposure must be controlled during their life cycle to minimize phototoxicity. Therefore it is desired to limit light exposure in each frame and to sample the frames as far apart as possible, leading to infrequent, poorly contrasted images, directly at odds with

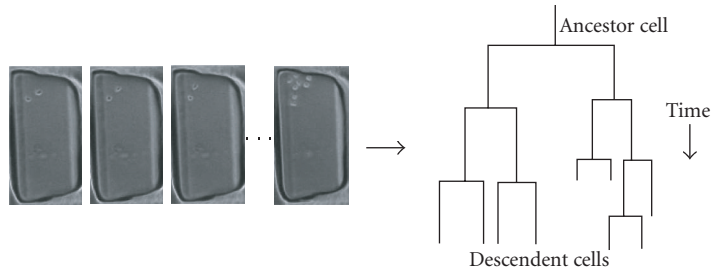

Figure 1: An image sequence (a) showing cell (small light circles) movement and division over time. A lineage tree (b) may be generated by detecting cell splitting and associating individual cells from image to image.

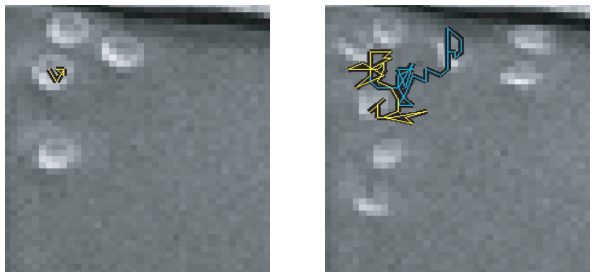

Figure 2: Close-up of an HSC phase contrast microscopic image with the superimposed track of one mature blood stem cell (a) 8 frames before and (b) 30 frames after splitting.

Figure 3: (a) 8 by 8 pixel detail of an HSC phase contrast microscope image. (b) A circular idealized cell model.

the data desired for easy tracking: frequent, high-contrast images. Cell staining techniques may be used to increase the contrast between cell and background, however different parts of tissue are undesirably stained unevenly, causing inhomogeneity. Fortunately the HSCs in our study have fairly regular shape and brightness patterns. Hence, a segmentation method which exploits these attributes should be able to perform better than simple thresholding.

Suppose we have an image sequence $I_{1:K} = \{I_1, I_2, \ldots, I_K\}$. The two fundamental tasks needed to construct a lineage tree, such as in Figure 1, are the detection of cells in each image and the subsequent association of the detected cells over time. The cell detection problem is essentially one of anomaly detection: the localization of groups of pixels inconsistent with the random behavior of the image background. A wide variety of semi automatic or automatic methods have been proposed to segment cell boundaries [2, 3] which can be divided into three major categories.

(1) Boundary based, generally employing deformable models such as snakes [7].
(2) Region based, such as split and merge [21], morphological operators [22], watershed [6], and region growing methods [23].
(3) Threshold based [8, 24, 25] applied to some extracted image feature.

We can make the problem much more specific by seeking particular features consistent with HSCs. From Figures 2 and 3(a), HSCs can be characterized as an approximately circular object with a darker interior and a brighter boundary—an effect due to phase contrast imaging modality. So rather than a heuristic thresholding approach, these cell attributes allow a more specific model, essentially a matched filter, more robust to noise and to low contrast. The model depicted in Figure 3(b) considers the following criteria:

(i) cell size: the radius r is known to lie in a limited range related to cell age;
(ii) boundary brightness: brighter due to phase contrast imaging;
(iii) interior brightness: tends to be dimmer than the boundary;
(iv) boundary uniformity or symmetry: want to assert uniformity to avoid a strong response when straddling cells, as shown in Figure 4.

As depicted in Figure 3(b), to model a dark region surrounded by a bright boundary, the proposed cell model consists of two concentric circles, with the radius of the internal circle being half that of the external one. To facilitate the analysis of the image as a function of cell center location (x_c, y_c) and radius r we construct the set of boundary pixels

$$B(x_c, y_c, r, I) = \left\{ I_{ij} \mid \left| (x_c - i)^2 + (y_c - j)^2 - r^2 \right| \leq \left(\frac{1}{2}\right)^2 \right\}, \quad (1)$$

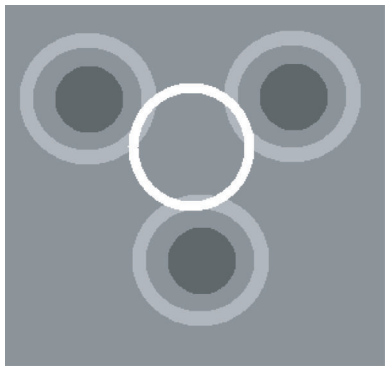

Figure 4: A scenario in which a spuriously hypothesized (white) boundary may have a large associated average brightness $\overline{B}$ and a low cell interior brightness $\overline{C}$. The uniformity constraint in the cell boundary is intended to address this case.

and the set of interior cell pixels

$$C(x_c, y_c, r, I) = \left\{ I_{ij} \mid (x_c - i)^2 + (y_c - j)^2 \leq \left(\frac{r}{2}\right)^2 \right\}, \tag{2}$$

from which we extract sample means

$$\overline{B} = \frac{\sum_i B_i}{|B|}, \qquad \overline{C} = \frac{\sum_i C_i}{|C|}, \tag{3}$$

where B_i or C_i is the ith element of the respective set.

The four cell criteria are then combined to formulate the following probabilistic cell model:

$$P(x_c, y_c, r \mid I_k) = P_{cb}(\overline{B}) \cdot P_{ci}(\overline{C}) \cdot P_{bu}(B), \tag{4}$$

where the cell boundary P_{cb}, cell interior P_{ci}, and boundary uniformity P_{bu} terms are elaborated below.

Based on a visual examination of the distribution of sample points of $\overline{B}$ derived from real imagery, the probability density of cell boundary P_{cb} is modeled as Gaussian with mean μ_{cb} and variance σ_{cb}^2

$$P_{cb}(\overline{B}) \sim N(\overline{B}; \mu_{cb}, \sigma_{cb}^2), \tag{5}$$

where μ_{cb} and σ_{cb}^2 are estimated empirically.

Similarly the probability density of dark region inside the cell P_{ci} is also modeled as Gaussian with mean μ_{ci} and variance σ_{ci}^2

$$P_{ci}(\overline{C}) \sim N(\overline{C}; \mu_{ci}, \sigma_{ci}^2), \tag{6}$$

where μ_{ci} and σ_{ci}^2 are again estimated empirically.

It should be mentioned that the parameters of model (4) are time invariant, consistent with most of our acquired data sets. Therefore in cases where the intensity or contrast of the image changes over time due to background noise or spatiotemporal illumination variations, the nonstationarity of the data might make (4) in error or inapplicable. In such cases, to improve the robustness of the proposed method, the time variations of the image sequence need to be removed by background estimation and subtraction, considered in future work.

As illustrated in Figure 4 we wish to penalize spurious cell detection. We propose to calculate an empirical cumulative density function (CDF) to discriminate background from cell boundary. The CDF on cell boundary pixel intensities is computed by

$$\mathrm{cdf}_n(B) = \frac{\sum_{i=1}^{n} B_i}{|B| \cdot \overline{B}}, \quad n \in 1 : |B|. \tag{7}$$

As a set of constant or uniform values in B corresponds to a straight line CDF, we use a Kolmogorov-Smirnov test on B to test its deviation from uniformity:

$$D(\mathrm{cdf}) = \max_{n \in [1:N]} \left| \mathrm{cdf}_n - \frac{n}{N} \right|. \tag{8}$$

An exponential function $P_{bu}(D)$ is used to penalize the nonuniformity as

$$P_{bu}(D) = \exp\{-2 \cdot N \cdot D(\mathrm{cdf})\}. \tag{9}$$

This completes the development of a simple model for the detection of cells in background noise. We will use the model to generate and test cell hypotheses in the following section.

3. CELL TRACKING

With a model in place describing the spatial pattern of pixels with the appearance of a cell, we move to the core of the problem: given a sequence of images $I_{1:K} = \{I_1, I_2, \ldots, I_K\}$ and a definition of our "target" (the cell model (4)), we need to associate the cells over time. Denote by $F_{1:K}$ a possible hypothesis of the K-frame association problem,

$$F_{1:K} = \{f_1, f_2, \ldots, f_K\}, \tag{10}$$

where f_k is a parametric representation of frame k. In the case of HSCs, f_k is defined as

$$f_k = \{(l_{k,j}, z_{k,j}, r_{k,j}, s_{k,j}),\ 1 \leq j \leq M_k\}, \tag{11}$$

where $l_{k,j}$ is the cell parent label, $z_{k,j}$ is the cell coordinate (x_c, y_c), $r_{k,j}$ is the radius, $s_{k,j}$ is the cell age corresponding to cell j, and M_k is the number of cells in frame k. The parent label $i = l_{k,j}$ associates cell j in frame k to parent cell i in the previous frame. The goal is to solve the spatiotemporal cell segmentation-association problem of Figure 5: we wish to estimate $F_{1:K}$ given the image sequence $I_{1:K}$ and given an initialization f_0 in frame zero.

3.1. MAP estimation

The proposed solution to the association problem is the maximum a posteriori estimation of $F_{1:K}$:

$$\hat{F}_{1:K} = \arg\max_{F_{1:K}} P(F_{1:K} \mid I_{1:K}, f_0). \tag{12}$$

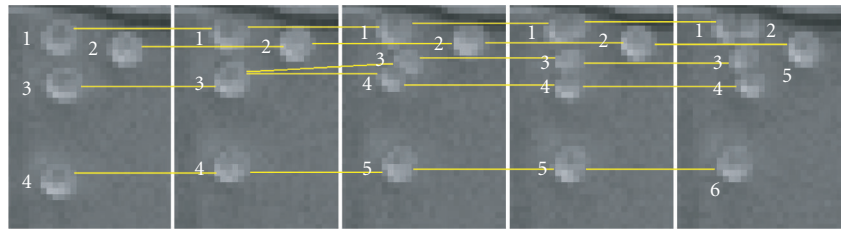

Figure 5: An illustration of cell association over time with numeric labels.

From Bayes' rule,

$$\begin{aligned} P(F_{1:K}, I_{1:K}, f_0) &= P(F_{1:K} \mid I_{1:K}, f_0) P(I_{1:K}, f_0) \\ &= P(I_{1:K} \mid F_{1:K}, f_0) P(F_{1:K}, f_0). \end{aligned} \tag{13}$$

As $P(I_{1:K}, f_0)$ is fixed, $\hat{F}_{1:K}$ does not depend on it, thus

$$P(F_{1:K} \mid I_{1:K}, f_0) \propto P(I_{1:K} \mid F_{1:K}, f_0) P(F_{1:K}, f_0). \tag{14}$$

At the same time $P(f_0)$ is fixed

$$P(F_{1:K}, f_0) = P(F_{1:K} \mid f_0) P(f_0) \propto P(F_{1:K} \mid f_0). \tag{15}$$

So we conclude that

$$\hat{F}_{1:K} = \arg\max_{F_{1:K}} P(I_{1:K} \mid F_{0:K}) \cdot P(F_{1:K} \mid f_0). \tag{16}$$

Since $F_{1:K} = \{f_1, f_2, \ldots, f_K\}$, the solution to (16) is realized, in principle, by examining and evaluating all possible cell parameterizations and associations. In virtually all tracking problems of this kind the problem is made tractable by searching over a limited number of hypotheses

$$\{F^h_{1:K} \mid h = 1, 2, \ldots\} \tag{17}$$

such that we find the best member of this set

$$\begin{aligned} &\hat{F}_{1:K} = F^{\hat{h}}_{1:K}, \\ &\text{where } \hat{h} = \arg\max_h P(I_{1:K} \mid F^h_{0:K}) \cdot P(F^h_{1:K} \mid f_0). \end{aligned} \tag{18}$$

The original, optimal solution is found if it is included among the hypotheses, that is, if

$$\arg\max_{F_{1:K}} P(F_{1:K} \mid I_{1:K}, f_0) \in \{F^h_{1:K}\}. \tag{19}$$

The key, here, to efficiency is to minimize the number of hypothesis; the key to quality of estimation is finding the most likely hypothesis. As these goals are in opposition, we are left with a complexity/quality tradeoff.

3.2. Evaluation of $P(I_{1:K} \mid F^h_{1:K})$

The proposed cell model $P(x_c, y_c, r \mid I_k) = P(z_c, r \mid I_k)$ from (4) evaluates the likelihood of a single cell, given an image. To solve the MAP problem we need to compute $P(I_{1:K} \mid F_{1:K})$, the likelihood of a given image sequence as a function of a specified cell parametrization and association. Since f_k provides a complete paramerized description of I_k, conditioned on $F_{1:k}$, $I_{1:k}$ is Markov:

$$P(I_{1:K} \mid F_{1:K}) = \prod_{k \in [1,K]} P(I_k \mid f_k). \tag{20}$$

The cell model (4) describes only the likelihood of a single cell; it says nothing about groups of cells, nor does it provide any kind of prior on z_c or r. Fortunately these latter aspects are straightforward.

(1) As the cells may be located anywhere with no prior bias, z_c is uniformly distributed over the image.
(2) We empirically define a size range $r \in [2, 4]$ pixels, within which the cell radius is uniformly distributed.
(3) Any hypothesis which has cells violating the minimum required separation between cells is assigned a probability of zero.

It follows, then, that as long as zero-probability hypotheses are not created, then all remaining hypotheses $\{f^h_k\}$ are equally likely a priori. Because $P(I_k)$ is fixed, and moreover because all valid hypotheses are equally likely, such that $P(z_c, r)$ is constant, we can conclude

$$P(I_k \mid z_c, r) \propto P(z_c, r \mid I_k), \tag{21}$$

implying that the evaluation of $P(I_k \mid z_c, r)$ can follow from evaluating $P(z_c, r \mid I_k)$. The proposed parametric cell model can be applied to each image frame I; a two-dimensional probability map is generated, and hypothesised cells are located at local maxima of this map. Although our cell model allows this probability map to be computed as a function of r for each $r \in [r_a, r_b]$, we have found that a value of $r_\circ = 2$ functions robustly. The locations of local maxima in $P(z \mid I, r_\circ)$ may either be used in the generation of hypotheses from I, or in computing $P(I \mid f)$, to assess an asserted cell arrangement.

First, to generate possible measurement hypotheses from I, find the spatial local maxima of $P(z)$ and keep only those maxima such that the likelihood of the ith maximum $P(z_{k,i} \mid I_k, r_\circ) > \tau$. Choosing T values of τ thus generates T sets of maxima, each a hypothesised measurement set for frame k,

$$z^\tau_k = \{z_{k,i} \mid P(z_{k,i} \mid I_k, r_\circ) > \tau,\ \tau \in [\tau_1, \tau_2]\}. \tag{22}$$

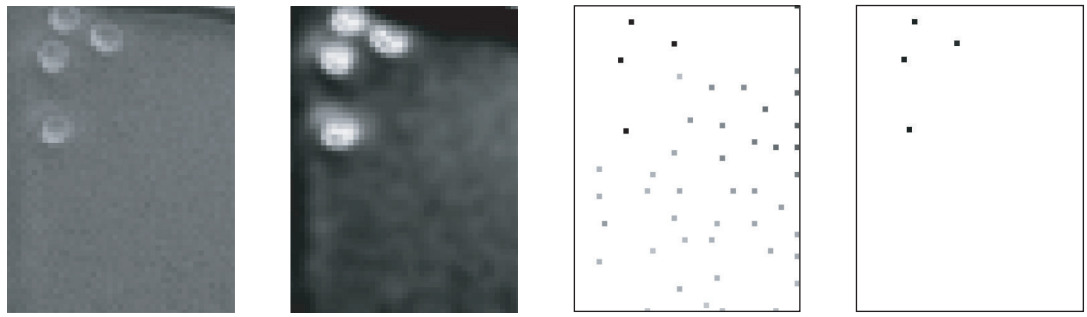

(a) (b) (c) (d)

FIGURE 6: (a) Microscope image I. (b) Probability map $P(z \mid I, r_\circ)$ obtained by applying cell model (4). (c) Local maxima of $P(z \mid I, r_\circ)$. (d) Thresholding the local maxima map.

We have found that a fixed threshold $\tau = 0.65$ works effectively for the HSC data set being considered here however, in general multiple τ would be used, leading to multiple measurement hypotheses.

Second, to compute $P(I \mid f)$ as depicted in Figure 7 the cells in f are divided into two sets:

(1) f_M: those cells in f which are located within δD of a maximum;
(2) $f_{\overline{M}}$: those cells in f which are not within δD of a maximum.

A third set contains the unmatched maxima:

(3) $\overline{f}_M$: those maxima which are not within δD of any point in f.

f_M contains the successful matches, $f_{\overline{M}}$ and $\overline{f}_M$ the failed ones. The fit between I_k and f_k^h is thus quantified as

$$P(I_k \mid f_k^h) = \left[\prod_{j \in f_M} P(z_{k,j} \mid I_k, r_\circ)\right] \cdot \left[\prod_{i \in \overline{f}_M} (1 - P(z_{k,i}^\tau \mid I_k, r_\circ))\right] \cdot \left[\prod_{j \in f_{\overline{M}}} P(z_{k,j} \mid I_k, r_\circ)\right], \tag{23}$$

where $P(z_{k,j} \mid I_k, r_\circ)$ is the probability of the location of the jth cell in the state f_k^h for frame k, and $P(z_{k,i}^\tau \mid I_k, r_\circ)$ is the probability of the ith maximum in frame k. As depicted in Figure 7, $P(I_k \mid f_k^h)$ is evaluated by applying (23).

3.3. Evaluation of $P(F_{1:K}^h \mid f_0)$

The second part of (18) is the evaluation of association hypotheses $\{F_{1:K}^h\}$. To track the HSCs over time, detected cells in the measurement hypothesis of the current frame z_k^τ must be associated to the most probable element in the previous frame.

Considering that for each image frame k, we associate cell features from $(k-1)$ only, Markovianity can be asserted on $F_{1:K}$ such that

$$P(F_{1:K} \mid f_0) = \prod_{k \in [1,K]} P(f_k \mid f_{k-1}), \tag{24}$$

where we recall that f_k is the set of cell properties in frame k. The cell age $s_{k,j}$ is updated as

$$s_{k,j} = \begin{cases} 1 & \text{if } \exists m \text{ such that, } l_{k,m} = l_{k,j} \\ & \text{(i.e., cell split),} \\ (s_{(k-1),l_{k,j}}) + 1 & \text{otherwise.} \end{cases} \tag{25}$$

Each cell in f_k must belong to one of the following sets.

Unassociated: $N = \{j \mid l_{k,j} = 0\}$.
Split: $S = \{j \mid l_{k,j} = l_{k,m} \text{ for } m \neq j\}$.
Regular: $R = \{j \mid j \notin \{N \cup S\}\}$.

In contrast with joint probabilistic data association (JPDA) [26–28] in which new tracks can not be initiated, our proposed method initiates new tracks for divided cells, therefore the following constraints are considered:

(i) each measurement must originate from cell or clutter;
(ii) each measurement can be associated to one cell;
(iii) up to two measurements in frame k can be associated to the same cell in frame $k-1$.

Asserting Markovianity we evaluate $P(f_k^h \mid f_{k-1}^h)$ in thef rest of this section. The association problem is resolved frame by frame by selecting the hypothesis with the maximum joint association probability. In this way the measurement hypothesis z_k^τ for frame k and association hypothesis f_{k-1}^h from the previous frame are used to generate hypotheses f_k^h. Therefore we have

$$P(f_k^h \mid f_{k-1}^h) = P(f_k^h \mid z_{1:k}^\tau, f_{k-1}^h) = P(f_k^h \mid z_k^\tau, f_{k-1}^h). \tag{26}$$

The filter step is

$$P(f_k^h \mid f_{k-1}^h) = P(f_k^h \mid z_{1:k}^\tau, f_{k-1}^h) = \frac{P(f_k^h \mid z_{1:k-1}^\tau) \cdot P(z_k^\tau \mid f_k^h)}{P(z_k^\tau \mid z_{1:k-1}^\tau)}, \tag{27}$$

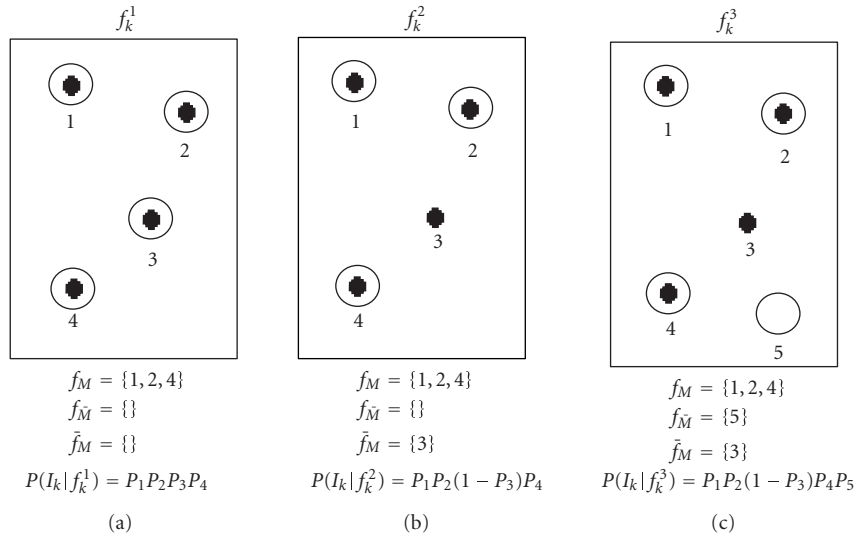

FIGURE 7: Having 4 maxima (solid dots), and 3 hypothesized sets of cells (large circles), for each hypothesis f_M, $f_{\bar{M}}$, and $\overline{f}_M$ are illustrated and then $P(I_k \mid f_k^h)$ is evaluated.

$P(z_k^\tau \mid z_{1:k-1}^\tau)$ is fixed and we have

$$P(f_k^h \mid f_{k-1}^h) = \lambda_k \cdot P(f_k^h \mid z_{1:k-1}^\tau) \cdot P(z_k^\tau \mid f_k^h), \tag{28}$$

where λ_k is a normalization constant. The first term of (28), $P(f_k^h \mid z_{1:k-1}^\tau)$, is a prediction step which is illustrated as follows. Because of the nonlinear and non-Gaussian nature of both measurements and dynamics, in contrast with JPDA, the Kalman filter is not considered for the prediction step. The prediction step in the proposed method is

$$\begin{aligned} P(f_k^h \mid z_{1:k-1}^\tau) &= \int P(f_k^h \mid f_{k-1}^h) P(f_{k-1}^h \mid z_{1:k-1}^\tau) df_{k-1}^h \\ &= \left[\prod_{j \in R \cup S} P_{\text{vel}}(z_{k,j}, z_{k-1,l_{k,j}}^\tau) \right] \\ &\quad \cdot \left[\prod_{j \in S} P_{\text{state}}(s_{k-1,j}) \right]. \end{aligned} \tag{29}$$

The former term P_{vel} is a nonlinear term to predict the location of the hypothetical cell j in frame k based on its dynamics and its location in frame $k-1$. The motion will be cell-type specific, and may further be influenced by environmental factors, chemical gradients, and so forth. In our context there are no deliberate experimental biases, and a Gaussian random walk was found to well-approximate hand-tracked cell motion. The latter term P_{state} predicts the likelihood of cell division in frame k. An age penalty such that cell division cannot happen below some age; this minimum age is cell-type specific and is asserted from biological experience.

The second term of (28), $P(z_k^\tau \mid f_k^h)$, is the likelihood of measurement z_k^τ given hypothesis f_k^h and is given by

$$\begin{aligned} P(z_k^\tau \mid f_k^h) = &\left[\prod_{j \in R \cup S} N(v_{k,j}, 0, S_{k,j}) \right] \\ &\cdot [P_{\text{sep}}(f_k^h)] \cdot \left[\prod_{j \in N} P_{\text{una}} \right], \end{aligned} \tag{30}$$

where $v_{k,j} = z_{k,i}^\tau - \hat{z}_{k,j}$ is an innovation term so that the ith measurement is within δD of the jth hypothesised cell location in frame k. P_{una} is a penalty on the association of unassociated cells, and P_{sep} is the probability of separation distance of a measurement pair. As we can see in the proposed method, the likelihood of measurement $z_{k,j}$ is penalized by the unlikely events such as minimum separation distance and unassociated cells.

4. EXPERIMENTAL RESULTS

We begin by evaluating the proposed cell model. The model generates cell hypotheses, as illustrated in Figure 6, where candidate cells are found as local maxima in $P(x_c, y_c, r) = P(z_c, r)$. Because of the availability of hand-labelled ground-truth data, a good assessment of cell detection is possible. The only unknown parameter in cell detection is τ, the probability threshold in declaring a cell present. Figure 8 shows the probability of false alarm and missed detection as a function on the chosen threshold τ_h over a sequence of HSC phase contrast microscope images. It is clear that a threshold yielding acceptably low failures of both types is $\tau = 0.65$.

Next, Figures 9 and 10 test the number of detected cells (using $\tau = 0.65$) and the detected spatial locations with manual ground truth. The greatest probability of misdetection

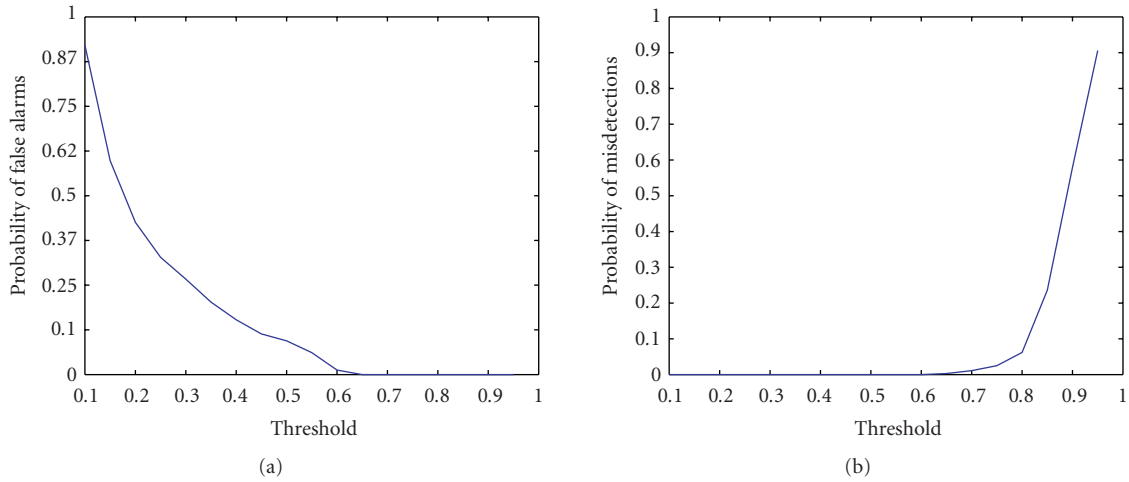

Figure 8: (a) Variation of the probability of false alarm as a function of the threshold τ_h. (b) Variation of the probability of missed detection as a function of the threshold τ_h.

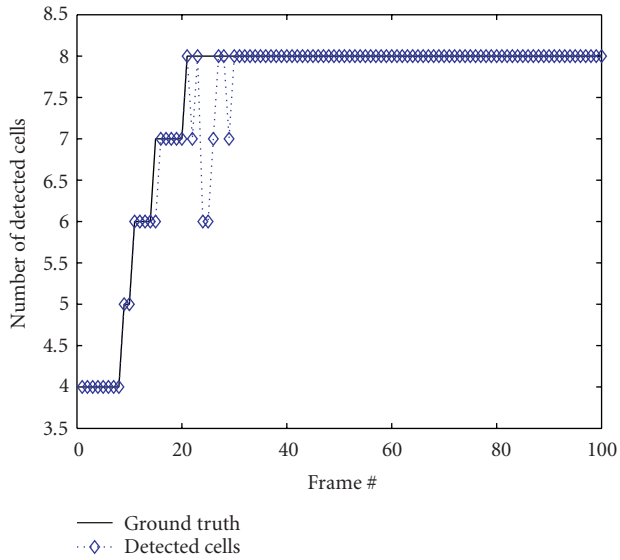

Figure 9: A comparison of ground truth (solid line) and the detected cells on the basis of the proposed cell model (dashed line).

occurs during division where a mature cell gives rise to two new cells. During division, notable between frames 9 to 29, the cells are inconsistent with a circular shape with a fixed radius. However, the divided cells are recognized as soon as the division process is completed, which takes at most five frames. As it can be seen in Figure 10, the maximum cell center spatial error is 1.8 pixels per cell. Considering the fact that manual ground truth is prone to error, the results obtained by the proposed method are very promising.

Results obtained by applying the proposed probabilistic cell tracking method are depicted in Figure 11. Cell centers are detected by applying the cell model (4), locating the local maxima in the probability map, and thresholding the local maxima map. Finally cell centers are associated using the proposed tracking method. Color coding is used to highlight associated cell centers such that different colors show the association of cell centers over time. It takes about 0.5 seconds for a well to be segmented and associated in the current stage using a *Pentium* 4 running at 1.6 Ghz.

As can be observed from Figure 11, by applying our probabilistic model-based tracking to HSC image sequence, it is able to identify and associate both nondividing and dividing cell centers correctly. However there are some cases, such as having a large number of proximate young divided cells or a few number of nearby dividing mature cells, in which some of the hypotheses have very similar probability, therefore deriving the best hypothesis for such a frame is very difficult and prone to error. Employing a more robust Bayesian approach will resolve those ambiguous situations over time by the further integration of information of neighboring frames, maintaining several hypotheses, and selecting the most likely one over the subsequent images.

5. CONCLUSIONS

Image cytometry is a practical approach to measure and extract cell properties from large volumes of microscopic cell images. As an important application of image cytometry, this paper presents a probabilistic model-based cell tracking method to locate and associate HSCs in phase contrast microscopic images.

Our statistical cell model, which is constructed after carefully observing HSCs in typical image sequences, captures the key properties of these cells. The close match between the model and imaged HSCs allowed for threshold selection yielding very low false alarm or missed detection. Cells in isolation are detected well; recently split cells provide a proper fit to the model and rely on association to resolve ambiguities.

Cell association is accomplished based on the proposed joint association method. As it can be observed in Figure 2 the cell dynamics can be well approximated by a random

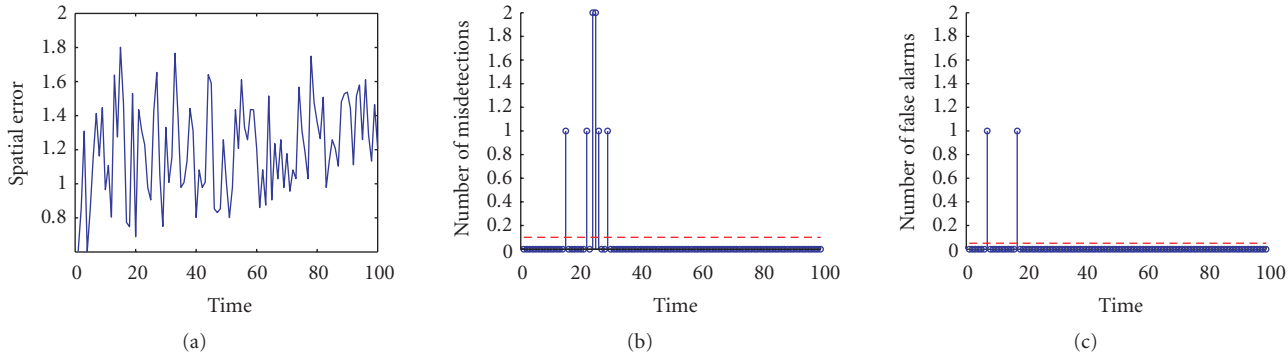

Figure 10: (a) RMS spatial error, the distance between detected cell centers and ground truth. (b) The location of missed detections with the superimposed average missed detection probability (0.0107). (c) The location of false alarms with the superimposed average false alarm probability (0.0027).

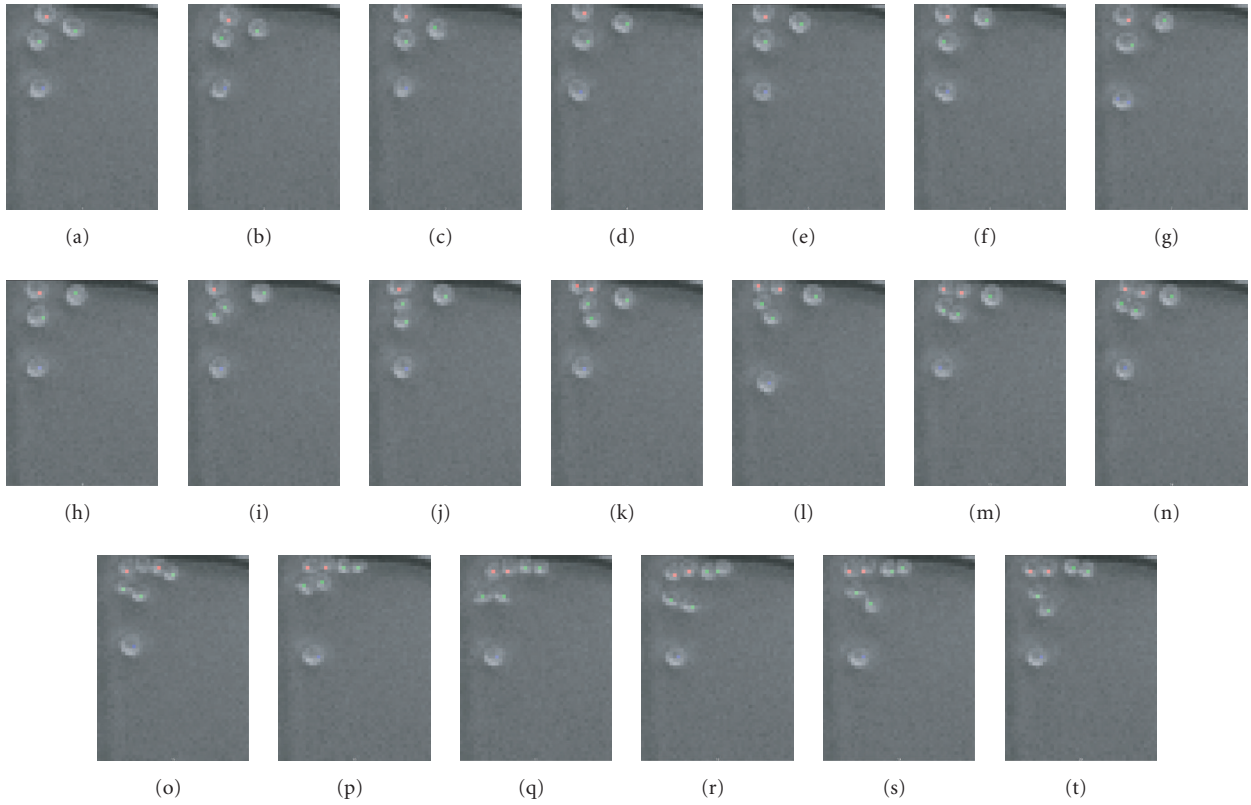

Figure 11: Detection and association of cell centers obtained by applying the proposed model-based tracking method. Results are superimposed on the original HSC images and each color shows a different cell track over time (frames 1–20).

walk as it has been considered in the proposed method to model the cell motion. It can be seen from the previous section that such a probabilistic model-based cell tracking method produces promising results and is able to identify and associate both dividing and nondividing cell centers correctly. However, there are some cases, such as a few proximate dividing cells or large number of nearby cells, in which the proposed method may be inaccurate. To resolve association ambiguities in such cases and to make the method more robust to noise and clutter, future work will be conducted to extend the proposed method by integrating the information over multiple neighboring frames.

Future work will also include improving the cell model to more accurately reflect unique properties of the cells under different conditions. Moreover further work is required to better preprocess the images with background subtraction to improve homogeneity and eliminate camera artifacts. There is also considerable interest in designing a parametric cell

model with additional degrees of freedom to generate lineage trees in which cells can be characterized by richer features so that cell properties can be more reliably extracted.

ACKNOWLEDGMENTS

This research has been funded by Natural Science and Engineering Research Council of Canada (NSERC). This research has been also performed in close cooperation with Chemical Engineering Department (CE) of the University of Waterloo (UW) and Terry Fox Laboratory (TFL) of the University of British Columbia (UBC). We would like to thank professor Connie Eaves and Mr. Brad Dykstra from TFL-UBC and researchers in Cancer Research Laboratory (CRL) of UBC for providing cell samples for this research and valuable inputs on biological properties of HSCs.

REFERENCES

[1] P. M. Banks, J. Chan, M. L. Cleary, et al., "Mantle cell lymphoma: a proposal for unification of morphologic, immunologic, and molecular data," *American Journal of Surgical Pathology*, vol. 16, no. 7, pp. 637–640, 1992.

[2] I. Baumann, R. Nenninger, H. Harms, et al., "Image analysis detects lineage-specific morphologic markers in leukemic blast cells," *American Journal of Clinical Pathology*, vol. 105, no. 1, pp. 23–30, 1996.

[3] E. Campo and E. S. Jaffe, "Mantle cell lymphoma. Accurate diagnosis yields new clinical insights," *Archives of Pathology and Laboratory Medicine*, vol. 120, no. 1, pp. 12–14, 1996.

[4] J. K.C. Chan, P. M. Banks, M. L. Cleary, et al., "A revised European-American classification of lymphoid neoplasms proposed by the International Lymphoma Study Group: a summary version," *American Journal of Clinical Pathology*, vol. 103, no. 5, pp. 543–560, 1995.

[5] Y. Cheng, "Mean shift, mode seeking, and clustering," *IEEE Transactions on Pattern Analysis and Machine Intelligence*, vol. 17, no. 8, pp. 790–799, 1995.

[6] T. Markiewicz, S. Osowski, L. Moszczyński, and R. Sałat1, "Myelogenous leukemia cell image preprocessing for feature generation," in *Proceedings of 5th International Workshop on Computational Problems of Electrical Engineering*, pp. 70–73, Jazłoweic, Ukraina, August 2003.

[7] V. Meas-Yedid, F. Cloppet, A. Roumier, A. Alcover, J.-C. Olivo-Marin, and G. Stamon, "Quantitative microscopic image analysis by active contours," in *Proceedings of Vision Interface Annual Conference - Medical Applications (VI '01)*, pp. 277–284, Ottawa, Ontario, Canada, June 2001.

[8] K. Wu, D. Gauthier, and M. D. Levine, "Live cell image segmentation," *IEEE Transactions on Biomedical Engineering*, vol. 42, no. 1, pp. 1–12, 1995.

[9] D. A. Forsyth and J. Ponce, *Computer Vision - A Modern Approach*, Prentice-Hall, Upper Saddle River, NJ, USA, 2003.

[10] A. Blake and M. Isard, *Active Contours*, Springer, New York, NY, USA, 1997.

[11] D. Marr, *Vision: A Computational Investigation into the Human Representation and Processing of Visual Information*, W. H. Freeman, San Francisco, Calif, USA, 1982.

[12] S. J. Osher and R. P. Fedkiw, *Level Set Methods and Dynamic Implicit Surfaces*, Springer, New York, NY, USA, 2002.

[13] J. A. Sethian, *Level Set Methods and Fast Marching Methods Evolving Interfaces in Computational Geometry, Fluid Mechanics, Computer Vision and Materials Science*, Cambridge University Press, Cambridge, UK, 1999.

[14] L. Shapiro and G. C. Stockman, *Computer Vision*, Prentice-Hall, Upper Saddle River, NJ, USA, 2001.

[15] E. Trucco and A. Verri, *Introductory Techniques for 3D Computer Vision*, Prentice-Hall, Upper Saddle River, NJ, USA, 1998.

[16] C. Rasmussen and G. D. Hager, "Probabilistic data association methods for tracking complex visual objects," *IEEE Transactions on Pattern Analysis and Machine Intelligence*, vol. 23, no. 6, pp. 560–576, 2001.

[17] E. Jervis, "Living cell tracking," http://cape.uwaterloo.ca/~ericjj.

[18] D. Comaniciu and P. Meer, "Cell image segmentation for diagnostic pathology," in *Advanced Algorithmic Approaches to Medical Image Segmentation: State-of-the-Art Applications in Cardiology, Neurology, Mammography and Pathology*, pp. 541–558, Springer, New York, NY, USA, 2001.

[19] D. Demandolx and J. Davoust, "Multiparameter image cytometry: from confocal micrographs to subcellular fluorograms," *Bioimaging*, vol. 5, no. 3, pp. 159–169, 1997.

[20] G. I. Nistor, M. O. Totoiu, N. Haque, M. K. Carpenter, and H. S. Keirstead, "Human embryonic stem cells differentiate into oligodendrocytes in high purity and myelinate after spinal cord transplantation," *GLIA*, vol. 49, no. 3, pp. 385–396, 2005.

[21] W. Bieniecki, "Oversegmentation avoidance in watershed-based algorithms for color images," in *Proceedings of IEEE International Conference on Modern Problems of Radio Engineering, Telecommunications and Computer Science (TCSET '04)*, pp. 169–172, Lviv-Slavsko, Ukraine, February 2004.

[22] D. Anoraganingrum, "Cell segmentation with median filter and mathematical morphology operation," in *Proceedings of IEEE International Conference on Image Analysis and Processing (ICIAP '99)*, pp. 1043–1046, Venice, Italy, September 1999.

[23] H.-S. Wu, J. Barba, and J. Gil, "Region growing segmentation of textured cell images," *Electronics Letters*, vol. 32, no. 12, pp. 1084–1085, 1996.

[24] N. Otsu, "A threshold selection method from gray-level histograms," *IEEE Transactions on Systems, Man and Cybernetics*, vol. 9, no. 1, pp. 62–66, 1979.

[25] C. Glasbey, "An analysis of histogram-based thresholding algorithm," *Graphical Models and Image Processing*, vol. 55, no. 6, pp. 532–537, 1993.

[26] Y. Bar-Shalom and K. Birmiwal, "Consistency and robustness of PDAF for target tracking in cluttered environments," *Automatica*, vol. 19, no. 4, pp. 431–437, 1983.

[27] S. Colegrove, A. Davis, and J. Ayliffe, "Track initiation and nearest neighbours incorporated into probabilistic data association," *Journal of Electrical and Electronics Engineering*, vol. 6, no. 3, pp. 191–198, 1986.

[28] Y. Bar-Shalom and T. E. Fortmann, *Tracking and Data Association*, Academic-Press, San Diego, Calif, USA, 1988.

Nezamoddin N. Kachouie received his B.S. degree in computer engineering from the Isfahan University of Technology (IUT). He received his M.S. degree in electrical and computer engineering from the Ryerson University, Canada, in 2004 and since then he has been with the Department of Systems Design Engineering at the University of Waterloo, Canada, completing his Ph.D. degree in the field of biomedical engineering.

He is interested in deformable models and Bayesian framework for biomedical applications of multiple target tracking. His current research focuses on segmentation and tracking of stem cells in biomedical multicellular videos by designing a model-based tracking system. This tracking system will be used to study stem cell behavior which is of crucial importance in drug and disease research. His research interests also include statistical signal processing, content-based image retrieval, image registration, object recognition, spatiotemporal image analysis, image denoising, optimization, and classification.

Paul Fieguth received the B.S. degree from the University of Waterloo, Ontario, Canada, in 1991 and the Ph.D. degree from the Massachusetts Institute of Technology, Cambridge, in 1995, both degrees in electrical engineering. He joined the Faculty at the University of Waterloo in 1996, where he is currently an Associate Professor in systems design engineering. He has held visiting appointments at the Cambridge Research Laboratory, at Oxford University, and the Rutherford Appleton Laboratory in England, and at INRIA/Sophia in France, with postdoctoral positions in computer science at the University of Toronto and in information and decision systems at MIT. His research interests include statistical signal and image processing, hierarchical algorithms, data fusion, and the interdisciplinary applications of such methods, particularly to remote sensing.

John Ramunas Since his graduation with a B.S. degree in biochemistry from the University of Waterloo in 2001 he has been working in the lab. of Eric Jervis developing technologies for studying and controlling cells, for example, arrays of glass-bottom microwells that allow high-quality long-term imaging of cells, and software for manually scoring characteristics of movies of cells cultured in these microwells. This scoring process is a bottleneck in the experiment pipeline so it is with great enthusiasm that he welcomes the advances offered by the work of Nezamoddin and Paul. He serves as a liason to help integrate these advances into the existing software and test them in an iterative cycle involving actual ongoing experiments. He will begin his Ph.D. at Stanford in 2006 after which other members of the Jervis lab. will continue the development cycle with the Fieguth lab.

Eric Jervis received his undergraduate and graduate degrees in chemical and biological engineering from the University of British Columbia. Upon completing his Ph.D. in 1998, he took a position in chemical engineering at the University of Waterloo and was subsequently granted tenure and promoted to the rank of Associate Professor in 2004. He is currently developing three lines of research that provide leading-edge opportunities for student training: (a) development of image-based lineage tracking tools for examining cell division symmetry and cell potential maintenance in stem cell cultures—a "lineage informatics" approach to cell culture analysis; (b) development of multiphoton-based methodologies for photoactivation of caged molecules for drug delivery; and (c) development of improved high-density bioreactor protocols with optical bioprocess monitoring instrumentation. These research themes are united by the application of high-resolution imaging and photonics-based analytical techniques. He is a Member of the Canadian Stem Cell National Centers of Excellence.

Hindawi Publishing Corporation
International Journal of Biomedical Imaging
Volume 2006, Article ID 79862, Pages 1–13
DOI 10.1155/IJBI/2006/79862

Reciprocal Benefits of Mass-Univariate and Multivariate Modeling in Brain Mapping: Applications to Event-Related Functional MRI, $H_2{}^{15}O$-, and FDG-PET

James R. Moeller[1, 2, 3] and Christian G. Habeck[2, 4]

[1] *New York State Psychiatric Institute, College of Physicians and Surgeons, Columbia University, New York, NY 10032, USA*
[2] *Cognitive Neuroscience Division, Taub Institute, College of Physicians and Surgeons, Columbia University, New York, NY 10032, USA*
[3] *Department of Psychiatry, College of Physicians and Surgeons, Columbia University, New York, NY 10032, USA*
[4] *Department of Neurology, College of Physicians and Surgeons, Columbia University, New York, NY 10032, USA*

Received 9 February 2006; Revised 17 August 2006; Accepted 18 August 2006

In brain mapping studies of sensory, cognitive, and motor operations, specific waveforms of dynamic neural activity are predicted based on theoretical models of human information processing. For example in event-related functional MRI (fMRI), the general linear model (GLM) is employed in mass-univariate analyses to identify the regions whose dynamic activity closely matches the expected waveforms. By comparison multivariate analyses based on PCA or ICA provide greater flexibility in detecting spatiotemporal properties of experimental data that may strongly support alternative neuroscientific explanations. We investigated conjoint multivariate and mass-univariate analyses that combine the capabilities to (1) verify activation of neural machinery we already understand and (2) discover reliable signatures of new neural machinery. We examined combinations of GLM and PCA that recover latent neural signals (waveforms and footprints) with greater accuracy than either method alone. Comparative results are illustrated with analyses of real fMRI data, adding to Monte Carlo simulation support.

1. INTRODUCTION

Inferential methods used in human brain mapping span a spectrum of experimental designs and statistical techniques. In the broadest terms the task is to recast the predictions of a theoretical description of neural information processing into testable properties of the neuroimaging data. A logical starting point is the mapping $\mathbf{u} \leftarrow F(\nu, \boldsymbol{\theta})$ in which $\mathbf{u}$ represents the data of a neuroimaging study, acquired using one of several imaging technologies; and ν represents the set of physiological mechanisms that have potentially influenced the measurement $\mathbf{u}$. Manifest evidence that the latent processes ν of experimental interest are the actual determinants of the imaging data $\mathbf{u}$ is achieved through the activation and modulation of the latent physiological (neural) processes by means of parametric manipulations of the stimulus input. F is the model of the conjoint influences of the latent physiological activity on $\mathbf{u}$. The vector $\boldsymbol{\theta}$ quantifies both the relative strength of each mechanism's contribution to $\mathbf{u}$ and the strength of interactions among different latent mechanisms.

A current example is the acquisition of the BOLD MRI signal (blood oxygenation-level-dependent signal), a surrogate measure of local neural activity, in studies involving event-related experimental designs. In event-related functional MRI (fMRI), the mapping is expressed as $\mathbf{u}(s,t) \leftarrow F(\nu(s,t), \boldsymbol{\theta})$, in which each $\nu(s,t)$ may be thought of as a "movie" of an aspect of information processing whose neural signal is manifest at one or more locations s in the brain, at one or more time points during data acquisition interval T, that is, for times $t \in T$. In modeling neuroimaging data, the aim is to infer the spatiotemporal properties of the underlying operations $\nu(s,t)$, and how these $\nu(s,t)$ jointly determine the measured $\mathbf{u}(s,t)$.

Model construction also includes a quantitative account of the spatiotemporal filtering of $F(\nu(s,t), \theta)$ introduced by the imaging technology. In the case of BOLD signal acquisition, $F(\nu(s,t), \boldsymbol{\theta})$ must be transformed to represent the convolution of the hypothetical neural signal with the hemodynamic response function. Caveats are that the hemodynamic response may be different for different brain regions, and

may also differ in the same brain region in different individuals, for example, in individuals of different ages.

In analyzing imaging data sets, there is a plethora of different observation models. From the perspective of inferential statistics, the choice of experimental design and observation model is dependent on both the abstract mapping $\mathbf{u}(s,t) \leftarrow F(\nu(s,t),\boldsymbol{\theta})$ and the spatiotemporal filtering of $F(\nu(s,t),\theta)$ introduced by the imaging technology. The choices depend on (a) what is known a priori about $\nu(s,t)$ and F and $\boldsymbol{\theta}$; (b) which mechanisms $\nu(s,t)$ and properties of $F(\nu(s,t),\boldsymbol{\theta})$ are of primary interest to the experimenter; and (c) the degree to which the features of interest are resolvable in the filtered representation of $F(\nu(s,t),\theta)$. In current neuroscience studies of human sensory processing and cognitive and motor operations, the observation models that are ordinarily applied to the data are of two classes [1–12]: the general linear model (GLM) used in mass-univariate analysis and the multivariate models based on PCA or ICA decomposition.

1.1. Mass-univariate analysis

In mass-univariate analyses one or more hypothetical models $F(\nu(s,t),\boldsymbol{\theta})$ are used to predict the data $\mathbf{u}(s,t)$. For each $F(\nu(s,t),\boldsymbol{\theta})$ the observation model consists of a set of explanatory variables, or design matrix, that is assumed to be a set of known and fixed predictors, and the model is applied identically to all voxels in the brain. In the design matrix the primary design variables provide a detailed description of the predictions regarding the behavior of the hypothetical operations $\nu(s,t)$ in different experimental conditions (i.e., different temporal epochs); and the secondary design variables describe potential nuisance effects that, were they not taken into account, would inflate the GLM estimate of random error. Standard linear methods are used to quantify the contributions of the predictor variables to the temporal waveforms of individual voxels. The aim is to identify voxels for which one or more $F(\nu(s,t),\boldsymbol{\theta})$ provide a plausible account of the local temporal activity in $\mathbf{u}(s,t)$. Moreover, in head-to-head comparisons of competing theoretical models the best-case scenario would be that in which only one model provides a high level of explanatory power.

1.2. Multivariate modeling

Multivariate models based on PCA or ICA decomposition have a somewhat different focus—on the waveform similarities in the dynamic neural activity of different brain regions. The underlying premise of this type of multivariate modeling is that multiple signals are generated in response to experimental stimulus input, and each signal is manifested in multiple brain regions. That is, similar neural trains of activity appear at multiple brain sites—with locations not only in sensory pathways, but also in limbic and temporoparietal pathways and areas of prefrontal cortex.

This generally accepted premise is a corollary of neuroscientific theory that describes the brain's analysis of sensory inputs in terms of "predictive coding strategies" [13–18]. From this theoretical perspective the brain mines stimulus inputs using complementary inferential modes: (a) specialized sensory coding methods, for example, the array of feature-specific coding schemes known to be deployed in the initial processing of visual stimuli; and (b) the contextual guidance provided by working memory and executive systems that relate immediate stimulus events to organism-generated goals. Concretely, predictive coding models suggest that signals generated in sensory pathways are likely to be fed forward for interpretation and synthesis to limbic and temporoparietal pathways associated with short- and long-term memories, and to the prefrontal cortices that are involved with working memory, including goal-directed response selection, motor planning, and error checking. Likewise, signals containing contextual and goal-specific information are fed back to sensory pathways, modifying sensorial representations of external stimulus events.

The observation models used in a multivariate analysis decompose the neuroimaging data $\mathbf{u}(s,t)$ into a series of components, in which each component represents a temporal waveform that is expressed to a stronger or weaker degree in a multiplicity of brain regions and not at all in other brain regions. In applications of unguided PCA and ICA, only mild constraints are imposed on the temporal waveforms and their respective spatial modes (i.e., topographic patterns of nonzero signal expression). Specifically in PCA, the series of waveforms are constrained to be mutually orthogonal, as are the series of spatial modes; and in ICA, either the series of temporal waveforms or the series of spatial modes are constrained to be maximally statistically independent.

Indeed, in the case of unguided PCA and ICA the individual components may, or may not, be related in a one-to-one fashion to either (a) the true neural signals $\nu(s,t)$ occurring in one or more task conditions (temporal epochs), or (b) particular behavioral and demographic experimental variables. On the other hand, these PCA and ICA decomposition methods are designed to provide an accurate approximation to the brain-wide footprint of the sites associated with the aggregate of latent neural signals $\nu(s,t)$. Ordinarily the experimental prediction is that the brain-wide footprint will be sparse in total anatomical extent, although spatially distributed.

Guided PCA and ICA observation models, on the other hand, are designed to further constrain the components of the PCA or ICA decomposition to spatiotemporal features of the data $\mathbf{u}(s,t)$ that most closely match the hypothesized neural processes $\nu(s,t)$ and their predicted activity in different experimental conditions.

1.3. Reciprocal benefits of mass-univariate and multivariate modeling

The practical reality is that no one modeling method alone will provide an exact description of the physiological mechanisms that are the actual determinants of the imaging data: neither the theoretical models $F(\nu(s,t),\boldsymbol{\theta})$, nor their instantiation in GLM, nor the major components of unguided or guided PCA or ICA. However, there is a potential advantage

to explore the footprint of a multivariate analysis with one or another theoretical model $F(\nu(s,t),\boldsymbol{\theta})$. A theoretical model can provide a parsimonious account of regional activity for some portion of the voxels within the multivariate footprint. This account represents an implicit judgment of similarity between theoretical neuroscientific predictions and the latent processes actually operating within the footprint. The standard GLM calculation of goodness-of-fit represents the true explanatory power achieved by $F(\nu(s,t),\boldsymbol{\theta})$ when contrasted with its distribution predicted by random Gaussian field theory. Goodness-of-fit is calculated on a voxel-by-voxel basis, but includes the footprint's anatomical extent and the level of type-I error protection as global parameters.

The practical advantage in applying the mass-univariate analysis to a multivariate footprint—rather than brain wide—is that the spatially constrained analysis identifies additional voxels in which $F(\nu(s,t),\boldsymbol{\theta})$ has actual explanatory power. The greatest reciprocal benefit is afforded when (a) the major temporal waveforms obtained from an PCA or ICA decomposition span the fixed predictor variables of the mass-univariate analysis; and (b) almost all, if not all regions for which the mass-univariate analysis provides a moderate-to-high level of explanatory power lay within the multivariate footprint. Perhaps the multivariate analysis that is best equipped to take advantage of these potential benefits is the multivariate linear model (MLM), a guided PCA that was among the first multivariate methods applied to event-related fMRI data. The conjoint MLM and mass-univariate analysis is based on a theoretical model $F(\nu(s,t),\boldsymbol{\theta})$ in which the temporal waveforms obtained from a MLM-PCA decomposition are constrained to match the fixed predictor variables of the mass-univariate analysis. MLM has the added virtue that the GLM-type mean contrast effects between experimental conditions are computed using a proper statistical method of whitening the data along the temporal dimension.

The essential strength of the MLM analysis is that, like mass-univariate analysis, it is based on our accrued knowledge about human information processing and the theoretical constructs derived there from. On the other hand, the strong reliance by MLM on current theory limits its capacity to uncover novel features of the data $\mathbf{u}(s,t)$ that reveal neural machinery not heretofore anticipated.

1.4. Utility of individual differences in brain mapping

The exploration of individual differences has been a dependable means for discovering novel neural machinery as chronicled in the research findings of cognitive psychology and clinical neuroscience [13, 19–23]. In brain mapping the main sources of information about individual differences are the interactions between brain regions, experimental task parameters, and endogenous variables. It is thus understandable that guided PCA methods were devised early on in the development of noninvasive brain imaging technologies to explore subject-related interaction effects. These models included the subprofile scaling model (SSM) [3, 12, 24, 25] and the partial least squares methods [6, 26]. These guided PCA were originally designed for application to data acquired with positron emission tomography (PET) with $H_2{}^{15}O$ perfusion and [^{18}F]Fluorodyoxyglucose, and topographic electroencephalography (EEG).

The authors and others [4, 5, 7, 8, 11, 27] have extended these initial developments in guided PCA to take advantage of the higher temporal resolution of event-related fMRI. The clear benefit of higher resolution is that more experimental tasks, and greater numbers of comparisons between experimental conditions and their parametric controls, can be built into study designs. Two of the newest guided PCA are the generalized partial least squares (gPLS) and ordinal trends (OrT) analyses [5, 7]. These guided PCA are designed to capture the joint influences of experimental task parameters and endogenous factors on latent neural signals of theoretical interest. In both gPLS and OrT the aim is to combine the verification of neural machinery that is reasonably well understood with the discovery of reliable signatures of new neural machinery.

1.5. Ordinal trends model

In this report we focus on the OrT analysis. The inferential strategy that is unique to OrT is its capacity to capture the joint influence of task parameters and endogenous factors on $\mathbf{u}(s,t)$ without resorting to classical latent variable modeling. In brain mapping, the latent variables are the neural processes $\nu(s,t)$ and their spatiotemporal properties; their observable counterparts are both the experimental predictor variables and subject variables, for example, indices of task performance, IQ, education and age. From the perspective of standard latent variable analysis [28], the method of estimating $\nu(s,t)$ relies on models that impose explicit constraints on the relationships among different $\nu(s,t)$ and between individual $\nu(s,t)$ and experimental predictor variables, behavioral scores and demographic factors. In contrast, an OrT analysis is based on the experimental design variables alone, without the use of either behavioral scores, demographic variables, or causal models that depict the relationship between latent brain circuitry and endogenous variables.

The OrT analysis is predicated on event-related experimental designs in which positive incremental changes in task parameters are expected to produce positive monotonic trends in the activity of individually targeted signals $\nu(s,t)$. OrT performs a separate analysis for each $\nu(s,t)$ with the aim of identifying one or more topographic patterns in $\mathbf{u}(s,t)$ that expresses positive ordinal trends on a subject-by-subject basis. OrT is a guided PCA: a specially designed linear transformation is applied to the neuroimaging data with the effect that maximal salience is assigned to topographic patterns whose expressions are monotonic across a specified series of experimental conditions, corresponding to the positive incremental changes expected in the level of the targeted neural signal.

Algebraically speaking, the multiplication of the data matrix by the OrT design matrix differentially alters the voxel-by-condition-by-subject variance of three types of latent patterns: see the appendix. First, the OrT transformation

discriminates among patterns that expressed mean trends in the predicted direction from patterns that expressed mean directional changes that are different from the predicted trend; and second, the transformation discriminates among different types of patterns within the first category. In the first category, the OrT design matrix discriminates among patterns in which the direction of the trend expressed is the same in all subjects from patterns that express condition-by-subject interactions in which the direction of the trend expressed is different for different subjects. Lastly, the design matrix is constructed to preserve the relative size of the voxel-by-task-by-subject variance accounted for by topographic patterns that express ordinal trends. On this basis the application of PCA, or singular value decomposition (SVD), to the transformed data set can be expected to produce major principal components that provided a good approximation to one or more target patterns, where each expresses ordinal trends on an individual subject basis.

Importantly, the data structure to which the OrT model is applied is not the raw fMRI data. Initially, the spatiotemporal data are preprocessed to remove the normal MR artifacts, for example, susceptibility and motion artifacts and artifacts associated with respiration and cardiac pulsations. Subsequently, a standard method of temporal averaging is applied to the "artifact-free" data to construct brain maps for individual subjects that represent the BOLD activity within different task conditions (epoch types) of the experimental design. This temporal averaging enhances the signal-to-noise characteristics of BOLD activity that is time-locked to stimulus-based, cue-based, and response-based epochs. These brain maps are the data structure to which the OrT model is applied, that is, the data consist of one brain map per subject per task condition (or epoch). More details of the time series modeling are provided in our example of an OrT analysis applied to real event-related fMRI data.

Robust inferential statistical methods have been designed for OrT applications to these types of data structures. Nonparametric statistics are used to control type-I error rates, for example, permutation test statistics and error statistics based on Monte Carlo simulations of random Gaussian fields; see the appendix. In addition, bootstrap resampling methods are applied to OrT topographic pattern estimates to evaluate the reliability of nonzero voxel weights. The reliability of individual voxel weights is computed as z-scores, where the higher the z-score the less likely it is that any subject is extraordinarily influential in determining voxel weight. The caveat is that in our current bootstrap procedure the areal extent of clustered voxels is not taken into account in calculating individual z-scores.

We suggest that OrT is likely to provide the greatest benefit in experiments that admit substantial interactions between experimental task parameters and endogenous variables. On the one hand, the OrT analysis is predicated on the notion that experimental control is sufficiently robust that positive incremental changes in task parameters produce positive ordinal trends in the activity of each targeted signal $\nu(s,t)$ of the theoretical model $F(\nu(s,t),\boldsymbol{\theta})$. That is, the OrT analysis is designed to recover the footprint of each $\nu(s,t)$ for which every subject (or almost every subject) expresses a positive ordinal trend. In particular, footprint recovery is possible in data sets in which there is substantial variation in the trajectories of subjects' positive ordinal trends. The worst-case scenario for which recovery of $\nu(s,t)$ may be feasible are data sets in which interactions between task parameters and endogenous variables take the form of additional latent processes that had not been included in (i.e., were not predicted by) the theoretical model $F(\nu(s,t),\boldsymbol{\theta})$. The additional latent processes may express mean trends similar to that of a targeted $\nu(s,t)$. But what distinguishes each of these latent processes from $\nu(s,t)$ is that the directional trend in task activity is different for different subjects. In other words, the experimental control over the operation of these latter latent processes is markedly less than that achieved with the targeted processes $\nu(s,t)$.

In applications to real data sets, for example, $H_2{}^{15}O$ PET data sets and event-related fMRI data sets, there are striking examples in which the OrT analysis appeared to provide a relatively unconfounded and unbiased estimator of a target pattern [7, 29]. By contrast, the corresponding map of GLM mean trend statistics deviated markedly from the OrT estimate of the target footprint, suggesting that the GLM map estimate is influenced by interactions between task parameters and endogenous variables. We have implemented Monte Carlo methods to simulate data sets that manifest similar differences between OrT and mass-univariate analyses [7]. The simulated data sets represent the worst case scenario in which there is substantial variation in the subject trajectories of target $\nu(s,t)$ activity plus, the superposition of several "nuisance" latent processes. The inclusion of these interaction effects in simulated data sets results in maps of GLM mean trend statistics that contain significant contributions from both target and nuisance processes. By contrast, the OrT analysis provides a substantially less confounded estimate of the target footprint.

In sum, OrT is likely to provide the greatest benefit in studies in which (a) enrollment criteria create subject samples that reflect the population level of phenotypic variation, and (b) experimental control is sufficiently strong that the latent neural processes of primary theoretical interest exhibit positive ordinal trends. This potential advantage is particularly relevant to studies of learning and memory for which there are ordinarily inherited and acquired differences among individuals.

2. EXAMPLE OF AN OrT ANALYSIS APPLIED TO EVENT-RELATED fMRI

We demonstrate here the practical utility of an OrT analysis with its application to the event-related fMRI data from a study of visual recognition and perceptual adaptation [29]. We describe below the essential information about experimental goals and design, the fMRI acquisition and preprocessing steps, as well as the OrT analytic design and the patterns of regional activations that represented experimental effects. The OrT computational methods are outlined in the appendix that includes (a) a step-by-step recipe of the

OrT computations, and (b) the attendant inferential statistical methods that are routinely applied.

2.1. Experimental aims

The aim of the fMRI study was to investigate the effects of stimulus repetition on behavioral and neurophysiological measures of adaptation. We used a modified, trial-based version of the possible/impossible object decision (IP-OD) task that was originally designed by Schacter et al. [30]. Unlike the original IP-OD task, our version was designed to measure repetition effects over delays of a few seconds rather than minutes. Our modified IP-OD task was benchmarked with the production of significant perceptual priming effects. Significant reaction time (RT) effects occurred for stimulus repetitions ($p < 0.0001$) and object type ($p < 0.005$), with a nonsignificant trend in the interaction between repetition number and object type ($p < 0.08$). In this two-alternative, forced-choice paradigm, the decision theoretic parameters of object discrimination, d' and bias, remained nearly constant across successive object presentations. The minimum d' and maximum bias were 2.92 ± 0.56 and -0.66 ± 0.57 (mean $\pm$ SD), recorded for initial presentations.

Ordinal trend analysis was applied to the fMRI BOLD signal. The analytic goal was to recover a latent component of the BOLD signal that appeared in multiple brain regions and that, with successive exposures of a test object, exhibited either a positive trend in every subject, or a negative trend in every subject. OrT was applied separately to possible and impossible objects [29]. We have limited our report here to the analysis of possible objects with the express purpose of illustrating the OrT methodology.

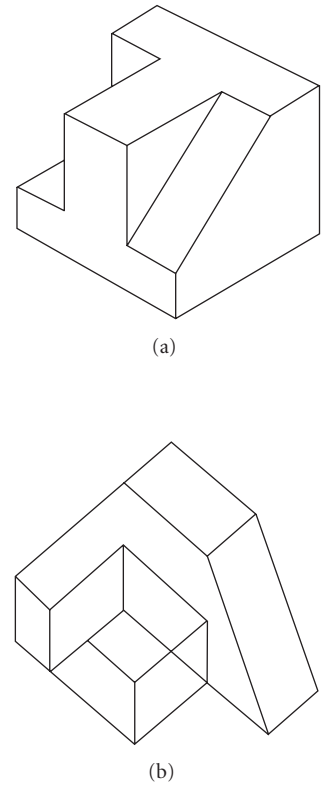

Figure 1: Examples of the visual stimuli used in the IP-OD task: (a) "possible" object; and (b) "impossible" object.

2.2. Materials and methods

2.2.1. Subjects

Fourteen healthy, right-handed subjects (age = 22.8 ± 3.8 [Mean $\pm$ SD]), recruited from the Columbia University student population, participated in the experiment. All subjects supplied informed consent, as approved by the Internal Review Board of the College of Physicians and Surgeons of Columbia University. Volunteers were screened for psychiatric and neurological illness via a questionnaire.

2.2.2. Task procedures

The stimuli used in the visuo-perceptual task consisted of "possible" and "impossible" objects (Figure 1). Possible objects were two-dimensional renderings of three-dimensional solid forms, where the latter are composed of a small number of intersecting planar surfaces. By contrast, the planar surfaces rendered in impossible objects did not come together to form actual 3D solid objects. With each stimulus presentation, that is, on each trial, the subject's task was to decide whether the visual stimulus was a possible or an impossible object—hence the term "object decision." Every trial was exactly-3000 milliseconds (ms) in duration: a trial began with a 500-ms ITI, followed by a fixation cue for 250 ms. Fifty milliseconds after fixation offset, the stimulus then appeared for 1000 ms; trials were terminated 1200 ms after stimulus offset. Practice trials were administered to confirm that participants understood what it meant to judge object type. Prior to commencement of fMRI scanning, subjects were told that (a) their memory of visual objects was being tested, (b) they would be viewing an extended series of object presentations, and (c) they should respond as quickly and as accurately as possible to each test object in the series.

The PI-OD task consisted of three test blocks, each with a different set of 13 possible and 13 impossible objects. Within a block each test object was presented four times. Altogether a block consisted of 104 test objects. The PI-OD task design was counterbalanced to obviate confounds between experimental effects [29].

With subjects laying supine in the MR scanner, task stimuli were back-projected onto a screen located at the foot of the MRI bed using an LCD projector. Subjects viewed the screen via a mirror system located in the head coil. Responses were made on an LUMItouch response system (Photon Control Company). PsyScope [31] was used to control task events and collect subject responses (reaction time and accuracy). In addition PsyScope electronically synchronized task events with the MRI acquisition computer.

2.2.3. fMRI data preprocessing

The several images acquired included T2*-weighted functional images, T1 "scout" images, and T2 anatomical images. Details regarding the acquisition parameters for these different images are reported in Habeck et al. [29]. All image preprocessing and analysis was done using the SPM99 program (Wellcome Department of Cognitive Neurology) and other code written in MATLAB (Mathworks, Natick, Mass). The following steps were taken in turn for each subject's GE-EPI data set: data were corrected for the timing of slice acquisition, using the first slice acquired in the TR as the reference. All GE-EPI images were realigned to the first volume of the first session. The T2-weighted structural image was coregistered to the first EPI volume using the mutual information coregistration algorithm implemented in SPM99. The latter high-resolution image was then used to determine parameters ($7 \times 8 \times 7$ nonlinear basis functions) for transformation into Talairach standard space [32] defined by the Montreal Neurologic Institute (MNI) template brain supplied with SPM99. This transformation was then applied to the GE-EPI data, which were resliced using sinc-interpolation to $2\,\text{mm} \times 2\,\text{mm} \times 2\,\text{mm}$.

2.3. Statistical Analysis

2.3.1. fMRI time-series and OrT modeling

A first-level, GLM-based, time series analysis was performed on individual subject image data [33] from which parameter images were constructed. A second-level OrT analysis was applied to these latter images for the group of 14 subjects. At the first level, the fMRI time-series analysis was applied voxel-wise, in which linearity and time-invariance were assumed in the physiological transformation of neural activity into a fMRI BOLD signal [34]. The steps in modeling followed the example of Friston et al. [35] and Zarahn [1, 36]: GE-EPI time-series were simultaneously modeled with regressors that represented the hypothesized BOLD response to the individual PI-OD trial types—relative to a baseline of intertrial intervals. The individual GLM regressors were constructed as convolutions of an indicator sequence (i.e., a train of discrete-time delta functions) representing delayed trial onsets, an assumed BOLD impulse response function (as represented by default in SPM99), and a rectangular function of trial duration. A predictor variable was created for each of eight-trial types—two-object types times four-object presentations; and eight images of GLM parameter estimates were produced for a subject. Subject images were each intensity normalized (via voxel-wise division by the image time series mean) and spatially smoothed with an isotropic Gaussian kernel (full-width-at-half-maximum = 8 mm).

These images of GLM parameters were subsequently submitted to an OrT analysis. An OrT analysis was performed on the first three-object presentations, based on the information that the largest change in RT occurred between the first and second, or first and third presentations. OrT patterns were constructed from the first few principal components, and their significance was evaluated using nonparametric test statistics (see the appendix). As a source of independent validation, change scores in OrT pattern expression were correlated with the perceptual measure of repetition suppression, that is, change scores in RT.

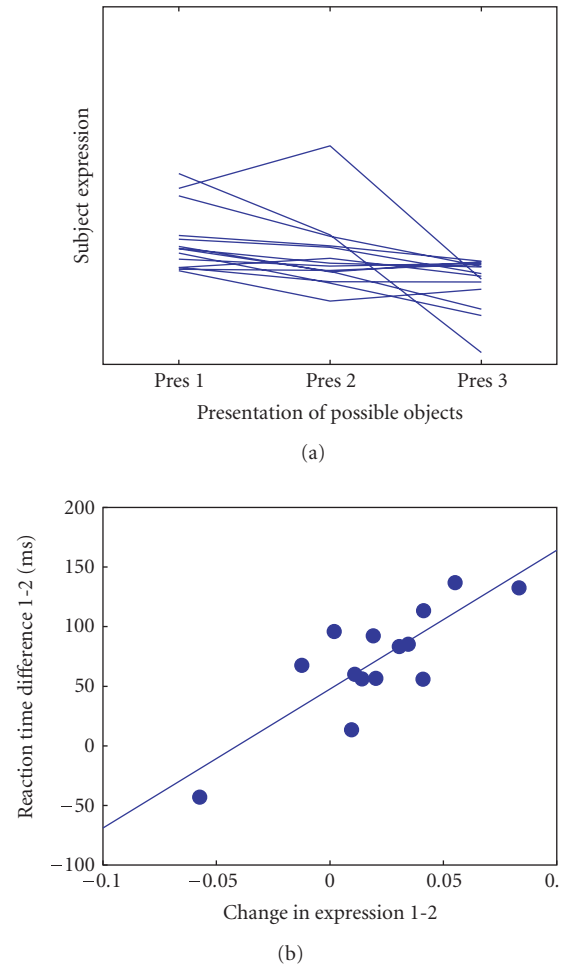

Figure 2: Results of an OrT guided PCA applied to the imaging data of 14 participants in the IP-OD study, for which negative ordinal trends were predicted across repeated object presentations (presentation number). A linear combination of the first two principal components (PCs) produced significant results: (a) negative monotonic trends exhibited by 12 of 14 subjects in the plot of presentation number versus pattern expression ($p < 0.01$); and (b) positive correlation ($p < 0.0005$) between the change score in OrT pattern expression (difference between first- and second-object presentations), and the corresponding change score in reaction time (index of perceptual repetition suppression).

3. RESULTS

A statistically significant OrT topographic pattern was obtained using the first two-principal components. All but two of the 14 subjects expressed positive ordinal trends (Figure 2(a)) with stimulus repetition ($p < 0.01$). The OrT pattern accounted for 16% of the total voxel-by-condition-by-subject variance in the untransformed fMRI data set. The OrT pattern estimate identified not only areas exhibiting

repetition suppression, but also brain areas that were positively increasing with successive presentations of each possible object, that is, "repetition augmentation." In addition the index of perceptual repetition suppression, that is, the change score in the difference in reaction time between the first- and second-object presentations, was significantly correlated ($R^2 = 0.67$, $p < 0.0005$) with the corresponding change score in OrT pattern expression (Figure 2(b)). The one subject who did not show perceptual repetition suppression was an outlier in this correlation analysis. Indeed, this subject was an outlier in the OrT analysis as well—exhibiting a negative, rather than positive OrT change score. Notwithstanding, the correlation between OrT expression and RT was significant without this subject outlier.

Our bootstrap resampling method confirmed that many of the nonzero voxel weights of the OrT pattern estimate were reliable (Table 1). Figure 3 maps the voxels with bootstrap z-scores ≥ 3.09, which is associated with uncorrected p-values ≤ 0.001. The bootstrapped OrT pattern revealed experimental effects in several areas of the visual pathway, including primary visual cortex, the precuneus and supramarginal gyrus, fusiform gyrus and parahippocampus, and the inferior frontal gyrus. Areas of increasing activation with successive object presentations populated regions predominantly in the left hemisphere, although right BA 39 exhibited increasing activation as well (Figure 3(a)). In contrast, areas of decreasing activation populated posterior dorsolateral regions of both hemispheres, ventrolateral regions of the right hemisphere, and a portion of right BA 44 (Figure 3(b)). It is unlikely that any subject was extraordinarily influential in determining the voxel weight of these superthreshold regions.

Lastly, we also performed a mass-univariate analysis in which the predictor variable was the mean contrast most similar to the positive ordinal trend prediction, that is, the linear mean trend across three-object presentations. Two brain areas were identified with F-values > 5.61, which are associated with uncorrected p-values < 0.001: these regions revealed a mean repetition suppression effect, but not a common directional trend in all subjects. Moreover, no voxel survived an SPM99 correction for multiple comparisons. (This Bonferroni-like correction uses a random Gaussian field adjustment that properly accounts for spatial dependences in the data.)

Table 1: Nearest gray-matter voxel locations assigned positive or negative weights ($|Z| > 3.09$) in the bootstrapped OrT pattern, which represents the neural effects of repeated presentations of "possible" objects. MNI coordinates, structure name, and Brodmann label are tabulated for (a) brain regions in which signal strength decreases with object repetition (*repetition suppression*); and (b) regions in which signal strength increases with object repetition (*repetition augmentation*). Localization with Talairach Demon available from http://ric.uthscsa.edu/projects/talairachdaemon.html.

X	Y	Z	Structure	Brodmann label
			Repetition suppression	
28	−84	16	Middle occipital gyrus	19
−24	−82	34	Precuneus	19
−12	−84	38	Precuneus	19
−24	−73	26	Precuneus	31
42	−54	−17	Fusiform gyrus	37
34	−56	51	Superior parietal lobule	7
24	−58	56	Precuneus	7
16	−28	−2	Thalamus	∗
−26	−88	16	Middle occipital gyrus	19
51	10	22	Inferior frontal gyrus	44
28	−38	−11	Parahippocampal gyrus	36
−42	−42	38	Supramarginal gyrus	40
			Repetition augmentation	
44	−70	42	Inferior parietal lobule	39
−18	−38	−11	Parahippocampal gyrus	36
−8	−58	46	Precuneus	7
−12	−52	52	Precuneus	7
−38	−16	60	Precentral gyrus	4
−40	−8	56	Precentral gyrus	6
−40	−14	38	Precentral gyrus	6
−44	−72	13	Middle temporal gyrus	39
−48	−72	36	Angular gyrus	39
−54	−36	26	Inferior parietal lobule	40
−20	−54	65	Postcentral gyrus	7
−46	−56	30	Superior temporal gyrus	39
6	−44	50	Precuneus	7
−16	0	26	Caudate body	∗

4. DISCUSSION

In current neuroscience studies of human sensory processing and cognitive and motor operations, the observation models that are applied to data sets have usually been one of two kinds: the general linear model (GLM) used in mass-univariate analysis and the multivariate models based on PCA or ICA decomposition. Although these two modeling strategies have an essential complementarity—in that the strengths of the one can be used to bolster the weaknesses of the other, it has been routine practice in brain mapping to apply these methods in isolation. The aim of this report has been to engender a better appreciation of the benefits of the complementarity between brain mapping methods.

It might come as a surprise that a similar kind of complementarity has previously been articulated in theories of predictive coding—as they are applied to the brain's mining of sensory inputs. Predictive coding describes a complementary set of inferential methods that are employed in human information processing to reconstruct external stimulus events from sensory signals. The latter spatiotemporal signals are those that are produced at the stage of sensory transduction, for example, in the retinal mosaic of the cone transduction of visual input. In the relationship between human information processing and brain mapping, these sensory signals correspond to the neuroimaging data

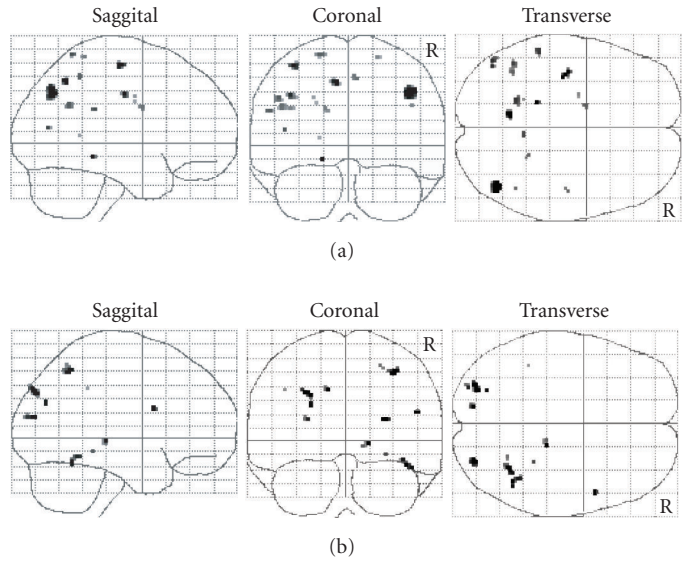

Figure 3: OrT pattern displayed in sagittal, coronal, and transverse projection views using SPM99 software. Voxels mapped have inverse coefficient of variation (ICV) values that exceed an absolute threshold of 3.09. (a) Repetition augmentation—regions that increase in activation with object repetition. (b) Repetition suppression—regions that decrease in activation with object repetition. (ICV values estimated using a bootstrap method. Anatomical designations for mapped voxel clusters are tabulated in Table 1.)

$\mathbf{u}(s,t)$. In human information processing, the goal is to extract information about external stimulus events that is relevant to both environment-organism homoeostasis and immediate goal-directed activity. Correspondingly, the goal of neuroscience is to mine the neuroimaging data $\mathbf{u}(s,t)$ for evidence that the latent processes of theoretical interest are indeed the neural processes that have been activated and modulated by the parametric manipulations of the stimulus input. In other words, the $\nu(s,t)$ of theoretical interest in brain mapping are analogous to the external stimulus events that are relevant to human thought and action.

In this analogy, the sensorial representations of external stimulus events correspond to the features of the neuroimaging data $\mathbf{u}(s,t)$ that are captured by the first principal components of PCA, or the task-related components of ICA. For example, in the simplest multivariate decomposition (e.g., unguided PCA), the neuroimaging data are encoded as a set of principal components without reference to experimental design variables or theoretical constructs. This type of coding would be analogous to sensorial representations in sensory pathways that are not modifiable by top-down, neural signals. But actually the brain has the capacity to modify sensorial representations with top-down signals: hence the better analogy is between modifiable sensorial representations and guided PCA and ICA, where the latter are designed to identify features of $\mathbf{u}(s,t)$ that share spatiotemporal features with the predicted neural signals $\nu(s,t)$. Theories of predictive coding emphasize the need to optimize the reciprocal flow of information between sensory pathways and brain areas associated with executive control as a means of maximizing the synthesis and interpretability of information about external stimulus events. The analogous concept is the aspect of brain mapping highlighted in this report, that is, conjoint multivariate and mass-univariate analysis.

The exploitation of conjoint multivariate and mass-univariate analyses is expected to benefit significantly from the new developments in guided PCA that combine the capability to verify the activation of the neural machinery that we already understand with the capability to discover reliable signatures of new neural machinery. The OrT analysis is presented as the latest example of a guided PCA that combines these capabilities. The means by which OrT achieves its expanded capability was examined; and OrT's practical utility is demonstrated in a group analysis of an event-related fMRI data from a study of visuo-perceptual adaptation.

4.1. Utility of OrT for event-related fMRI

The substantive finding of the OrT analysis was that a statistically significant OrT topographic pattern was identified in which lateral occipital cortex was among the most salient regions that exhibited reductions in the BOLD signal with successive stimulus exposures. This finding is consistent with the results of similar types of visual adaptation studies that have reported group mean reductions in lateral occipital functional activity—in blood flow and the BOLD signal [30, 37]. But, the OrT pattern is also consistent with the predictions of cognitive neuroscientists who argue that the neural correlates of visual adaptation and perceptual learning are not limited to neural response suppression in lateral occipital regions [38, 39]. Consistent with these latter predictions, the OrT pattern revealed significant regional effects of stimulus repetition in temporoparietal and prefrontal areas. These

brain regions support processing of higher-level perceptual attributes and spatial attention, and are distinguishable from the processes of preattentive feature extraction and visual imagery that take place in primary sensory pathways.

The difference between brain areas that reveal repetition suppression and those that exhibit increased activity with object repetition may reveal two different brain analyses that are performed on visual stimuli. We speculate that the predominantly left-hemisphere effects, which are associated with increased activity with object repetition, may be associated with analyses of intersecting curved and planar surfaces and their assignment to the same or different 3D solid objects. By contrast, the regions that show object suppression populate posterior regions of both hemispheres and may be associated with the operations of preattentive feature extraction and visual imagery. This interpretation is consistent with the Kosslyn et al. theory of object perception [40–42].

The relevance of the latent neural activity identified by OrT to perceptual repetition suppression was further affirmed by a strong, significant correlation between subject decreases in RT between the first- and second-object presentations and the corresponding change score in OrT pattern expression. On the other hand, the RT change score may have been influenced by endogenous factors unrelated to the OrT neural signal, as 33% of the subject variation in RT change scores was not accounted by OrT change scores. We therefore performed a brain-wide, mass-univariate search to detect the influence of perceptual or motor processing on RT via neural processes other than those captured by OrT. Correlations between the RT change score and regional activity was computed on a voxel-basis with the OrT change score partialled out. Two isolated brain areas were identified with F-values > 6.70, which are associated with uncorrected p-values < 0.001. However, neither region survived an SPM99 correction for multiple comparisons.

Although the correlation between OrT pattern expression and RT change scores was quite strong, its interpretation is not altogether straightforward. There is the likelihood that activity of latent $v(s,t)$ revealed in the OrT pattern is different from the neural activity that is responsible for the perceptual suppression effects manifested in RT. The physiological events that are antecedents of response selection and response execution may be too brief to accurately resolve in the BOLD signal. On the other hand, the strong correlation between OrT pattern expression and RT reductions with stimulus repetition might be the result of a top-down process that operates over a more extended timeframe, for example, its operation may extend, say, from fifty milliseconds post stimulus onset to three hundred milliseconds post response initiation. In other words, the strong correlation between OrT pattern expression and RT change scores may reflect a functional coupling of two distinct aspects of learning and memory.

The question therefore remains as to whether the latent signal associated with the OrT pattern represents a bottom-up flow of information from sensory cortex to limbic, temporoparietal and prefrontal cortices, or represents top-down feedback to sensory pathways, or a combination of these two signals. A more elaborate experimental design and a more elaborate OrT analysis is needed to answer this question. Indeed, a model of local neural processing with multiple inputs is needed, namely, a model that includes both bottom-up and top-down input signals, and possibly a modulation of these inputs by hysteresis effects associated with prior stimulus events. Penny et al. [15] have described such a model, "bilinear dynamic systems." Were we to redesign our experiment to dissociate these different signals, OrT would be applied separately to the images of GLM trial parameters associated with the different input signals (each having first been convolved with the local hemodynamic response function). The resulting OrT analyses would likely provide more definitive answers regarding the nature of the latent signals that exhibited ordinal trends across successive stimulus repetitions.

Finally, the linear mean trend of the mass-univariate analysis was statistically nonsignificant. Moreover, of the two isolated regions that exhibited relatively large F-statistics neither manifested a significant correlation between RT change scores and the corresponding difference in voxel activity. The effect size of GLM mean contrasts appeared to have been diluted by features of the latent physiological (neural) processes that were not well described by the fixed predictor variables, including the contributions of subject-dependent factors.

4.2. Novel approaches to type-I error control

Of practical interest in inferential statistics is whether guided PCA and ICA—and OrT in particular—can augment the sensitivity of mass-univarate analysis while maintaining control over type-I errors. The facts are that in routine applications of mass-univariate methods, theoretical models oftentimes supply only rough approximations to the architecture of the underlying neural information processing. That is, the level of explanatory power is only modest to moderate for voxels containing real experimental effects. This practical reality collides with the need to control type-I error rates in brain-wide maps of GLM goodness-of-fit statistics. In order to control the false positive detection rate, mass-univariate analysis requires that a Bonferroni-like correction be applied. But the outcome of Bonferroni-like corrections for multiple comparisons is predictable, namely, a substantial portion of voxels that contain real experimental effects will not be identified as statistically significant.

Development of inferential methods that reduce the stiff penalty of high type-II error rates—in exchange for tight control over type-I errors—is an ongoing project in brain mapping, for example, type-I error control based on the statistics of false discovery rate (FDR) [43, 44], conjunction analysis and meta-analyses [45, 46]. But oftentimes investigators resort to less formal remedial approaches to further enhance the detection of voxels with real experimental effects: albeit they are willing to tolerate false-positive rates higher than $p = 0.05$. Currently researchers report, on a routine basis, brain maps of experimental effects based on single voxel statistics, for example, $p < 0.001$ for a standard F- or t-statistic—in lieu of imposing the more stringent, multivoxel Bonferroni-like correction.

However we would offer as an alternative to FDR, conjunction analysis and the informal approaches, conjoint multivariate and mass-univariate analyses. We suggest that multivariate modeling supplies essential information about latent neural processing that mass-univariate modeling lacks, namely, information about the similarities in $\mathbf{u}(s,t)$ activity between brain voxels. We anticipate that conjoint multivariate and mass-univariate modeling will provide real improvements in the detection of voxels with real experimental effects while maintaining control of the false-positive detection rate. Moreover, we expect these improvements will be realized in all multivariate methods including MLM, gPLS, OrT, and other forms of guided PCA and ICA, for example, probabilistic PCA and ICA.

Among multivariate methods the OrT analysis is unique in its method of controlling type-I errors. By comparison, in MLM and related PPCA and PICA, eigenvalue statistics are used to limit the number of principal components to the smallest set for which the complementary set of components is not distinguishable from the statistics of random Gaussian fields. In MLM specifically, the presumption is that on average the time-by-subject scores of the significant principal components account for at least a modest portion of the variance in a majority of the voxels that contain real experimental effects—specifically those effects described by the associated theoretical model $F(\nu(s,t),\boldsymbol{\theta})$ and the corresponding GLM. Implicit in PPCA and PICA modeling—as well as in MLM—is the presumption that all nuisance sources of region-by-condition-by-subject variance can be accurately articulated for inclusion in their respective observation models: of particular importance are the competing sources of variance with effect sizes that are comparable to those of main experimental interest, including nuisance sources that are partially correlated with the experimental design variables. By contrast, in an OrT analysis it is expected that across the spectrum of latent variable effects, the least is known about the spatiotemporal properties of nuisance effects: indeed, less is known about most nuisance effects than about the latent neural processes of experimental interest. For these reasons, OrT controls the type-I error rate using nonparametric statistics that are different from eigenvalue statistics [7]. Further in its applications to date, OrT analysis has appeared to provide relatively unconfounded and unbiased estimators of target patterns. One example of OrT pattern estimation is illustrated in our review of a group analysis of event-related fMRI data from a study of visuo-perceptual adaptation.

5. CONCLUSIONS

The aim of this report is to explicate the potential benefits of conjoint multivariate and mass-univariate analyses in human brain mapping. The practical reality is that neither modeling technique alone provides an exact description of the physiological mechanisms that are the actual determinants of the imaging data. We argue that it takes conjoint mass-univariate and multivariate analyses to determine the exactness of either modeling approach.

We began by reviewing the benefits that are afforded by MLM—a guided PCA approach that is strongly reliant on theoretical constructs of neural information processing, and speculated as to how MLM could best be combined with mass-univariate analysis to achieve a reciprocal advantage. On the other hand, because over reliance on conventional neuroscientific theory has its drawbacks, additional guided PCA methods are recommended to uncover novel features of the data $\mathbf{u}(s,t)$ that are associated with neural machinery not heretofore anticipated. The new OrT statistical analysis was presented as the latest example of a guided PCA that combines the capabilities not only to verify the activation of the neural machinery that we already understand, but also discover reliable signatures of new neural machinery. We examined the details as to how OrT achieves its expanded capacity through the exploration of individual differences and the interactions between experimental task parameters and endogenous factors. We suggest that OrT analysis, as well as several other guided PCA and ICA, is especially relevant to studies of memory and learning for which there are ordinarily inherited and acquired differences among individuals.

Finally we argue that conjoint multivariate and mass-univariate modeling is a novel approach that significantly enhances the detection of real experimental effects while maintaining control of the false-positive detection rate. Moreover, we expect these improvements will be realized in all multivariate methods including MLM, partial least squares (PLS and gPLS), OrT and other forms of guided PCA and ICA.

APPENDIX

Listed below are the six computational steps of the OrT analysis. This computational recipe for OrT assumes that the imaging data have undergone sufficient preprocessing to yield one image per subject per task condition. Details are provided below for the case in which there are three-task conditions, denoted below as B, E_1 and E_2. However, our recipe can be generalized to any number of task conditions (two or greater).

Step 1. Application of a projection operator, P, by multiplication from the right according to YP, to eliminate strictly task-independent effects: $\mathbf{P}$ is constructed from the set of $2N$ eigenimages of the Helmert-transformed data matrix $\mathbf{H}'\mathbf{Y}$, where N is the group sample size. The Eigen decomposition can be written as $\mathbf{Y}'\mathbf{H}\mathbf{H}'\mathbf{Y}\mathbf{W} = \mathbf{W}\boldsymbol{\Lambda}$ with the Helmert matrix

$$\mathbf{H} = \begin{pmatrix} -\mathbf{I}_N & \mathbf{I}_N \\ \mathbf{I}_N & \mathbf{I}_N \\ \mathbf{0} & -2\mathbf{I}_N \end{pmatrix}. \tag{A.1}$$

The matrix $\mathbf{W}$ contains the $2N$ eigenimages as column vectors, and $\boldsymbol{\Lambda}$ is a $2N$-diagonal matrix containing the nonzero eigenvalues. The matrix $\mathbf{W}\mathbf{W}'$ corresponds to the projection matrix $\mathbf{P}$ of the Helmert eigenimages. The modified data matrix $\mathbf{YP}$ has the same dimensions as the original data matrix $\mathbf{Y}$. However, $\mathbf{YP}$ contains N fewer activation patterns and has rank $2N$, that is, a lower rank than the matrix $\mathbf{Y}$, which has rank $3N$.

Removal of the task-independent subject effects is necessary in order to obviate their being confounded with

the target patterns of experimental interest. Moreover, task-independent subject effects are not usually of interest as they describe effects that remained unchanged by the experimental design manipulation.

Step 2. Application of the OrT design matrix, Q, by multiplication from the left according to $[Q(Q'Q)^{-1/2}]'YP$, to increase the salience of ordinal trend effects. In the case of three-task conditions,

$$\mathbf{Q} = \begin{pmatrix} \mathbf{I_N} & \mathbf{0} \\ \mathbf{I_N} & \mathbf{I_N} \\ \mathbf{0} & \mathbf{I_N} \end{pmatrix}. \tag{A.2}$$

Step 3. Singular value decomposition (SVD) is applied to the mean centered $[Q(Q'Q)^{-1/2}]'YP$ matrix. This is equivalent to applying principal components analysis (PCA), that is,

$$\mathbf{P'Y'Q(Q'Q)^{-1}Q'YPV} = \mathbf{V}\Sigma \tag{A.3}$$

in which $\mathbf{V}$ contains $2N$ orthogonal eigenimages as column vectors; and Σ is a $2N$-diagonal matrix of the eigenvalues.

Step 4. The first K eigenimages are tested for the presence of an ordinal trend.

For the first K singular images, a $2N \times K$ predictor array is calculated according to $[E_1 - B; E_1 + B - 2E_2]$. B is obtained by projection of all K images onto the raw data pertaining to condition B, that is, $B = Y(1 : N, :)V(:, 1 : K)$. Likewise for E_1 and E_2, we have $E_1 = Y(N + 1 : 2N, :)V(:, 1 : K)$, and $E_2 = Y(2N + 1 : 3N, :)V(:, 1 : K)$. We then conduct a linear regression to best predict the dependent variable of the regression, which is a $2N$ column vector $[1; -1]$, with the $2N \times K$ predictor array described above,

$$\begin{pmatrix} \mathbf{1} \\ \mathbf{-1} \end{pmatrix} \approx \begin{pmatrix} \mathbf{E_1 - B} \\ \mathbf{E_1 + B - 2E_2} \end{pmatrix} \beta. \tag{A.4}$$

This linear multivariate regression analysis is a type of discriminant analysis that produces the linear combination of the K eigenimages, according to $V(:, 1 : K)\beta$, whose mean expression changes maximally across task conditions. For the test of significance of the ordinal trend, we compute the task-subject scores for this new linear-combination image according to the right-hand side of the above regression equation. The test of significance is based on the minimum number of exceptions to a perfect segregation of the two contrast scores $\mathbf{C}_1$ and $\mathbf{C}_2$ that are calculated from the resultant pattern's expression according to $\mathbf{C}_1 = \mathbf{E_1} - \mathbf{B}$ and $\mathbf{C}_2 = \mathbf{E}_1 + \mathbf{B} - \mathbf{E}_2$, respectively. The number of exceptions is an inverse correlate to the maximum number of subjects who exhibit monotonic task-activity curves as can be appreciated from Figure 4. Monte-Carlo simulations of random Gaussian fields provide the type-I error rate of ordinal trends based on the minimum number of exceptions to a perfect segregation of scores.

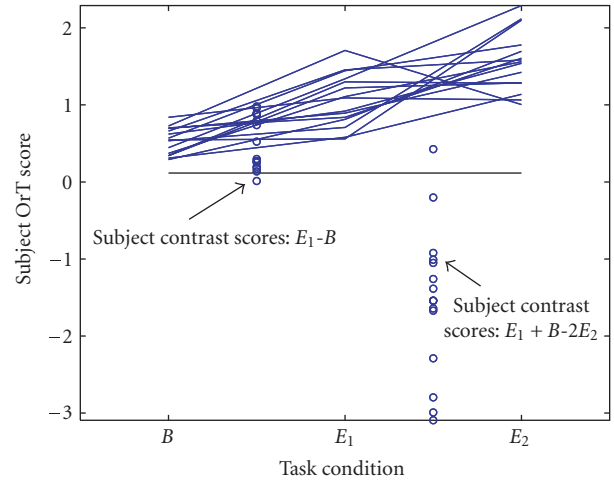

FIGURE 4: Sample graphic output of an OrT analysis for the imaging data of 15 subjects, for which positive ordinal trends were predicted across task conditions B, E_1, and E_2. Statistical significance is a function of the maximal separation achieved between subject contrast scores $C_1 = E_1 - B$ and $C_2 = E_1 + B - E_2$, calculated for arbitrary linear combinations for a fixed number of PCs. The optimum segregation (horizontal line) between the two sets of contrast values (columns of open circles) is displayed for a linear combination of the first three PCs. Level of segregation achieved with this number of PCs is one exception, which is significant at $p < 0.005$. The overlay of the B-E_1-E_2 trends for the 15 subjects (uniramous line segments) identifies the exceptional individual.

Step 5. Bootstrap resampling methods [47] are applied to OrT topographic pattern estimates to evaluate the reliability of nonzero voxel weights. The reliability of individual voxel weights is computed as z-scores, where the higher the z-score the less likely it is that any subject is extraordinarily influential in determining voxel weights. In the bootstrap, Steps 1–4 that were performed on the original subject sample are repeated 100–1000 times on samples of subjects that have been chosen randomly with replacement from the original subject pool. The inverse coefficient of variation (ICV) serves as the measure of the reliability of the regional weight at each voxel in the topographic pattern. ICV is computed from the point estimate of the regional weights, w_{voxel}, and the variability of the resampling process around this point estimate, captured as the standard deviation σ_{voxel}, as

$$\text{ICV}_{\text{voxel}} = \frac{w_{\text{voxel}}}{\sigma_{\text{voxel}}} \sim N(0, 1) \tag{A.5}$$

and is approximately standard-normally distributed. The larger the absolute magnitude of $\text{ICV}_{\text{voxel}}$, the smaller the relative variability of the regional weight about its point estimate value. Common benchmark thresholds are chosen as 1.64, 2.33, and 3.09, which corresponds to a one-tailed p-level of 0.05, 0.01, and 0.001, respectively.

Step 6. Forward application of pattern estimates into new data sets [48–53]: a pattern $\mathbf{v}$ from a guided PCA—in particular an OrT analysis—can be projected into any data matrix $\mathbf{Y}$ according to the algebraic rule $\mathbf{Yv}'$—provided that

the row vector **v** and the vectorized images in **Y** are all coregistered to the same brain atlas; and the same voxel mask has been applied to every image. The resulting column vector consists of the levels of expression of **v** in the individual images in **Y**, for example, for each subject and experimental condition.

The subject-by-condition scores **v** are normally used to evaluate correlations between the regional activity associated with a latent neural process $\nu(s,t)$ and (a) hypothetical responses of $\nu(s,t)$ to experimental task challenges, or (b) experimental relevant behavioral and demographic variables. In addition, the OT forward application is a useful tool for testing whether the topographic footprint of a latent process found in one parametric series of experimental conditions is also evident in the images of other task conditions within the same experiment, or in the images obtained in independent, but theoretically related experimental studies.

ACKNOWLEDGMENTS

The authors thank two anonymous reviewers for a critical reading of the manuscript for this article and their many helpful questions and suggestions. This work was supported by federal Grants NINDS RO1 NS35069, NIA RO1 AG16714, and NINDS RO1 NS02138

REFERENCES

[1] E. Zarahn, "Using larger dimensional signal subspaces to increase sensitivity in fMRI time series analyses," *Human Brain Mapping*, vol. 17, no. 1, pp. 13–16, 2002.

[2] K. J. Worsley, J.-B. Poline, K. J. Friston, and A. C. Evans, "Characterizing the response of PET and fMRI data using multivariate linear models," *NeuroImage*, vol. 6, no. 4, pp. 305–319, 1997.

[3] J. R. Moeller, S. C. Strother, J. J. Sidtis, and D. A. Rottenberg, "Scaled subprofile model: a statistical approach to the analysis of functional patterns in positron emission tomographic data," *Journal of Cerebral Blood Flow and Metabolism*, vol. 7, no. 5, pp. 649–658, 1987.

[4] M. J. McKeown and T. J. Sejnowski, "Independent component analysis of fMRI data: examining the assumptions," *Human Brain Mapping*, vol. 6, no. 5-6, pp. 368–372, 1998.

[5] A. R. McIntosh, W. K. Chau, and A. B. Protzner, "Spatiotemporal analysis of event-related fMRI data using partial least squares," *NeuroImage*, vol. 23, no. 2, pp. 764–775, 2004.

[6] A. R. McIntosh, F. L. Bookstein, J. V. Haxby, and C. L. Grady, "Spatial pattern analysis of functional brain images using partial least squares," *NeuroImage*, vol. 3, no. 3, pp. 143–157, 1996.

[7] C. G. Habeck, J. W. Krakauer, C. Ghez, et al., "A new approach to spatial covariance modeling of functional brain imaging data: ordinal trend analysis," *Neural Computation*, vol. 17, no. 7, pp. 1602–1645, 2005.

[8] D. Hu, L. Yan, Y. Liu, et al., "Unified SPM-ICA for fMRI analysis," *NeuroImage*, vol. 25, no. 3, pp. 746–755, 2005.

[9] K. J. Friston, A. P. Holmes, J.-B. Poline, et al., "Analysis of fMRI time-series revisited," *NeuroImage*, vol. 2, no. 1, pp. 45–53, 1995.

[10] K. J. Friston and J. Ashburner, "Generative and recognition models for neuroanatomy," *NeuroImage*, vol. 23, no. 1, pp. 21–24, 2004.

[11] C. F. Beckmann and S. M. Smith, "Tensorial extensions of independent component analysis for multisubject FMRI analysis," *NeuroImage*, vol. 25, no. 1, pp. 294–311, 2005.

[12] G. E. Alexander, M. J. Mentis, J. D. Van Horn, et al., "Individual differences in PET activation of object perception and attention systems predict face matching accuracy," *NeuroReport*, vol. 10, no. 9, pp. 1965–1971, 1999.

[13] D. Fernandez-Duque, J. A. Baird, and M. I. Posner, "Executive attention and metacognitive regulation," *Consciousness and Cognition*, vol. 9, no. 2, pp. 288–307, 2000.

[14] K. Friston, "Learning and inference in the brain," *Neural Networks*, vol. 16, no. 9, pp. 1325–1352, 2003.

[15] W. Penny, Z. Ghahramani, and K. Friston, "Bilinear dynamical systems," *Philosophical Transactions of the Royal Society of London Series B: Biological Sciences*, vol. 360, no. 1457, pp. 983–993, 2005.

[16] A. A. Petrov, B. A. Dosher, and Z.-L. Lu, "The dynamics of perceptual learning: an incremental reweighting model," *Psychological Review*, vol. 112, no. 4, pp. 715–743, 2005.

[17] D. C. Van Essen, "Corticocortical and thalamocortical information flow in the primate visual system," *Progress in Brain Research*, vol. 149, pp. 173–185, 2005.

[18] S. Zeki, "The Ferrier Lecture 1995 behind the seen: the functional specialization of the brain in space and time," *Philosophical Transactions of the Royal Society of London Series B: Biological Sciences*, vol. 360, no. 1458, pp. 1145–1183, 2005.

[19] D. Eidelberg, J. R. Moeller, K. Kazumata, et al., "Metabolic correlates of pallidal neuronal activity in Parkinson's disease," *Brain*, vol. 120, no. 8, pp. 1315–1324, 1997.

[20] P. M. Thompson, T. D. Cannon, K. L. Narr, et al., "Genetic influences on brain structure," *Nature Neuroscience*, vol. 4, no. 12, pp. 1253–1258, 2001.

[21] S. M. Kosslyn, J. T. Cacioppo, R. J. Davidson, et al., "Bridging psychology and biology: the analysis of individuals in groups," *American Psychologist*, vol. 57, no. 5, pp. 341–351, 2002.

[22] J. Fan, J. Fossella, T. Sommer, Y. Wu, and M. I. Posner, "Mapping the genetic variation of executive attention onto brain activity," *Proceedings of the National Academy of Sciences of the United States of America*, vol. 100, no. 12, pp. 7406–7411, 2003.

[23] J. R. Gray, C. F. Chabris, and T. S. Braver, "Neural mechanisms of general fluid intelligence," *Nature Neuroscience*, vol. 6, no. 3, pp. 316–322, 2003.

[24] J. R. Moeller and S. C. Strother, "A regional covariance approach to the analysis of functional patterns in positron emission tomographic data," *Journal of Cerebral Blood Flow and Metabolism*, vol. 11, no. 2, pp. A121–A135, 1991.

[25] D. Eidelberg, J. R. Moeller, V. Dhawan, et al., "The metabolic topography of parkinsonism," *Journal of Cerebral Blood Flow and Metabolism*, vol. 14, no. 5, pp. 783–801, 1994.

[26] A. R. McIntosh, "Mapping cognition to the brain through neural interactions," *Memory*, vol. 7, no. 5-6, pp. 523–548, 1999.

[27] F.-H. Lin, A. R. McIntosh, J. A. Agnew, G. F. Eden, T. A. Zeffiro, and J. W. Belliveau, "Multivariate analysis of neuronal interactions in the generalized partial least squares framework: simulations and empirical studies," *NeuroImage*, vol. 20, no. 2, pp. 625–642, 2003.

[28] J. Cohen, P. Cohen, S. G. West, and L. S. Aiken, *Applied Multiple Regression/Correlation Analysis for the Behavioral Sciences*, Lawrence Erlbaum, Mahwah, NJ, USA, 3rd edition, 2003.

[29] C. G. Habeck, H. J. Hilton, E. Zarahn, T. Brown, and Y. Stern, "An event-related fMRI study of the neural networks underlying repetition suppression and reaction time priming in implicit visual memory," *Brain Research*, vol. 1075, no. 1, pp. 133–141, 2006.

[30] D. L. Schacter, E. Reiman, A. Uecker, M. R. Polster, L. S. Yun, and L. A. Cooper, "Brain regions associated with retrieval of structurally coherent visual information," *Nature*, vol. 376, no. 6541, pp. 587–590, 1995.
[31] J. D. Cohen, B. MacWhinney, M. Flatt, and J. Provost, "PsyScope: a new graphic interactive environment for designing psychology experiments," *Behavioral Research Methods, Instruments, and Computers*, vol. 25, no. 2, pp. 257–271, 1993.
[32] J. Talairach and P. Tournoux, *A Co-planar Stereotaxic Atlas of a Human Brain*, Stuttgart, Trieme, 1988.
[33] K. J. Friston, P. Fletcher, O. Josephs, A. Holmes, M. D. Rugg, and R. Turner, "Event-related fMRI: characterizing differential responses," *NeuroImage*, vol. 7, no. 1, pp. 30–40, 1998.
[34] N. K. Logothetis, J. Pauls, M. Augath, T. Trinath, and A. Oeltermann, "Neurophysiological investigation of the basis of the fMRI signal," *Nature*, vol. 412, no. 6843, pp. 150–157, 2001.
[35] K. J. Friston, A. Holmes, J.-B. Poline, C. J. Price, and C. D. Frith, "Detecting activations in PET and fMRI: levels of inference and power," *NeuroImage*, vol. 4, no. 3, pp. 223–235, 1996.
[36] E. Zarahn, "Testing for neural responses during temporal components of trials with BOLD fMRI," *NeuroImage*, vol. 11, no. 6, pp. 783–796, 2000.
[37] Z. Kourtzi and N. Kanwisher, "Representation of perceived object shape by the human lateral occipital complex," *Science*, vol. 293, no. 5534, pp. 1506–1509, 2001.
[38] R. J. Dolan, G. R. Fink, E. Rolls, et al., "How the brain learns to see objects and faces in an impoverished context," *Nature*, vol. 389, no. 6651, pp. 596–599, 1997.
[39] M. D. Rugg, L. J. Otten, and R. N. A. Henson, "The neural basis of episodic memory: evidence from functional neuroimaging," *Philosophical Transactions of the Royal Society of London Series B: Biological Sciences*, vol. 357, no. 1424, pp. 1097–1110, 2002.
[40] S. M. Kosslyn, O. Koenig, A. Barrett, C. B. Cave, J. Tang, and J. D. Gabrieli, "Evidence for two types of spatial representations: hemispheric specialization for categorical and coordinate relations," *Journal of Experimental Psychology: Human Perception and Performance*, vol. 15, no. 4, pp. 723–735, 1989.
[41] C. B. Cave and S. M. Kosslyn, "The role of parts and spatial relations in object identification," *Perception*, vol. 22, no. 2, pp. 229–248, 1993.
[42] B. M. Bly and S. M. Kosslyn, "Functional anatomy of object recognition in humans: evidence from positron emission tomography and functional magnetic resonance imaging," *Current Opinion in Neurology*, vol. 10, no. 1, pp. 5–9, 1997.
[43] S. P. Ellis, M. D. Underwood, V. Arango, and J. J. Mann, "Mixed models and multiple comparisons in analysis of human neurochemical maps," *Psychiatry Research: Neuroimaging*, vol. 99, no. 2, pp. 111–119, 2000.
[44] C. R. Genovese, N. A. Lazar, and T. Nichols, "Thresholding of statistical maps in functional neuroimaging using the false discovery rate," *NeuroImage*, vol. 15, no. 4, pp. 870–878, 2002.
[45] C. J. Price and K. J. Friston, "Cognitive conjunction: a new approach to brain activation experiments," *NeuroImage*, vol. 5, no. 4, pp. 261–270, 1997.
[46] K. J. Friston, A. P. Holmes, C. J. Price, C. Büchel, and K. J. Worsley, "Multisubject fMRI studies and conjunction analyses," *NeuroImage*, vol. 10, no. 4, pp. 385–396, 1999.
[47] B. Efron, E. Halloran, and S. Holmes, "Bootstrap confidence levels for phylogenetic trees," *Proceedings of the National Academy of Sciences of the United States of America*, vol. 93, no. 23, pp. 13429–13434, 1996.
[48] J. R. Moeller and D. Eidelberg, "Divergent expression of regional metabolic topographies in Parkinson's disease and normal ageing," *Brain*, vol. 120, no. 12, pp. 2197–2206, 1997.
[49] M. Trošt, P. C. Su, A. Barnes, et al., "Evolving metabolic changes during the first postoperative year after subthalamotomy," *Journal of Neurosurgery*, vol. 99, no. 5, pp. 872–878, 2003.
[50] C. G. Habeck, B. C. Rakitin, J. R. Moeller, et al., "An event-related fMRI study of the neurobehavioral impact of sleep deprivation on performance of a delayed-match-to-sample task," *Cognitive Brain Research*, vol. 18, no. 3, pp. 306–321, 2004.
[51] C. G. Habeck, B. C. Rakitin, J. R. Moeller, et al., "An event-related fMRI study of the neural networks underlying the encoding, maintenance, and retrieval phase in a delayed-match-to-sample task," *Cognitive Brain Research*, vol. 23, no. 2-3, pp. 207–220, 2005.
[52] M. Carbon and D. Eidelberg, "Functional imaging of sequence learning in Parkinson's disease," *Journal of the Neurological Sciences*, in press.
[53] M. Trošt, S. Su, P. Su, et al., "Network modulation by the subthalamic nucleus in the treatment of Parkinson's disease," *NeuroImage*, vol. 31, no. 1, pp. 301–307, 2006.

James R. Moeller received an M.A. degree in mathematics in 1974 and a Ph.D. degree in mathematical and experimental psychology in 1976 from the University of Michigan. In 1977, he joined the division of human visual psychophysics at the David Sarnoff Research Center/RCA in Princeton, New Jersey. He contributed to research on computational theories of visual psychophysics and neural modeling applied to image understanding. He subsequently joined the Department of Neurology, Sloan-Kettering Institute, Division of Neuroimaging, in 1984, and in 1989 moved to Columbia University, joining the Department of Psychiatry. He has authored or coauthored more than 80 refereed journal articles. At Columbia his initial research interests included novel applications of multivariate analysis and pattern recognition methods to functional neuroimaging. His research projects have included the development of neuroimaging biomarkers for use in the diagnosis of specific CNS disease, as well as assessments of disease progression and treatment efficacy. His original work in Parkinson's and Alzheimer's diseases expanded to include hereditable disorders, thereby applying neurogenomics to the study of prodromal states of CNS disease. His research today is focused on developments in electromagnetic brain stimulation and computational methods of human brain mapping, with applications to $H_2{}^{15}O$ PET, functional MRI, and topographic electroencephalography.

Christian G. Habeck originally trained as a Particle Physicist, and received his M.S. degree from the University of Durham, UK, in 1994 and his Ph.D. degree from the University of Sussex, UK, in 1998. He then did a Postdoctoral fellowship at the Neurosciences Institute in La Jolla, Calif, performing large-scale computer simulations of biophysically realistic neural networks. Since 2000, he has been in the Cognitive Neuroscience Division of the Taub Institute, Department of Neurology, Columbia University Medical Center, specializing in multivariate approaches to neuroimaging analysis for EEG, PET, and MRI data in close collaboration with James R. Moeller, coauthor on the current article.

Hindawi Publishing Corporation
International Journal of Biomedical Imaging
Volume 2006, Article ID 49515, Pages 1–11
DOI 10.1155/IJBI/2006/49515

A Review on MR Image Intensity Inhomogeneity Correction

Zujun Hou

Biomedical Imaging Lab., Singapore Bioimaging Consortium, 30 Biopolis Street, Matrix #07-01, Singapore 138671

Received 11 October 2005; Revised 18 January 2006; Accepted 17 February 2006

Intensity inhomogeneity (IIH) is often encountered in MR imaging, and a number of techniques have been devised to correct this artifact. This paper attempts to review some of the recent developments in the mathematical modeling of IIH field. Low-frequency models are widely used, but they tend to corrupt the low-frequency components of the tissue. Hypersurface models and statistical models can be adaptive to the image and generally more stable, but they are also generally more complex and consume more computer memory and CPU time. They are often formulated together with image segmentation within one framework and the overall performance is highly dependent on the segmentation process. Beside these three popular models, this paper also summarizes other techniques based on different principles. In addition, the issue of quantitative evaluation and comparative study are discussed.

1. INTRODUCTION

With the frequent application of the magnetic resonance (MR) imaging method to clinical diagnosis, automatic analysis of the acquired images using techniques from computer vision and pattern recognition has received considerable attention. In developing such computer-aided diagnosis tools, a commonly encountered problem is to correct the intensity inhomogeneity (IIH) in MR images.

The IIH (also termed as the intensity nonuniformity, the bias field, or the gain field in the literature) usually refers to the slow, nonanatomic intensity variations of the same tissue over the image domain. It can be due to imaging instrumentation (such as radio-frequency nonuniformity, static field inhomogeneity, etc.) or the patient movement [1–5]. This artifact is particularly severe in MR images captured by surface coils. Two real MR images with severe IIH artifact are shown in Figure 1(a), where one can see that the intensity varies significantly for the pixels of the same tissue and the intensity values overlap markedly between the pixels of the different tissues. For comparison, the IIH corrected images by a surface fitting technique [6] are given in Figure 1(b), from which the improvement in image quality is clearly visible. The estimated IIH maps are given in Figure 1(c).

Let $\mathbf{x}$ denote the measured intensity and $\mathbf{x}'$ the true intensity. Then the most popular model in describing the IIH effect is

$$\mathbf{x} = \boldsymbol{\alpha}\mathbf{x}' + \boldsymbol{\xi}, \tag{1}$$

where $\boldsymbol{\alpha}$ denotes the IIH effect and $\boldsymbol{\xi}$ the noise. Notation of bold letters refers to 2D or 3D MR data. Figure 2 displays the widely used BrainWeb [7] simulated MR images, where on Figure 2(a) is the original image, on Figure 2(b) the image with IIH artifact, on Figure 2(c) the image with noise, and on Figure 2(d) the image with both IIH artifact and noise. From Figure 2, one can see the visual difference resulting from the IIH artifact and the noise.

To simplify the computation, one often ignores the noise and takes the logarithmic transform of intensity

$$y_i = \log x_i = \log x_i' + \log \alpha_i = y_i' + \beta_i, \tag{2}$$

where x_i is the intensity at voxel i ($i = 1, \ldots, n$). Here, to avoid numerical problems, care should be taken for those pixels/voxels with low intensities, which are usually excluded from computation.

In general, the presence of IIH can significantly reduce the accuracy of image segmentation and registration, hence decreasing the reliability of subsequent quantitative measurement. A number of techniques have been proposed to deal with this issue. In general, if a map of the IIH in the image domain (Figure 1(c) for instance) is known or can be estimated, then it is simple to correct the IIH by division in (1) or subtraction in the log-domain (2). One can obtain the IIH map from measurement in vivo [8–15], typically of a uniform phantom, [16–20], which often requires extra measurement (and increases the scanning time) or needs additional hardware which may not be readily available in some clinical departments. Also there are theoretical modeling approaches

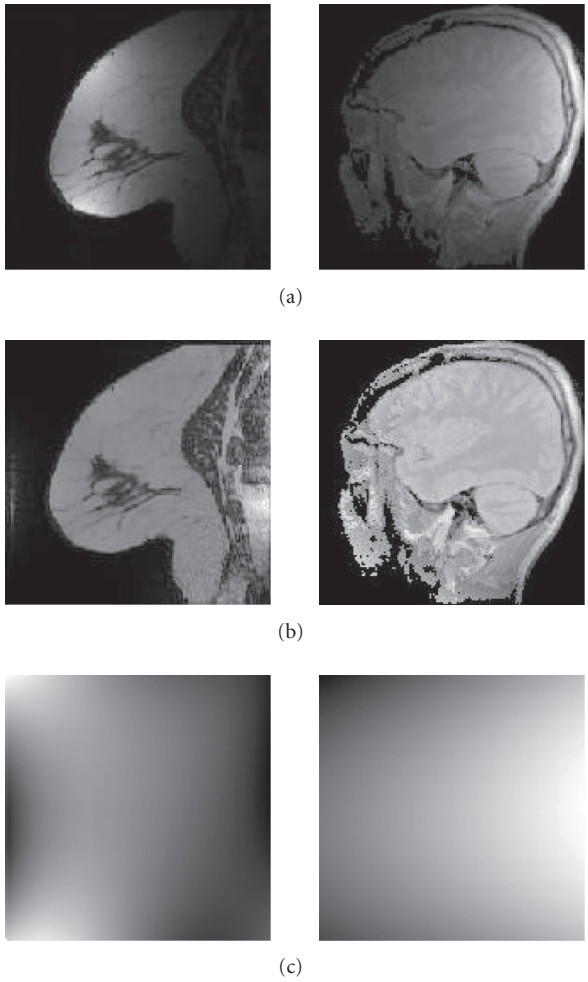

Figure 1: Sample MR images with severe intensity inhomogeneity: original images (a), corrected images (b), and estimated inhomogeneity maps (c).

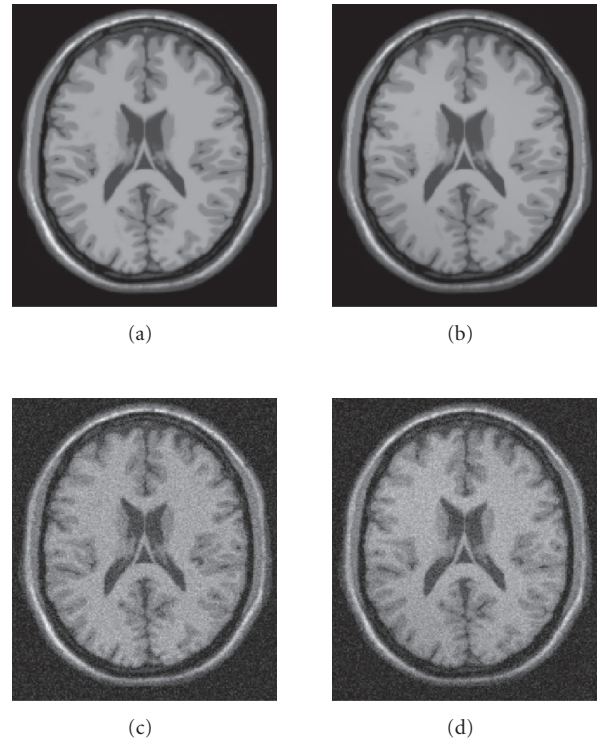

Figure 2: BrainWeb simulated images: original image (a), image with 40% inhomogeneity (b), image with 9% noise (c), and image with both artifacts (d).

[21–28] to approximate the IIH map. However, due to the complexity that causes the IIH, it is difficult to model the IIH under a variety of imaging conditions. In particular, the object-induced IIH is hard to be accounted for by phantom study or theoretical modeling.

More often, the IIH map is derived retrospectively from the image data alone. A number of research efforts have been put in this direction and many techniques have been proposed. Popular mathematical models for IIH description can be classified as follows:

(1) low-frequency model, which assumes the IIH to constitute low-frequency components in frequency domain and the IIH map can be recovered by lowpass filtering;
(2) hypersurface model, which fits the IIH map by a smooth functional, whose parameters are usually obtained using regression;
(3) statistical model, which assumes the IIH to be a random variable or a random process and the IIH map can be derived through statistical estimation;
(4) others, which are based on different principles, and sometimes without explicit assumptions on the IIH field.

With this in mind, the IIH correction methods are categorized into lowpass filtering, statistical modeling, surface fitting and others, which are detailed, respectively, in the following sections.

For an early literature review, interested readers are referred to [29], where an evaluation of the IIH correction effect for brain tumor segmentation is also reported. This paper attempts to summarize the recent progress and focus will be on mathematical modeling for IIH removal. Nevertheless, it is by no means an exhaustive summary. For simplicity, the description will be on single-channel data only.

2. LOWPASS FILTERING

Since the IIH is slowly varying in the image domain, its spectrum in frequency domain will be concentrated in the low-frequency end. Therefore the IIH could be separated from the true image by a lowpass filter, $\mathcal{L}$. After lowpass filtering in log-domain, one would approximately have

$$\mathcal{L}\{\mathbf{y}\} \approx \beta. \tag{3}$$

This procedure to correct the IIH is similar to the homomorphic filtering in digital image processing for the correction of illumination inhomogeneity [30]. In fact, (1) easily reminds

one of the illumination-reflectance model in optical imaging [30], where the artifact from the illumination inhomogeneity is often termed "shading" in the literature. Thus, techniques for shading correction, such as the homomorphic filtering, can be adopted for IIH removal and the converse also holds. An investigation of applying IIH correction methods to deal with the shading problem in microscopic images has been carried out in [31].

Due to their simplicity and efficiency in implementation, lowpass filtering methods have been widely used [30–43]. For a summary, interested readers are referred to [42]. Also in [42], the impact of filter width on IIH correction was investigated and it was found that these methods should be used with care to avoid intensity distortion and artificial artifacts in the corrected images. Basically, for MR images, due to the overlapping spectrum between the patient data and the IIH, the effectiveness of most conventional lowpass filtering in removing the IIH is generally quite limited.

Luo et al. [44] presented a technique to recover low-frequency components which correspond to anatomic structure and are lost during the lowpass filtering. The method expresses the signal with a linear combination of singularity functions. The higher-frequency components are assumed to be less affected by the IIH and are used to reconstruct the true image, after which the ratio between the observed and estimated image is used for IIH map approximation.

Recently, lowpass filtering methods have been extended using the wavelet transform [45, 46] and were shown to be effective in removing IIH in images acquired by surface coils and phase array coils. Compared with usual lowpass filtering methods, the multiresolution analysis allows one to select an optimal scale from which the approximate band in the wavelet transform domain is used for estimating the IIH map.

In [47], an improvement of a lowpass filtering method [43] was presented. The method varies the filter kernel size to minimize the segmentation error. The idea is generally similar to [45, 46] in addressing IIH correction from the scale space, but differs in the criterion to determine the optimal scale.

3. SURFACE FITTING

Since the inhomogeneity field is slowly varying, it is natural to approximate the IIH by a parametric smooth functional [6, 48–58]. Very often, the parameter estimation is linked to image segmentation. In this way, the two different problems, IIH correction and image segmentation, are formulated in one framework and solved simultaneously. Alternatively, the parameter searching can be guided through the variation of some global image feature in an iterative process. A typical example is to minimize the entropy of gray-level histogram.

3.1. Segmentation

A large category of surface fitting approaches search the parameters by fitting with respect to a set of tissue points encoding information about the IIH. Let $I = \{1, \ldots, n\}$ index the voxel coordinates of brain tissue. Then, in order to determine the parameters of this functional, one needs to find/segment a set of voxels $S_I \subseteq I$ which convey information about the IIH map. Among these methods, the essential difference lies in the identification of S_I, and hence decoding the IIH information from S_I.

Dawant et al. [48] proposed to manually select S_I such that they belong to the same type of tissue. As a result, the intensity variation among these voxels can largely be attributed to IIH. However, expert supervision to select points is time consuming and error prone, especially for volume data. Wang et al. [59] has presented an automated method for generating the reference points.

Meyer et al. [49] employed the LCJ method [60] to preliminarily segment the image and then fit a smooth functional over the segmented image. The LCJ segmentation method assumes the image to be piecewise smooth and requires that the different objects are well separated at the boundaries, which is quite stringent in practice, particularly when image quality is poor due to perturbation such as noise, partial volume artifact, or IIH. Beside that, not every clinical department can afford the computer cost to run the parallel LCJ algorithm.

Liew and Yan [58] approximated the IIH as a stack of B-spline surfaces with continuity constraints across slices. The estimation of IIH interwines with a fuzzy c-means clustering process. In [61, 62], segmentation that utilizes local scale as homogeneous criteria has been presented and applied to IIH correction.

When a statistical classifier, such as Gaussian classifier or random field modeling, is exploited [50, 53, 63], the process is similar to the parameter estimation in Section 4, where the parameters are associated with a probability distribution and can be estimated with common statistical estimation methods such as maximum-likelihood estimation.

3.2. Entropy minimization

As a frequently used criterion to characterize the intensity distribution of an image, entropy has been employed to design algorithms for image restoration, thresholding, or classification [64, 65]. Also, it has been utilized to quantify the image property with IIH present and guide the parameter searching for IIH removal [54–57].

It is assumed that the intensity distribution of the original image is multimodal, and the presence of IIH causes the intensity overlapping between objects. Figure 3 shows the histograms of brain tissue in a BrainWeb-simulated image (Figure 3(a)) and the head image in Figure 1 (Figure 3(b)). On Figure 3(a), the solid line is the histogram without inhomogeneity, where the modes corresponding to different tissues are very distinctive. With the presence of IIH (dashed-dotted line), the valleys between different modes are markedly flattened. For the head image with severe IIH, the histogram (Figure 3(b)) is so flat that the modes corresponding to the gray matter and the white matter are difficult to distinguish. The flattening of the histogram leads to the increase in the entropy of the image, therefore, the IIH

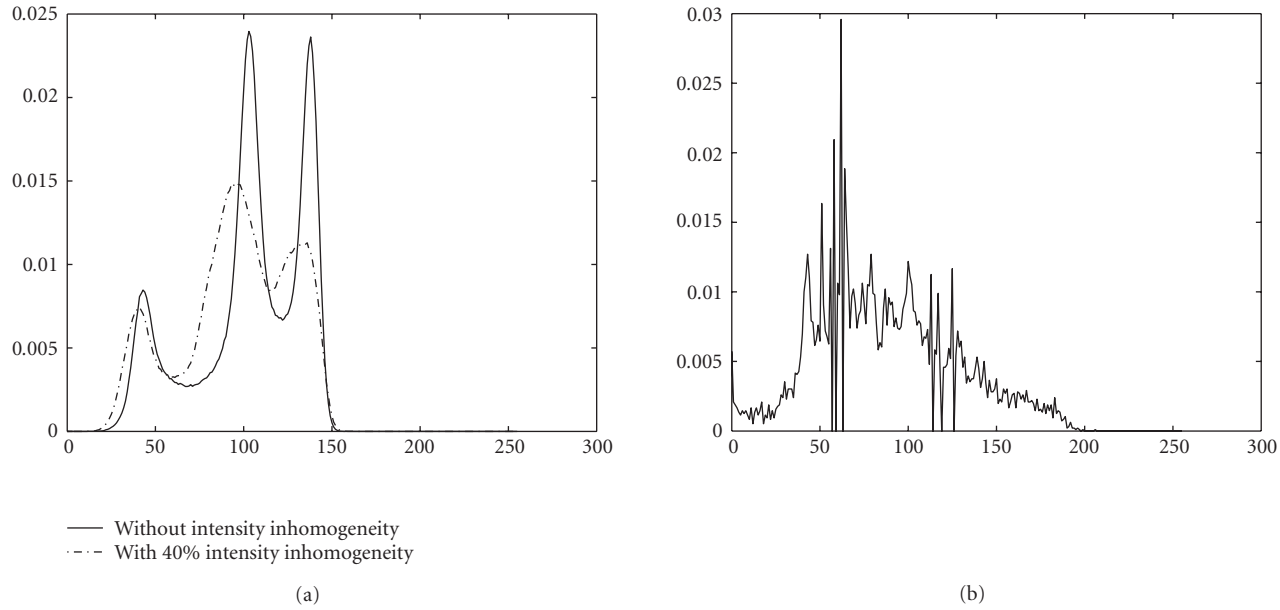

FIGURE 3: Histogram of brain tissue with the presence of intensity inhomogeneity. (a) Corresponds to a BrainWeb-simulated image: without intensity inhomogeneity (solid line) and with 40% intensity inhomogeneity (dashed-dotted line), and on (b) the head image (Figure 1).

correction can be achieved through searching the parameter space of the IIH model such that the entropy of the image is reduced. It should be pointed out that direct minimization on the entropy would lead to the null field [55, 66]. To avoid this pitfall, constraints over the solution space are necessary. Mangin [55] constrained the solution to minimize the distance between the mean values of the restored and the original image. In [57], the restored image was constrained to have the same mean value as the original one.

Evidently, other quantities relevant to image features, variance for example, can also be applicable in a similar fashion. Again, constraints upon the solution space are necessary.

4. STATISTICAL MODELING

The statistical methods [67–71] may assume that the IIH follows a distribution, the Gaussian distribution for example, or model the IIH as a random process, such as the Markov random field.

4.1. Bayesian framework

The Bayes' rule has frequently been employed to estimate the IIH map when the IIH is modeled by a distribution. Let β be a random vector $(\beta_1, \ldots, \beta_n)$ with probability density $p(\beta)$. To estimate β, one can maximize the conditional probability of β given $\mathbf{y}$ (the log-transform of $\mathbf{x}$) as follows:

$$\hat{\beta} = \max_{\beta} p(\beta \mid \mathbf{y}). \tag{4}$$

This is called the *maximum a posterior* (MAP) estimate and, by the Bayes rule, is equivalent to

$$\hat{\beta} = \max_{\beta} p(\mathbf{y} \mid \beta)\, p(\beta). \tag{5}$$

Wells et al. [67] used the Gaussian distribution to model the entire log-transformed bias field and the observed intensity at voxel i:

$$p(\beta) = G_{\psi_\beta}(\beta), \tag{6}$$

$$p(y_i \mid \Gamma_i, \beta_i) = G_{\psi_{\Gamma_i}}(y_i - \mu(\Gamma_i) - \beta_i), \tag{7}$$

where Γ_i is the tissue class at voxel i with mean value $\mu(\Gamma_i)$, and

$$G_{\psi_{\mathbf{x}}}(\mathbf{x}) = (2\pi)^{-n/2} \mid \psi_{\mathbf{x}} \mid^{-1/2} \exp\left(-\frac{1}{2} \mathbf{x}^T \psi_{\mathbf{x}}^{-1} \mathbf{x} \right), \tag{8}$$

with $\psi_{\mathbf{x}}$ as the covariance matrix. By assuming the statistical independence of voxel intensities and from (7), one can derive

$$\begin{aligned} p(\mathbf{y} \mid \beta) &= \prod_i p(y_i \mid \beta_i) \\ &= \prod_i \sum_{\Gamma_i} p(y_i \mid \Gamma_i, \beta_i)\, p(\Gamma_i). \end{aligned} \tag{9}$$

When the image data is not polluted by IIH, the above method is simply the tissue classification using a mixture Gaussian model. Hence, this method essentially interleaves the IIH correction with a Gaussian classifier. Guillemaud and Brady [68] observed that the effect of IIH correction by Wells et al. algorithm is substantially affected by the Gaussian classifier. In real images, it is very possible for the histogram to deviate from the mixture Gaussian distribution. A modification was then proposed by introducing a tissue class Γ_{other} with a non-Gaussian distribution

$$p(y_i \mid \beta_i) = \sum_{\Gamma_j} p(y_i \mid \Gamma_j)\, p(\Gamma_j) + \lambda p(\Gamma_{\text{other}}). \tag{10}$$

With this modification, the IIH is only estimated with respect to the Gaussian classes. Including the non-Gaussian component makes the Gaussian classifier less influenced by possible outliers arising in images.

4.2. Spatial modeling

In the method by Wells et al. the IIH correction has not explicitly considered the context of IIH map. Since the IIH field is slowly varying in the image domain, the values of the IIH map in neighboring pixels/voxels would be close. When this spatial relation is taken into account in the IIH modeling, one would likely arrive at a smoother approximation of the IIH map. A useful tool for spatial modeling is the Markov random field (MRF), which is first employed by Geman and Geman [72] for image segmentation. Held et al. [69] have employed the MRF to model IIH. According to the Hamersly-Clifford theorem [73], the prior probability $p(\mathbf{y})$ is given by the Gibbs distribution

$$p(\mathbf{y}) \propto \exp\{-U(\mathbf{y})\} \tag{11}$$

with the Gibbs energy

$$U(\mathbf{y}) = \alpha \sum_{\langle i,j \rangle} (y_i - y_j)^2 + \beta \sum_i y_i^2, \tag{12}$$

where $\langle i, j \rangle$ sums over every voxel i and its neighbours j.

4.3. The N3 method

Different from most IIH correction method which involves a classification step, Sled et al. [74] proposed a nonparametric nonuniform intensity normalization (N3) method which searches for the IIH field to maximize the frequency content of the image intensity distribution. The method simplified the problem in log-domain as a deconvolution problem by realizing that if v_1 and v_2 are two independent random variables with distributions V_1 and V_2, respectively, then the distribution of their sum is the convolution of V_1 and V_2 [75]. To constrain the solution space, the IIH field is modeled as a Gaussian distribution with small variance. Code for this method is publicly available.[1]

5. OTHER APPROACHES

5.1. Comparison between local and global statistics

There are efforts [76, 77] to estimate the IIH by comparing a local statistic with the global one. The two statistics are assumed to characterize the same population. These methods essentially relate the IIH correction to tissue segmentation, and the implicit assumptions are (1) the constant intensity for a tissue and (2) that the intensity variation within a tissue is solely due to IIH. Not surprisingly, these methods are sensitive to the estimation of tissue statistics, which is nontrivial in practice.

When GM and WM are combined as one class and the local statistic is estimated from a sample in a local region as done in [76, 77], the method can be regarded as a generalized white matter method by Dawant et al. [48], where the reference tissue is the combination of GM and WM. Also, it can be taken as a lowpass filtering estimation. Although it is usually much easier to identify GM and WM together than to identify WM alone, a potential problem is that the local sample could fail to adequately characterize the feature of the combined tissue class even though there is no artifact like IIH.

A possible solution is to carry out more detail tissue classification in each local region. For example, the technique proposed in [78, 79][2] estimated the global tissue mean values by empirical thresholding, while the local statistics are derived through fitting the local histogram with a theoretical distribution. After obtaining estimations of local correction factors, a smooth function is fitted among these data and applied to the whole brain volume for IIH removal.

5.2. Image feature-based methods

An image feature-based technique was reported in [80], where the IIH correction was decomposed into row and column correction. The correction factor at a voxel is firstly related to first-order difference at other voxels in the same row/column, then combined with those calculated in the rows/columns from the initial to the current one. The rationale underlying the computation is obscure from the description. However, it is very similar to that in [81]. In the latter technique, a smooth "variation" image was firstly derived from normalized intensity gradient field, where pixels with low intensity or high gradient magnitude are excluded. Then numerical integration was applied to the "variation" (first-order derivative) image to obtain an image, which only contains small variations and was used to determine the IIH map.

Vovk et al. [82, 83] proposed to use the probability distribution of image features for IIH correction, where the image feature includes the intensity and the second spatial derivative of the image. Similar to the usual intensity histogram, the joint probability distribution also contains information for classifying tissues and such information was encoded by entropy. The correction factor was derived so that the entropy would decrease, similar to [57].

5.3. Estimate without explicit modeling

There are methods [84–88] which consider the IIH as model parameters formulated in a segmentation framework. Suppose the segmentation is to optimize a functional $\Phi(\mathbf{y}, \theta, \beta)$, where $\mathbf{y}$ denotes the observed data, β the IIH term, and θ

[1] http://www.bic.mni.mcgill.ca/software/N3

[2] Available with the BrainSuite package (http://neuroimage.usc.edu/).

other parameters. Then one way to estimate β can be obtained by

$$\frac{\partial \Phi}{\partial \beta} = 0. \tag{13}$$

Rajapakse and Kruggel [84] used an MRF formulation, whereas Farag and his group exploited the fuzzy c-means clustering framework [85–88].

It is noted that in these methods no explicit assumption has been made on the IIH field, which can be advantageous over model-based methods, since the assumptions with a model could be violated in practice. On the other hand, the absence of constraints on the IIH solution could result in erroneous IIH maps that deviate far away from the truth. In addition, voxel-wise updating the IIH in an iterative process is time-consuming, hence techniques such as multigrid computing may help reduce the computation load.

5.4. Registration against template

Image registration has also been utilized to aid the IIH correction [89, 90]. In [90], the patient data was registered against a tissue reference template, which allows to estimate the IIH map by direct comparison between two images. Here human intervention was employed to ensure the correct correspondence between the distorted and the reference image.

5.5. Shape recovery

Lai and Fang [91] transformed the IIH correction into the problem of shape recovery with orientation constraint and solved the latter using regularization theory. The approach may result in solving a linear equation with a large matrix.

5.6. Deformed thin plate model

Bansal et al. [92] modelled the IIH field as a thin plate deforming elastically under a body force:

$$\mu \nabla^2 \beta + (\lambda + \mu) \nabla (\nabla \cdot \beta) + b(\beta) = 0, \tag{14}$$

where μ and λ are the elasticity constants. The body force $b(\beta)$ is evaluated to minimize the entropy of the observed image.

6. DISCUSSION

6.1. Integrated approaches

As seen from the description above, many IIH correction methods relate the problem with image segmentation and solve these two problems alternatively through an iteration process. Evidently, accurate segmentation would significantly ease the burden of IIH correction. Conversely, if the IIH has been precisely removed, the segmentation accuracy will in general be improved. Thus, it is not surprising to see overwhelming techniques addressing these two problems within a common framework.

Actually, it has been a trend in computer vision to imitate the human intelligent system and solve the different problems simultaneously. A typical computer vision system may consist of several individual processes, which can be solved sequentially. However, the solution of one process could be beneficial to the solution of another one and the converse may also hold. As an example, image denoising and edge detection are two closely related problems. And it is common to require a denoising algorithm able to preserve image edge structures, and an edge detection method robust against noise. For the problem of IIH correction, beside the connection with image segmentation as mostly noted, there are efforts that relate the solution to image registration, because the image quality can impose an impact on the accuracy of image registration and conversely a good registration against a template could greatly help derive a high-quality image. In addition, there even exist attempts to address these three processes, IIH correction, segmentation, and registration together [93, 94].

Among some processes, their relationship may not be very intimate, but different implementation order could result in different performance. In [68], it was found that denoising after IIH correction is more preferable. Madabhushi and Udupa [95] investigated the interplay between IIH correction and intensity standardization, and concluded that the better sequence is IIH correction followed by intensity standardization.

6.2. Validation and comparative study

For end users, it is natural to ask questions such as how to assess the performance of an IIH correction method, which method should be recommended when a practical medical image processing system encounters the problem of IIH correction, or if there is a method which exclusively outperforms others. To answer these questions, we need to do extensive comparisons under a variety of data sets. However, this turns out to be a difficult task, because the true amount of IIH is unknown for real data. The lack of ground truth is a common problem in evaluating a computer vision algorithm. There are two possible ways to circumvent this difficulty. One is to approximate the golden standard by experts' estimation, which is often a tedious task. Alternatively, we can use synthetic data. In IIH correction, the simulated brain images [7, 96] from the Montreal Neurological Institute[3] have been widely employed for validation.

(1) *Criteria*

The criteria that have been frequently used are listed in the following.

Cr-I The variance of the fully or a partially segmented image, which is supposed to decrease after the IIH correction. When this criterion is used for comparing different methods, the result could be misleading

[3] http://www.bic.mni.mcgill.ca/brainweb

because the variance is scale-variant. Usually, the mean-preserving condition is utilized to avoid this problem.

Cr-II The coefficient of variation, cv, of class Γ_i:

$$cv(\Gamma_i) = \frac{\sigma(\Gamma_i)}{\mu(\Gamma_i)}. \quad (15)$$

It can be shown that this quantity overcomes the limitation of the image variance. But the cv alone only characterizes the within-class scatter and a criterion that also takes into account the between-class scatter is as follows.

Cr-III The coefficient of joint variations between two classes

$$cjv(\Gamma_1, \Gamma_2) = \frac{\sigma(\Gamma_1) + \sigma(\Gamma_2)}{|\mu(\Gamma_1) - \mu(\Gamma_2)|}. \quad (16)$$

Moreover, one can also use the relative change of cjv as defined below:

$$\frac{cjv_a - cjv_b}{cjv_b} \times 100\%, \quad (17)$$

where the subscripts a and b denote after and before IIH correction.

Cr-IV Mean-square error, which directly measures the distance between the derived and the true IIH map.

Cr-V Segmentation accuracy, which indirectly reflects the effect of IIH correction. Care should be taken in interpreting the segmentation result since the latter could be complicated by other factors, like subject, scanner, noise, segmentation method, and so forth.

Cr-VI Stability, which means that an IIH correction algorithm is recursively applied to the corrected volume. For a good algorithm, the extracted IIH map is assumed to converge rapidly.

Cr-VII Computer requirement and CPU time.

From the list, one can observe that most criteria have their own limitations and some are applicable to simulated data only. However, simulated data might not adequately characterize real ones. For example, in [47], the proposed method was reported to be inferior to methods such as the N3 in terms of cv or cjv when tested on simulated data, but the order is reversed when tested against real volumes. Furthermore, the adaptivity of an algorithm is also important. For a method with good adaptivity, the approximated IIH map would approach a constant when the real IIH approaches zero.

(2) *Comparative study*

Compared to the numerous techniques for IIH correction, only a few studies have been carried out towards the comparative evaluation of existing algorithms. Sled et al. [97] have compared three IIH correction methods, the expectation maximization (EM) [67], the white matter (WM) [48], and the N3 method [74] using simulated T1, T2, and PD weighted data. It was shown that the WM method performs better than the other two methods for T1 weighted volumes, which might be due to the high contrast between the WM and other tissues in T1 weighted images. The EM method made excessively large corrections to voxels that fall outside the classifier's tissue model, as is consistent with that pointed out in [68]. Overall, the N3 method performs the most stable for all simulated images.

Velthuizen et al. [29] have evaluated four IIH correction methods (a phantom method [17], two lowpass filtering methods [36, 39], and a surface fitting method with reference points selected from white matter [48]) in brain tumor segmentation. The surface fitting method was found to be inferior to others, which could be due to the way the reference points were generated. As mentioned in Section 3.1, the latter is crucial to the performance of the surface fitting method. An automatic method to generate such reference points has been presented in [59]. Hou and Huang [98] have also developed a similar technique based on order statistics, which is very well comparable with the state-of-the-art IIH correction methods.

Although it turned out no improvement in tumor assessment after the IIH correction [29], it does not mean that IIH correction is not an obstacle to automatic medical image processing in general, since the tumor segmentation is characterized by the localization of the tumor region as well as the intensity contrast with surrounded tissue. Thus, the tumor segmentation could be less affected by the IIH artifact.

A more comprehensive study was presented in [66], where six algorithms, *n3* [74], *hum* [42], *eq* [43], *bfc* [78], *spm* (statistical parametric mapping)[4] [52], and *cma*[5] were compared against BrainWeb-simulated data as well as real volumes including repeated scans of the same subject, scans under different magnetic fields and different scanners. Three of the methods (*hum*, *eq*, and *cma*) are lowpass filtering based. The *spm* method is based on surface-fitting, and its parameters are estimated through integration with a tissue mixture model. It was found that the IIH maps obtained by filtering based methods can exhibit higher-frequency structures pertaining to brain anatomy. The *spm* method could be unstable when operating on relatively uniform image volumes and could lead to spurious solution for some volume. Overall, the *n3* and the *bfc* methods are superior to the other four methods. At lower bias levels, the estimated bias by *bfc* is more accurate than that by *n3*, and at higher bias levels, the order reverses. Nevertheless, none of the six methods performs ideally under all the circumstances investigated.

The problem of the *spm* might be similar to that of the EM method by Wells et al. [67]. Both methods utilized the mixture Gaussian classifier, which may be inadequate to model the image intensity distribution arising in practice. It should be pointed out that the *spm* method used in [66] is the SPM99 version, which has been updated to version SPM2 in 2003 with substantial improvement in theoretical modeling

[4] It is a part of the SPM99 software released by the Wellcome Department of Imaging Neuroscience (http://www.fil.ion.ucl.ac.uk/spm).

[5] Available in the Nautilos Library from the Center for Morphometric Analysis at the Massachusetts General Hospital.

or algorithmic design, and the latest version is SPM5. As to the three filtering-based methods, they lack a scheme to adapt the filtering strength to data quality, which may explain the inefficiency compared with the *n3* and the *bfc* methods. As mentioned in Section 2, filtering methods [45–47] with data adaptivity have been developed recently, which might outperform their conventional counterparts.

Although further comparative study using more extensive MR images is necessary, it might be inappropriate for end users to expect an algorithm superior to others and exclusively applicable. In general, each method has its underlying assumptions and limitations and the choice of which method to use is intimately interwined with the problem to solve, the source, and quality of the data. Many methods have attempted to correct the IIH artifact in brain MR images, some of which require the removal of the scalp/skull before the correction process, while others do not. Although sophisticated methods may be able to correct for IIH more accurately, one would also have to consider the expense of computer cost as well as the final segmentation error. Among the publicly available softwares, the N3 method has been widely used and its performance has been well demonstrated, while the BFC method can be advantageous when the image is also contaminated by severe noise [98].

7. CONCLUSION

This paper presented a summary of the recent progress on MR image IIH correction. The most popular models to describe the IIH field are the low frequency, the hypersurface, and the statistical model. Filtering methods are fast, easy to code and widely used. With optimization in scale space, the filtering method can also be adaptive to image data. Surface fitting and statistical methods are easy to integrate with other knowledge such as segmentation, registration, or some image feature, thus could in principle provide more reliable solution, which have been and will be the trend in the field. Some techniques based on other IIH correction principles were also reviewed in the paper. In future, it might be of interest to have more extensive investigations on evaluation of existing methods.

REFERENCES

[1] G. H. Glover, C. E. Hayes, N. J. Pelc, et al., "Comparison of linear and circular polarization for magnetic resonance imaging," *Journal of Magnetic Resonance*, vol. 64, no. 2, pp. 255–270, 1985.

[2] I. Harvey, P. S. Tofts, J. K. Morris, D. A. G. Wicks, and M. A. Ron, "Sources of T_1 variance in normal human white matter," *Magnetic Resonance Imaging*, vol. 9, no. 1, pp. 53–59, 1991.

[3] A. Simmons, P. S. Tofts, G. J. Barker, and S. R. Arridge, "Sources of intensity nonuniformity in spin echo images at 1.5T," *Magnetic Resonance in Medicine*, vol. 32, no. 1, pp. 121–128, 1994.

[4] G. J. Barker, A. Simmons, S. R. Arridge, and P. S. Tofts, "A simple method for investigating the effects of non-uniformity of radiofrequency transmission and radiofrequency reception in MRI," *British Journal of Radiology*, vol. 71, no. 841, pp. 59–67, 1998.

[5] M. Alecci, C. M. Collins, M. B. Smith, and P. Jezzard, "Radio frequency magnetic field mapping of a 3 Tesla birdcage coil: experimental and theoretical dependence on sample properties," *Magnetic Resonance in Medicine*, vol. 46, no. 2, pp. 379–385, 2001.

[6] M. Styner, C. Brechbuhler, G. Szekely, and G. Gerig, "Parametric estimate of intensity inhomogeneities applied to MRI," *IEEE Transactions on Medical Imaging*, vol. 19, no. 3, pp. 153–165, 2000.

[7] D. L. Collins, A. P. Zijdenbos, J. G. Sled, N. J. Kabani, C. J. Holmes, and A. C. Evans, "Design and construction of a realistic digital brain phantom," *IEEE Transactions on Medical Imaging*, vol. 17, no. 3, pp. 463–468, 1998.

[8] P. A. Narayana, W. W. Brey, M. V. Kulkarni, and C. L. Sievenpiper, "Compensation for surface coil sensitivity variation in magnetic resonance imaging," *Magnetic Resonance Imaging*, vol. 6, no. 3, pp. 271–274, 1988.

[9] W. W. Brey and P. A. Narayana, "Correction for intensity falloff in surface coil magnetic resonance imaging," *Medical Physics*, vol. 15, no. 2, pp. 241–245, 1988.

[10] R. Stollberger and P. Wach, "Imaging of the active b1 field in vivo," *Magnetic Resonance in Medicine*, vol. 35, no. 2, pp. 246–251, 1996.

[11] P. J. Reber, E. C. Wong, R. B. Buxton, and L. R. Frank, "Correction of off resonance-related distribution in echo-planar imaging using EPI-based field maps," *Magnetic Resonance in Medicine*, vol. 39, pp. 328–330, 1998.

[12] K. R. Thulborn, F. E. Boada, G. X. Shen, J. D. Christensen, and T. G. Reese, "Correction of B1 inhomogeneities using echo-planar imaging of water," *Magnetic Resonance in Medicine*, vol. 39, no. 3, pp. 369–375, 1998.

[13] J. G. Sled and G. B. Pike, "Correction for B_1 and B_0 variation in quantitative T_2 measurements using MRI," *Magnetic Resonance in Medicine*, vol. 43, no. 4, pp. 589–593, 2000.

[14] A. Fan, W. W. Wells, J. W. Fisher, et al., "A unified variational approach to denoising and bias correction in MR," in *Proceedings of the International Conference on Information Processing in Medical Imaging (IPMI '03)*, C. J. Taylor and J. A. Noble, Eds., vol. 2732 of *Lecture Notes in Computer Science*, pp. 148–159, Ambleside, UK, July 2003.

[15] J. Wang, M. Qiu, Q. X. Yang, M. B. Smith, and R. T. Constable, "Measurement and correction of transmitter and receiver induced nonuniformities in vivo," *Magnetic Resonance in Medicine*, vol. 53, no. 2, pp. 408–417, 2005.

[16] B. R. Condon, J. Patterson, D. Wyper, A. Jenkins, and D. M. Hadley, "Image nonuniformity in magnetic resonance imaging: its magnitude and methods for its correction," *The British Journal of Radiology*, vol. 60, pp. 83–87, 1987.

[17] D. A. G. Wicks, G. J. Barker, and P. S. Tofts, "Correction of intensity nonuniformity in MR images of any orientation," *Magnetic Resonance Imaging*, vol. 11, no. 2, pp. 183–196, 1993.

[18] M. Ticher, C. R. Meyer, R. Gupta, and D. M. Williams, "Polynomial modeling and reduction of RF body coil spatial inhomogeneity in MRI," *IEEE Transactions on Medical Imaging*, vol. 12, no. 2, pp. 361–365, 1993.

[19] F. B. Mohamed, S. Vinitski, S. H. Faro, and C. F. Gonzalez, "Optimization of tissue segmentation of brain MR images based on multispectral 3d feature maps," *Magnetic Resonance Imaging*, vol. 17, no. 3, pp. 403–409, 1999.

[20] G. Collewet, A. Davenel, C. Toussaint, and S. Akoka, "Correction of intensity nonuniformity in spin-echo T1-weighted images," *Medical Resonance Imaging*, vol. 20, no. 4, pp. 365–373, 2002.

[21] E. R. McVeigh, M. J. Bronskill, and R. M. Henkelman, "Phase and sensitivity of receiver coils in magnetic resonance imaging," *Medical Physics*, vol. 13, no. 6, pp. 806–814, 1986.

[22] P. B. Roemer, W. A. Edelstein, C. E. Hayes, S. P. Souza, and O. M. Mueller, "The NMR phased array," *Magnetic Resonance in Medicine*, vol. 16, no. 2, pp. 192–225, 1990.

[23] D. C. Noll, C. H. Meyer, J. M. Pauly, D. G. Nishimura, and A. Macovski, "A homogeneity correction method for magnetic resonance imaging with time-varying gradients," *IEEE Transactions on Medical Imaging*, vol. 10, no. 4, pp. 629–637, 1991.

[24] C. E. Hayes, N. Hattes, and P. B. Roemer, "Volume imaging with MR phased arrays," *Magnetic Resonance in Medicine*, vol. 18, no. 2, pp. 309–319, 1991.

[25] S. E. Moyher, D. N. Vigneron, and S. J. Nelson, "Surface coil MR imaging of the human brain with an analytic reception profile correction," *Journal of Magnetic Resonance Imaging*, vol. 5, no. 2, pp. 139–144, 1995.

[26] C. M. Collins, Q. X. Yang, J. H. Wang, et al., "Different excitation and reception distributions with a single-loop transmit-receive surface coil near a head-sized spherical phantom at 300 MHz," *Magnetic Resonance in Medicine*, vol. 47, no. 5, pp. 1026–1028, 2002.

[27] B. P. Sutton, D. C. Noll, and J. A. Fessler, "Fast, iterative image reconstruction for MRI in the presence of field inhomogeneities," *IEEE Transactions on Medical Imaging*, vol. 22, no. 2, pp. 178–188, 2003.

[28] M. Markl, R. Bammer, M. T. Alley, et al., "Generalized reconstruction of phase contrast MRI: analysis and correction of the effect of gradient field distortions," *Magnetic Resonance in Medicine*, vol. 50, no. 4, pp. 791–801, 2003.

[29] R. P. Velthuizen, A. B. Cantor, H. Lin, L. M. Fletcher, and L. P. Clarke, "Review and evaluation of MRI nonuniformity corrections for brain tumor response measurements," *Medical Physics*, vol. 25, no. 9, pp. 1655–1666, 1998.

[30] R. C. Gonzalez and R. E. Woods, *Digital Image Processing*, Addison-Wesley, Singapore, 1993.

[31] D. Tomaževič, B. Likar, and F. Pernuš, "Comparative evaluation of retrospective shading correction methods," *Journal of Microscopy*, vol. 208, no. 3, pp. 212–223, 2002.

[32] J. Haselgrove and M. Prammer, "An algorithm for compensation of surface-coil images for sensitivity of the surface coil," *Magnetic Resonance Imaging*, vol. 4, no. 6, pp. 469–472, 1986.

[33] L. Axel, J. Constantini, and J. Listerud, "Intensity correction in surface coil MR imaging," *American Journal of Roentgenology*, vol. 148, no. 2, pp. 418–420, 1987.

[34] K. O. Lim and A. Pfefferbaum, "Segmentation of MR brain images into cerebrospinal fluid spaces, white and gray matter," *Journal of Computer Assisted Tomography*, vol. 13, no. 4, pp. 588–593, 1989.

[35] T. L. Jernigan, G. A. Press, and J. R. Hesselink, "Methods for measuring brain morphologic features on magnetic resonance images: validation and normal aging," *Archives of Neurology*, vol. 47, no. 1, pp. 27–32, 1990.

[36] P. A. Narayana and A. Borthakur, "Effect of radio frequency inhomogeneity correction on the reproducibility of intracranial volumes using MR image data," *Magnetic Resonance in Medicine*, vol. 33, no. 3, pp. 396–400, 1995.

[37] L. L. Wald, L. Carvajal, S. E. Moyher, et al., "Phased array detectors and an automated intensity-correction algorithm for high-resolution MR imaging of the human brain," *Magnetic Resonance in Medicine*, vol. 34, no. 3, pp. 433–439, 1995.

[38] J. W. Murakami, C. E. Hayes, and E. Weinberger, "Intensity correction of phased-array surface coil images," *Magnetic Resonance in Medicine*, vol. 35, no. 4, pp. 585–590, 1996.

[39] B. Johnston, M. S. Atkins, B. Mackiewich, and M. Anderson, "Segmentation of multiple sclerosis lesions in intensity corrected multispectral MRI," *IEEE Transactions on Medical Imaging*, vol. 15, no. 2, pp. 154–169, 1996.

[40] P. Irarrazabal, C. H. Meyer, D. G. Nishimura, and A. Macovski, "Inhomogeneity correction using an estimated linear field map," *Magnetic Resonance in Medicine*, vol. 35, no. 2, pp. 278–282, 1996.

[41] A. L. Reiss, M. T. Abrams, H. S. Singer, J. L. Ross, and M. B. Denckla, "Brain development, gender and IQ in children: a volumetric imaging study," *Brain*, vol. 119, no. 5, pp. 1763–1774, 1996.

[42] B. H. Brinkmann, A. Manduca, and R. A. Robb, "Optimized homomorphic unsharp masking for MR grayscale inhomogeneity correction," *IEEE Transactions on Medical Imaging*, vol. 17, no. 2, pp. 161–171, 1998.

[43] M. S. Cohen, R. M. Dubois, and M. M. Zeineh, "Rapid and effective correction of RF inhomogeneity for high field magnetic resonance imaging," *Human Brain Mapping*, vol. 10, no. 4, pp. 204–211, 2000.

[44] J. Luo, Y. Zhu, P. Clarysse, and I. Magnin, "Correction of bias field in MR images using singularity function analysis," *IEEE Transactions on Medical Imaging*, vol. 24, no. 8, pp. 1067–1085, 2005.

[45] C. Han, T. S. Hatsukami, and C. Yuan, "A multi-scale method for automatic correction of intensity non-uniformity in MR images," *Journal of Magnetic Resonance Imaging*, vol. 13, no. 3, pp. 428–436, 2001.

[46] F. Lin, Y. Chen, J. W. Belliveau, and L. L. Wald, "A wavelet-based approximation of surface coil sensitivity profiles for correction of image intensity inhomogeneity and parallel imaging reconstruction," *Human Brain Mapping*, vol. 19, no. 2, pp. 96–111, 2003.

[47] J. D. Gispert, S. Reig, J. Pascau, J. J. Vaquero, P. Garcia-Barreno, and M. Desco, "Method for bias field correction of brain T1-weighted magnetic resonance images minimizing segmentation error," *Human Brain Mapping*, vol. 22, no. 2, pp. 133–144, 2004.

[48] B. M. Dawant, A. P. Zijdenbos, and R. A. Margolin, "Correction of intensity variations in MR images for computer-aided tissue classification," *IEEE Transactions on Medical Imaging*, vol. 12, no. 4, pp. 770–781, 1993.

[49] C. R. Meyer, P. H. Bland, and J. Pipe, "Retrospective correction of intensity inhomogeneities in MRI," *IEEE Transactions on Medical Imaging*, vol. 14, no. 1, pp. 36–41, 1995.

[50] K. V. Leemput, F. Maes, D. Vandermeulen, and P. Suetens, "Automated model-based bias field correction of MR images of the brain," *IEEE Transactions on Medical Imaging*, vol. 18, no. 10, pp. 885–896, 1999.

[51] J. Ashburner and K. Friston, "Multimodal image coregistration and partitioning: a unified framework," *NeuroImage*, vol. 6, no. 3, pp. 209–217, 1997.

[52] J. Ashburner and K. Friston, "MRI sensitivity correction and tissue classification," *NeuroImage*, vol. 7, no. 4, part II, p. S706, 1998.

[53] J. Ashburner, *Computational neuroanatomy*, Ph.D. thesis, University College London, London, UK, 2000.

[54] J. Ashburner and K. J. Friston, "Voxel-based morphometry: the methods," *NeuroImage*, vol. 11, no. 6, part I, pp. 805–821, 2000.

[55] J. F. Mangin, "Entropy minimization for automatic correction of intensity nonuniformity," in *Proceedings of IEEE Workshop on Mathematical Methods in Biomedical Image Analysis*, pp. 162–169, Hilton Head Island, SC, USA, 2000.

[56] B. Likar, J. B. A. Maintz, M. A. Viergever, and F. Pernuš, "Retrospective shading correction based on entropy minimization," *Journal of Microscopy*, vol. 197, no. 3, pp. 285–295, 2000.

[57] B. Likar, M. A. Viergever, and F. Pernuš, "Retrospective correction of MR intensity inhomogeneity by information minimization," *IEEE Transactions on Medical Imaging*, vol. 20, no. 12, pp. 1398–1410, 2001.

[58] A. W.-C. Liew and H. Yan, "An adaptive spatial fuzzy clustering algorithm for 3-D MR image segmentation," *IEEE Transactions on Medical Imaging*, vol. 22, no. 9, pp. 1063–1075, 2003.

[59] D. Wang, S. E. Rose, J. B. Chalk, D. M. Doddrell, and J. Semple, "Improved version of white matter method for correction of non-uniform intensity in MR images: application to the quantification of rates of brain atrophy in Alzheimer's disease and normal aging," in *Proceedings of Medical Imaging 2000: Image Processing*, vol. 3979 of *Proceedings of SPIE*, pp. 760–771, San Diego, Calif, USA, February 2000.

[60] S. P. Liou, A. H. Chiu, and R. C. Jain, "A parallel technique for signal-level perceptual organization," *IEEE Transactions on Pattern Analysis and Machine Intelligence*, vol. 13, no. 4, pp. 317–325, 1991.

[61] P. K. Saha, J. K. Udupa, and D. Odhner, "Scale-based fuzzy connected image segmentation: theory, algorithms, and validation," *Computer Vision and Image Understanding*, vol. 77, no. 2, pp. 145–174, 2000.

[62] A. Madabhushi, J. K. Udupa, and A. Souza, "Generalized scale: theory, algorithms, and application to image inhomogeneity correction," in *Proceedings of Medical Imaging 2004: Image Processing*, vol. 5370 of *Proceedings of SPIE*, pp. 765–776, San Diego, Calif, USA, February 2004.

[63] S. Prima, N. Ayache, T. Barrick, and N. Roberts, "Maximum likelihood estimation of the bias field in MR brain images: investigating different modelings of the Imaging process," in *Proceedings of the 4th International Conference on Medical Image Computing and Computer-Assisted Intervention (MICCAI '01)*, vol. 2208 of *Lecture Notes in Computer Science*, pp. 811–819, Utrecht, The Netherlands, October 2001.

[64] A. Jannetta, J. C. Jackson, C. J. Kotre, I. P. Birch, K. J. Robson, and R. Padgett, "Mammographic image restoration using maximum entropy deconvolution," *Physics in Medicine and Biology*, vol. 49, no. 21, pp. 4997–5010, 2004.

[65] M. I. Reis and N. C. Roberty, "Maximum entropy algorithms for image reconstruction from projections," *Inverse Problems*, vol. 8, pp. 623–644, 1992.

[66] J. B. Arnold, J. Liow, K. A. Schaper, et al., "Qualitative and quantitative evaluation of six algorithms for correcting intensity nonuniformity effects," *NeuroImage*, vol. 13, no. 5, pp. 931–943, 2001.

[67] W. M. Wells III, W. E. L. Grimson, R. Kikinis, and F. A. Jolesz, "Adaptive segmentation of MRI data," *IEEE Transactions on Medical Imaging*, vol. 15, no. 4, pp. 429–442, 1996.

[68] R. Guillemaud and M. Brady, "Estimating the bias field of MR images," *IEEE Transactions on Medical Imaging*, vol. 16, no. 3, pp. 238–251, 1997.

[69] K. Held, E. R. Kops, B. J. Krause, W. M. Wells III, R. Kikinis, and H. M. Gartner, "Markov random field segmentation of brain MR images," *IEEE Transactions on Medical Imaging*, vol. 16, no. 6, pp. 878–886, 1997.

[70] Y. Zhang, M. Brady, and S. Smith, "Segmentation of brain MR images through a hidden Markov random field model and the expectation-maximization algorithm," *IEEE Transactions on Medical Imaging*, vol. 20, no. 1, pp. 45–57, 2001.

[71] J. L. Marroquin, B. C. Vemuri, S. Botello, F. Calderon, and A. Fernandez-Bouzas, "An accurate and efficient Bayesian method for automatic segmentation of brain MRI," *IEEE Transactions on Medical Imaging*, vol. 21, no. 8, pp. 934–945, 2002.

[72] S. Geman and D. Geman, "Stochastic relaxation, Gibbs distributions, and the Bayesian restoration of images," *IEEE Transactions on Pattern Analysis and Machine Intelligence*, vol. 6, no. 6, pp. 721–741, 1984.

[73] J. Besag, "Spatial interation and the statistical analysis of lattice systems," *Journal of the Royal Statistical Society B*, vol. 36, no. 2, pp. 192–225, 1974.

[74] J. G. Sled, A. P. Zijdenbos, and A. C. Evans, "Nonparametric method for automatic correction of intensity nonuniformity in MRI data," *IEEE Transactions on Medical Imaging*, vol. 17, no. 1, pp. 87–97, 1998.

[75] L. Devroye, *Non-Uniform Random Variate Generation*, Prentice-Hall, Englewood Cliffs, NJ, USA, 1986.

[76] S. K. Lee and M. W. Vannier, "Post-acquisition correction of MR inhomogeneities," *Magnetic Resonance in Medicine*, vol. 36, no. 2, pp. 275–286, 1996.

[77] C. DeCarli, D. G. M. Murphy, M. Tran, and D. Teichberg, "Local histogram correction of MRI spatially dependent image pixel intensity nonuniformity," *Journal of Magnetic Resonance Imaging*, vol. 6, no. 3, pp. 519–528, 1996.

[78] D. W. Shattuck, S. R. Sandor-Leahy, K. A. Schaper, D. A. Rottenberg, and R. M. Leahy, "Magnetic resonance image tissue classification using a partial volume model," *NeuroImage*, vol. 13, no. 5, pp. 856–876, 2001.

[79] D. W. Shattuck and R. M. Leahy, "BrainSuite: an automated cortical surface identification tool," *Medical Image Analysis*, vol. 6, no. 2, pp. 129–142, 2002.

[80] A. Koivula, J. Alakuijala, and O. Tervonen, "Image feature based automatic correction of low-frequency spatial intensity variations in MR images," *Magnetic Resonance Imaging*, vol. 15, no. 10, pp. 1167–1175, 1997.

[81] E. A. Vokurka, N. A. Thacker, and A. Jackson, "A fast model independent method for automatic correction of intensity nonuniformity in MRI data," *Journal of Magnetic Resonance Imaging*, vol. 10, no. 4, pp. 550–562, 1999.

[82] U. Vovk, F. Pernuš, and B. Likar, "Multi-feature intensity inhomogeneity correction in MR images," in *Proceedings of the 7th International Conference on Medical Image Computing and Computer-Assisted Intervention (MICCAI '04)*, pp. 283–290, Saint-Malo, France, September 2004.

[83] U. Vovk, F. Pernuš, and B. Likar, "MRI intensity inhomogeneity correction by combining intensity and spatial information," *Physics in Medicine and Biology*, vol. 49, no. 17, pp. 4119–4133, 2004.

[84] J. C. Rajapakse and F. Kruggel, "Segmentation of MR images with intensity inhomogeneities," *Image and Vision Computing*, vol. 16, no. 3, pp. 165–180, 1998.

[85] D. L. Pham and J. L. Prince, "Adaptive fuzzy segmentation of magnetic resonance images," *IEEE Transactions on Medical Imaging*, vol. 18, no. 9, pp. 737–752, 1999.

[86] D. L. Pham and J. L. Prince, "An adaptive fuzzy c-means algorithm for image segmentation in the presence of intensity inhomogeneities," *Pattern Recognition Letters*, vol. 20, no. 1, pp. 57–68, 1999.

[87] M. N. Ahmed, S. M. Yamany, N. A. Mohamed, and A. A. Farag, "A modified fuzzy c-means algorithm for MRI bias-field estimation and adaptive segmentation," in *Proceedings of the International Conference on Medical Image Computing and Computer-Assisted Intervention (MICCAI '99)*, pp. 72–81, Cambridge, UK, September 1999.

[88] M. N. Ahmed, S. M. Yamany, N. Mohamed, A. A. , Farag, and T. Moriarty, "A modified fuzzy c-means algorithm for bias field estimation and segmentation of MRI data," *IEEE Transactions on Medical Imaging*, vol. 21, no. 3, pp. 193–199, 2002.

[89] K. J. Friston, J. Ashburner, C. D. Frith, J. D. Heather, J. B. Poline, and R. S. J. Frackowiak, "Spatial registration and normalization of images," *Human Brain Mapping*, vol. 3, no. 3, pp. 165–189, 1995.

[90] C. Studholme, V. Cardenas, E. Song, F. Ezekiel, A. Maudsley, and M. Weiner, "Accurate template-based correction of brain MRI intensity distortion with application to dementia and aging," *IEEE Transactions on Medical Imaging*, vol. 23, no. 1, pp. 99–110, 2004.

[91] S. H. Lai and M. Fang, "A new variational shape-from-orientation approach to correcting intensity inhomogeneities in magnetic resonance image," *Medical Image Analysis*, vol. 3, no. 4, pp. 409–424, 1999.

[92] R. Bansal, L. H. Staib, and B. S. Peterson, "Correcting nonuniformities in MRI intensities using entropy minimization based on an elastic model," in *Proceedings of the 7th International Conference on Medical Image Computing and Computer-Assisted Intervention (MICCAI '04)*, pp. 78–86, Saint-Malo, France, September 2004.

[93] B. Fischl, D. H. Salat, E. Busa, et al., "Whole brain segmentation: automated labeling of neuroanatomical structures in the human brain," *Neuron*, vol. 33, no. 3, pp. 341–355, 2002.

[94] J. Ashburner and K. J. Friston, "Unified segmentation," *NeuroImage*, vol. 26, no. 3, pp. 839–851, 2005.

[95] A. Madabhushi and J. K. Udupa, "Interplay between intensity standardization and inhomogeneity correction in MR image processing," *IEEE Transactions on Medical Imaging*, vol. 24, no. 5, pp. 561–576, 2005.

[96] C. Cocosco, V. Kollokian, R. S. Kwan, and A. Evans, "Brain web: online interface to a 3D MRI simulated brain database," *NeuroImage*, vol. 5, no. 4, part II, p. S425, 1997.

[97] J. G. Sled, A. P. Zijdenbos, and A. C. Evans, "A comparison of retrospective intensity non-uniformity correction methods for MRI," in *Proceedings of the15th International Conference in Information Processing in Medical Imaging*, vol. 1230 of *Lecture Notes in Computer Science*, pp. 459–464, Poultney, Vt, USA, June 1997.

[98] Z. Hou and S. Huang, "Preliminary segmentation based on order statistics for intensity inhomogeneity correction in brain MR images," Technique Report, Singapore Bioimaging Consortium, Singapore, 2002, available upon request.

Zujun Hou is with Singapore Bioimaging Consortium as a Research Scientist. His research interest has evolved from ecology and bioremediation, chaotic system dynamics, to image processing and pattern recognition, with current focus on medical image processing and biometrics. He received the B.S. degree from the Department of Physics in Beijing Normal University, China, in 1991, the M.S. and the Ph.D. degrees from the Department of Physics and the Department of Computational Science in National University of Singapore, in 1999 and 2003, respectively.